Universitatea “POLITEHNICA” din Timişoara
Facultatea de Electronică şi Telecomunicaţii

Daniel-Cornel Belega

# Habilitation Thesis
# Teză de Abilitare

2013

# Contents

# 1. ABSTRACT

## 1.1. ABSTRACT

In the habilitation thesis my main professional and research results achieved during the period 2002 – 2013 are presented. The above period follows the public presentation of my doctoral thesis which was in 2001.

In the aforementioned period my main research fields were: *Signal Processing*, *Analog-to-Digital Converter* (ADC) *Testing*, and *Synchrophasor Measurements*.

In *Signal Processing* my work was focused on the parameter estimation of a sine-wave by both frequency-domain and time-domain methods. The frequency-domain methods used are the Interpolated Discrete Fourier Transform (IpDFT) method and the Energy-Based (EB) method. Conversely, the time-domain methods used are the sine-fitting algorithms. In *ADC Testing* I worked on the analysis of the estimation accuracy of some of the most important dynamic parameters of an ADC, which are the Effective Number Of Bits (*ENOB*) and SIgnal-to-Noise And Distortion ratio (*SINAD*), achieved by means of the frequency-domain and time-domain sine-fitting algorithms when the sine-wave test signal is non-coherent sampled. In *Synchrophasor Measurements* my work is recent (beginning in 2011) and it is performed in order to find the best frequency-domain and time-domain algorithms which should be adopted for fast and accurate synchrophasor estimation. The used frequency-domain methods are based on the DFT and the used time-domain algorithms are based on Least Squares (LS) algorithm.

The habilitation thesis contains three Sections. In the first Section an overview of my teaching and research activities is performed. Also, the achievements related to both these activities are revealed. In the next Section my main contributions to each aforementioned research field are presented in a separate subsection.

In the first subsection the IpDFT and EB methods are separately presented. In the EB method both direct and indirect procedures are considered. For each method the expressions for the variances of parameter estimators are given. Besides, for the IpDFT method the expressions of the combined standard uncertainty and the PDF of the frequency estimator are given. Also, the criterion proposed for selection of the optimal window to be used in the IpDFT method is presented. Furthermore, two multipoint IpDFT methods for frequency estimation are described and their performances are compared. Besides, the expression of the combined standard uncertainty of the frequency estimator achieved by the most suited to be used in practice multipoint IpDFT is given. Then, the performance of the average-based IpDFT method is presented. Also, the effectiveness of a multipoint IpDFT method for amplitude estimation as compared with the IpDFT method is revealed. It should be noted that the multipoint IpDFT methods reduces the detrimental effect of the spectral interference due to the fundamental image component to the parameter estimation achieved by the IpDFT

method. Conversely, the results of the comparison between the theoretical means of the sum-squared fitting and residual errors achieved by the three-parameter sine-fitting (3PSF) algorithm with frequency *a priori* estimated by the IpDFT method (3PSF-IpDFT algorithm) and the four-parameter sine-fitting (4PSF) algorithm are presented. In the second subsection the procedure used to estimate the *SINAD* and *ENOB* parameters by a sine-fitting algorithm is given. Then, the expressions for the mean and variance of the *ENOB* estimates provided by a sine-fitting algorithm are presented. In the third subsection the synchrophasor estimation results achieved by some DFT-based estimators in the case of an electrical signal with decaying dc offset component are presented. Then, the performance of the IpDFT synchrophasor estimator is presented. In all subsections computer simulations and experimental results are shown. The last Section of the habilitation thesis presents the perspectives of future works. There are specified new possible research directions in the aforementioned fields and a new research field.

It is worth noticing that the main results achieved in *Signal Processing* field were published in 12 papers (all as first author) in the following prestigious measurements ISI journal: *IEEE Transactions on Instrumentation and Measurement*, *Measurement*, *IET Science Measurement and Technology*, *Computer Standards & Interfaces*, and *Measurement Techniques*. Also, the main results achieved in *ADC Testing* were published in 5 papers (all as first author) in *IEEE Transactions on Instrumentation and Measurement* and *Measurement* journals. Moreover, I am coauthor of the Chapter entitled "*Dynamic testing of analog-to-digital converters by means of the sine-fitting algorithms*," of the book *Design, Modeling, and Testing of Data Converters*, which is now in press at Springer-Verlag Publisher, Germany. The main results achieved in *Synchrophasor Measurements* were published in 2 papers (one as first authors) in the *IEEE Transactions on Instrumentation and Measurement* journal.

## 1.2. REZUMAT

În cadrul tezei de abilitare sunt prezentate cele mai importante rezultate profesionale şi ştiinţifice pe care le-am obţinut în perioada 2002 – 2013. Această perioadă urmează prezentării publice a tezei mele de doctorat, care a avut loc în 2001.

În perioada mai sus amintită principalele mele domenii de cercetare au fost: *Prelucrarea Semnalelor*, *Testarea Convertoarelor Analog-Numerice* (CAN) şi *Măsurarea Sincrofazorilor*.

În *Prelucrarea Semnalelor* am lucrat la estimarea parametrilor unui semnal sinusoidal pe baza metodelor în domeniul frecvenţă şi în domeniul timp. Metodele în domeniul frecvenţă folosite au fost metoda de interpolare a transformatei Fourier discrete (metoda IpDFT) şi metoda bazată pe energia semnalului (metoda EB). Pe de altă parte, metodele în domeniul timp folosite au fost algoritmii de determinare a celui mai potrivit semnal sinusoidal. În *Testarea CAN* am analizat exactitatea de estimare a unora dintre cei mai importanţi parametri dinamici ai unui CAN, care sunt numărul de biţi efectivi (*ENOB*) şi raportul semnal-zgomot plus distorsiuni (*SINAD*) pe baza metodelor în domeniul frecvenţă şi în domeniul timp de determinarea a celui mai potrivit semnal sinusoidal. În *Măsurarea Sincrofazorilor* cercetarea mea este recentă (începând din anul 2011) şi are drept scop determinarea celor mai performanţi algoritmi în domeniul freveņţă şi în domeniul timp care să permită estimarea cu exactitate şi rapiditate a sincrofazorilor. Algoritmii în domeniul frecvenţă utilizaţi au fost bazaţi pe transformata Fourier discretă, iar în domeniul timp pe algoritmul celor mai mici pătrate.

Teza de abilitare conţine trei Secţiuni. In prima Secţiune sunt prezentate activităţile mele didactice şi de cercetare. De asemenea, sunt prezentate realizările pe care le-am obţinut în cadrul acestor activităţi. In următoarea Secţiune sunt prezentate, în cadrul unei subsecţiuni, cele mai importante rezultate ştinţifice pe care le-am obţinut în fiecare dintre domeniile de cercetare ştiinţifică menţionate anterior.

În prima subsecţiune metodele IpDFT şi EB sunt prezentate separat. În cadrul metodei EB sunt folosite ambele proceduri, cea directă şi cea indirectă. Pentru fiecare dintre metode sunt date expresiile varianţelor estimatorilor parametrilor. În plus, pentru metoda IpDFT sunt date expresiile incertitudinii compuse, precum şi a funcţiei densităţii de probabilitate a estimatorului frecvenţei. De asemenea, este prezentat criteriul propus pentru alegerea ferestrei optime folosite în cadrul metodei IpDFT. În continuare, sunt descrise două metode multipunct IpDFT folosite pentru estimarea frecvenţei, iar performanţele lor sunt comparate. În plus, este dată expresia incertitudinii compuse a estimatorului frecvenţei furnizat de cea mai potrivită metodă multipunct IpDFT pentru a fi utilizată în practică. Apoi, performanţele metodei IpDFT pe baza mediei sunt prezentate. De asemenea, eficienţa unei metode multipunct IpDFT pentru estimarea amplitudinii în raport cu metoda IpDFT este pusă în evidenţă. Trebuie remarcat faptul că metodele multipunct IpDFT sunt folosite pentru a reduce efectul nedorit al interferenţei spectrale din partea componentei imagine a fundamentalei asupra estimării parametrilor pe baza metodei IpDFT. Pe de altă parte, sunt prezentate rezultatelor comparării mediilor teoretice ale sumelor pătratelor erorilor de potrivire şi reziduale obţinute pe baza algoritmilor de potrivire cu trei parametrii estimați (algoritmul 3PSF), în care frecvența a fost *a priori* estimată pe baza metodei IpDFT (algoritmul 3PSF-IpDFT) şi de potrivire cu patru parametrii estimați (algoritmul 4PSF). În subsecțiunea a doua este prezentată procedura folosită pentru estimarea parametrilor *SINAD* şi *ENOB* ai unui CAN pe baza unui algorithm de determinare a celui mai potrivit semnal sinusoidal. Apoi, sunt date expresiile mediei şi varianței estimatorului *ENOB* obținut pe baza acestei proceduri. În subsecțiunea a treia sunt prezentate rezultatele estimării sincrofazorilor obținute folosind o serie de estimatori bazați pe DFT în cazul în care semnalul electric conține o componentă de decalaj exponențială. Apoi, este prezentată performanța estimatorului sincrofazorului obținut pe baza algoritmului IpDFT. În toate subsecțiunile sunt prezentate rezultate obținute prin simulare şi pe cale experimentală. Ultima Secțiune a tezei de abilitare prezintă perspective ale dezvoltării viitoare. Sunt prezentate noi posibile direcții de cercetare în domeniile specificate anterior, precum şi un nou domeniu de cercetare.

Trebuie menționat faptul că principalele rezultate ştiințifice obținute în *Prelucrarea Semnalelor* au fost publicate în 12 articole (toate ca prim autor) în următoarele prestigioase reviste ISI de măsurări: *IEEE Transactions on Instrumentation and Measurement*, *Measurement*, *IET Science Measurement and Technology*, *Computer Standards & Interfaces* şi *Measurement Techniques*. De asemenea, principalele rezultate ştiințifice obținute în *Testarea CAN* au fost publicate în 5 articole (toate ca prim autor) în cadrul revistelor *IEEE Transactions on Instrumentation and Measurement* şi *Measurement*. Mai mult, sunt coautorul Capitolului intitulat "*Dynamic testing of analog-to-digital converters by means of the sine-fitting algorithms*," al cărții intitulate *Design, Modeling, and Testing of Data Converters*, care este, în momentul de față, în curs de publicare la Editura Springer-Verlag, Germania. Principalele rezultate ştiințifice obținute în *Măsurarea Sincrofazorilor* au fost publicate în 2 articole (unul ca prim autor) în cadrul revistei *IEEE Transactions on Instrumentation and Measurement*.

# 2. TEHNICAL PRESENTATION

## 2.1. OVERVIEW OF ACTIVITY AND RESULTS, 2002 – 2013

The title of my PhD thesis was “Contributions to the Analog-to-Digital Converters Testing”. I presented the thesis at “Politehnica” University of Timişoara in 2001. After my thesis I worked in three research fields, which are: *Signal Processing*, *Analog-to-Digital Converter (ADC) Testing*, and *Synchrophasor Measurements*. In these fields, during the period 2002 – 2013, I published more than 60 papers, among which 19 papers (18 as first author) in the following prestigious ISI measurement journals: *IEEE Transactions on Instrumentation and Measurement*, *Measurement*, *IET Science Measurement and Technology*, *Computer Standards & Interfaces*, and *Measurement Techniques*.

In the first two research fields I worked in principal with Professor Dominique Dallet with the Laboratoire d’Intégration du Matériau au Systèm (IMS), University of Bordeaux, France, and with Professor Dario Petri with the Department of Industrial Engineering, University of Trento, Italy. In *Synchrophasor Measurement* field I worked with Professor Dario Petri and the members of his research team. The papers written in collaborations can be found using the following personal web pages of the Professor Dominique Dallet:

http://www.ims-bordeaux.fr/IMS/pages/pageAccueilPerso.php?email=dominique.dallet

and the Professor Dario Petri:

http://disi.unitn.it/users/dario.petri

In the *Signal Processing* field I worked on the parameter estimation of a sine-wave by means of both frequency-domain and time-domain methods. Two frequency-domain methods were analyzed, which are the Interpolated Discrete Fourier Transform (IpDFT) method and the Energy-Based (EB) method. Conversely, the analyzed time-domain methods were the three-parameter sine-fitting (3PSF), the four-parameter sine-fitting (4PSF), and the multi-harmonic sine-fitting (MHSF) algorithms.

A great part of my research work was dedicated to the IpDFT method. That method is often used in practice since it allows us to compensate both the spectral leakage effect due to the finite duration of the observation interval and the picket-fence effect due to the granularity between adjacent DFT samples. Moreover, it is very simple to understand and to apply. In the IpDFT method the cosine windows are often adopted. In particular, when the Maximum Sidelobe Decay (MSD) windows, also known as class I Rife-Vincent windows, are adopted the IpDFT parameter estimators are provided by simple analytical expressions. I derived the analytical expressions for the $H$-term MSD window coefficients ($H \geq 2$) [Belega 05a] and its Discrete-Time Fourier Transform (DTFT) [Belega 07a]. One of my most important contributions to the IpDFT method was the derivation of the expressions for the variances of the parameter estimators in the case of a sine-wave corrupted by an additive white noise [Belega 09a]. Also, the expression of the frequency estimation error due to the spectral interference from the fundamental component was derived [Belega 12a], [Belega 09b]. Furthermore, when the MSD window is adopted two constraints for the integer part of the acquired sine-wave cycles and the number of analyzed samples were derived to ensure an accurate estimation of the frequency by the IpDFT method [Belega 09c]. Also, the expression of the combined standard uncertainty of the frequency estimator was derived [Belega 10a]. Based on that expression a criterion for selection of the optimal MSD window to be adopted was proposed [Belega 11a]. Moreover, the expression of the

Probability Density Function (PDF) of the frequency estimator provided by the IpDFT method was derived when some commonly used cosine windows are adopted [Belega 12a].

To reduce the detrimental effect of the spectral interference from the fundamental image component to the parameter estimates achieved by the IpDFT method, which occurs at small number of acquired sine-wave cycles, the multipoint IpDFT methods should be used. A novel multipoint IpDFT method for frequency estimation was proposed [Belega 08a] and another one, already proposed in the scientific literature, was generalized for a higher window order [Belega 10a]. Both above multipoint IpDFT methods are based on the MSD windows and use an odd number of selected DFT samples. It has been shown that both these methods exhibit almost the same effectiveness in reducing the contribution of the spectral interference on the estimated frequency, but the latter one involve more simple mathematical expressions [Belega 10b]. For that method the expressions for the estimation errors due to the spectral interference from the fundamental image component and the variance were derived in the case of a sine-wave corrupted by an additive white noise [Belega 10a]. Then, using these expressions the combined standard uncertainty of the frequency estimation was derived [Belega 10a]. Also, the accuracy of the average-based IpDFT method for frequency estimation was analyzed [Belega 13a]. Furthermore, a multipoint IpDFT method for amplitude estimation, already proposed in the scientific literature, was generalized for a higher window order [Belega 09d]. That method is based on the MSD windows and uses an odd number of selected DFT samples. The expression of the estimation errors due to the spectral interference from the fundamental image component was derived and compared with that of the IpDFT method.

EB method is also often used because it is very simple to understand and to apply, and it provides accurate estimates of sine-wave parameters using very simple formulas. My work on the EB method was focused on the analysis of the effect of the algorithm error, spectral interference from the fundamental image component, and additive white noise superimposed to the sine-wave on the frequency and amplitude estimations [Belega 12b]. Also, the root mean square (rms) of the frequency and amplitude estimation error achieved taking into account all three contributions above were derived [Belega 12b]. The amplitude was estimated by both direct and indirect procedures. In the indirect procedure the amplitude is estimated by means of the frequency estimate achieved *a priori* by the EB method. The overall rms values of the amplitude estimation errors achieved by both above approaches were compared through computer simulations and experimental results [Belega 12c].

It should be noted that the statistical performance of the amplitude IpDFT estimator was compared with that of the amplitude EB estimator achieved by direct procedure through both computer simulations and experimental results in the case of a noisy harmonically distorted sine-wave [Belega 10c].

Furthermore, the performance provided by the three-parameter sine-fitting (3PSF) algorithm with frequency estimated by the IpDFT algorithm (3PSF-IpDFT algorithm) and the four-parameter sine-fitting (4PSF) algorithm when estimating the noise power of a sine-wave corrupted by white Gaussian noise was investigated. To this aim, the expressions for the expected sum-squared fitting and residual errors were derived assuming that the number of analyzed samples is sufficiently large [Belega 12d].

The aforementioned results achieved to the considered frequency-domain and time-domain methods are presented in subsection 2.2.

After my doctoral thesis, which was focused on the ADC testing, I worked on the ADC dynamic testing in multi-tone mode [Belega 04]. It was shown that in that mode the accuracy of the used sine-wave test signals can be smaller than that of the sine-wave test signal used in the single-tone mode, and the required accuracy of the used sine-waves decreases as the number of tones increase. Then, I analyzed the estimation accuracy of the ADC dynamic parameter Effective Number Of Bits (*ENOB*) achieved by means of the beat test using the IpDFT method [Belega 05b]. Furthermore, the selection of the optimal window to be used in the spectral analysis based on the EB method was investigated for both single-tone and dual-tone modes [Belega 07b]. It was defined a novel performance parameter which allows us to choose the optimal window which should be adopted in the aforementioned ADC test. Then, the performances of the frequency-domain and time-domain sine-fitting algorithms when estimating *ENOB* parameter were analyzed [Belega 11a], [Belega 11b]. In the former sine-fitting algorithms the parameters of the ADC output signal are estimated by the frequency-domain methods, whereas in the latter algorithms by the time-domain methods. As frequency-domain methods were used the IpDFT and EB methods, whereas as time-domain methods were used the 3PSF-IpDFT and the 4PSF algorithms. It is worth noticing that the frequency-domain sine-fitting algorithms are novel procedures proposed to scientific community for the ADC testing by our research team. It was shown through both computer simulations and experimental results that the frequency-domain sine-fitting algorithms provide the same accurate *ENOB* estimates as the time-domain sine-fitting algorithms, but the required processing effort is much lower. Another important contribution is the derivation of the expressions for the mean and the variance of the *ENOB* estimator provided by a sine-fitting algorithm in the case of an ideal ADC and an ADC affected by harmonics, spurious tones, and additive white Gaussian noise [Belega 13b]. Also, a constraint for the frequency used in the 3PSF algorithm for accurate estimation of the *ENOB* was derived [Belega 07c].

It is worth noticing that I am author of the book entitle "*Analog-to-Digital Converter Testing*" (2004), which is the first Romanian book dedicated to the ADC testing. Also, I am coauthor of the Chapter entitled "*Dynamic testing of analog-to-digital converters by means of the sine-fitting algorithms*," of the book *Design, Modeling, and Testing of Data Converter*, which is now in press at Springer Verlag Publishing House. Moreover, I was scientific director of the following national grants supported by National University Research Council, Ministry of Education and Research (CNCSIS), Romania, focused on the ADC testing: *Dynamic Testing of Analog-to-Digital Converters in Multi-Tone Mode* (2004), *Dynamic Characterization and Modelling of Analog-to-Digital Converters Used in High Speeed Data Comunications* (2006), and *New Methods for Dynamic Characterization of High Resolution Analog-to-Digital Converters* (2007). The instruments and computers acquired for the experimental setups of the above grants were used to equip a laboratory from my Department.

The results specified above related to the sine-fitting algorithms are presented in subsection 2.3.

I began the work in the *Synchrophasor Measurement* field relative recent, in 2011. The first works were focused on the parameters estimation of an electrical signal in transient conditions, which contains the decaying dc offset. The behavior of the full-cycle DFT phasor estimator during transients has been analyzed. The theoretical expressions of the DFT-phasor estimator were derived in the case when the observation interval contains both an abrupt variation in the fundamental component amplitude and/or phase [Petri 11]. Using the achieved results, the worst-case phasor amplitude error during the whole estimation transient was determined [Petri 11]. The knowledge of the behavior of the phasor amplitude estimator during transients allows us to detect whether the disturbance contains or not a significant decaying dc offset. Furthermore, it was shown that the full-cycle DFT phasor estimator is sensitive to both harmonics and wideband noise and the accuracy is smaller in the transient conditions (with decaying dc offset) than in the steady state conditions (without decaying dc offset [Belega 11c]. The following works were focused on the synchrophasor estimation accuracy provided by the frequency-domain and time-domain algorithms. The analyses were performed under steady state, dynamic, and transient conditions. The considered test conditions comply with the IEEE Standard C37.118.1-2011 about synchrophasor measurements for power systems. The used frequency-domain algorithms were the classical DFT-based algorithm, the IpDFT algorithm, and the four-parameter model (4PM) and six-parameter model (6PM) algorithms [Belega 13c], [Barchi 13a]. In the latter two algorithms firstly the dynamic phasor is approximated by its Taylor's series expansion truncated to the $K$th order term ($K \geq 1$) and then the DFT of the approximated phasor is calculated. In the 4PM and 6PM algorithms $K = 1$ and $K = 2$, respectively. Conversely, the phasor components can be estimated by applying the Least Squares (LS) or the Weighted Least Squares (WLS) algorithms to the above approximated phasor. The accuracy of the phasor estimator achieved by both above algorithms, called LS-based or WLS-based estimators, were analyzed. Some of the above achieved results on the synchrophasor estimation are presented in subsection 2.4.

It is worth noticing that for 11 papers published in the ISI journals during the period 2007-2010, I received from the CNCSIS the Prizes for Research Results.

The experience gained in the aforementioned research fields was very useful for my teaching activity in several disciplines: Measurement Techniques, Sensors and Transducers (second year, undergraduate level), Electrical and Electronic Measurements (first year, undergraduate level), and Digital Signal Processors and Acquisition Systems (first year, graduate level). I wrote the books entitled *Electrical and Electronic Measurements* (2005) and *Measurement Techniques, Sensors and Transducers. Practical Applications* (2010) as support for the first two disciplines. Furthermore, I wrote the problem books, entitled *Electrical and Electronic Measurements. Problems*, which is used also as support for the above specified disciplines. In that book there exist several problems related to the statistical performance of the IpDFT method.

I am reviewer for the following ISI foreign journals: *IEEE Transactions on Instrumentation and Measurement* (from 2008), *IET Science Measurement and Technology* (from 2009), *Measurement* (from 2011), *Digital Signal Processing* (from 2012), *IEEE Transactions on Power Delivery* (from 2013), and *IET Signal Processing* (from 2013). Untill now I performed 73 reviews for the above journals, in which 57 were for the *IEEE Transactions on Instrumentation and Measurement* journal. For that activity I received from the IEEE Instrumentation and Measurement Society for two times the Prizes: *Recognition as one of Transactions "Outstanding Reviewers of 2009"* and *"Outstanding Reviewers of 2012"*, respectively.

Also, I was reviewer for several conferences, such as IEEE Instrumentation and Measurement Technology conference (IMTC), International Measurement Confederation (IMEKO) TC4 conference, IEEE International Symposium on Circuits and Systems (ISCAS).

Furthermore, it should be noted that in 2010 and 2013, I was selected by Thomson Reuters to participate at the Academic Reputation Survey, data from which supports the *Times Higher Education World University Ranking*.

## 2.2. CONTRIBUTIONS TO SIGNAL PROCESSING FIELD

### 2.2.1. FREQUENCY-DOMAIN METHODS

### A. Windowing Approach

In that subsection the parameters often used in the derived expressions are defined. Moreover, my contributions to the expressions of these parameters are presented.

We consider a discrete-time sine-wave $x(m)$ of frequency $f$, amplitude $A$, and initial phase $\phi$, achieved from a continuous-time sine-wave sampled at frequency $f_s$, i.e.,

$$x(m) = A\sin(2\pi fm + \phi), \quad m = 0,1,2,\ldots \tag{1}$$

The frequency $f$ represents the ratio between the continuous-time waveform frequency $f_x$ and the sampling frequency $f_s$. It is assumed smaller than 0.5 to satisfy the Nyquist theorem. When $M$ samples are acquired, we can write:

$$f = \frac{f_x}{f_s} = \frac{\nu}{M} = \frac{l+\delta}{M}, \tag{2}$$

where $l$ and $\delta$ ($-0.5 \le \delta < 0.5$) are respectively the integer and the fractional parts of the number of acquired sine-wave cycles $\nu$. It should be noticed that $\nu$ represents also the sine-wave frequency expressed in bins and it is usually evaluated by estimating $l$ and $\delta$ separately. When the sampling process is coherent we have $\delta = 0$ [Ferrero 92]. Otherwise, if a non-coherent sampling occurs, we have $\delta \neq 0$ [Ferrero 92]. That case is very common in practical applications due to the lack of synchronization between the sine-wave and sampling frequencies. In this case the spectral leakage phenomenon occurs. It can be reduced by windowing the acquired signal [Marple 87], [Harris 78], i.e. by analyzing the sequence $x_w(m) = x(m)\cdot w(m)$, $m = 0, 1,\ldots, M - 1$, where $w(\cdot)$ is the adopted window, which usually belonging to the cosine class [Harris 78], [Nutall 81], [Offelli 90a]. The $H$-term cosine window is defined as:

$$w(m) = \sum_{h=0}^{H-1} (-1)^h a_h \cos\left(2\pi h \frac{m}{M}\right), \quad m = 0,1,\ldots,M-1 \tag{3}$$

where $a_h$, $h = 0, 1,\ldots, H - 1$, are the window's coefficients.

The Discrete Fourier Transform (DFT) of the signal $x_w(m)$ is given by:

$$X_w(k) = \frac{A}{2j}\left[W(k-\nu)e^{j\phi} - W(k+\nu)e^{-j\phi}\right], \qquad k = 0,1,\ldots,M-1 \tag{4}$$

where $W(\cdot)$ is the Discrete-Time Fourier Transform (DTFT) of the window $w(\cdot)$, which is given by:

$$W(\lambda)=\sin(\pi\lambda)e^{-j\pi\frac{M-1}{M}\lambda}W_0(\lambda), \quad \lambda\in[0, \quad M), \tag{5}$$

where

$$W_0(\lambda)=\sum_{h=0}^{H-1}(-1)^h 0.5a_h\left[\frac{e^{-j\frac{\pi}{M}h}}{\sin\frac{\pi}{M}(\lambda-h)}+\frac{e^{j\frac{\pi}{M}h}}{\sin\frac{\pi}{M}(\lambda+h)}\right], \qquad \lambda\in[0, M). \tag{6}$$

For $|\lambda| << M$ and enough high values of $M$, we have [Nuttall 81]:

$$W(\lambda)=\frac{M\lambda\sin(\pi\lambda)}{\pi}e^{-j\pi\frac{M-1}{M}\lambda}\sum_{h=0}^{H-1}\frac{(-1)^h a_h}{\lambda^2-h^2}. \tag{7}$$

It should be noticed that the second term in (4) represents the image part of the spectrum.
The coefficients of the most commonly used two-term ($H$ = 2), three-term ($H$ = 3), and four-term ($H$ = 4) cosine class windows are given in Table 1 [Nuttall 81], [Offelli 90a]. These windows are:

- Maximum Sidelobe Decay (MSD) windows:
- Minimum Sidelobe Level (MSL) windows;
- Rapid Sidelobe Decay with Minimum Sidelobe Levels (RSD-MSL) windows;
- Minimum Error Energy (MEE) windows.

It should be noted that the MSD windows are known also as class I Rife-Vincent windows [Rife 70], the two-term MSD window is known also as Hann window, and the two-term Minimum Sidelobe Level (MSL) is known also as Hamming window [Nuttal 81]. Some interesting window features listed in Table 2 are: peak sidelobe level, sidelobe level decaying rate, Normalized Peak Signal Gain (*NPSG*), Normalized Noise Power Gain (*NNPG*), Equivalent Noise BandWidth (*ENBW*), Equivalent Noise BandWidth of the squared window (*ENBW0*), and minimum Scalloping Loss (*SL*), which is reached at $\delta$ = –0.5 (*SL*(–0.5)) [Harris 78]. The parameters *NPSG*, *NNPG*, and *ENBW* have the following expressions [Harris 78], [Belega 07b], [Belega 12c]:

$$NPSG\overset{\Delta}{=}\frac{1}{M}\sum_{m=0}^{M-1}w(m)=a_0 \tag{8}$$

$$NNPG\overset{\Delta}{=}\frac{1}{M}\sum_{m=0}^{M-1}w^2(m)=a_0^2+\frac{1}{2}\sum_{h=1}^{H-1}a_h^2 \tag{9}$$

$$ENBW\overset{\Delta}{=}M\,\frac{\sum_{m=0}^{M-1}w^2(m)}{\left(\sum_{m=0}^{M-1}w(m)\right)^2}=\frac{NNPG}{(NPSG)^2}=1+\frac{1}{2}\sum_{h=1}^{H-1}\left(\frac{a_h}{a_0}\right)^2 \tag{10}$$

The parameter *ENBW0* is defined as [Petri 02], [Novotný 07]:

$$ENBW0 \overset{\Delta}{=} M \frac{\sum_{m=0}^{M-1} w^4(m)}{\left(\sum_{m=0}^{M-1} w^2(m)\right)^2} = \frac{\frac{1}{M}\sum_{m=0}^{M-1} w^4(m)}{(NNPG)^2}. \quad (11)$$

In [Belega 12c], we derived the expressions of the nominator of (11) for $H = 2$, 3, and 4, which are:
- for $H = 2$:

$$\frac{1}{M}\sum_{m=0}^{M-1} w^4(m) = a_0^4 + \frac{3a_1^4}{8} + 3a_0^2 a_1^2 \quad (12)$$

- for $H = 3$:

$$\frac{1}{M}\sum_{m=0}^{M-1} w^4(m) = a_0^4 + \frac{3\left(a_1^4 + a_2^4\right)}{8} + 3a_0^2\left(a_1^2 + a_2^2\right) + \frac{3a_1^2 a_2^2}{2} + 3a_0 a_1^2 a_2 \quad (13)$$

- for $H = 4$:

$$\frac{1}{M}\sum_{m=0}^{M-1} w^4(m) = a_0^4 + \frac{3\left(a_1^4 + a_2^4 + a_3^4\right)}{8} + 3a_0^2\left(a_1^2 + a_2^2 + a_3^2\right) + \frac{3\left(a_1^2 a_2^2 + a_1^2 a_3^2 + a_2^2 a_3^2\right)}{2}$$
$$+ 3a_0 a_1^2 a_2 + \frac{a_1^3 a_3}{2} + \frac{3a_1 a_3 a_2^2}{2} + 6a_0 a_1 a_2 a_3. \quad (14)$$

The parameter $SL$ is defined as [Harris 78]:

$$SL(\delta) \overset{\Delta}{=} \frac{|W(\delta)|}{|W(0)|} = \frac{|W(\delta)|}{M \cdot NPSG}. \quad (15)$$

Table 1. Coefficients of some commonly used two-, three-, and four-term cosine windows.

| Window | $H$ | $a_0$ | $a_1$ | $a_2$ | $a_3$ |
|---|---|---|---|---|---|
| Max. sidelobe decay (msd2) | 2 | 0.5 | 0.5 | | |
| Min. sidelobe level (msl2) | | 0.53836 | 0.46164 | | |
| Max. sidelobe decay (msd3) | 3 | 0.375 | 0.5 | 0.125 | |
| Rapid sidelobe decay with min. sidelobe level (rsd-msl3) | | 0.40897 | 0.5 | 0.09103 | |
| Min. sidelobe level (msl3) | | 0.4243801 | 0.4973406 | 0.0782793 | |
| Min. error energy (mee3) | | 0.408960 | 0.499247 | 0.091793 | |
| Max. sidelobe decay (msd4) | 4 | 0.3125 | 0.46875 | 0.1875 | 0.03125 |
| Rapid sidelobe decay with min. sidelobe level (rsd-msl4) | | 0.338946 | 0.481973 | 0.161054 | 0.018027 |
| Min. sidelobe level (msl4) | | 0.3635819 | 0.4891775 | 0.1365995 | 0.0106411 |
| Min. error energy (mee4) | | 0.350139 | 0.48526 | 0.149889 | 0.014712 |

Table 2 Some important features for some commonly used two-, three-, and four-term cosine windows.

| Window | Peak sidelobe (dB) | Decay rate (dB/octave) | *NPSG* | *NNPG* | *ENBW* | *ENBW0* | *SL*(-0.5) |
|---|---|---|---|---|---|---|---|
| msd2 | −31.47 | 18 | 0.5 | 0.375 | 1.5 | 1.9444 | 0.8488 |
| msl2 | −43.19 | 6 | 0.53836 | 0.3964 | 1.3676 | 1.8223 | 0.8186 |
| msd3 | −46.74 | 30 | 0.375 | 0.2734 | 1.9444 | 2.6265 | 0.9054 |
| rsd-msl3 | −64.19 | 18 | 0.40897 | 0.2964 | 1.7721 | 2.4139 | 0.8866 |
| msl3 | −71.48 | 6 | 0.4243801 | 0.3068 | 1.7037 | 2.3290 | 0.8775 |
| mee3 | −60.86 | 6 | 0.408960 | 0.2961 | 1.7703 | 2.4160 | 0.8861 |
| msd4 | −60.95 | 42 | 0.3125 | 0.2256 | 2.3100 | 3.1673 | 0.9313 |
| rsd-msl4 | −82.60 | 30 | 0.338946 | 0.2442 | 2.1253 | 2.9220 | 0.9192 |
| msl4 | −98.17 | 6 | 0.3635819 | 0.2612 | 1.9761 | 2.7277 | 0.9067 |
| mee4 | −84.18 | 6 | 0.350139 | 0.2517 | 2.0529 | 2.8320 | 0.9133 |

The $H$-term MSD window ($H \geq 2$) has the most rapidly spectrum sidelobe decaying rate among all the cosine windows of a given number of terms $H$ [Nuttall 81]. In [Belega 05a], I derived the analytical expressions for the coefficients of the $H$-term MSD window ($H \geq 2$), which were not given before in the scientific literature. That derivation is presented in the following.

***Proposition 1***: *The coefficients $a_h$, $h = 0, 1,\ldots, H-1$, of the H-term MSD window ($H \geq 2$) are given by the following expressions:*

$$a_0 = \frac{C_{2H-2}^{H-1}}{2^{2H-2}}, \quad a_h = \frac{C_{2H-2}^{H-h-1}}{2^{2H-3}}, \quad h = 1,2,\ldots,H-1 \tag{16}$$

in which $C_m^p = m!/((m-p)!\,p!)$.

*Proof*:
The coefficients of the $H$-term MSD window must satisfy the following conditions [Nuttall 81]:

$$\sum_{h=0}^{H-1} a_h = 1 \tag{17}$$

$$\sum_{h=0}^{H-1} (-1)^h a_h = 0 \tag{18}$$

$$\sum_{h=0}^{H-1} (-1)^h h^{2n} a_h = 0, \quad n = 1,2,\ldots,H-2. \tag{19}$$

The coefficients $a_h$, $h = 0, 1,\ldots, H-1$, given by (16) are the coefficients of the $H$-term MSD window if they satisfy the following conditions, imposed by (17) – (19):

$$\sum_{h=0}^{H-1} a_h = 1 \Leftrightarrow 2\sum_{h=0}^{H-2} C_{2H-2}^{h} + C_{2H-2}^{H-1} = 2^{2H-2} \tag{20}$$

$$\sum_{h=0}^{H-1} (-1)^h a_h = 0 \Leftrightarrow 2\sum_{h=0}^{H-2} (-1)^{h+1} C_{2H-2}^{h} + (-1)^H C_{2H-2}^{H-1} = 0 \tag{21}$$

$$\sum_{h=0}^{H-1} (-1)^h h^{2n} a_h = 0 \Leftrightarrow (-1)^{H-1} \sum_{h=0}^{H-1} (-1)^h (H-1-h)^{2n} C_{2H-2}^{h} = 0, \quad n = 1,2,\ldots,H-2. \tag{22}$$

Based upon the equality $C_q^p = C_q^{q-p}$ we have:

$$2\sum_{h=0}^{H-2} C_{2H-2}^{h} + C_{2H-2}^{H-1} = \sum_{h=0}^{H-1} C_{2H-2}^{h} + \sum_{h=0}^{H-2} C_{2H-2}^{h} = \sum_{h=0}^{H-1} C_{2H-2}^{h} + \sum_{h=0}^{H-2} C_{2H-2}^{H+h} = \sum_{h=0}^{H-1} C_{2H-2}^{h} + \sum_{h=H}^{2H-2} C_{2H-2}^{h}$$
$$= \sum_{h=0}^{2H-2} C_{2H-2}^{h} = 2^{2H-2}.$$

Thus, the condition (20) is fulfilled.

We can write:

$$2\sum_{h=0}^{H-2} (-1)^{h+1} C_{2H-2}^{h} + (-1)^H C_{2H-2}^{H-1} = \sum_{h=0}^{H-1} (-1)^{h+1} C_{2H-2}^{h} + \sum_{h=0}^{H-2} (-1)^{h+1} C_{2H-2}^{h}$$
$$= \sum_{h=0}^{H-1} (-1)^{h+1} C_{2H-2}^{h} + \sum_{h=0}^{H-2} (-1)^{H-h-1} C_{2H-2}^{H-h-2} = \sum_{h=0}^{H-1} (-1)^{h+1} C_{2H-2}^{h} + (-1)^H \sum_{h=0}^{H-2} (-1)^{h+1} C_{2H-2}^{H-h-2}$$
$$= \sum_{h=0}^{H-1} (-1)^{h+1} C_{2H-2}^{h} + (-1)^{2H} \sum_{h=H}^{2H-2} (-1)^{h+1} C_{2H-2}^{h} = \sum_{h=0}^{2H-2} (-1)^{h+1} C_{2H-2}^{h}.$$

The last sum is equal to zero [Coşniţă 72]. Thus, the condition (21) is fulfilled.

We have:

$$\sum_{h=H}^{2H-2} (-1)^h (H-1-h)^{2n} C_{2H-2}^{h} = \sum_{h=0}^{H-2} (-1)^{h+H} (1+h)^{2n} C_{2H-2}^{H+h} = (-1)^H \sum_{h=0}^{H-2} (-1)^h (1+h)^{2n} C_{2H-2}^{H-h-2}$$
$$= (-1)^H \sum_{h=0}^{H-2} (-1)^{H-h-2} (H-1-h)^{2n} C_{2H-2}^{h} = \sum_{h=0}^{H-1} (-1)^h (H-1-h)^{2n} C_{2H-2}^{h},$$

which implies:

$$\sum_{h=0}^{2H-2} (-1)^h (H-1-h)^{2n} C_{2H-2}^{h} = 2\sum_{h=0}^{H-1} (-1)^h (H-1-h)^{2n} C_{2H-2}^{h}, \quad n = 1,2,\ldots,H-2.$$

The last equality is equal to zero [Coşniţă 72], which ensures that the condition (22) is fulfilled.
Since all conditions (20) – (22) are fulfilled it follows that the *Proposition 1* is true.

Based on the expressions of the $H$-term MSD window coefficients ($H \geq 2$) in [Belega 09a], we derived the analytical expressions for the parameters *NPSG*, *NNPG*, *ENBW*, and $SL(\delta)$ of that window. These expressions are much simple than (8) – (10), and (15), which are given before in the scientific literature, since they depend only on the window's number of terms, $H$. They are:

$$NPSG = \frac{C_{2H-2}^{H-1}}{2^{2H-2}}, \tag{23}$$

$$NNPG = \frac{C_{4H-4}^{2H-2}}{2^{4H-4}}, \tag{24}$$

$$ENBW = \frac{C_{4H-4}^{2H-2}}{\left(C_{2H-2}^{H-1}\right)^2}, \tag{25}$$

$$SL(\delta) = \frac{\sin(\pi\delta)}{\pi\delta} \cdot \frac{[(H-1)!]^2}{\prod_{h=1}^{H-1}\left(h^2 - \delta^2\right)}. \tag{26}$$

Furthermore, based on the derived expressions for the coefficients, in [Belega 07a], we derived the analytical expression of the DTFT of the $H$-term MSD window ($H \geq 2$). That derivation is presented here.

***Proposition 2:*** *The DTFT of the H-term MSD window (H ≥ 2) is given by the expression:*

$$W(\lambda) = \frac{M\sin(\pi\lambda)}{2^{2H-2}\pi\lambda} e^{-j\pi\frac{M-1}{M}\lambda} \frac{(2H-2)!}{\prod_{h=1}^{H-1}\left(h^2 - \lambda^2\right)}, \quad \lambda \in [0, M), \tag{27}$$

*Proof:*
By substituting (16) in (7) we achieve:

$$\begin{aligned} W(\lambda) &= \frac{M\lambda\sin(\pi\lambda)}{\pi} e^{-j\frac{\pi(M-1)}{M}\lambda} \sum_{h=0}^{H-1}(-1)^h \frac{a_h}{\lambda^2 - h^2} \\ &= \frac{M\lambda\sin(\pi\lambda)}{\pi} e^{-j\frac{\pi(M-1)}{M}\lambda} \left[\sum_{h=1}^{H-1}(-1)^h \frac{C_{2H-2}^{H-h-1}}{2^{2H-3}} \frac{1}{\lambda^2 - h^2} + \frac{C_{2H-2}^{H-1}}{2 \cdot 2^{2H-3}} \frac{1}{\lambda^2}\right], \quad \lambda \in [0, M). \end{aligned} \tag{28}$$

We have the following equality:

$$\sum_{h=1}^{p}(-1)^h \frac{C_{2p}^{p-h}}{x^2 - h^2} + \frac{C_{2p}^{p}}{2x^2} = \frac{(-1)^p(2p)!}{2\prod_{h=0}^{p}\left(x^2 - h^2\right)}. \tag{29}$$

The above equality can be proved by multiply first each side by $x \pm h$ ($h = 0, 1,\ldots, p$) and then is given to $x$ the values $\pm h$. To put in evidence the necessity of the term $C_{2p}^{p} / 2x^2$ in the left side of the above equality each side is multiplied by $x^2$ and then is given to $x$ the value zero.
By replacing the equality (29), with $p = H - 1$, in (28) we achieve for $W(\lambda)$ the expression (27).

Fig. 1 shows the DTFT spectrum of the *msd2* and *msl2* windows (Fig. 1(a)) and the *msd3*, *rsd-msl3*, and *msl3* windows (Fig. 1(b)).

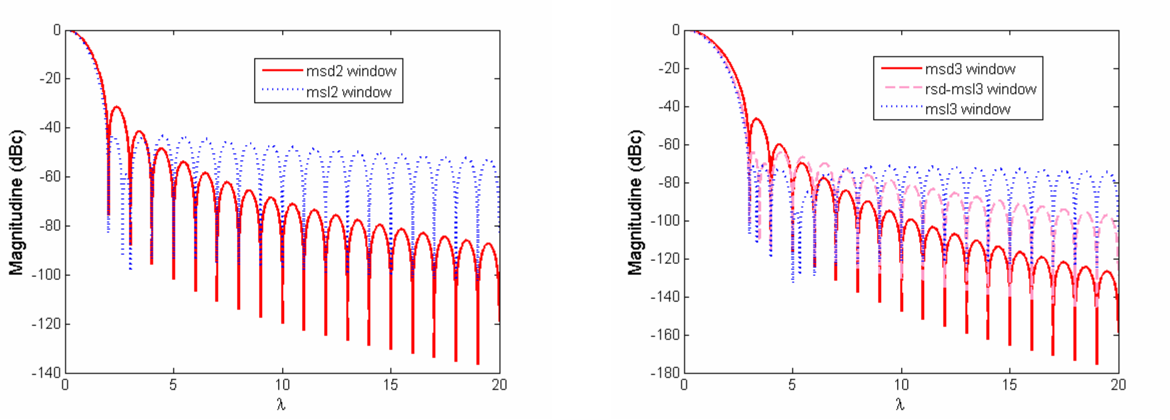


(a) (b)

Fig. 1. DTFT spectrum of the: (a) *msd2* and *msl2* windows, and (b) *msd3*, *rsd-msl3*, and *msl3* windows.

If the frequency signal-to-noise ratio is higher than 20 dB, the integer part $l$ of the acquired sine-wave cycles can be determinate with very high probability by applying a maximum search procedure to the discrete spectrum samples $|X_w(k)|$, $k = 1, 2, \ldots, M/2 - 1$ [Offelli 92]. Thus, the sine-wave frequency $\nu$ and the fractional frequency $\delta$ are estimated with the same uncertainty.

## B. Interpolated DFT Method

Frequency-domain methods based on the DFT are characterized by robustness toward signal model inaccuracies and low computational effort. On the other hand, they have inherent limitations due to the spectral leakage effect due to the finite duration of the observation interval and the picket-fence effect due to the granularity between adjacent DFT samples [Marple 86], [Offelli 90b], [Ferrero 92]. A frequency-domain procedure often used to compensate both above effects is the so-called Interpolated Discrete Fourier Transform (IpDFT) method [Rife 70], [Jain 79], [Grandke 83], [Petri 90], [Offelli 90b], [Schoukens 92], [Offelli 92], [Belega 09a], [Belega 12a]. That method provides accurate sine-wave parameter estimates, it is very simple to understand and to apply, and it is well suited for real-time applications. Moreover, in particular, when the MSD windows are adopted the IpDFT parameter estimators are provided by simple analytical expressions.

### 1) *Parameter estimation*

In the following the estimation of the sine-wave parameters $\delta$, $A$, and $\phi$, by the IpDFT method is presented. The expressions of the parameter estimators will be used in our further derivations.

To estimate $\delta$ by the IpDFT method, the ratio $\alpha$ of the two maximum DFT spectrum samples is determined:

$$\alpha = \frac{|X_w(l+i)|}{|X_w(l-1+i)|}, \tag{30}$$

where $i = 0$ if $|X_w(l - 1)| > |X_w(l + 1)|$ and $i = 1$ if $|X_w(l - 1)| < |X_w(l + 1)|$.

In practice the number of acquired sine-wave cycles and the number of samples are usually quite high (e.g. $v \geq 15$ and $M \geq 512$). Thus, the effect of the spectral interference from the image component on the spectrum samples close to the peak (that is for $k = -1$, 0, and 1) is negligible [Offelli 92], [Belega 12a], and (4) becomes:

$$X_w(l+k) \cong \frac{A}{2j} W(k-\delta) e^{j\phi}, \qquad k = -1, 0, 1 \tag{31}$$

By using (31), the expression (30) becomes:

$$\alpha \cong \frac{|W(i-\delta)|}{|W(-1+i-\delta)|}. \tag{32}$$

Based on (30), an estimate of $\delta$ can be derived by inverting the relationship (32) [Offelli 90b], [Belega 12a]:

$$\hat{\delta}_{ip} = g(\alpha), \tag{33}$$

where the function $g(\cdot)$ depends on the adopted window.
The function $g(\cdot)$ is often approximated in least squares sense by a polynomial [Offeli 90b]. However, if a MSD window is used analytical expression for the function $g(\cdot)$ can be easily achieved by replaced (27) in (32) [Belega 09a]:

$$\hat{\delta}_{ip} = g(\alpha) = \frac{(H-1+i)\alpha - H + i}{\alpha + 1}. \tag{34}$$

From (31) the amplitude $A$ can be estimated as:

$$\hat{A}_{ip} = \frac{2|X_w(l)|}{\left|W(-\hat{\delta}_{ip})\right|}, \tag{35}$$

which for the particular case of the $H$-term MSD ($H \geq 2$) is given by [Belega 09a]:

$$\hat{A}_{ip} = \frac{2^{2H-1} \pi \hat{\delta}_{ip} |X_w(l)|}{M \sin(\pi \hat{\delta}_{ip})(2H-2)!} \prod_{h=1}^{H-1} \left(h^2 - \hat{\delta}_{ip}^2\right). \tag{36}$$

From (31) and (5) it follows that the phase $\phi$ can be estimated by:

$$\hat{\phi}_{ip} = \arg[X_w(l)] - \pi \hat{\delta}_{ip} + \pi \frac{\hat{\delta}_{ip}}{M} - \frac{\pi}{2} sign(\hat{\delta}_{ip}) - \arg\left[W_0\left(-\hat{\delta}_{ip}\right)\right], \tag{37}$$

where $sign(z)$ is the sign function of $z$, that is equal to $-1$ when $z < 0$, to 0 when $z = 0$, and to 1 when $z > 0$.

The estimators $\hat{\nu}_{ip} = l + \hat{\delta}_{ip}$, $\hat{A}_{ip}$, and $\hat{\phi}_{ip}$ represent the parameters of the sine fit returned by the IpDFT method based on the $H$-term cosine window.

**2) *Variances of the parameter estimators***

In [Offelli 92], there were derived the expressions for the variance of the sine-wave parameter estimators provided by the IpDFT method based on the $H$-term cosine window. However, these expressions are complicated and relatively difficult to apply. Hence, in [Belega 12a], we derived more simple analytical expressions for the above estimators and also, in [Belega 09a], for the particular case in which the $H$-term MSD window is adopted. The derivation of these expressions is given in the following.

Let us assume now that the integer part $l$ is high enough to ensure that the contribution of the spectral interference due to the image component on the estimator (33) is negligible. Moreover, in order to model real-life situations, we assume that a stationary white noise with zero mean and variance $\sigma_n^2$ is added to the discrete-time sine-wave (1).

- *Variance of the estimator* $\hat{\delta}_{ip}$

By applying the law of uncertainty propagation [GUM 95] to expressions (33) and (30) we obtain, respectively:

$$\sigma^2_{\hat{\delta}_{ip},\,n} = \left(\frac{\partial g}{\partial \alpha}\right)^2 \sigma^2_{\alpha}. \tag{38}$$

and:

$$\sigma^2_{\alpha} = \frac{1}{\left|X_w(l-1+i)\right|^2}\left(1+\alpha^2-2\alpha\rho_1\right)\sigma^2_{X_w}, \tag{39}$$

where $\rho_1$ is the correlation coefficient between two adjacent DFT spectrum samples $|X_w(j)|$ and $|X_w(j+1)|$, and $\sigma^2_{X_w}$ is the variance of a DFT spectrum sample $|X_w(j)|$, given by [Petri 02], [Novotný 06], [Novotný 07]:

$$\sigma^2_{X_w} = \frac{M\ NNPG}{2}\sigma^2_n. \tag{40}$$

The correlation coefficient $\rho_1$ is given by [Novotný 07]:

$$\rho_1 = \frac{a_0\ a_1 + 0.5\sum_{h=1}^{H-2} a_h\ a_{h+1}}{NNPG} = \frac{a_0\ a_1 + 0.5\sum_{h=1}^{H-2} a_h\ a_{h+1}}{a_0^2 + 0.5\sum_{h=1}^{H-1} a_h^2}, \tag{41}$$

in which *NNPG* is given by (9).
By using (39) – (41) and (31), the expression (38) becomes:

$$\sigma^2_{\hat{\delta}_{ip},n} \cong \left(\frac{\partial g}{\partial \alpha}\right)^2 \frac{M}{A^2\left|W(-1+i-\delta)\right|^2}\left[2a_0^2 - 2\alpha a_0 a_1 + \alpha^2\left(a_0^2 + a_{H-1}^2\right) + \sum_{h=0}^{H-2}\left(a_{h+1} - \alpha a_h\right)^2\right]\sigma_n^2, \tag{42}$$

where $\alpha$ and $W(\cdot)$ are provided by (32) and by (5), respectively.

In [Belega 09a], we derived, for the particular case of the $H$-term MSD window ($H \geq 2$), the expression of correlation coefficient $\rho_1$:

$$\rho_1 = \frac{2H-2}{2H-1}. \tag{43}$$

Based on (25) – (27), (31), and (43), the expression (38) becomes:

$$\begin{aligned}\sigma_{\hat{\delta}_{ip},n} = \sigma_{\hat{\nu}_{ip},n} &\cong \frac{2(H-|\delta|)}{(2H-1)!}\frac{\pi\delta}{\sin(\pi\delta)}\frac{\prod_{h=1}^{H-1}(h^2-\delta^2)}{A}\sqrt{\frac{C_{4H-4}^{2H-2}}{2M}}\sqrt{\frac{2(4H-3)(\delta^2-|\delta|)+2H^2-1}{2H-1}}\sigma_n \\ &= \frac{H-|\delta|}{2H-1}\frac{1}{A\,SL(\delta)}\sqrt{\frac{2ENBW}{M}}\sqrt{\frac{2(4H-3)(\delta^2-|\delta|)+2H^2-1}{2H-1}}\sigma_n.\end{aligned} \tag{44}$$

• *Variance of the estimator* $\hat{A}_{ip}$

According to the uncertainty propagation law [GUM 95], the variance of the estimator (35) is given by:

$$\sigma^2_{\hat{A}_{ip},n} = \frac{4}{\left|W(-\delta)\right|^2}\sigma^2_{X_w} + \frac{4\left|X_w(l)\right|^2}{\left|W(-\delta)\right|^4}D^2(\delta)\sigma^2_{\hat{\delta}_{ip},n} - \frac{8}{\left|W(-\delta)\right|^3}\left|X_w(l)\right|D(\delta)\,\rho\left(\left|X_w(l)\right|,\hat{\delta}_{ip}\right)\sigma_{X_w}\sigma_{\hat{\delta}_{ip},n}, \tag{45}$$

where $D(\delta) = \frac{\partial\left|W(-\delta)\right|}{\partial\delta}$; for $\delta \in [-0.5, 0.5)$, from (7) we obtain:

$$D(\delta) = \frac{\partial\left|W(-\delta)\right|}{\partial\delta} = \frac{M}{\pi}\left(sin(\pi\delta) + \pi\delta\,cos(\pi\delta)\right)\sum_{h=0}^{H-1}\frac{(-1)^h a_h}{\lambda^2 - h^2} - \frac{2M\delta^2\,sin(\pi\delta)}{\pi}\sum_{h=0}^{H-1}\frac{(-1)^h a_h}{\left(\delta^2 - h^2\right)^2}. \tag{46}$$

the variance $\sigma^2_{X_w}$ is given by (40) and the variance $\sigma^2_{\hat{\delta}_{ip},n}$ by (42), and $\rho\left(\left|X_w(J)\right|, \hat{\delta}_{ip}\right)$ is the correlation coefficient between $|X_w(l)|$ and $\hat{\delta}_{ip}$.

With good approximation, (45) can be written as:

$$\sigma^2_{\hat{A}_{ip},n} \cong \frac{4}{\left|W(-\delta)\right|^2}\sigma^2_{X_w} + \frac{A^2}{\left|W(-\delta)\right|^2} D^2(\delta)\sigma^2_{\hat{\delta}_{ip},n} - \frac{4A}{\left|W(-\delta)\right|^2} D(\delta)\,\rho\left(\left|X_w(l)\right|, \hat{\delta}_{ip}\right)\sigma_{X_w}\sigma_{\hat{\delta}_{ip},n}. \tag{47}$$

From (40) and (42) it follows that, for the values of $M$ commonly used in practice (e.g. $M \geq 128$), the first term in the right hand side of (47) prevails on the others. Thus, with high accuracy we have:

$$\sigma^2_{\hat{A}_{ip},n} \cong \frac{4}{\left|W(-\delta)\right|^2}\sigma^2_{X_w}. \tag{48}$$

Now, using (40), (10), and (15) we obtain:

$$\sigma^2_{\hat{A}_{ip},n} \cong \frac{2}{M \cdot SL^2(\delta)} \frac{NNPG}{(NPSG)^2}\sigma^2_n = \frac{2\,ENBW}{M \cdot SL^2(\delta)}\sigma^2_n. \tag{49}$$

- *Variance of the estimator* $\hat{\phi}_{ip}$

The variance of the estimator (37) is given by [Offelli 92]:

$$\sigma^2_{\hat{\phi}_{ip},n} = \sigma^2_{\varphi} + \pi^2\sigma^2_{\hat{\delta}_{ip},n}, \tag{50}$$

where $\sigma^2_{\hat{\delta}_{ip},n}$ is given by (42) and $\sigma^2_{\varphi}$ is the variance of the $arg[X_w(l)]$, which is given by [Offelli 92], [Novotný 07]:

$$\sigma^2_{\varphi} \cong \frac{2ENBW}{MA^2 SL^2(\delta)}\sigma^2_n. \tag{51}$$

By replacing (51) in (50) the variance of the estimator $\hat{\phi}_{ip}$ becomes:

$$\sigma^2_{\hat{\phi}_{ip},n} = \frac{2ENBW}{MA^2 SL^2(\delta)}\sigma^2_n + \pi^2\sigma^2_{\hat{\delta}_{ip},n}. \tag{52}$$

**3) *Combined standard uncertainty of the estimator*** $\hat{\delta}_{ip}$

In [Belega 12a], we derived the expression for the combined standard uncertainty of the estimator $\hat{\delta}_{ip}$, which was not given before in the previous works focused on this subject. Furthermore, in [Belega 12a], we verified the accuracies of the derived expressions through computer simulations. The derivation of the combined standard uncertainty expression and the performed computer simulations are presented in the following.

We consider that the discrete-time sine-wave (1) is corrupted by a stationary white noise with zero mean and variance $\sigma_n^2$. From (35) and (37) it follows that in the IpDFT method the amplitude and the phase are estimated by means of the fractional frequency estimator $\hat{\delta}_{ip}$ returned by (33). Hence, their estimation accuracies depend on the estimation accuracy of the $\hat{\delta}_{ip}$. Expressions (4) and (30) show that the estimator $\hat{\delta}_{ip}$ is affected by the image component, whose effect is particularly significant when the number of acquired signal cycles $\nu$ is small. Also, the estimator $\hat{\delta}_{ip}$ is affected by the wideband noise. Thus, the fractional frequency can be expressed as:

$$\hat{\delta}_{ip} = \delta + \Delta_{\hat{\delta}_{ip}, si} + \Delta_{\hat{\delta}_{ip}, n}, \tag{53}$$

where $\Delta_{\hat{\delta}_{ip},si}$ and $\Delta_{\hat{\delta}_{ip},n}$ are the contributions of the spectral interference and wideband noise to the estimator $\hat{\delta}_{ip}$.

According to (4) and (30) the contribution of the spectral interference depends on the adopted window, the integer and fractional parts $l$ and $\delta$, and the sine-wave phase $\phi$. Thus, we can write:

$$\Delta_{\hat{\delta}_{ip},si}(l, \delta, \phi) = \hat{\delta}_{ip} - \delta. \tag{54}$$

In [Belega 12a] and [Belega 09b], we shown that when the MSD, MSL, RSD-MSL windows are adopted the following relationships occurs:

$$\begin{aligned}
|X_w(l-1)| - \frac{A}{2}|W(-1-\delta)| &\cong p\frac{A}{2}|W(2l-1+\delta)| \\
|X_w(l)| - \frac{A}{2}|W(-\delta)| &\cong -p\frac{A}{2}|W(2l+\delta)| \\
|X_w(l+1)| - \frac{A}{2}|W(1-\delta)| &\cong p\frac{A}{2}|W(2l+1+\delta)|
\end{aligned} \tag{55}$$

where $p$ is a function of both $\delta$ and $\phi$, i.e. $p = p(\delta, \phi)$, and for a given value of $\delta$, $p$ is an almost sinusoidal function of $\phi$ with amplitude equal to 1.

In the following we will derive the expression of the error $\Delta_{\hat{\delta}_{ip},si}$. The Taylor series expansion of the expression (33) truncated at the first-order term provides:

$$\Delta_{\hat{\delta}_{ip},si} \cong \frac{\partial g}{\partial \alpha}\Delta\alpha. \tag{56}$$

Using (32) and (55), the ratio $\alpha$ can be expressed as:

$$\alpha = \frac{|W(i-\delta)| + (-1)^{i+1} p |W(2l+i+\delta)|}{|W(-1+i-\delta)| + (-1)^{i} p |W(2l-1+i+\delta)|} = \frac{|W(i-\delta)|}{|W(-1+i-\delta)|}(1+\varepsilon), \tag{57}$$

in which $\varepsilon$ represents the effect of spectral interference, which is given by:

$$\varepsilon = \frac{(-1)^{i+1} p \left( \frac{|W(2l+i+\delta)|}{|W(i-\delta)|} + \frac{|W(2l-1+i+\delta)|}{|W(-1+i-\delta)|} \right)}{1 + (-1)^{i} p \frac{|W(2l-1+i+\delta)|}{|W(-1+i-\delta)|}}.$$

Since $|W(2l-1+i+\delta)| << |W(-1+i-\delta)|$ and $|p| \le 1$, the above expression can be approximated as:

$$\varepsilon \cong (-1)^{i+1} p \left( \frac{|W(2l+i+\delta)|}{|W(i-\delta)|} + \frac{|W(2l-1+i+\delta)|}{|W(-1+i-\delta)|} \right). \tag{58}$$

Comparing (32) and (57), we achieve:

$$\Delta\alpha = \frac{|W(i-\delta)|}{|W(-1+i-\delta)|}\varepsilon, \tag{59}$$

in which $\varepsilon$ is given by (58).
By replacing (59) in (56) we obtain:

$$\Delta_{\hat{\delta}_{ip},si} \cong (-1)^{i+1} p \frac{\partial g}{\partial \alpha} \frac{|W(i-\delta)|}{|W(-1+i-\delta)|} \left( \frac{|W(2l+i+\delta)|}{|W(i-\delta)|} + \frac{|W(2l-1+i+\delta)|}{|W(-1+i-\delta)|} \right). \tag{60}$$

Since $|p| \le 1$, it follows that the maximum of $\Delta_{\hat{\delta}_{ip},si}$ is given by:

$$\Delta_{\hat{\delta}_{ip},si\_\max} \cong \left|\frac{\partial g}{\partial \alpha}\right| \frac{|W(i-\delta)|}{|W(-1+i-\delta)|} \left( \frac{|W(2l+i+\delta)|}{|W(i-\delta)|} + \frac{|W(2l-1+i+\delta)|}{|W(-1+i-\delta)|} \right), \tag{61}$$

Since $\Delta_{\hat{\delta}_{ip},si}$ is proportional to $p$, it follows that it is an almost sinusoidal function of $\phi$. Hence, the rms value of $\Delta_{\hat{\delta}_{ip},si}$ is $\sigma_{\hat{\delta}_{ip},si} = \Delta_{\hat{\delta}_{ip},si\_\max} / \sqrt{2}$.

In particular, if the $H$-term MSD window ($H \geq 2$) is adopted, in [Belega 09b], we derived the expression of $\Delta_{\hat{\delta}_{ip},\, si\_\max}$, which is given by:

$$\Delta_{\hat{\delta}_{ip},\, si\_\max} = \frac{2|\delta|(l+\delta)(H-|\delta|)}{(2l+\delta)(2l+\delta+(-1)^{i+1}H)} \frac{\prod_{h=1}^{H-1}\left(h^2-\delta^2\right)}{\prod_{h=1}^{H-1}\left[(2l+\delta)^2-h^2\right]}. \tag{62}$$

Fig. 2 shows the values of $\Delta_{\hat{\delta}_{ip},\, si\_\max}$ returned by computer simulations and (62) for the three-term (Fig. 2(a)) and four-term (Fig. 2(b)) MSD, RSD-MSL, and MSL windows. The integer part $l$ was varied in the range $[H + 1, 50]$ with a step equal to 1, while $\delta$ was fixed to $-0.2$. For each value of $l$, 100 values equally spaced in the range $[0, 2\pi)$ rad were taken for the sine-wave phase $\phi$. The number of acquired samples $M$ was set equal to 1024. The function $g(\cdot)$ was derived *a priori* by fitting the inverse function of (33) using a polynomial of degree 7. In order to make negligible the contribution of the spectral interference, the function $g(\cdot)$ was determined assuming $M$ = 4096 and $l$ = 313. The fractional frequency $\delta$ was varied in the range $[-0.5, 0)$ with a step of 1/50. For each value of $\delta$ the sine-wave phase $\phi$ was chosen at random in the range $[0, 2\pi)$ rad.

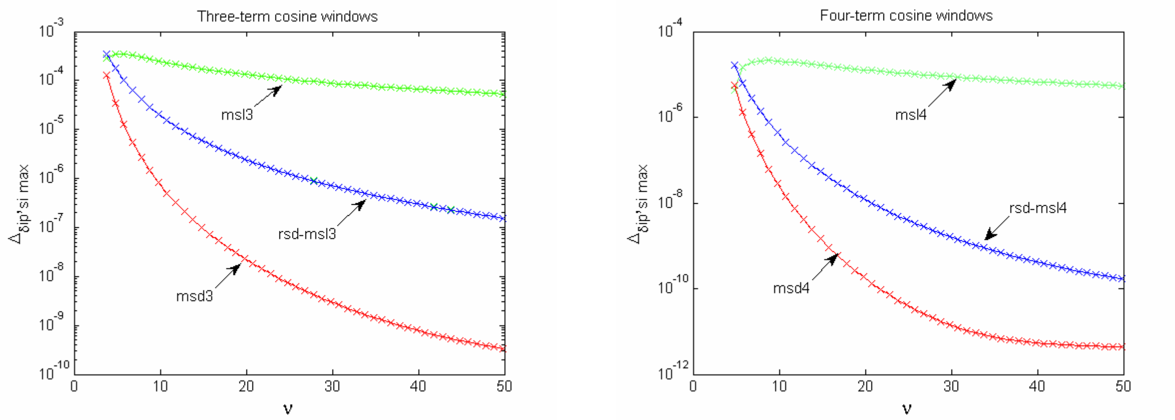


(a) (b)

Fig. 2. $\Delta_{\hat{\delta}_{ip},\, si\_\max}$ versus $\nu$ for $\delta = -0.2$ and (a) three-term and (b) four-term MSD, RSD-MSL, and MSL cosine windows. Values returned by (62) are represented by continuous lines, while values returned by simulations are represented by crosses.

Fig. 2 shows that the agreement between the simulation and theoretical results is very good. Furthermore, the maximum of the spectral interference contribution decreases as the window sidelobe decay rate increases. Thus, for a given $H$, the smaller and the higher spectral interference contributions are achieved when the MSD window and the MSL window are adopted, respectively.

The expression for the Cramér-Rao Lower Bound (CRLB) for unbiased $\delta$ estimators due to wideband noise is [Offelli 92], [Kay 93]:

$$\left(\sigma^2_{\hat{\delta},n}\right)_{CR} \cong \frac{6}{\pi^2}\frac{\sigma_n^2}{A^2 M}. \tag{63}$$

Thus, from (42) and (63) it follows that the statistical efficiency $E_{\hat{\delta}_{ip}}$ of the fractional frequency estimator (33) is:

$$E_{\hat{\delta}_{ip}} = \frac{\left(\sigma^2_{\hat{\delta},n}\right)_{CR}}{\sigma^2_{\hat{\delta}_{ip},n}} \cong \left(\frac{\partial g}{\partial \alpha}\right)^{-2} \frac{\left|W(-1+i-\delta)\right|^2}{\pi^2 M^2} \frac{6}{2a_0^2 - 2\alpha a_0 a_1 + \alpha^2\left(a_0^2 + a_{H-1}^2\right) + \sum_{h=0}^{H-2}\left(a_{h+1} - \alpha a_h\right)^2}. \tag{64}$$

Fig. 3 shows the theoretical and simulated statistical efficiency $E_{\hat{\delta}_{ip}}$ as a function of $\delta$ for the same windows as in previous figure. The sine-wave amplitude $A$ was set to 1, the integer part $l$ of the acquired sine-wave cycles was chosen equal to 123, and the number of acquired samples $M$ was set to 1024. The sine-wave was corrupted by a uniform noise modelling the quantization performed by an ideal 12-bit Analog-to-Digital Converter (ADC) with Full-Scale Range (*FSR*) equal to 5. Non-coherent sampling was studied and the fractional frequency $\delta$ was varied in the ranges [–0.5, 0) and (0, 0.5) with a step of 1/40. The sine-wave phase $\phi$ was chosen at random in the range [0, $2\pi$) rad. For each value of $\delta$, the efficiency $E_{\hat{\delta}_{ip}}$ was evaluated using 10,000 records. The function $g(\cdot)$ was determined as in the previous figure, by considering both positive and negative values of $\delta$.

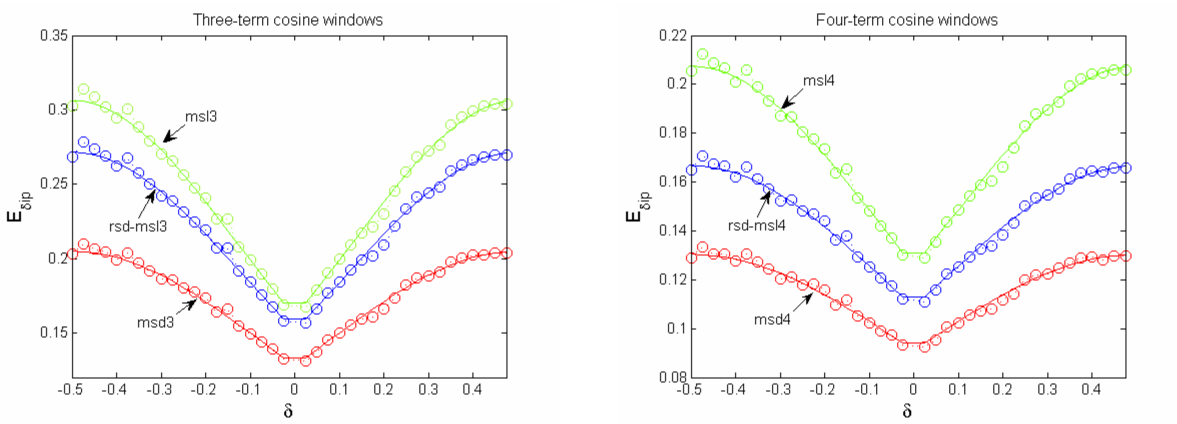


(a) (b)

Fig. 3. Efficiency $E_{\hat{\delta}_{ip}}$ versus $\delta$ for (a) three-term and (b) four-term MSD, RSD-MSL, and MSL cosine windows. The theoretical and simulation results are represented by continuous lines and circles, respectively.

Fig. 3 shows a very good agreement between simulation and theoretical results. Moreover, for a given value of $H$, the best and the worst statistical efficiencies are achieved when the MSL window and the MSD window are adopted, respectively. It can be seen also that the statistical efficiency $E_{\hat{\delta}_{ip}}$ is an even function of $\delta$. It should be noted that the same behavior as in Fig. 3 is achieved in the case of both uniform and Gaussian noise.

The uncertainty contributions leading to (62) and (42) are clearly due to different physical phenomena, so they can be considered statistically independent. Thus, according to [GUM 95], the combined standard uncertainty of the fractional frequency estimator $\hat{\delta}_{ip}$ or of the deviation $\Delta_{\hat{\delta}_{ip}} = \hat{\delta}_{ip} - \delta$ is:

$$\sigma_{\hat{\delta}_{ip}} = \sqrt{\frac{\Delta^2_{\hat{\delta}_{ip}, si\_max}}{2} + \sigma^2_{\hat{\delta}_{ip}, n}}, \tag{65}$$

in which $\Delta_{\hat{\delta}_{ip}, si\_max}$ and $\sigma^2_{\hat{\delta}_{ip}, n}$ are given by (61) and (42), respectively.

It is worth noticing that the values of $\sigma_{\hat{\delta}_{ip}}$ provided by (65) decreases as $H$ decreases, whereas (61) shows that $\Delta_{\hat{\delta}_{ip}, si\_max}$ decreases as $H$ increases. Thus, there exists a value of $H$ that ensures a minimum value for $\sigma_{\hat{\delta}_{ip}}$, i.e. an optimal number of terms $H_{opt}$. For the MSD window the maximum of the combined standard uncertainty, $\sigma_{\hat{\delta}_{ip} \max}$ is reached at $\delta = -0.5$. Based on the above observations in [Belega 11a], we proposed a criterion for the selection of the optimal MSD window to be used in the IpDFT method, i.e. for determination of $H_{opt}$. This is presented in the following. Let us define ${}_H\left(\sigma_{\hat{\delta}_{ip} \max}\right)_{\sigma_n = \sigma_q}$, as the value of $\sigma_{\hat{\delta}_{ip} \max}$ achieved using the $H$-term MSD window when $\sigma_n = \sigma_q$, where $\sigma_q$ is the ideal quantization noise of the ADC of the used acquisition board. Then, since $\sigma_n \geq \sigma_q$, the following proposition holds [Belega 11a]:

***Proposition 3***: *If* ${}_H(\sigma_{\hat{\delta}_{ip} \max})_{\sigma_n = \sigma_q} < {}_{H+1}(\sigma_{\hat{\delta}_{ip} \max})_{\sigma_n = \sigma_q}$, *then* ${}_H(\sigma_{\hat{\delta}_{ip} \max})_{\sigma_n} < {}_{H+1}(\sigma_{\hat{\delta}_{ip} \max})_{\sigma_n}$ *for any* $\sigma_n \geq \sigma_q$.

This implies that the optimal MSD window to be used in the IpDFT method can be selected by means of the following two-step procedure:

- if ${}_2(\sigma_{\hat{\delta}_{ip} \max})_{\sigma_n = \sigma_q} < {}_3(\sigma_{\hat{\delta}_{ip} \max})_{\sigma_n = \sigma_q}$, then $H_{opt} = 2$, that is the optimal MSD window is the two-term or Hann window.
- if ${}_2(\sigma_{\hat{\delta}_{ip} \max})_{\sigma_n = \sigma_q} > {}_3(\sigma_{\hat{\delta}_{ip} \max})_{\sigma_n = \sigma_q}$, then we continue the comparison by increasing the value of $H$ until ${}_{H^*}(\sigma_{\hat{\delta}_{ip} \max})_{\sigma_n = \sigma_q} < {}_{H^*+1}(\sigma_{\hat{\delta}_{ip} \max})_{\sigma_n = \sigma_q}$, $H$ = 3, 4,…. The first value of $H$ satisfying the previous relationship provides the optimal MSD window, that is $H_{opt} = H^*$.

For values of $l$ used in practice (e.g. $l \geq 15$) we usually obtain $H_{opt}$ = 2 or 3.

**4) *Probability density function of* $\hat{\delta}_{ip}$**

It is well known that the statistical behavior of a random variable – and so the quality of the estimator – is completely described by its Probability Density Function (PDF). In [Belega 12a], we derived the expression of the PDF of the estimator $\hat{\delta}_{ip}$, which was not derived before in the scientific literature. Moreover, in that paper the accuracy of the derived expression of PDF was verified by means of both computer simulations and experimental results. All these derivations are presented in the following.

It is worth noticing that in practical applications we often suppose to repeatedly acquire the sine-wave signal (1) using a non-coherent sampling. In such a situation, while the fractional frequency $\delta$ assumes a constant value, the unknown phase $\phi$ can be modelled as a random variable uniformly distributed in the range $[0, 2\pi)$ rad. Based on the behavior of $p$ it follows that the contribution $\Delta_{\hat{\delta}_{ip},si}$ of the spectral interference can be modelled as a random variable with a U-shaped PDF [Wagdy 89]:

$$\rho_{\hat{\delta}_{ip},si}\left(\Delta_{\hat{\delta}_{ip},si}\right)=\frac{1}{\pi\sqrt{\Delta^2_{\hat{\delta}_{ip},si\_\max}-\Delta^2_{\hat{\delta}_{ip},si}}}. \tag{66}$$

Since $\delta$ is fixed, the contribution $\Delta_{\hat{\delta}_{ip},n}$ due to the wideband noise exhibits a normal distribution with standard deviation equal to $\sigma_{\hat{\delta}_{ip}}$ [Offelli 92]. Thus, from the statistical theory it is well known that the PDF of $\Delta_{\hat{\delta},n}$ is given by:

$$\rho_{\hat{\delta}_{ip},n}\left(\Delta_{\hat{\delta}_{ip},n}\right)=\frac{1}{\sqrt{2\pi}\,\sigma_{\hat{\delta}_{ip},n}}e^{-\frac{\Delta^2_{\hat{\delta}_{ip},n}}{2\sigma^2_{\hat{\delta}_{ip},n}}}. \tag{67}$$

The PDF $\rho_{\hat{\delta}_{ip}}$ of the estimator $\hat{\delta}_{ip}$ is simply a shifted version of the PDF $\rho_{\Delta_{\hat{\delta}_{ip}}}$ of the deviation $\Delta_{\hat{\delta}_{ip}}$. Since the random variables $\Delta_{\hat{\delta}_{ip},si}$ and $\Delta_{\hat{\delta}_{ip},n}$ are statistically independent, from the statistical theory [Widrow 96] it is well known that this latter PDF can be derived by the convolution of their respective PDFs $\rho_{\hat{\delta}_{ip},si}$ and $\rho_{\hat{\delta}_{ip},n}$, which are provided by (66) and (67), respectively. Thus, we obtain:

$$\rho_{\Delta_{\hat{\delta}_{ip}}}(a)=\int_{-\infty}^{+\infty}\rho_{\hat{\delta}_{ip},si}(t-a)\rho_{\hat{\delta}_{ip},n}(t)\,dt=\frac{1}{\sqrt{2\pi}}\int_{\frac{-\Delta_{\hat{\delta}_{ip},si\_\max}+a}{\sigma_{\hat{\delta}_{ip},n}}}^{\frac{\Delta_{\hat{\delta}_{ip},si\_\max}+a}{\sigma_{\hat{\delta}_{ip},n}}}\frac{e^{-\frac{t^2}{2}}}{\pi\sqrt{\Delta^2_{\hat{\delta}_{ip},si\_\max}-(t\sigma_{\hat{\delta}_{ip},n}-a)^2}}\,dt, \tag{68}$$

which can be evaluated by using numerical methods.

We verified the accuracy of (68) through both computer simulations and experimental results. Thus, Fig. 4 shows the simulated and theoretical PDF $\rho_{\Delta_{\hat{\delta}_{ip}}}$ as a function of the deviation $\Delta_{\hat{\delta}_{ip}}$ when the integer part $l$ of the acquired sine-wave cycles is equal to 6 (Fig. 4(a)) and 34 (Fig. 4(b)), respectively. The *rsd-msl3* window was adopted. The sine-wave was characterized by $A = 1$ and $\delta = 0.3$ when $l = 6$ and $\delta = -0.2$ when $l = 34$. The sine-waves were corrupted by a white Gaussian noise with zero mean and variance $\sigma_n^2$ such that the corresponding Signal-to-Noise Ratio ($SNR$) was 65 dB. For each value of $l$, 50,000 runs were performed by choosing the sine-wave phase $\phi$ at random in the range [0, $2\pi$) rad. The function $g(\cdot)$ was determined as in the simulations related to Fig. 2. The theoretical behavior of $\rho_{\Delta_{\hat{\delta}_{ip}}}$ was achieved by a numerical integration of (68) performed by the trapezes formula. The histogram of $\Delta_{\hat{\delta}_{ip}}$ estimates obtained by simulation was properly scaled in order to achieve a PDF estimate.

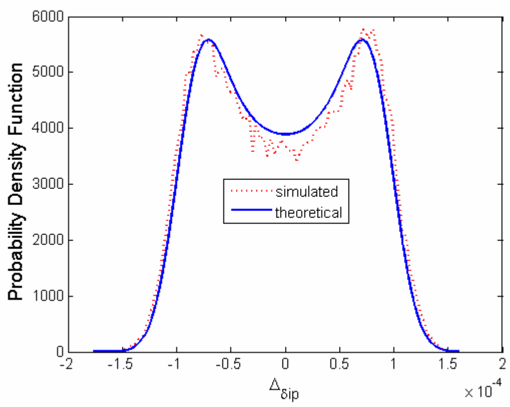


(a)

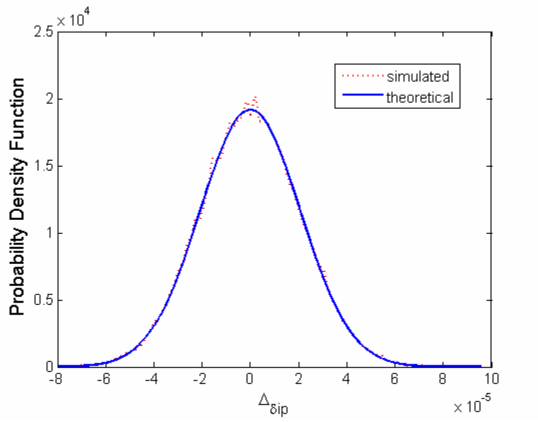


(b)

Fig. 4. PDF $\rho_{\Delta_{\hat{\delta}_{ip}}}$ achieved by simulation and by (68) versus $\Delta_{\hat{\delta}_{ip}}$ when: (a) $\delta = 0.3$ and $l = 6$ and (b) $\delta = -0.2$ and $l = 34$. The *rsd-msl3* window was adopted.

Notice the good agreement between the simulation and theoretical results. The same behavior was achieved also when other windows were adopted and both uniform and Gaussian noise is used.

In the experimental runs the sine-waves were supplied by an Agilent 33220A signal generator and were acquired using a 12-bit data acquisition board NI-6023E, developed by National Instruments. The $FSR$ and the sampling frequency were set to 10 V and 100 kHz, respectively. The sine-waves were characterized by an amplitude $A$ = 2 V and a frequency equal to 619 Hz and 3.3 kHz, respectively. Considering records of $M$ = 1024 samples, these frequencies correspond to a value of $l$ equal to 6 and 34, respectively. The *rsd-msl3* window was adopted. For each frequency 10,000 records were acquired and the related $\hat{\delta}_{ip}$ estimates were determined. Fig. 5 shows the estimation error PDFs achieved both from experimental data and expression (68). In particular, the histogram of $\Delta_{\hat{\delta}_{ip}}$ estimates obtained experimentally was properly scaled in order to obtain a PDF estimate. The theoretical PDF was achieved by numerical integration of (68). In the experimental data, the value of $\delta$ returned by the four-parameter sine-fitting (4PSF) algorithm was used as a reference because of its very high accuracy. The initial parameters of the algorithm were estimated by means of the IpDFT method based on the rectangular window [Bilau 04]. The algorithm iterations were stopped when the magnitude of the differences between the values estimated in two consecutive iterations was less than $10^{-6}$ for any estimated parameter.

Fig. 5 shows that the estimates achieved by experimental data strongly agree with theoretical results. Moreover, Fig. 5 looks very similar to Fig. 4 since both simulation and experimental results were achieved using almost the same $SNR$ value.

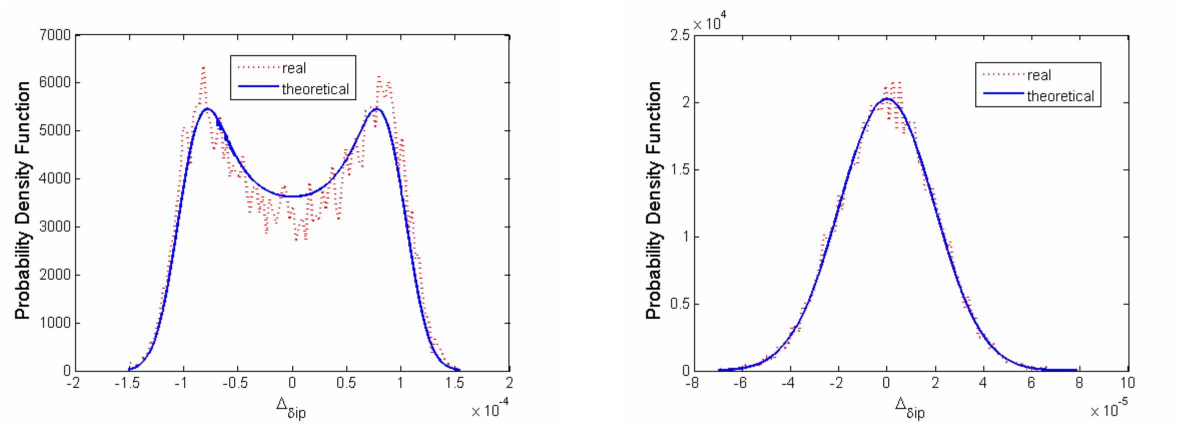


Fig. 5. PDF $\rho_{\Delta_{\hat{\delta}_{ip}}}$ achieved by experimental data and by (68) versus $\Delta_{\hat{\delta}_{ip}}$ when the sine-wave frequencies were: (a) 619 Hz and (b) 3.3 kHz. The *rsd-msl3* window was adopted.

## C. Multipoint Interpolated DFT Methods

To reduce the detrimental effect of the spectral interference from the fundamental image component to the parameter estimates achieved by the IpDFT method, which occurs at small number of acquired sine-wave cycles, the Multipoint IpDFT (MIpDT) methods should be used [Agrež 00], [Agrež 07], [Belega 08a], [Belega 10a], [Belega 10b], [Agrež 02], [Belega 09d]. Our contributions to these approaches are presented in the following.

### 1) *Frequency estimation*

The errors of the spectral interference from the fundamental image component on the frequency estimation achieved by the IpDFT method can be reduced by using a suitable window function [Belega 09c]. However, they still high, especially at small number of acquired sine-wave cycles. A further reduction of these errors can be performed by increasing the number of spectrum interpolation points, i.e. by using the MIpDFT methods [Agrež 00], [Agrež 07], [Belega 08a], [Belega 10a], [Belega 10b]. In [Belega 08a], we proposed a novel MIpDFT method for frequency estimation, which will be called MIpDFT$_1$ method in the following. Moreover, in [Belega 10a], we generalized the MIpDFT method proposed in [Agrež 00] in order to use that method for any MSD window. That method will be called MIpDFT$_2$ method in the following. Both MIpDFT$_1$ and MIpDFT$_2$ methods are based on the MSD windows and use an odd number of selected DFT samples. Also, in [Belega 10b] we compared by means of computer simulations the effectiveness in reducing the detrimental effect of the spectral interference and the statistical performances of both MIpDFT methods in the case of multi-frequency signals. The above contributions are presented in the following.

- *MIpDFT$_1$ method*

From (55) the DFT spectral line $|X_w(l)|$ can be written as:

$$\left|X_w(l)\right| = \frac{A}{2}\left|W(-\delta)\right| + \Delta(l), \tag{69}$$

in which the first term is the short-range leakage contribution of the window spectrum weighted by $A/2$, while the second one, $\Delta(l)$, is due to the long-range spectral leakage of the image part of the signal. As we already specified the term $\Delta(i)$ is either a positive or negative real-valued quantity. Moreover, it decreases for increasing values of its arguments and takes values with opposite signs in adjacent frequency bins.

In order to estimate $\delta$ by the MIpDFT$_1$ method when the number of interpolation points is $2J + 1$, the following ratio ${}_{2J+1}\widetilde{\alpha}_H$ is determined [Belega 08a]:

$${}_{2J+1}\widetilde{\alpha}_H = \frac{\sum_{i=0}^{J} C_J^{J-i}\left|X_w(l-i)\right|}{\sum_{i=0}^{J} C_J^{J-i}\left|X_w(l+i)\right|}. \tag{70}$$

It should be observed that in the numerator and denominator of the ratio ${}_{2J+1}\widetilde{\alpha}_H$ appears the $J$-order finite differences of $\Delta(l-i)$ and $\Delta(l+i)$, respectively, which are equal to [Coşniţă 72]:

$$\left|\Delta^J(l-J)\right| = \sum_{i=0}^{J}(-1)^{J-i} C_J^{J-i}\left|\Delta(l-i)\right|, \tag{71}$$

$$\left|\Delta^J(l+J)\right| = \sum_{i=0}^{J}(-1)^{J-i} C_J^{J-i}\left|\Delta(l+i)\right|. \tag{72}$$

As specified above $\Delta(i)$ takes values with opposite signs in adjacent frequency bins. Thus, by summation the influences of the long-range leakage tails are reduced. Hence, the following equalities practically holds true:

$$\sum_{i=0}^{J} C_J^{J-i}\left|X_w(l-i)\right| = 0.5A\sum_{i=0}^{J} C_J^{J-i}\left|W(i+\delta)\right| \tag{73}$$

$$\sum_{i=0}^{J} C_J^{J-i}\left|X_w(l+i)\right| = 0.5A\sum_{i=0}^{J} C_J^{J-i}\left|W(i-\delta)\right|. \tag{74}$$

By replacing the above expressions in (70) we achieve:

$$
{}_{2J+1}\widetilde{\alpha}_H = \frac{\sum_{i=0}^{J} C_J^{J-i} \left| W(i+\delta) \right|}{\sum_{i=0}^{J} C_J^{J-i} \left| W(i-\delta) \right|}. \tag{75}
$$

Using (27) the above relationship becomes:

$$
{}_{2J+1}\widetilde{\alpha}_H = \frac{\sum_{i=0}^{J} C_J^{J-i} \dfrac{1}{(i+\delta)\prod_{h=1}^{H-1}\left(h^2-(i+\delta)^2\right)}}{\sum_{i=0}^{J} C_J^{J-i} \dfrac{1}{(i-\delta)\prod_{h=1}^{H-1}\left(h^2-(i-\delta)^2\right)}}. \tag{76}
$$

.

After some calculus the numerator of the above expression is given by:

$$
\begin{aligned}
\sum_{i=0}^{J} C_J^{J-i} \frac{1}{(i+\delta)\prod_{h=1}^{H-1}\left(h^2-(i+\delta)^2\right)} &= \frac{1}{\delta\prod_{h=1}^{H-1}\left(h^2-\delta^2\right)} \\
\times \left\{ \sum_{i=1}^{J} C_J^{J-i} \left[ \frac{(H-i-\delta)(H-i+1-\delta)\dots(H-1-\delta)}{(H+\delta)(H+1+\delta)\dots(H+i-1+\delta)} \right] + C_J^J \right\}&.
\end{aligned} \tag{77}
$$

In the following we demonstrate the equality

$$
\sum_{i=1}^{J} C_J^{J-i} \left[ \frac{(H-i-x)(H-i+1-x)\dots(H-1-x)}{(H+x)(H+1+x)\dots(H+i-1+x)} \right] + C_J^J = \frac{(2H+J-2)!}{(2H-2)!\prod_{h=H}^{H+J-1}(h+x)}. \tag{78}
$$

where $x$ is a real number.
After some calculus the above equality becomes:

$$
\begin{aligned}
C_J^J &+ \frac{H-1-x}{H+x} C_J^{J-1} + \dots + \frac{(H-i-1-x)(H-i-x)\dots(H-1-x)}{(H+x)(H+1+x)\dots(H+i+x)} C_J^{J-i-1} \\
&+ \dots \frac{(H-J-x)(H-J+1-x)\dots(H-1-x)}{(H+x)(H+1+x)\dots(H+J-1+x)} C_J^0 = \frac{(2H+J-2)!}{(2H-2)!\prod_{h=H}^{H+J-1}(h+x)}.
\end{aligned} \tag{79}
$$

To prove the equality (79), first each side is multiplied by $H + i + x$, $i = 0, 1, 2,\dots, J - 1$ and then are given to $x$ the values $(-H - i)$. Thus, we obtain:

$$C_{2H-2}^{0} C_J^{J-i-1} + C_{2H-2}^{1} C_J^{J-i-2} + \ldots + C_{2H-2}^{J-i-1} C_J^{0} = C_{2H+J-2}^{J-i-1}. \tag{80}$$

The above equality is true since the left side is the coefficient of $x^{J-i-1}$ of the product of the binomials $(1+x)^{2H-2}$ $(1+x)^J$ and the right side is the coefficient of $x^{J-i-1}$ of the binomial $(1+x)^{2H+J-2}$.

Then, to put in evidence the necessity of $C_J^J$ in the left side of the equality (79), each side of this equality is multiplied by $H-1-x$ and then to $x$ the value $(1-H)$ is given. Thus, we obtain:

$$C_{2H-2}^{0} C_J^{J} + C_{2H-2}^{1} C_J^{J-1} + \ldots + C_{2H-2}^{J} C_J^{0} = C_{2H+J-2}^{J}. \tag{81}$$

The above equality is true since the left side is the coefficient of $x^J$ of the product of binomials $(1+x)^{2H-2}$ $(1+x)^J$ and the right side is the coefficient of $x^J$ of the binomial $(1+x)^{2H+J-2}$.

Thus, the equality (79) is true.

By replacing $x = \delta$ in (79), the numerator of the expression (76) becomes:

$$\sum_{i=0}^{J} C_J^{J-i} \frac{1}{(i+\delta)\prod_{h=1}^{H-1}\left(h^2-(i+\delta)^2\right)} = \frac{1}{\delta\prod_{h=1}^{H-1}\left(h^2-\delta^2\right)} \frac{(2H+J-2)!}{(2H-2)!\prod_{h=H}^{H+J-1}(h+\delta)}. \tag{82}$$

By using the same procedure is proved that the denominator of the (76) is given by

$$\sum_{i=0}^{J} C_J^{J-i} \frac{1}{(i-\delta)\prod_{h=1}^{H-1}\left(h^2-(i-\delta)^2\right)} = \frac{1}{\delta\prod_{h=1}^{H-1}\left(h^2-\delta^2\right)} \frac{(2H+J-2)!}{(2H-2)!\prod_{h=H}^{H+J-1}(h-\delta)}. \tag{83}$$

From (82) and (83) the ratio ${}_{2J+1}\widetilde{\alpha}_H$ is given by:

$${}_{2J+1}\widetilde{\alpha}_H = \frac{\prod_{h=H}^{H+J-1}(h-\delta)}{\prod_{h=H}^{H+J-1}(h+\delta)}. \tag{84}$$

Thus, the estimator of the fractional frequency is the solution of the following equation:

$$\prod_{h=H}^{H+J-1}\left(h - {}_{2J+1}\widetilde{\delta}_H\right) - {}_{2J+1}\widetilde{\alpha}_H \prod_{h=H}^{H+J-1}\left(h + {}_{2J+1}\widetilde{\delta}_H\right) = 0. \tag{85}$$

For some particular values of $J$ the estimator ${}_{2J+1}\widetilde{\delta}_H$ is given by analytical expressions:

- for $J = 1$ (three-point interpolation) we have:

$$
{}_3\tilde{\delta}_H = H\frac{1 - {}_3\tilde{\alpha}_H}{1 + {}_3\tilde{\alpha}_H}. \tag{86}
$$

- for $J = 2$ (five-point interpolation) ${}_5\tilde{\delta}_H$ is given by:

$$
{}_5\tilde{\delta}_H = \frac{(2H+1)(1+{}_5\tilde{\alpha}_H) - \sqrt{(1+{}_5\tilde{\alpha}_H)^2 + 16\,{}_5\tilde{\alpha}_H H(H+1)}}{2(1-{}_5\tilde{\alpha}_H)}. \tag{87}
$$

- for $J = 3$ (seven-point interpolation) we achieve:

$$
{}_7\tilde{\delta}_H = \sqrt[3]{-v + \sqrt{v^2 + u^3}} - \sqrt[3]{v + \sqrt{v^2 + u^3}} - \frac{(H+1)({}_7\tilde{\alpha}_H - 1)}{{}_7\tilde{\alpha}_H + 1}, \tag{88}
$$

in which $u = \frac{4\,{}_7\tilde{\alpha}_H (H+1)^2}{({}_7\tilde{\alpha}_H + 1)^2} - \frac{1}{3}$ and $v = \frac{4\,{}_7\tilde{\alpha}_H (1-{}_7\tilde{\alpha}_H)(H+1)^3}{(1+{}_7\tilde{\alpha}_H)^3}$.

- *$MIpDFT_2$ method*

To estimate $\delta$ by the $MIpDFT_2$ method based on the $H$-term MSD window ($H \geq 2$) when the number of interpolation points is $2J + 1$, the following ratio ${}_{2J+1}\alpha_H$ is determined [Belega 10a]:
- for $1 \leq J \leq H - 1$ (i.e. for interpolation points inside the windowed sine-wave spectrum main lobe) ${}_{2J+1}\alpha_H$ is given by:

$$
{}_{2J+1}\alpha_H = \frac{\sum_{i=1}^{J} C_{2J-2}^{J-i}\left[|X_w(l+i)| - |X_w(l-i)|\right] - \sum_{i=1}^{J-2} C_{2J-2}^{J-i-2}\left[|X_w(l+i)| - |X_w(l-i)|\right]}{\sum_{i=1}^{J} C_{2J}^{J-i}\left[|X_w(l+i)| + |X_w(l-i)|\right] + C_{2J}^{J}|X_w(l)|}, \tag{89}
$$

- for $J \geq H$, ${}_{2J+1}\alpha_H$ is given by:

$$
{}_{2J+1}\alpha_H = \frac{\sum_{i=1}^{H-1}\left(C_{2J-2}^{J-i} - C_{2J-2}^{J-i-2}\right)\left[|X_w(l+i)| - |X_w(l-i)|\right] + \sum_{i=H}^{J}\left(C_{2J-2}^{J-i} - C_{2J-2}^{J-i-2}\right)(-1)^i s\left[|X_w(l+i)| + |X_w(l-i)|\right]}{\sum_{i=1}^{H-1} C_{2J}^{J-i}\left[|X_w(l+i)| + |X_w(l-i)|\right] + C_{2J}^{J}|X_w(l)| + \sum_{i=H}^{J} C_{2J}^{J-i}(-1)^i s\left[|X_w(l+i)| - |X_w(l-i)|\right]}. \tag{90}
$$

in which $s$ is equal either to 1 if $|X_w(l + 1)| > |X_w(l - 1)|$ or to $-1$ if $|X_w(l + 1)| < |X_w(l - 1)|$.
Notice that the numerator of (90) contains the differences between the symmetrical pairs of components $|X_w(l \pm i)|$ weighted by $\left(C_{2J-2}^{J-i} - C_{2J-2}^{J-i-2}\right)$ when they fall inside the spectrum main lobe, and the sums between the same pairs of components weighted by $(-1)^i \cdot s \cdot \left(C_{2J-2}^{J-i} - C_{2J-2}^{J-i-2}\right)$ when they are

outside the spectrum main lobe. In fact, when the considered pair is outside the spectrum main lobe, the sign associated with one of the components $|X_w(l - i)|$ or $|X_w(l + i)|$ is negative because of the $W(i \pm \delta)$ value, so their, summation is considered in (90). In addition, the obtained results are multiplied by $(-1)^i \cdot s$ in order to obtain a quantity with the same sign as the differences between the components inside the spectrum main lobe. A similar observation holds also for the denominator of (90).

Thus, using (69), the differences $(\Delta(l + i) - \Delta(l - i))$ appear in the numerator of ${}_{2J+1}\alpha_H$. Conversely, the $2J$- order finite difference of $\Delta(l - J)$:

$$\Delta^{2J}(l-J) = \sum_{i=1}^{J} (-1)^{J-i} C_{2J}^{J-i} [\Delta(l-i) + \Delta(l+i)] + (-1)^J C_{2J}^{J} \Delta(l) \tag{91}$$

appear in the denominator of ${}_{2J+1}\alpha_H$. When $\nu$ is high enough, the terms $\Delta(l \pm i)$, $i = 0, 1, \ldots, J$ are close to each other and thus the differences $(\Delta(l + i) - \Delta(l - i))$ are very small and $\left|\Delta^{2J}(l-J)\right| << \left|\Delta(l)\right|$. This implies that the influence of the terms $\Delta(i)$ on ${}_{2J+1}\alpha_H$ is negligible. Thus, using (27), in [Belega 10b], we determined the expressions of the numerator and the denominator of ${}_{2J+1}\alpha_H$:

$$Num({}_{2J+1}\alpha_H) \cong \frac{AM\sin(\pi\delta)}{\pi 2^{2H-2}} \cdot \frac{(2H+2J-3)!}{\prod_{h=1}^{H+J-1}(h^2-\delta^2)} \tag{92}$$

$$Den({}_{2J+1}\alpha_H) \cong \frac{AM\sin(\pi\delta)}{2^{2H-1}\pi\delta} \cdot \frac{(2H+2J-2)!}{\prod_{h=1}^{H+J-1}(h^2-\delta^2)}. \tag{93}$$

From the above rations it follows that the fractional frequency $\delta$ can be estimated by:

$${}_{2J+1}\hat{\delta}_H = (H+J-1)\,{}_{2J+1}\alpha_H. \tag{94}$$

It is worth noticing that for $J = 3$ we have ${}_3\tilde{\delta}_H = {}_3\hat{\delta}_H$.

In [Belega 10b], we compared the effectiveness of both $\text{MIpDFT}_1$ and $\text{MIpDFT}_2$ methods in the case of the following multi-frequency signal:

$$\begin{aligned} x(m) = A_0 &+ A_1 \sin\left(2\pi\frac{l_1+\delta_1}{M}m+\phi_1\right) + A_2 \sin\left(2\pi\frac{l_2+\delta_2}{M}m+\phi_2\right) \\ &+ A_3 \sin\left(2\pi\frac{l_3+\delta_3}{M}m+\phi_3\right) + A_4 \sin\left(2\pi\frac{l_4+\delta_4}{M}m+\phi_4\right), \quad m = 0,1,\ldots,M-1 \end{aligned} \tag{95}$$

in which $A_0 = 0.1$, $A_1 = 2$, $A_2 = 0.5$, $A_3 = 0.07$, $A_4 = 0.1$, $\phi_1 = 0.4$ rad, $\phi_2 = 0.8$ rad, $\phi_3 = 1.2$ rad, $\phi_4 = 1$ rad, $l_1 = 5$, $l_2 = 19$, $l_3 = 42$, $l_4 = 125$, and $M = 1024$. Also, $\delta_1 = \delta_2 = \delta_3 = \delta_4 = \delta$, where $\delta$ varies in the range $(-0.5, 0.5)$ with a step of 0.04. For each value of $\delta$ the phases $\phi_1$, $\phi_2$, $\phi_3$, and $\phi_4$ were uniformly distributed in the range $[0, 2\pi)$ rad and 1000 runs were done. The maximum of the modulus of the estimation error of $\delta_k$, $|\Delta\delta_k|_{\max}$ occurring during the variation of phases was retained. Fig. 6 shows the errors $|\Delta\delta_k|_{\max}$ ($k$ = 1, 2, 3, 4) obtained by both MIpDFT methods and the IpDFT method as a function of $\delta$ when the three-term MSD window is adopted. In the MIpDFT methods three- and five-point interpolation were considered.

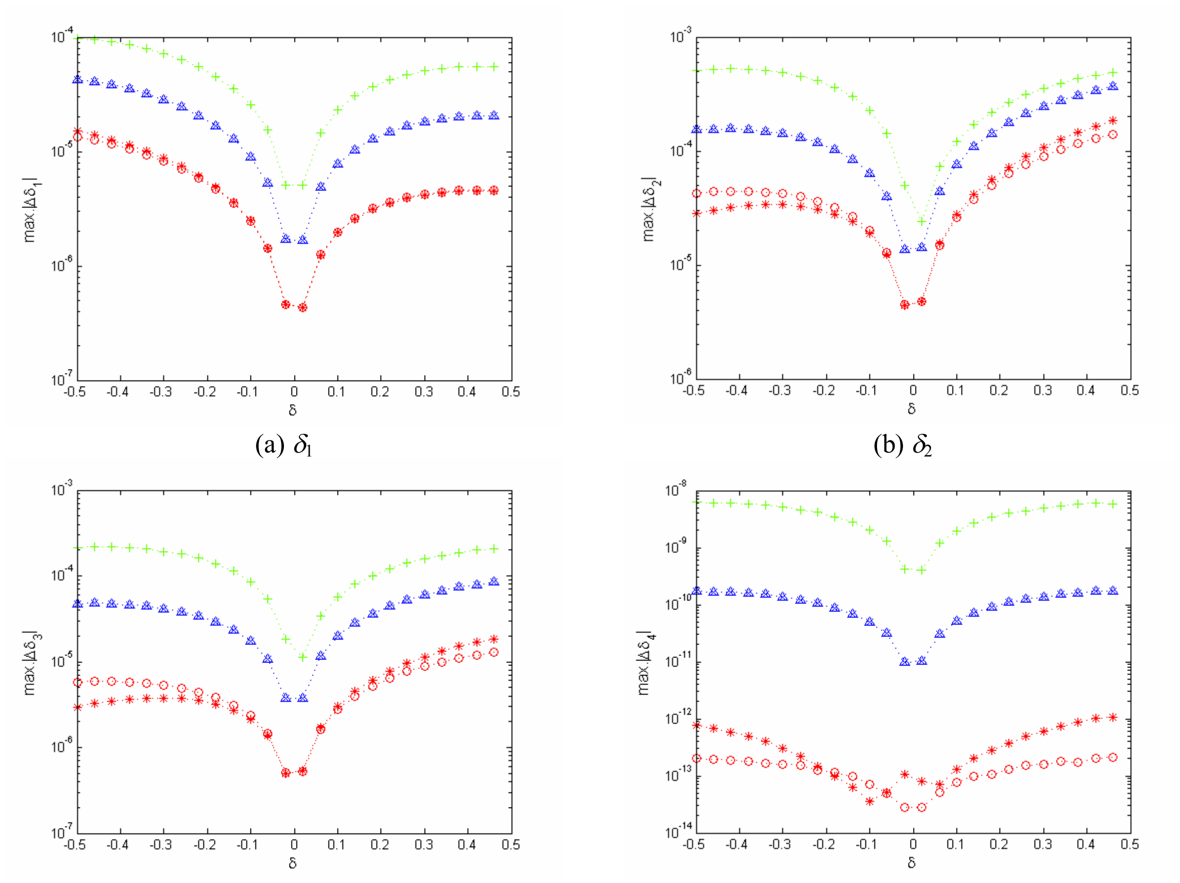


(a) $\delta_1$ (b) $\delta_2$

(c) $\delta_3$ (d) $\delta_4$

Fig. 6. Errors $|\Delta\delta_k|_{\max}$ as a function of $\delta$ when the three-term MSD window is used. $\delta_k$ is estimated by the MIpDFT$_1$ method ('*'-five-point interpolation, 'x'-three-point interpolation), the MIpDFT$_2$ method ('o'-five-point interpolation, 'Δ'-three-point interpolation), and the IpDFT method ('+').

In Fig. 6 it can be see that both MIpDFT methods reduce the systematic errors as the number of points involved in the interpolation increases (i.e. $J$ increases). The results obtained for three-point interpolation are the same since the $\delta_k$ estimator is the same in both methods. For five-point interpolation the MIpDFT methods have almost the same effectiveness in the reduction of systematic errors of $\delta_k$ ($k$ = 1, 2, 3) estimates, but the MIpDFT$_2$ method slightly increases the $\delta_4$ estimation accuracy. Both MIpDFT methods have a higher effectiveness in the reduction of systematic errors of $\delta_k$ estimates than the IpDFT method. Nevertheless, it was proven by simulation that the systematic errors decrease as $H$ increases. In addition, the accuracy of the $\delta_k$ estimates depends on the mutual frequency component span [Belega 08a]. To avoid spectral interferences from the nearby components it is necessary to fulfil this relationship: $(l_{k+1} - l_k) > 2H + 1$, $k = 0, 1, \ldots, K$, in which $l_0$ corresponds to the DC component and $K$ is the number of multi-frequency signal components [Belega 08a].
Moreover, we compared the statistical performance of the MIpDFT$_1$ and MIpDFT$_2$ methods using the above multi-frequency signal corrupted by an additive white Gaussian noise with zero mean and $\sigma_n$

standard deviation. $\sigma_n$ was established as a function of the *SNR*, which varied in the range [40, 100] dB with a step of 10 dB. The values of $\delta_k$ were set as follows: $\delta_1 = 0.1$, $\delta_2 = -0.4$, $\delta_3 = 0.3$, and $\delta_4 = -0.25$. For each *SNR*, 100 value sets for the phases $\phi_1$, $\phi_2$, $\phi_3$, and $\phi_4$ uniformly distributed in the range $[0, 2\pi)$ rad were generated. For each set, 1000 runs were performed and the maximum bias of $\delta_k$ was calculate. The three-term MSD window was adopted and three- and five-point interpolation were considered in both MIpDFT methods. Fig. 7 shows the magnitude of the absolute value of the bias of $\delta_k$ estimates obtained by both MIpDFT methods and the IpDFT method.

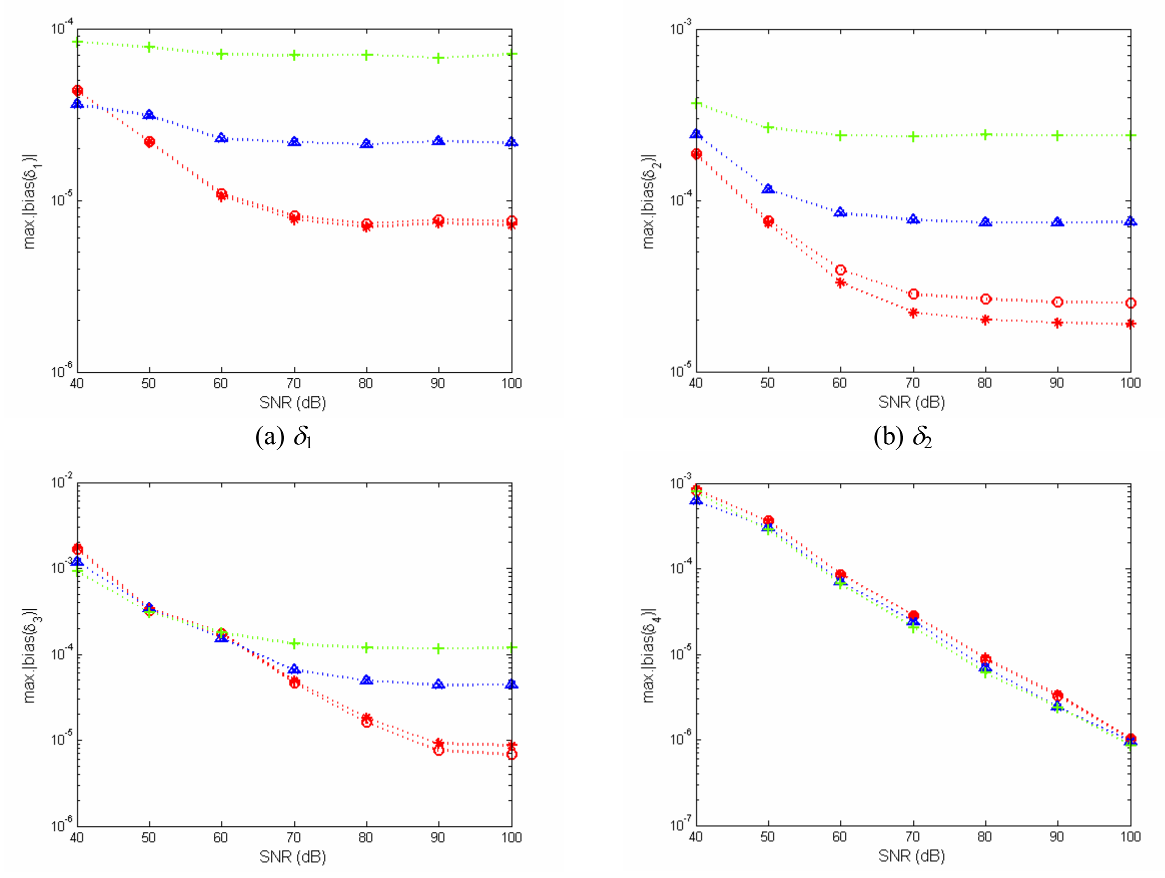


(a) $\delta_1$ (b) $\delta_2$

(c) $\delta_3$ (d) $\delta_4$

Fig. 7. Magnitude of the absolute value of the bias of the $\delta_k$ estimates as a function of *SNR* when the three-term MSD window is used. $\delta_k$ is estimated by the MIpDFT$_1$ method ('*'-five-point interpolation, 'x'-three-point interpolation), the MIpDFT$_2$ method ('o'-five-point interpolation, 'Δ'-three-point interpolation), and the IpDFT method ('+').

In Fig. 7 it can be see that the results obtained for three-point interpolation are the same and for five-point interpolation the results obtained by both MIpDFT methods are very close. When the MIpDFT methods are used, for a given value of *J*, the accuracy of $\delta_k$ estimates depends on the position of the frequency component (i.e. on $l_k$) and on *SNR*. In addition, for a given *J*, the accuracy of the $\delta_k$ estimates depends, as for a signal without noise, on the mutual frequency component span.

For large $l_k$, the errors due to the spectral interferences become smaller than the errors due to the noise and so, the accuracy of $\delta_k$ estimates is practically unchanged (see Fig. 7(d)). This behavior is also obtained for small *SNR* < 40 dB. For this reason the MIpDFT methods are well suited to be used when $l_k$ is not so large and for relative greater *SNR* (i.e. for signal corrupted with relative small power noise). In these cases more accurate estimates are achieved.

Fig. 8 shows the statistical efficiency in respect to the corresponding CRLB of $\delta_3$ estimators provided by both MIpDFT methods and the IpDFT method as a function of $\delta_3$. *SNR* was set to 70 dB. $\delta_3$ varies in the range [–0.5, 0.5) with a step of 1/25. The phases of the components were set as follows: $\phi_1 = 0$ rad, $\phi_2 = \pi/3$ rad, $\phi_3 = 3\pi/4$ rad, and $\phi_4 = \pi/6$ rad. For each $\delta_3$, 5000 runs were done.

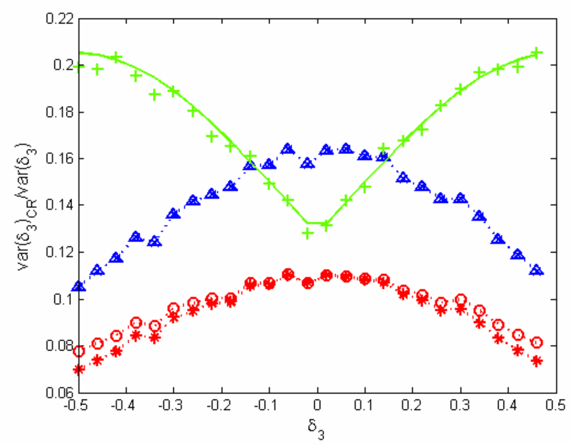


Fig. 8. Statistical efficiency of the $\delta_3$ estimators provided by the MIpDFT$_1$ method ('*'-five-point interpolation, 'x'-three-point interpolation), the MIpDFT$_2$ method ('o'-five-point interpolation, 'Δ'-three-point interpolation), and the IpDFT method ('+') as a function of $\delta_3$. Continuous line represents the theoretical results.

In Fig. 8, it can be observed that when the MIpDFT methods are used the statistical efficiency decreases as the number of interpolation points increases. Also, it can be observed that for five-point interpolation the MIpDFT$_2$ method is slightly more efficient than the method MIpDFT$_1$ for $|\delta|$ close to 0.5. Moreover, it should be remarked that for $|\delta|$ values close to zero the three-point IpDFT methods provide more accurate estimates than the IpDFT method [Belega 08b]. This behavior was obtained also for the $\delta_1$, $\delta_2$, and $\delta_4$ estimates. Simulations were carried out for different values of phases $\varphi_k$ ($k$ = 1, 2, 3, 4), amplitudes $A_k$ ($k$ = 1, 2, 3, 4), and *SNR* between 30 and 80 dB and a similar behavior as in Fig. 8 was always achieved.

As it can be observed that the MIpDFT$_2$ method has almost the same effectiveness in reducing the spectral interference from the image component as the MIpDFT$_1$ method, but the related fractional frequency estimator has a more simple analytical expression. Hence, in [Belega 10a], we analyzed the accuracy of the estimator ${}_{2J+1}\hat{\delta}_H$ . To this aim, we derived the expression for the combined standard uncertainty of the estimator ${}_{2J+1}\hat{\delta}_H$ , which was not derived in the previous works focused on the MIpDFT$_2$ method. That derivation is given in the following.

Observing that the parameters $H$ and $J$ appear in (92)-(94) only as the single term ($H$ + $J$), the following conclusions can be drawn when the number of interpolations points $2J + 1$ is higher than or equal to 3 [Belega 09e]:

• The $\delta$ estimator obtained by the $H$-term MSD widow and $(2J + 1)$ – point interpolation is equal to the one derived by the two-term MSD window and $(2J + 2H – 3)$-point interpolation:

$$ {}_{2J+1}\hat{\delta}_H = {}_{2J+2H-3}\hat{\delta}_2 . \tag{96} $$

In particular, from (96) it follows that these two estimators are affected by the same interference error from the image component and exhibit the same wideband noise sensitivity. Thus, the use of the two-term MSD window with a suitable number of interpolation points allows us to achieve the same accuracy as the $H$-term MSD ($H \geq 3$).

• The $\delta$ estimator obtained by the $H$-term MSD widow and $(2J + 1)$-point interpolation is equal to the one derived by the $(H + J - 1)$-term MSD window and three-point interpolation:

$$ {}_{2J+1}\hat{\delta}_H = {}_3\hat{\delta}_{H+J-1}. \tag{97} $$

From (97) it follows that both these estimators are affected by the same interference error from the image component, that is:

$$ \Delta_{{}_{2J+1}\delta_H, si} = \Delta_{{}_3\delta_{H+J-1}, si} \tag{98} $$

and the same standard uncertainty due to the wideband noise component:

$$ \sigma_{{}_{2J+1}\hat{\delta}_H, n} = \sigma_{{}_3\hat{\delta}_{H+J-1}, n}. \tag{99} $$

In [Belega 09f], we shown that the interference error $\Delta_{{}_3\delta_{H+J-1}, si}$ is phase dependent and exhibits a sine-wave like behavior with amplitude:

$$ \Delta_{{}_3\delta_{H+J-1}, si\_\max} = \frac{2(l+\delta)|\delta|}{2l+\delta} \cdot \frac{\prod_{h=1}^{H+J-1}\left(h^2-\delta^2\right)}{\prod_{h=1}^{H+J-1}\left[(2l+\delta)^2-h^2\right]}. \tag{100} $$

and power $\left(\Delta_{{}_3\delta_{H+J-1}, si\_\max}\right)^2/2$. Also, in [Belega 09f], we derived the expression for the standard uncertainty $\sigma_{{}_3\hat{\delta}_{H+J-1}, n}$ due to the wideband noise, which is:

$$ \sigma_{{}_3\hat{\delta}_{J+H-1}, n} = \frac{2\pi\delta}{A\sin(\pi\delta)} \frac{\prod_{h=1}^{H+J-1}(h^2-\delta^2)}{(2H+2J-2)!} \sqrt{\frac{C_{4H+4J-8}^{2H+2J-4}}{M}} \sqrt{\frac{(4H+4J-7)[(4H+4J-5)^2\delta^2+(H+J-1)^2]}{(H+J-1)(2H+2J-3)}}\,\sigma_n. \tag{101} $$

The uncertainty contributions leading to (100) and (101) are clearly due to different physical phenomena, so they can be considered statistically independent. Thus, according to [GUM 95], the combined standard uncertainty of the MIpDFT$_2$ normalized frequency estimator obtained with the $H$-term MSD window and $(2J + 1)$ interpolation points is:

$$ \sigma_{{}_{2J+1}\hat{\delta}_H} = \sqrt{\frac{\left(\Delta_{{}_3\delta_{H+J-1}, si\_\max}\right)^2}{2} + \sigma^2_{{}_3\hat{\delta}_{H+J-1}, n}}. \tag{102} $$

Besides, we compared the accuracy of the combined standard uncertainty $\sigma_{_{2J+1}\hat{\delta}_H}$ as a function of the number of used interpolation points through by both computer simulations and experimental results. Fig. 9 shows the combined standard uncertainty returned by the MIpDFT$_2$ method for the different number of interpolation points and the IpDFT method as a function of $\nu$. The combined standard uncertainty related to the IpDFT method is $\sigma_{\hat{\delta}_{ip}}$, and it is given by (65). The amplitude of the sine-wave was equal to 2 and the phase $\phi$ was chosen at random in the range $[0, 2\pi)$ rad. The normalized frequency $\nu$ was varied between 3.5 and 20.5 with a step of 1/25. The sine-wave was corrupted by an additive Gaussian noise with zero mean and standard deviation $\sigma_n$, chosen in such a way that the *SNR* was equal to 70 dB. For each value of $\nu$, 1000 runs of $M = 1024$ samples each were performed and the standard uncertainty of the normalized frequency estimates was evaluated. Both the IpDFT method and the MIpDFT$_2$ method with 3, 5, and 7- point interpolation were used. The maximum number of interpolation points was equal to 7 to avoid the use of the DC component as an interpolation point. The two-term MSD window was adopted in both methods. The most accurate estimator is marked with black solid line.

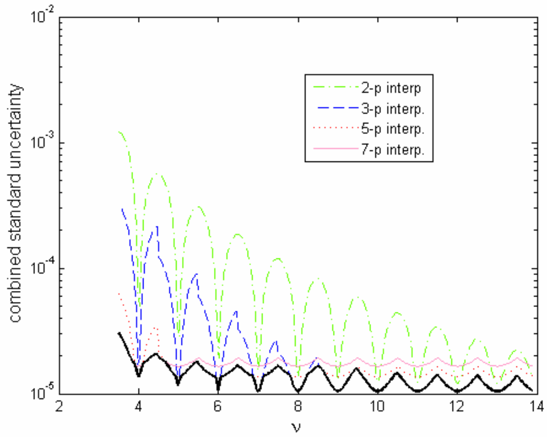


Fig. 9. Combined standard uncertainty returned by the MIpDFT$_2$ and the IpDFT methods as a function of acquired number of cycles $\nu$. In the MIpDFT$_2$ method, 3, 5, and 7-point interpolation are used. The sine-wave is corrupted by an additive Gaussian noise and the *SNR* is 70 dB. The two-term MSD window and $M = 1024$ are used.

From Fig. 9 we can see that when $\nu$ is less than 4.7 bins the best estimator is almost always the one with 7-point interpolation. Conversely, minimum combined uncertainty is achieved almost for any frequency by using the 5-point or the 3-point interpolation when $\nu$ is between about 4.7 and 7.8 bins or it is larger than 7.8 bins respectively.

In the experimental runs the sine-waves were obtained from an Agilent 33220A signal generator by setting the amplitude to 2 V and the frequencies to 0.50, 0.60, 0. 73, 0.85, 0.91, 1.05, 1.20, 1.33, 1.40, 1.55, 1.62, 1.77, 1.90, 2.00, 2.15, and 2.20 kHz, respectively. It should be noted that the adopted generator employs a 14-bit Digital-to-Analog Converter (DAC). The signals were acquired using a 12-bit data acquisition board NI-6023E. The *FSR* and the sampling frequency were set to 10 V and to 119.05 kHz, respectively. For each frequency 500 runs of $M = 1024$ samples each were performed and the standard uncertainties of the normalized frequency estimates were evaluated. Both the IpDFT method and the MIpDFT$_2$ method with 3, 5, and 7 interpolation points were considered and the two-term MSD window was adopted. The values of the integer part $l$ of the number of acquired sine-wave cycles were between 4 and 19 bins with a step of 1 bin, whereas the fractional part $\delta$ assumed values in the range (–0.1727, 0.4931) bins.

The effective number of bits (*ENOB*) of the acquisition board was about 11.1 bits. Thus, we can state that the power of the noise superimposed to the generated sine-wave is quite close to the power introduced by a 12 bit ideal quantizer, although the effective bits do not allow us to conclude whether the dominant noise is due to wideband noise or nonlinearity.

The combined standard uncertainties of the normalized frequency estimates obtained by both the IpDFT method and the MIpDFT method with 3 and 5 interpolation points are shown in Fig. 10 as a function of $\nu$. Moreover, the behavior of the ratios $\sigma_{{}_3\hat{\delta}_H}/\sigma_{\hat{\delta}_{ip}}$ and $\sigma_{{}_5\hat{\delta}_H}/\sigma_{\hat{\delta}_{ip}}$ are reported in Fig. 11 as a function of $\nu$. Any combined standard uncertainty was determined both experimentally and by using (65) and (102) assuming an ideal 12 bit quantization.

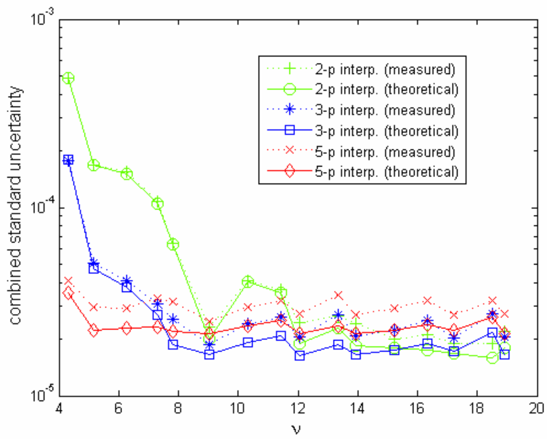


Fig. 10. Combined standard uncertainties $\sigma_{\hat{\delta}_{ip}}$, $\sigma_{{}_3\hat{\delta}_H}$, and $\sigma_{{}_5\hat{\delta}_H}$ determined both experimentally and by (65) and (102) as a function of acquired number of cycles $\nu$. The theoretical results are determined assuming the sine-wave corrupted by only the ideal quantization noise of the 12 bits acquisition board.

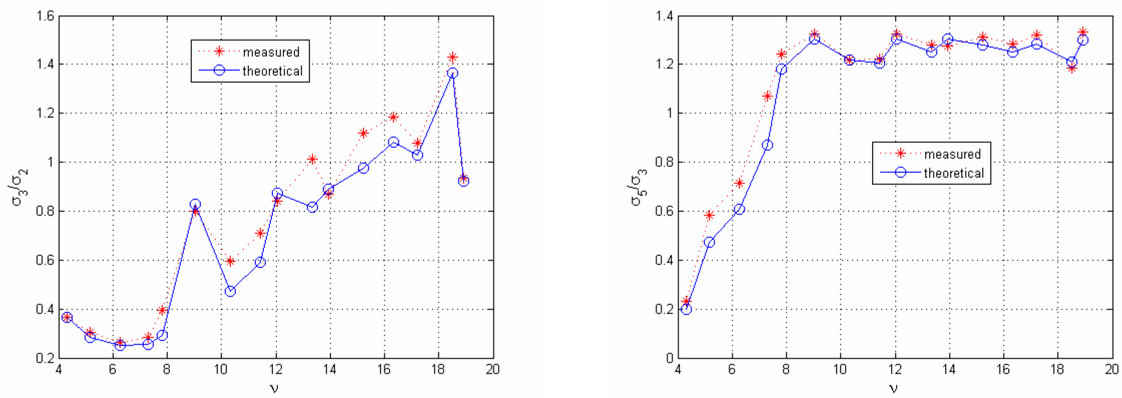


(a) (b)

Fig. 11. Ratios $\sigma_{{}_3\hat{\delta}_H}/\sigma_{\hat{\delta}_{ip}}$ (a) and $\sigma_{{}_5\hat{\delta}_H}/\sigma_{{}_3\hat{\delta}_H}$ (b) determined both experimentally and by (65) and (102) as a function of acquired number of cycles $\nu$. The theoretical results are determined assuming the sine-wave corrupted by only the ideal quantization noise of the 12 bits acquisition board.

Figs. 10 and 11 show that the experimental and theoretical results are quite close to each other. This confirms the fact that the superimposed wideband noise is mainly due to quantization. Moreover, the optimal number of interpolation points achieved from the experimental and simulation results is the same for the majority of considered signal frequencies. For the remaining frequencies the experimental and theoretical uncertainties are very close (see Fig. 10).

A particular three-point IpDFT method is the so-called average-based IpDFT method [Andria 89], [Novotný 06], [Belega 13a]. This method estimates the frequency of a sine-wave by the average of the two estimates achieved using the IpDFT method. In [Andria 89], was analyzed through computer simulations the effect of the additive wideband noise on the normalized frequency estimation when the classes I, II, and III Rife-Vincent windows are adopted. A general expression for the variance of the normalized frequency estimator provided by the average-based IpDFT method based on the MSD windows was derived in [Novotný 06]. In [Belega 13a], I analyzed the contribution of the spectral interference from the fundamental image component on the frequency estimation achieved by the average-based IpDFT, aspect which was not previously analyzed. Also, I derived a much simple expression for the variance of the frequency estimator than in [Novotný 06]. Furthermore, I derived the expression for the combined standard uncertainty of the frequency estimator provided by the average-based IpDFT method. I verified the accuracy of the derived expressions by means of computer simulations and the effectiveness of that method through both computer simulations and experimental results. The most important part of that work is presented in the following.

To estimate the fractional part $\delta$ by the average-based IpDFT method when the $H$-term MSD window ($H \geq 2$) is used the following ratios $\alpha_i$, $i = 1, 2$, are determined:

$$\alpha_i = \frac{|X_w(l+i-1)|}{|X_w(l-2+i)|}, \quad i = 1, 2. \tag{103}$$

By neglecting the effect of the spectral interference from the image component, from (27) we obtain:

$$\alpha_i \cong \frac{|W(i-1-\delta)|}{|W(-2+i-\delta)|}, \quad i = 1, 2. \tag{104}$$

From (104), using (27) it follows that the fractional part $\delta$ can be estimated either by $\delta_1$ or $\delta_2$, which are given by:

$$\delta_i = \frac{(H-2+i)\alpha_i - H + i - 1}{\alpha_i + 1}. \tag{105}$$

The estimator provided by the average-based IpDFT method is the average of the $\delta_1$ and $\delta_2$ [Andria 89], [Novotný 06]:

$$\hat{\delta}_{avg} = \frac{\delta_1 + \delta_2}{2}. \tag{106}$$

Using (103) after some calculations the following expression of $\hat{\delta}_{avg}$ can be achieved [Andria 89]:

$$\hat{\delta}_{avg} = \frac{2H-1}{2} \frac{|X_w(l)|\,(|X_w(l+1)| - |X_w(l-1)|)}{(|X_w(l-1)| + |X_w(l)|)(|X_w(l+1)| + |X_w(l)|)}. \tag{107}$$

In [Belega 13a], I derived the expression of the contribution of the spectral interference from the spectral interference of the fundamental image component to the estimator $\hat{\delta}_{avg}$, which is given by:

$$\Delta_{\hat{\delta}_{avg}, si} \cong p \frac{2\delta(l+\delta)(\delta^2 + 2l\delta + H^2)}{(2l+\delta)} \frac{\prod_{h=1}^{H-1}(h^2 - \delta^2)}{\prod_{h=1}^{H}\left[(2l+\delta)^2 - h^2\right]}, \tag{108}$$

where $p$ is defined as in (55). Thus, the error $\Delta_{\hat{\delta}_{avg}, si}$ is an almost sinusoidal function of $\phi$ with amplitude equal to:

$$\Delta_{\hat{\delta}_{avg}, si\_\max} \cong \frac{2|\delta|(l+\delta)|l(\delta^2 + 2l\delta + H^2)|}{(2l+\delta)} \frac{\prod_{h=1}^{H-1}(h^2 - \delta^2)}{\prod_{h=1}^{H}\left[(2l+\delta)^2 - h^2\right]}, \tag{109}$$

and its rms value is equal to $\Delta_{\hat{\delta}_{avg,}, si\_\max} / \sqrt{2}$.

We consider that the discrete-time sine-wave (1) is corrupted by a stationary white noise with zero mean and variance $\sigma_n^2$. In this case the estimator $\hat{\delta}_{avg}$ is affected by both the spectral interference from the fundamental image component and the wideband noise.
Also, in [Belega 13a], I derived a much simple expression for the variance of the estimator $\hat{\delta}_{avg}$ due to a stationary white noise of zero mean and variance $\sigma_n^2$ superimposed to the discrete-time sine-wave than in [Novotný 06], which is:

$$\sigma^2_{\hat{\delta}_{avg}, n} \cong \frac{\pi^2\delta^2}{A^2 \sin^2(\pi\delta)} \frac{\prod_{h=1}^{H-1}(h^2 - \delta^2)^2}{[(2H-1)!]^2} \times \frac{C_{4H-4}^{2H-2}}{2M}\left[(H+\delta)^4 + (H-\delta)^4 + 4\delta^2 + 16H\delta^2\rho_1 - 2(H^2 - \delta^2)^2\rho_2\right]\sigma_n^2, \tag{110}$$

where $\rho_1 = \rho_1(|X_w(j)|, |X_w(j+1)|)$ and $\rho_2 = \rho_2(|X_w(j-1)|, |X_w(j+1)|)$ are the correlation coefficients between the DFT spectral lines $|X_w(j)|$ and $|X_w(j+1)|$ and the DFT spectral lines $|X_w(j-1)|$ and $|X_w(j+1)|$, respectively. The correlation coefficient $\rho_1$ is given by (43), whereas $\rho_2$ was derived in [Belega 08b] and have the expression:

$$\rho_2 = \frac{(2H-3)(2H-2)}{2H(2H-1)}. \tag{111}$$

Since the contributions from the spectral interference and additive wideband noise are from two different physical phenomena, they can be considered statistically independent and according to [GUM 95], the combined standard uncertainty of the normalized frequency estimator provided by the average-based IpDFT method is given by:

$$\sigma_{\hat{\delta}_{avg}} = \sqrt{\frac{\Delta^2_{\hat{\delta}_{avg},si\_\max}}{2} + \sigma^2_{\hat{\delta}_{avg},n}}, \tag{112}$$

where $\Delta_{\hat{\delta}_{avg},si\_\max}$ and $\sigma^2_{\hat{\delta}_{avg},n}$ are given by (109) and (110), respectively.

I verified the accuracies of the relationships (109), (110), and (112) by means of computer simuations. Moreover, I compared the combined standard uncertainty of the estimator $\hat{\delta}_{avg}$ with those of the estimators provided by the three-point $\text{IpDFT}_2$ method and the IpDFT method through both computer simulations and experimental results. For the latter two methods the expressions of the combined standard uncertainties are given by (102) and (65), respectively. Fig. 12 shows the theoretical expressions of the combined standard uncertainties achieved by all above methods as a function of $\nu$ when the two-term MSD window is adopted. The sine-wave was corrupted by a Gaussian noise with zero mean and variance corresponding to a *SNR* equal to 60 dB (Fig. 12(a)) and 90 dB (Fig. 12(b)), respectively. The frequency $\nu$ was varied in the range [2, 10] with a step of 1/20.

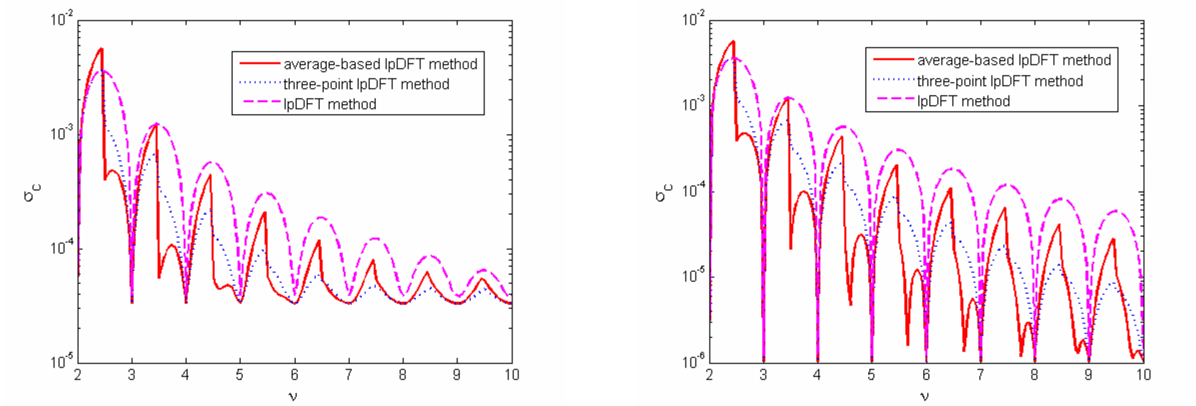


(a) (b)

Fig. 12. Theoretical combined standard uncertainties achieved by all considered methods versus $\nu$ when the two-term MSD window is adopted and *SNR* is equal to (a) 60 dB and (b) 90 dB.

From Fig. 12 it can be seen that when the effect of the spectral interference is much higher than that of the wideband noise for each $\nu$ there exist an interval of negative values of $\delta$ in which the average-based IpDFT method outperforms the other methods. In this case for $\delta$ values close to zero both the average-based and the three-point IpDFT methods provides almost the same estimates, which are more accurate than those provided by the IpDFT method. For the remaining $\delta$ values, that are positive ones, the three-point IpDFT method outperforms the other methods. The upper limit value of $\nu$ up to which the above described behavior is achieved increases as *SNR* increases. It is equal to 6 when *SNR* = 60 dB and to 16 when *SNR* = 90 dB.

Moreover, it was observed that when both spectral interference and wideband noise contributions are important, which occurs for $6 < \nu \leq 14$ when *SNR* = 60 dB and for $16 < \nu \leq 45$ when *SNR* = 90 dB, for positive values of $\delta$ the three-point $IpDFT_2$ method provides more accurate estimates than the other methods and for negative and null values of $\delta$ the estimates provides by both the average-based IpDFT method and the three-point $IpDFT_2$ method are almost the same, and more accurate than those provided by the IpDFT method. For $\nu > 14$ when *SNR* = 60 dB and for $\nu > 45$ when *SNR* = 90 dB the effect of the wideband noise is much higher than that of the spectral interference. In this case the IpDFT method provides the best estimates, except the situations in which the values of $\delta$ are close to zero, where the other methods performed the best.

In the experimental runs the sine-waves were supplied by an Agilent 33220A signal generator and acquired using a data acquisition board NI-6023E. The full scale range and the sampling frequency were set to 10 V and 100 kHz, respectively. Two set of frequencies were considered. In the first set the sine-waves frequencies were varied between 250 and 340 Hz with a step of 10 Hz in order to obtain different values of $\nu$ in the range (2.5, 3.5), and in the second set between 630 and 740 Hz with the same step in order to obtain different values of $\nu$ in the range (6.5, 7.5). The amplitude of all sine-waves was equal to 2 V. For each frequency value 1000 runs of $M$ = 1024 samples each were performed and the variances of the normalized frequency estimator provided by all considered methods were calculated. The two-term MSD window was adopted in all methods. It should be noticed that the parameter SIgnal-to-Noise And Distortion ratio (*SINAD*) estimated by means of the IpDFT method for the frequencies of the second set was about 60 dB. The variances achieved by the considered methods for both frequency sets are depicted in Fig. 13 as a function of $\nu$, estimated by its mean value achieved using the three-point $IpDFT_2$ method.

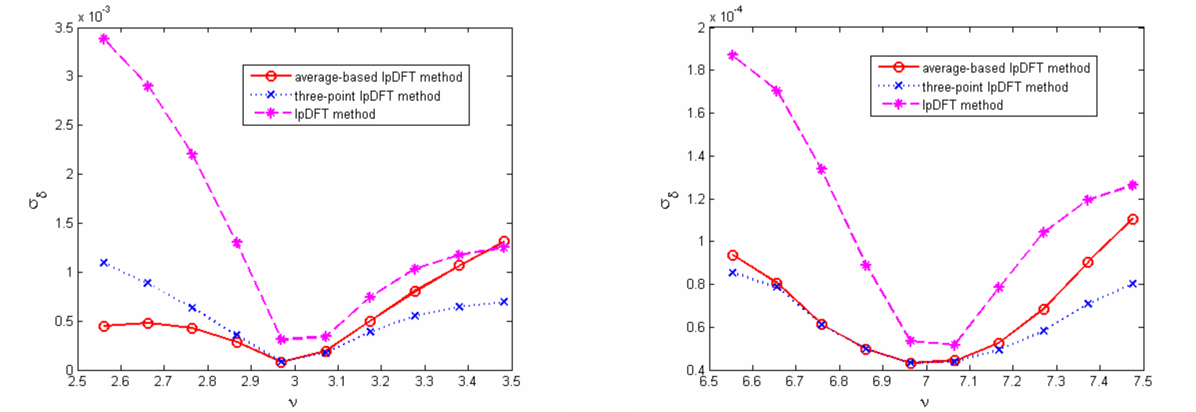


(a) (b)

Fig. 13. Variances of the normalized frequency estimators provided by the average-based IpDFT method,the three-point $IpDFT_2$ method, and the IpDFT method versus ν for the (a) first and (b) second set of sine-wave frequencies. The value of $\nu$ was estimated by its mean value achieved using the three-point $IpDFT_2$ method.

For the achieved values of $\nu$, Fig. 13 looks similar to Fig. 12(a) since both experimental and simulation results were achieved using close *SNR* values. Thus, in Fig. 13(a) it can be seen that for negative values of $\delta$ the average-based IpDFT method provides more accurate estimates than the three-point $IpDFT_2$ method, for values of $\delta$ very close to zero the estimates provided by the above two methods are almost the same, and for positive values of $\delta$ the three-point IpDFT$_2$ method provides more accurate estimates than the average-based IpDFT method. Fig. 13(b) shows that for negative and close to zero values of $\delta$ both average-based and three-point IpDFT$_2$ methods provide almost the same accurate estimates, and for positive values of $\delta$ the three-point IpDFT$_2$ method provides the best estimates. In all situations shown in Fig. 13 the estimates provided by both average-based and three-point IpDFT$_2$ methods are more accurate than those provided by the IpDFT method.

**2) *Amplitude estimation***

One of the most efficient MIpDFT methods for amplitude estimation was proposed in [Agrež 02]. That MIpDFT method is based on the rectangular and Hann windows and use an odd number of selected DFT samples. In [Belega 09d], we performed a generalization of that method in order to use any MSD window in that MIpDFT method, which is presented in the following.

We consider that the $H$-term MSD window ($H \geq 2$) is adopted and the number of interpolation point is equal to $2J + 1$ ($J \geq 1$). Based on the observation that the $2J$-order finite difference of $\Delta(l - J)$, $\left|\Delta^{2J}(l-J)\right|$, given by (91), is much smaller than $|\Delta(l)|$, and using (31) the following equality is fulfilled:

$$\sum_{i=1}^{J} C_{2J}^{J-i}\left[\left|X_w(l-i)\right|+\left|X_w(l+i)\right|\right]+C_{2J}^{J}\left|X_w(l)\right| \cong \frac{A}{2}\left[\sum_{i=1}^{J} C_{2J}^{J-i}\left[\left|W(i+\delta)\right|+\left|W(i-\delta)\right|\right]+C_{2J}^{J}\left|W(\delta)\right|\right]. \qquad (113)$$

Based on (113) we proposed the following amplitude estimator:

$${}_{2J+1}\hat{A}_H = 2\frac{\sum_{i=1}^{J} C_{2J}^{J-i}\left[\left|X_w(l-i)\right|+\left|X_w(l+i)\right|\right]+C_{2J}^{J}\left|X_w(l)\right|}{\sum_{i=1}^{J} C_{2J}^{J-i}\left[\left|W(i+\delta)\right|+\left|W(i-\delta)\right|\right]+C_{2J}^{J}\left|W(\delta)\right|}. \qquad (114)$$

By replacing (93) in (114) we achieve:

$${}_{2J+1}\hat{A}_H = \frac{2^{2H-1}\pi\delta\prod_{h=1}^{H+J-1}\left(h^2-\delta^2\right)}{M\sin(\pi\delta)(2H+2J-2)!}\left[\sum_{i=1}^{J} C_{2J}^{J-i}\left[\left|X_w(l-i)\right|+\left|X_w(l+i)\right|\right]+C_{2J}^{J}\left|X_w(l)\right|\right]. \qquad (115)$$

Furthermore, in [Belega 09d], we derived the expression of the amplitude estimation error due to the spectral interference from the fundamental image component. That expression is:

$$\Delta_{{}_{2J+1}A_H,si} = {}_{2J+1}\hat{A}_H - A \cong \frac{A(-1)^J p\delta \prod_{h=1}^{H+J-1}\left(h^2-\delta^2\right)}{(2l+\delta)\prod_{h=1}^{H+J-1}\left[(2l+\delta)^2-h^2\right]}, \tag{116}$$

in which $p$ is defined as in (55).

From the above expression it follows that the maximum of the error $\Delta_{{}_{2J+1}A_H,si}$ is given by :

$$\Delta_{{}_{2J+1}A_H,si\_\max} \cong \frac{A\,|\,\delta\,|\prod_{h=1}^{H+J-1}\left(h^2-\delta^2\right)}{(2l+\delta)\prod_{h=1}^{H+J-1}\left[(2l+\delta)^2-h^2\right]}. \tag{117}$$

From (117) the ratio between the maximum amplitude estimation errors achieved for $(2J + 1)$ and $(2J + 3)$-point interpolation and the same $H$ is given by:

$$\frac{\Delta_{{}_{2J+1}A_H,si\_\max}}{\Delta_{{}_{2J+3}A_H,si\_\max}} \cong \frac{(2l+\delta)^2-(H+J)^2}{(H+J)^2-\delta^2}, \tag{118}$$

and the ratio between the maximum amplitude estimation errors achieved for windows with $(H + 1)$ and $H$ terms and the same number of interpolation point, $J$, is given by:

$$\frac{\Delta_{{}_{2J+1}A_H,si\_\max}}{\Delta_{{}_{2J+1}A_{H+1},si\_\max}} \cong \frac{(2l+\delta)^2-(H+J)^2}{(H+J)^2-\delta^2}. \tag{119}$$

If $l$ is high enough (for example $l \geq 6$) from (118) and (119) it follows that the errors due to the spectral interferences decrease as the number of interpolation points, $J$, increases and the number of terms of the adopted window, $H$, increases.

Also, we analyzed through computer simulations the statistical performance of the MIpDFT method in the case of the multi-frequency signal (95) corrupted by white Gaussian noise of zero mean and variance $\sigma_n^2$. The multi-frequency signal was characterized by: $A_0 = 0.1$, $A_1 = 2$, $A_2 = 0.5$, $A_3 = 0.07$, $A_4 = 0.1$, $l_1 = 5$, $l_2 = 13$, $l_3 = 24$, $l_4 = 125$, $\delta_1 = 0.1$, $\delta_2 = -0.4$, $\delta_3 = 0.3$, $\delta_4 = -0.25$, and $M = 1024$. The phase components $\phi_1$, $\phi_2$, $\phi_3$, and $\phi_4$ are uniformly distributed on $[0, 2\pi)$ rad. $\sigma_n$ was established as a function of the *SNR*, which varies in the range [40, 100] dB with an increment of 10 dB. For each *SNR* the worst bias of $A_k$ estimations (worst case) occurring during the phase variation is retained. Each time 1000 runs are done to calculate the mean value. Fig. 14 shows the magnitude of the absolute value of the bias of the $A_k$ estimates as function of *SNR*. $A_k$ was estimated by MIpDFT method (3 and 5-point interpolation) and the IpDFT method. When the MIpDFT method was used, $\delta_k$ $(k = 1, 2, 3, 4)$ were estimated by the $\text{MIpDFT}_1$ method (see previous subsection). The three-term MSD window was adopted.

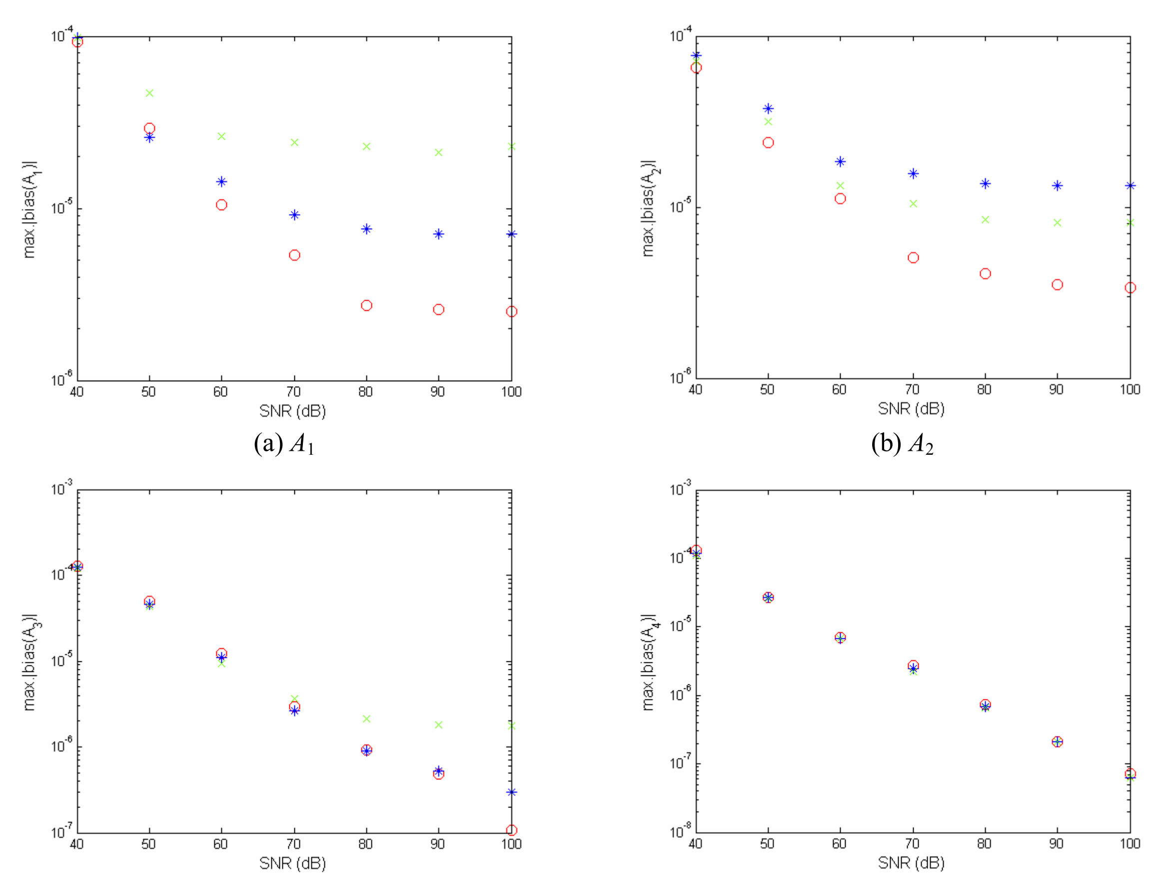


(a) $A_1$ (b) $A_2$

(c) $A_3$ (d) $A_4$

Fig. 14. Magnitude of the absolute value of the bias of $A_k$ ($k$ = 1, 2, 3, 4) estimates as a function of *SNR* obtained by the MIpDFT method (‘o’-5 point interpolation, ‘*’-3 point interpolation) and the IpDFT method (‘x’).

From Fig. 14 it can be seen that for a given $J$, different results are obtained for the values of $l_k$. Hence, it follows that for a given $J$, the accuracy of $A_k$ estimations depends on the position of the frequency component (i.e. on $l_k$). It can also be observed in Fig. 14 that for a given $J$ the accuracy of $A_k$ estimates increases as *SNR* increases. This behavior is due to the fact that as *SNR* increases the influence of the noise on the of $A_k$ estimates decreases and so, the achieved estimates are more accurate. Moreover, for a given $J$, the accuracy of $A_k$ estimates depends on the mutual frequency separation of components span. To avoid spectral interferences from the nearby components, it is necessary to fulfill this relationship: $(l_{k+1} - l_k) > 2H + 1$, $k = 0, 1, \ldots, K$, in which $l_0$ corresponds to the DC component and $K$ is the number of multi-frequency signal components [Belega 08a].

For high $l_k$ the errors due to the spectral interference become smaller than those due to noise and so, the accuracy of $A_k$ estimates is practically unchanged (as in Fig. 14(d)). Thus, the MIpDFT method is well suited when $l_k$ is not too high and for relative greater *SNR* (i.e. for signals corrupted by a relative small power noise).

Moreover, we evaluated the statistical efficiency of the amplitude estimator provided by the MIpDFT method in respect to the corresponding CRLB as the function of the number of interpolation points. It has been shown that for the same MSD window the statistical efficiency decreases as the number of interpolation point increases.

## D. Energy-Based Method

Another frequency-domain method often used in the applications is the so-called Energy-Based (EB) method. That method is very simple to understand and to apply. Besides, it provides accurate sine-wave parameter estimates using very simple formulas [Petri 90], [Offelli 90a], [Solomon 94], [Petri 02], [Benetazzo 92], [Novotný 07], [Belega 12b], [Belega 12c]. In [Belega 12b], we observed that the estimation errors achieved when the EB method is used are due to independent phenomena, that are the algorithm error, the interference from other spectral components of the signal, and the wideband noise superimposed to the signal. Then, we separately analyzed each above contribution on the frequency and amplitude estimation when the three- and four-term MSD, RSD-MSL, MSL, and MEE windows are used in [Belega 12b] and [Belega 12c], respectively. It is worth noticing that usually two-term windows are not used in the EB method since the related algorithm error is quite high. These analyses, which were not performed in the previous works on this subject, are presented in the following.

### 1) *Frequency estimation*

The estimator for the parameter $\delta$ provided by the EBM is [Petri 90], [Offelli 90a]:

$$\hat{\delta}_{eb} = \frac{\sum_{k=-H}^{H} k\left|X_w(l+k)\right|^2}{\sum_{k=-H}^{H} \left|X_w(l+k)\right|^2}. \tag{120}$$

Notice that only $(2H + 1)$ DFT samples centered around the spectrum peak are considered. For $\delta \neq 0$, all of them, except one, fall inside the window spectrum main lobe. This choice ensures a good tradeoff between algorithm uncertainty, algorithm selectivity of nearby spectral components, and computational effort. Notice that the denominator of (120) is the sum of the square modulus of all the considered DFT samples, while at the numerator the same quantities are multiplied by their frequency distance (expressed in bins) from the spectrum peak (located in $l$) before to be summed up.

#### a) *Effect of algorithm error*

We consider at first a pure sine wave and assume that the effect of the spectral interference from the fundamental image component on the $\hat{\delta}_{eb}$ estimator (120) is negligible, as occurs when the number of acquired sine-wave cycles ν is high enough. In this case, using (31), the relationship (120) can be written as:

$$\hat{\delta}_{eb,a\lg} \cong \frac{\sum_{k=-H}^{H} k\left|W(k-\delta)\right|^2}{\sum_{k=-H}^{H} \left|W(k-\delta)\right|^2}. \tag{121}$$

Thus, the $\delta$ estimation error due to the algorithm is approximately given by:

$$\Delta_{\hat{\delta}_{eb,alg}}(\delta) \cong \hat{\delta}_{eb,alg} - \delta \cong \frac{\sum_{k=-H}^{H} k\left|W(k-\delta)\right|^2}{\sum_{k=-H}^{H}\left|W(k-\delta)\right|^2} - \delta. \tag{122}$$

From (122) it follows that the algorithm error $\Delta_{\hat{\delta}_{eb},\mathrm{alg}}$ is an odd function of $\delta$ and the algorithm estimates exactly the sine-wave frequency, that is $\Delta_{\hat{\delta}_{eb},alg}$ (0) = 0, in the case when $\delta = 0$ (coherent sampling). Fig. 15 shows the absolute value of that error achieved by (122) and computer simulations as a function of $\delta$, for $0 < \delta < 0.5$, and the considered cosine windows. The sine-wave phase $\phi$ was uniformly distributed in the range $[0, 2\pi)$ rad. The integer part $l$ was equal to 513 and the number of acquired samples was $M = 8192$. The fractional part $\delta$ of the acquired sine-wave cycles was varied in the range [0.01, 0.5) with a step of 0.01.

Fig. 15 shows that the theoretical and simulation results are in very good agreement. Also, from Fig. 15 it follows that the maximum of the algorithm error, $\Delta_{\hat{\delta}_{eb},alg\_max}$, is reached for a value $\delta_{\mathrm{alg\_max}}$, which depends on the adopted window. Moreover, such fractional frequencies differ from the values of $\delta$ associated to the maximum amplitude estimation error [Belega 07b]. The values of $\delta_{\mathrm{alg\_max}}$ and $\Delta_{\hat{\delta}_{eb},alg\_max}$ achieved for the above considered three- and four-term cosine windows are reported in Table 3.

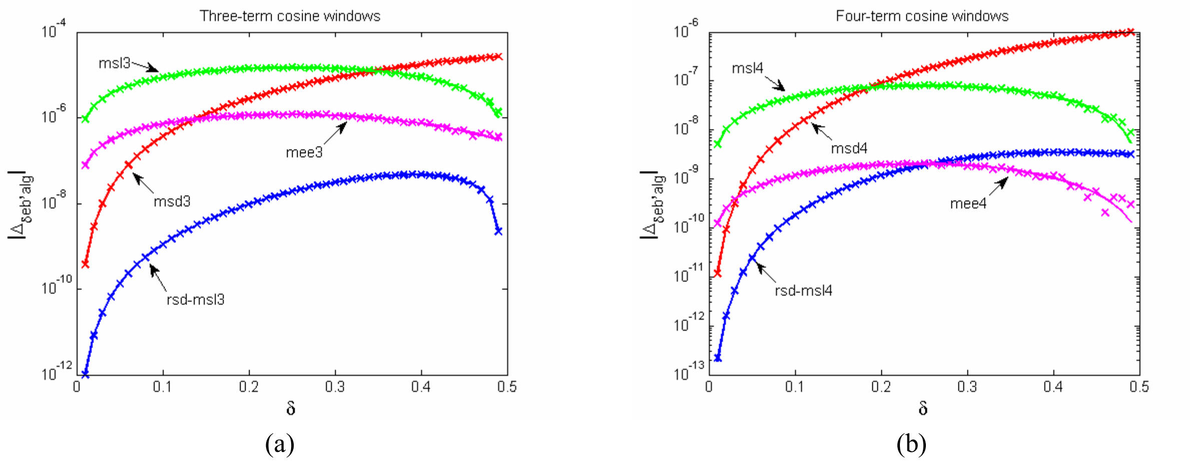


Fig. 15. Absolute value of the algorithm error $\Delta_{\hat{\delta}_{eb},\mathrm{alg}}$ achieved by (122) and computer simulations versus $\delta$ for some commonly used (a) three-term and (b) four-term cosine windows. The theoretical and simulation results are represented by continuous lines and crosses, respectively.

Table 3. Values of $\delta_{\text{alg\_max}}$ and $\Delta_{\hat{\delta}_{eb},\, a\lg\_\max}$ for some commonly used three- and four-term cosine windows.

| Window | $H$ | $\delta_{\text{alg\_max}}$ | $\Delta_{\hat{\delta}_{eb},\, a\lg\_\max}$ |
|---|---|---|---|
| Max. sidelobe decay (msd3) | 3 | – 0.50 | 2.77E–5 |
| Rapid sidelobe decay with min. sidelobe level (rsd-msl3) | | 0.39 | 4.65E–8 |
| Min. sidelobe level (msl3) | | – 0.25 | 1.47E–5 |
| Min. error energy (mee3) | | – 0.25 | 1.18E–6 |
| Max. sidelobe decay (msd4) | 4 | – 0.50 | 1.02E–6 |
| Rapid sidelobe decay with min. sidelobe level (rsd-msl4) | | – 0.41 | 3.45E–9 |
| Min. sidelobe level (msl4) | | – 0.25 | 8.03E–8 |
| Min. error energy (mee4) | | – 0.25 | 2.01E–9 |

The results reported in Table 3 show that, when the three-term cosine windows are considered, the smallest maximum algorithm error is provided by the *rsd-msl3* window. Conversely, when the four-term cosine windows are used, the optimal choice with respect to the algorithm error is the *mee4* window.

**b)** ***Effect of spectral interference from the image component***

We assume now a pure sine-wave and consider the effect of the spectral interference from the image component on the $\hat{\delta}_{eb}$ estimator (120), that is:

$$\Delta_{\hat{\delta}_{eb},si}(l,\delta,\phi) = \hat{\delta}_{eb} - \hat{\delta}_{eb,\, a\lg} \tag{123}$$

From (4), (31), and (120) it follows that for a given window such an effect depends on the sine-wave phase $\phi$, the integer part $l$, and the fractional part $\delta$ of the number of acquired sine-wave cycles.
We shown by means of computer simulations that for $\delta \neq 0$, the error $\Delta_{\hat{\delta}_{eb},si}$ exhibits a sine-wave like behavior with respect to the signal phase. Thus, when considering a pure sine-wave with a phase uniformly distributed in the range [0, $2\pi$) rad, the effect of spectral interference $\Delta_{\hat{\delta}_{eb},si}$ can be modeled as a random variable with zero mean and standard deviation:

$$\sigma_{\hat{\delta}_{eb},si} = \Delta_{\hat{\delta}_{eb},si\_\max} / \sqrt{2}, \tag{124}$$

where $\Delta_{\hat{\delta}_{eb},si\_\max}$ represents the maximum of (123) with respect to the signal phase.

Fig. 16 shows $\Delta_{\hat{\delta}_{eb},si\_\max}$ achieved for $\delta = 0.2$ and the above considered three- and four-term cosine windows. All the values of $l$ belonging to the ranges represented in abscissa were considered. For each of them, 200 equidistant values in the range $[0, 2\pi)$ rad were taken for the sine-wave phase.

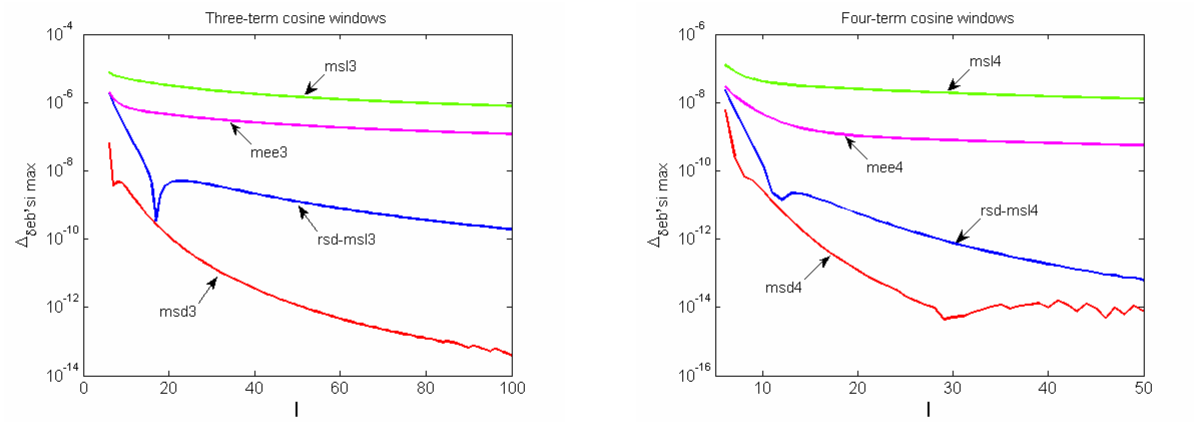


(a) (b)

Fig. 16. Maximum interference error $\Delta_{\hat{\delta}_{eb},si\_\max}$ as a function of the integer part $l$ of the number of acquired sine-wave cycles, for $\delta = 0.2$ and commonly used (a) three-term and (b) and four-term cosine windows.

As expected, Fig. 16 shows that $\Delta_{\hat{\delta}_{eb},si\_\max}$ decreases as the number of the acquired sine-wave cycles increases. Moreover $\Delta_{\hat{\delta}_{eb},si\_\max}$ decreases as the decay rate of the window sidelobes increases. In particular, $\Delta_{\hat{\delta}_{eb},si\_\max}$ is minimum when using the MSD windows, while the largest errors are achieved if the MSL and MEE windows are adopted. In fact these later windows have a sidelobe decay rate of only 6 dB/octave (see Table 2).

**c) *Effect of wideband noise***

We assume that the integer part $l$ of the number of acquired sine-wave cycles is high enough that the $\hat{\delta}_{eb}$ estimator is virtually not affected by the spectral interference from the image component. Moreover, in order to model common real-life situations, we assume that a stationary white noise with zero mean and variance $\sigma_n^2$ is added to the digitized sine-wave. In this case, for values of $|\delta|$ not too small, we derived the expression of the estimator mean, which is:

$$E[\hat{\delta}_{eb}] \cong \hat{\delta}_{eb,a\lg}. \tag{125}$$

in which $E[\cdot]$ represents the expectation operator.
Moreover, we derived the expressions of the estimator variance, which is given bellow:

$$\sigma^2_{\hat{\delta}_{eb},n} \cong \frac{16}{M \cdot NNPG}\left[2\sum_{i=1}^{H-2}\sum_{j=i+1}^{H-1} i\,j\,b_i b_j\,\rho(i,j) + \sum_{i=-H+1}^{-1}\sum_{j=1}^{H-1} i\,j\,b_{|i|} b_{|j|}\,\rho(i,j) + \sum_{i=1}^{H-1} i^2 b_i^2\right]\frac{\sigma_n^2}{A^2}, \tag{126}$$

where *NNPG* is given by (9), the coefficients $b_i$ by:

$$b_i = \begin{cases} a_0, & for \quad i = 0 \\ \dfrac{a_i}{2}, & for \quad i = 1, 2, \ldots, H-1 \\ 0, & for \quad i \geq H \end{cases} \tag{127}$$

and $\rho(i, j)$ is the correlation coefficient between the spectral samples $|X_w(l + i)|$ and $|X_w(l + j)|$ [Novotný 07]:

$$\rho(i,j) = \rho(d) = \frac{\sum_{k=-H+1}^{H-1-d} b_{|k|} b_{|k+d|}}{NNPG}, \tag{128}$$

in which $d = |i - j|$.

A very important conclusion drawn from (126) is that the variance $\sigma^2_{\hat{\delta}_{eb},n}$ depends only on the window used.

Using (63) and (126) it follows that the statistical efficiency $E_{\hat{\delta}_{eb}}$ of the EB method with respect to the corresponding unbiased CRLB is:

$$E_{\hat{\delta}_{eb}} \stackrel{\Delta}{=} \frac{(\sigma^2_{\hat{\delta},n})_{CR}}{\sigma^2_{\hat{\delta}_{eb},n}} \cong \frac{3 \cdot NNPG}{8\pi^2 \left[ 2\sum_{i=1}^{H-2} \sum_{j=i+1}^{H-1} i\, j b_i b_j \rho(i,j) + \sum_{i=-H+1}^{-1} \sum_{j=1}^{H-1} i\, j b_{|i|} b_{|j|} \rho(i,j) + \sum_{i=1}^{H-1} i^2 b_i^2 \right]}. \tag{129}$$

In Fig. 17 the statistical efficiencies $E_{\hat{\delta}_{eb}}$ achieved by (129) and computer simulations is depicted as a function of $\delta$ for all considered windows. The sine-wave amplitude $A$ was set to 2, the integer part $l$ of the acquired sine-wave cycles was set to 73, and the sine-wave phase $\phi$ was chosen at uniformly distributed in the range $[0, 2\pi)$ rad. The number of acquired samples $M$ was set to 1024. The sine-wave was corrupted by a Gaussian noise with zero mean and standard deviation corresponding to a *SNR* of 50 dB. The fractional part $\delta$ of the acquired sine-wave cycles was varied in the range $[-0.5, 0.5)$ with a step of 1/33. For each value of $\delta$, 10000 runs were performed and the efficiency $E_{\hat{\delta}_{eb}}$ was calculated.

Fig. 17 shows a very good agreement between the theoretical and the simulation results. It should be noted that behaviors very similar to those reported in Fig. 17 were always achieved for different values of $A$, $l$, *SNR*, and using both uniform and Gaussian noise.

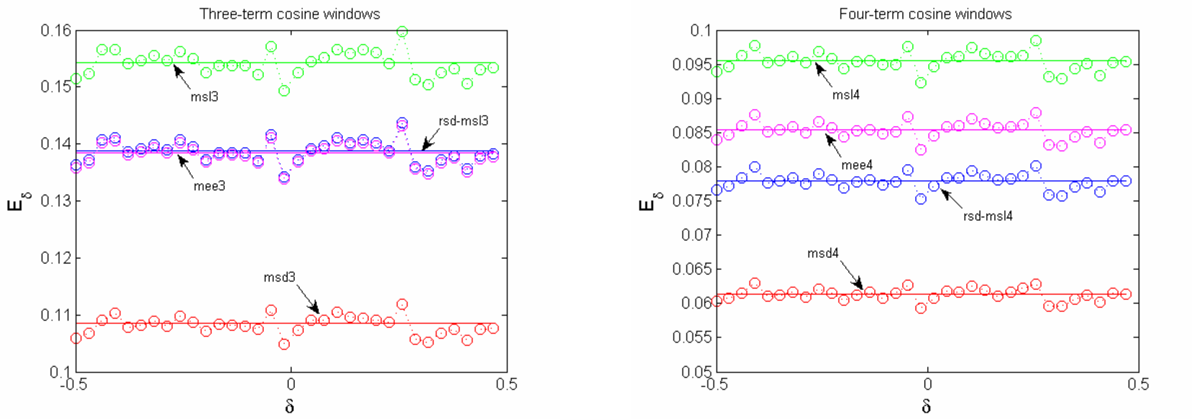


(a) (b)

Fig. 17. Efficiency $E_{\hat{\delta}_{eb}}$ achieved by (129) and computer simulations versus $\delta$ for commonly used (a) three-term and (b) four-term cosine windows. The continuous lines are obtained from (129), while the circles represent the simulation results.

From the above figure it follows that for a given data record, the estimator standard deviation $\sigma_{\hat{\delta}_{eb}}$ increases as the window order $H$ increases. Moreover, for a given window order, the MSL and the MSD windows provide the best and the worst statistical efficiency, respectively.

**d) *rms error of the frequency estimates***

From the results derived above, we evaluated the rms error of the EBM frequency estimate, $\Delta_{\hat{\delta}_{eb}} = \hat{\delta}_{eb} - \delta$, when applied to a single data record of $M$ samples. To this aim, all the three contributions previously analyzed, and we can write:

$$\hat{\delta}_{eb} \cong \delta + \Delta_{\hat{\delta}_{eb},alg} + \Delta_{\hat{\delta}_{eb},si} + \Delta_{\hat{\delta}_{eb},n} \tag{130}$$

in which $\Delta_{\hat{\delta}_{eb},n}$ represents the estimation error due to wideband noise.

In order to model common real-life situations the phase of the input sine-wave is assumed unknown. Accordingly, the contribution of the spectral interference error $\Delta_{\hat{\delta}_{eb},si}$ to the rms error of $\Delta_{\hat{\delta}_{eb}}$ is provided by the corresponding rms value $\sigma_{\hat{\delta}_{eb},si}$. Conversely, the contribution of the algorithm error $\Delta_{\hat{\delta}_{eb},alg}$ is fixed, since it depends only on the estimated parameter $\delta$.

The three contributions in (130) result from three different phenomena, which is the algorithm, the spectral interference, and noise. Thus, they can be considered statistically independent and the rms error of $\Delta_\delta$ can be expressed as:

$$rms(\Delta_{\hat{\delta}_{eb}}) = \sqrt{\Delta^2_{\hat{\delta}_{eb},alg} + \sigma^2_{\hat{\delta}_{eb},si} + \sigma^2_{\hat{\delta}_{eb},n}}. \tag{131}$$

It is worth noticing that the results derived in the previous subsections show that one of the terms in the square root can be negligible, depending on the values of $l$ and $SNR$.

We verified the accuracies of the derived expressions through computer simulations. Moreover, we compared using both computer simulations and experimental results the overall accuracies of the sine-wave fractional frequency estimator provided by the EB method, IpDFT method, and four-parameter sine-fitting (4PSF) algorithm [Std. 1057], [Händel 00], [Bilau 04] .

The parameters of the sine-wave used in computer simulations were $A$ = 2, $l$ = 99, and $\phi$ uniformly distributed in the range [0, 2π) rad. The fractional part $\delta$ of the number of observed periods was varied in the range [–0.5, 0.5) with a step of 1/33. The sine-wave was digitized by means of an ideal 12-bit bipolar ADC with $FSR$ = 10. For each value of $\delta$, 1000 runs of $M$ = 1024 samples each were performed and both the mean value and the standard deviation of the $\delta$ estimators provided by all the considered methods were evaluated. The *rsd-msl3* window was adopted in the EB method, while the *msd2* window was used in the IpDFT method. The initial estimates required by the 4PSF algorithm were achieved by means of the IpDFT method based on the rectangular window [Bilau 04] and the iterations were stopped when all the differences among related parameters estimated in two consecutive steps were smaller than $10^{-6}$. Fig. 18 shows the absolute values of the bias and the mean (Fig. 18(a)), and the standard deviation (Fig. 18(b)), of the $\delta$ estimators provided by all the considered methods.

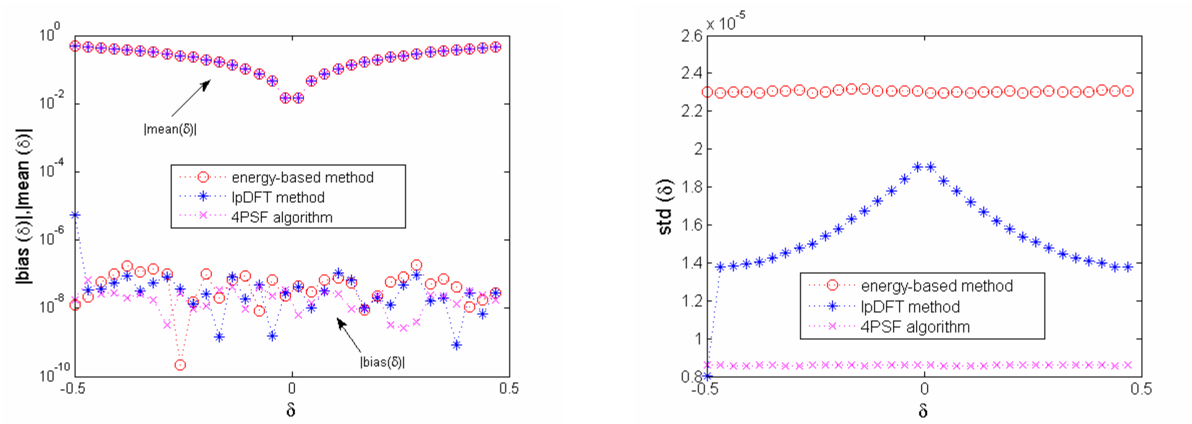


(a) (b)

Fig. 18. Absolute values of (a) the bias (bottom graphs) and the mean (upper graphs), and (b) the standard deviation of the $\delta$ estimators provided by all the considered methods versus $\delta$.

The results reported in Fig. 18 show that:

– for all the considered estimators, the absolute values of the bias are small as compared to the related standard deviation and very close each other (see Fig. 18(a) and (b));

– the estimators provided by the 4PSF algorithm and the EB method have the smallest and the highest standard deviation respectively; however, the standard deviations of all estimators are relatively close each other (see Fig. 18(b));

– the standard deviation of each estimator is negligible with respect to the related mean value (see both Fig. 18(a) and 18(b)).

Thus we can conclude that, for most practical applications, all the considered methods provide almost the same frequency estimation accuracy.

In the experimental setup the sine waves were supplied by an Agilent 33220A signal generator. They were characterized by an amplitude of 2 V and frequencies 5.3, 8.9, 12.1, 15.7, 19.3, and 23.1 kHz, respectively. The signals were acquired using a 12-bit data acquisition board NI-6023E. The *FSR* and the sampling rate were set to 10 V and 100 kHz, respectively. For each frequency, 1000 runs of $M = 1024$ samples were acquired and the mean value and the standard deviation of the estimators provided by the EB method, the IpDFT method, and the 4PSF algorithm were computed using the same figures employed in the computer simulations. Fig. 19 shows the mean value (Fig. 19(a)) and the standard deviation (Fig. 19(b)) for each estimator as a function of frequency.
As we can see, the achieved results confirm the conclusions already drawn from computer simulations: the returned values are very close (see Fig. 19(a)), the standard deviations provided by all methods are relatively close each other (see Fig. 19(b)), even though the 4PSF method exhibits the smallest one, and the standard deviation of each estimator is negligible compared with its mean value (see Figs. 19(a) and 19(b)).

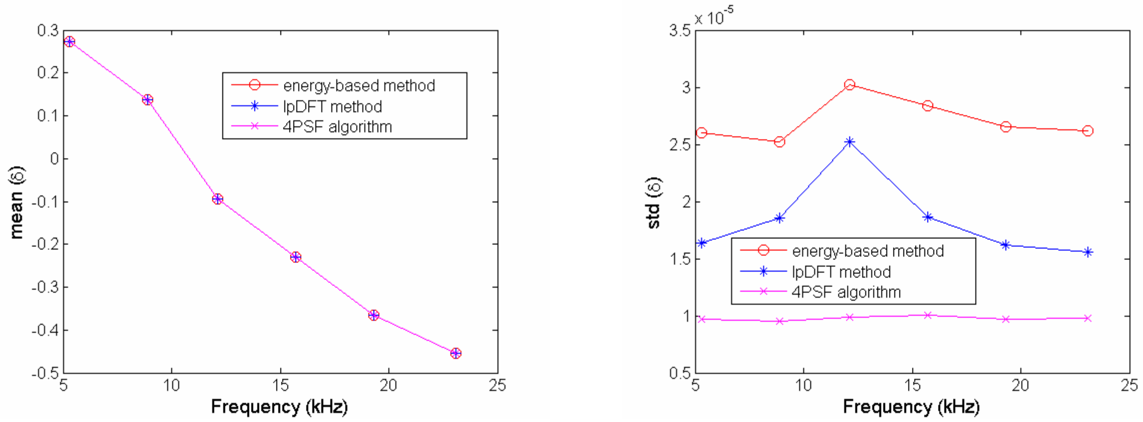


(a) (b)

Fig. 19. (a) Mean value and (b) standard deviation of the $\delta$ estimators provided by all the considered methods versus the sine-wave frequency.

## 2) *Amplitude estimation*

The EB method allows us to estimate the amplitude $A$ using two different procedures: direct and indirect procedures.

• *Direct procedure*

In this case the amplitude $A$ is estimated as [Petri 90], [Offelli 90a]:

$$\hat{A}_{eb(d)} = \frac{2}{M}\sqrt{\frac{\sum_{k=-H}^{H}\left|X_w(l+k)\right|^2}{NNPG}}, \tag{132}$$

where *NNPG* is given by (9).

• *Indirect procedure*

By neglecting the effect of the image component of the spectrum, the amplitude $A$ can be estimated from (31) as:

$$\hat{A}_{eb(i)} = \frac{2|X_w(l)|}{|W(-\hat{\delta}_{eb})|}, \tag{133}$$

where $\hat{\delta}_{eb}$ is the estimator of the fractional frequency $\delta$ provided by EB method, given by (120).

We separately analyze the specific effects of the algorithm error, the spectral interference from the image component, and the wideband noise on the accuracy of the amplitude estimators provided by the direct and the indirect procedures.

**a) *Effect of algorithm error***

Let us assume a pure sine-wave. By neglecting the effect of the spectral interference from the image component on the estimated amplitude the accuracy of both procedures can be evaluated as shown in the following.

• *Direct procedure*

Using (31) the amplitude estimator given by (132) can be expressed as:

$$\hat{A}_{eb(d),a\lg} \cong \frac{A}{M}\sqrt{\frac{\sum_{k=-H}^{H}|W(k-\delta)|^2}{NNPG}}. \tag{134}$$

Thus, the relative amplitude error due to the algorithm is given by:

$$\gamma_{d,a\lg}(\delta) \cong \frac{1}{M}\sqrt{\frac{\sum_{k=-H}^{H}|W(k-\delta)|^2}{NNPG}} - 1. \tag{135}$$

• *Indirect procedure*

Using (31) the amplitude estimator (133) can be expressed as:

$$\hat{A}_{eb(i),a\lg} \cong \frac{A|W(-\delta)|}{|W(-\hat{\delta}_{eb,a\lg})|}, \tag{136}$$

where the estimator $\hat{\delta}_{eb,a\lg}$ due to the algorithm error, is given by (121).

In this case the relative amplitude error due to the algorithm is given by:

$$\gamma_{i,alg}(\delta) \cong \frac{|W(-\delta)|}{\left|W\left(-\hat{\delta}_{eb,alg}\right)\right|} - 1. \tag{137}$$

When coherent sampling occurs, i.e. when $\delta = 0$, we have $\hat{A}_{eb(d),alg} = \hat{A}_{eb(i),alg} = A$, which imply $\gamma_{d,\,alg} = \gamma_{i,\,alg} = 0$. Moreover, since $|W(\cdot)|$ is an even function, it follows that both $|\gamma_{d,\,alg}|$ and $|\gamma_{i,\,alg}|$ are even functions.

Fig. 20 shows the absolute value of the relative errors $\gamma_{d,\,alg}$ and $\gamma_{i,\,alg}$ as a function of $\delta$ for the considered three- and four-term cosine windows. The fractional frequency $\delta$ was varied in the range [–0.5, 0) with a step of 0.01.

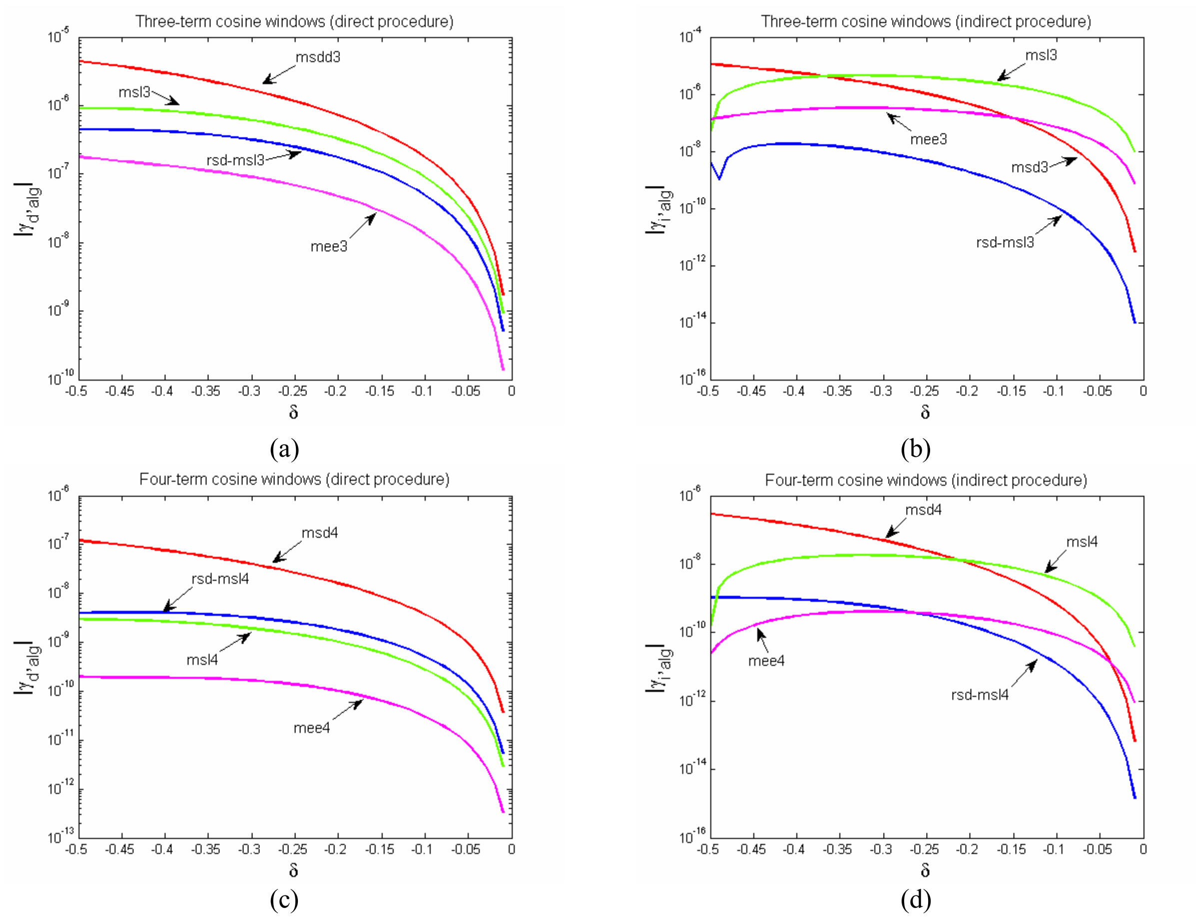


Fig. 20. (a) Absolute value of the relative errors $\gamma_{d,\,alg}$ and $\gamma_{i,\,alg}$ versus $\delta$ for (a), (b) the three-term and (c), (d) the four-term cosine windows.

When the direct procedure is employed the errors $|\gamma_{d,\,alg}|$ decrease as $|\delta|$ decreases. Thus, the maximum of the $|\gamma_{d,\,alg}|$ is reached for $\delta = -0.5$. Moreover, it can be seen that the errors $|\gamma_{d,\,alg}|$ decrease as the window order increases. The best accuracy is achieved when the MEE windows are adopted. Indeed they minimize the spectral leakage energy outside the spectrum main lobe [Offelli 90a]. The worst accuracy occurs when the MSD windows are adopted. Conversely, when the indirect procedure is employed, the value of $\delta$ for which $|\gamma_{i,\,alg}|$ is maximum depends of the adopted window. Among the three-term cosine windows, the *rsd-msl3* window provides the best accuracy. In particular, by comparing Figs. 20(a) and 20(b) we can see that the smallest error is achieved when the indirect method and the *rsd-msl3* window are adopted. Fig. 20(d) shows that the *mee4* or the *rsd-msl4* windows provide the most accurate results, depending on the value of $\delta$. Specifically, for $|\delta| > 0.25$, the best results are provided by the *mee4* window. Moreover, for $|\delta| \geq 0.45$ or $|\delta| \leq 0.15$, the indirect procedure based on the *mee4* or the *rsd-msl4* windows provide the smallest relative estimation error. For the remaining values of $\delta$, the most accurate estimates are provided by the direct procedure based on the *mee4* window.

**b)** ***Effect of the spectral interference from the image component***

We assume a pure sine-wave, but consider a non negligible spectral interference from the image component. Hence, the relative amplitude error due to the spectral interference is given by:

$$\gamma_{d,si}(l,\delta,\phi)=\frac{\hat{A}_{eb(d)}-\hat{A}_{eb(d),a\lg}}{A}=\frac{2}{AM\sqrt{NNPG}}\left(\sqrt{\sum_{k=-H}^{H}\left|X_w(l+k)\right|^2}-\frac{A}{2}\sqrt{\sum_{k=-H}^{H}\left|W(k-\delta)\right|^2}\right) \quad (138)$$

and

$$\gamma_{i,si}(l,\delta,\phi)=\frac{\hat{A}_{eb(i)}-\hat{A}_{eb(i),a\lg}}{A}=\frac{2\left|X_w(l)\right|}{A\left|W\left(-\hat{\delta}_{eb}\right)\right|}-\frac{\left|W(-\delta)\right|}{\left|W\left(-\hat{\delta}_{eb,a\lg}\right)\right|}. \quad (139)$$

for the direct and the indirect procedure, respectively. Notice that the above errors depend on the values of $l$, $\delta$, and $\phi$. In practice in order to avoid the spectral interference from DC component we need to ensure that $l \geq 2H+2$.

It was shown through computer simulations that the errors $\gamma_{d,si}$ and $\gamma_{i,si}$ exhibits a sinusoidal behavior with respect to the sine-wave phase. Thus, assuming a phase $\phi$ varying at random in the range $[0, 2\pi)$ rad, the effect of the spectral interference can be modelled as a random variable with zero mean and standard deviation:

$$\sigma_{\hat{A}_{eb(d)},si}=\frac{A\gamma_{d,si\_\max}}{\sqrt{2}}, \quad (140)$$

$$\sigma_{\hat{A}_{eb(i)},si}=\frac{A\gamma_{i,si\_\max}}{\sqrt{2}}, \quad (141)$$

where $\gamma_{d,\ si\_max}$ and $\gamma_{i,\ si\_max}$ are the maximum of (138) and (139) with respect to the signal phase, respectively.

Fig. 21 shows the maximum values of $\gamma_{d,\ si\_max}$ and $\gamma_{i,\ si\_max}$ as a function of $\nu$ for all the considered three- and four-term windows. The number of acquired sine-wave cycles $\nu$ was varied in the range [5.5, 100.4] with a step of 0.1, when considering three-term windows, and in the range [5.5, 50.4], always using the same step, when the four-term cosine windows are adopted. The number of acquired samples was $M = 1024$. For each value of $\nu$ the phase $\phi$ was varied in the range $[0, 2\pi)$ rad with a step

of π/50 rad. For each value of the integer part $l$, the maximum of the $\gamma_{d,\, si\_max}$ and the $\gamma_{i,\, si\_max}$, achieved for all the considered values of $\delta$ in the range [–0.5, 0.5) is shown in the figure.
As we can see, the maximum of $\gamma_{d,\, si\_max}$ and $\gamma_{i,\, si\_max}$ decreases as the decay rate of the window sidelobe increases. Moreover, the most accurate results are achieved with the direct procedure.

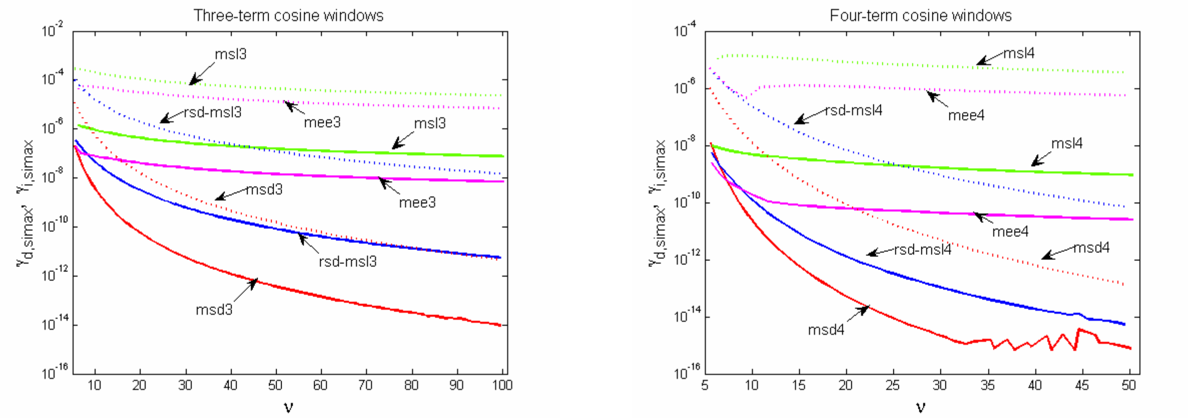


(a) (b)

Fig. 21. Maximum of errors $\gamma_{d,\, si\_max}$ and $\gamma_{i,\, si\_max}$ versus $\nu$ for commonly used (a) three-term and (b) four-term cosine windows. Both the direct procedure (continuous lines) and the indirect procedures (dotted lines) are considered.

### c) *Effect of the wideband noise*

We assume that the integer part of the acquired sine-wave cycles is high enough that the effect of the spectral interference on the estimated amplitude can be neglected. Moreover, in order to model common real-life situations, we corrupt the sine-wave signal by an additive white Gaussian noise with zero mean and variance $\sigma_n^2$. In the following the expressions for the statistical efficiency of the amplitude estimators provided by the two considered procedures are derived.

• *Direct procedure*

The variance of the estimator (132) is given by [Petri 02], [Novotný 97]:

$$\sigma^2_{\hat{A}_{eb(d)},n} \cong \frac{2ENBW0}{M}\sigma_n^2, \tag{142}$$

where $ENBW0$ is given by (11), with the numerator given by (12) and (13) for $H = 3$ and $H = 4$, respectively.
Since the single-tone CRLB for unbiased amplitude estimators is given with very good accuracy by [Offelli 92], [Kay 93]:

$$\left(\sigma_{\hat{A}}\right)_{CR} \cong \frac{2}{M}\sigma_n^2, \tag{143}$$

the statistical efficiency of the estimator $\hat{A}_d$ is:

$$E_{\hat{A}_{eb(d)}} = \frac{\left(\sigma_{\hat{A}}^2\right)_{CR}}{\sigma_{\hat{A}_{eb(d)},n}^2} \cong \frac{1}{ENBW0}. \tag{144}$$

• *Indirect procedure*

Using a similar derivation as for the variance of the amplitude estimator provided by the IpDFT method, since the variance $\sigma_{X_w}^2$ is much higher than the variance $\sigma_{\hat{\delta}_{eb},n}^2$, almost the same expression for the variance of the amplitude estimator provided by the EB method using the indirect procedure is achieved, which is given by:

$$\sigma_{\hat{A}_{eb(i)},n}^2 \cong \frac{2\,ENBW}{M \cdot SL^2(\delta)}\sigma_n^2. \tag{145}$$

Using (143) and (145), the statistical efficiency of the estimator $\hat{A}_{eb(i)}$ results:

$$E_{\hat{A}_{eb(i)}} = \frac{\left(\sigma_{\hat{A}}^2\right)_{CR}}{\sigma_{\hat{A}_{eb(i)},n}^2} \cong \frac{SL^2(\delta)}{ENBW}. \tag{146}$$

From (144) and (146) it follows that the ratio between the statistical efficiencies of the two considered procedures is:

$$\frac{E_{\hat{A}_{eb(d)}}}{E_{\hat{A}_{eb(i)}}} \cong \frac{ENBW}{ENBW0 \cdot SL^2(\delta)}. \tag{147}$$

It is worth noticing that $E_{\hat{A}_{eb(d)}} / E_{\hat{A}_{eb(i)}} < 1$ for any value of $\delta$ in the range [–0.5, 0.5) and all the considered three- and four-term cosine windows. Thus, the indirect procedure provides a statistically more efficient amplitude estimator than the direct procedure. In particular, the minimum and the maximum values of the ratio $E_{\hat{A}_{eb(d)}} / E_{\hat{A}_{eb(i)}}$ are given by:

$$\left(\frac{E_{\hat{A}_{eb(d)}}}{E_{\hat{A}_{eb(i)}}}\right)_{\min} \cong \frac{ENBW}{ENBW0}, \tag{148}$$

and

$$\left(\frac{E_{\hat{A}_{eb(d)}}}{E_{\hat{A}_{eb(i)}}}\right)_{\max} \cong \frac{ENBW}{ENBW0 \cdot SL^2(-0.5)}. \tag{149}$$

respectively.

As we already specified the expression (145) holds also for the IpDFT method. When the *SNR* is smaller than about 70 dB, very accurate estimates can be achieved by applying the IpDFT method based on the two-term MSD window. In fact, when the IpDFT method based on the MSD windows is applied, the corresponding algorithm error is negligible [Belega 12a]. Conversely, the EB method requires the use of a three-term cosine window even though $SNR \leq 70$ dB because the algorithm error associated to the two-term cosine windows is too high. Hence, in these situations, the IpDFT method provides a higher statistical efficiency than the EB method.

Fig. 22 shows the statistical efficiencies $E_{\hat{A}_{eb(d)}}$ and $E_{\hat{A}_{eb(i)}}$ as a function of $\delta$ obtained by both (144), (146) and computer simulations. The sine-wave amplitude $A$ was set to 2, the integer part of the acquired sine-wave cycles $l$ was equal to 93, and the number of acquired samples $M$ was set to 1024. The sine-wave phase $\phi$ was chosen at random in the range $[0, 2\pi)$ rad. The sine-wave was corrupted by a Gaussian noise with zero mean and standard deviation corresponding to a *SNR* of 50 dB. The fractional frequency $\delta$ was varied with a step of 1/33 and for each value of $\delta$, 5000 runs were performed.

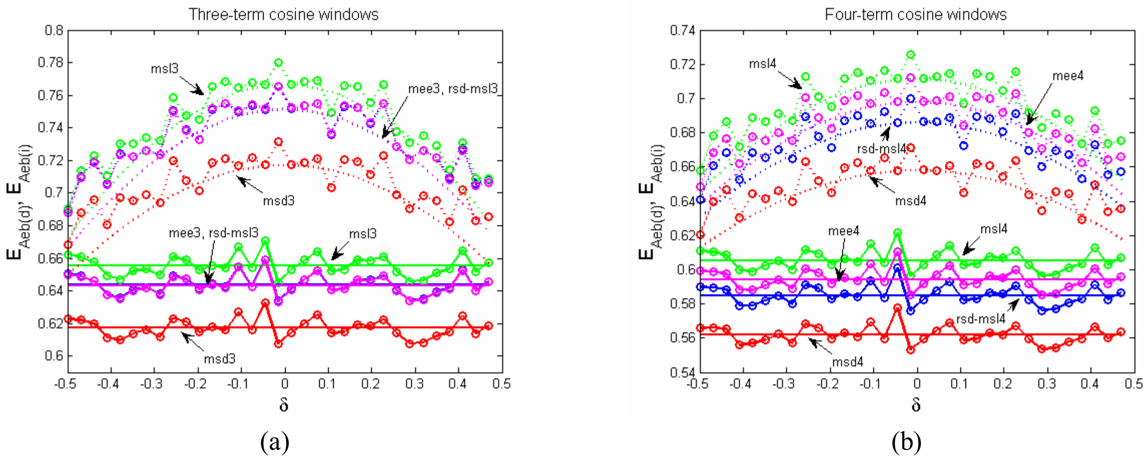


Fig. 22. Statistical efficiencies $E_{\hat{A}_{eb(d)}}$ and $E_{\hat{A}_{eb(i)}}$ obtained by the theoretical expressions (lines) and computer simulations (circles) versus $\delta$ for commonly used (a) three-term and (b) four-term cosine windows. Both the direct procedure (continuous lines) and the indirect procedures (dotted lines) are considered.

As we can see, the agreement between theoretical and simulation results is very good. Moreover, Fig. 22 shows very clearly that, for a given window, the indirect method provides a higher statistical efficiency. Many other simulations were performed for different values of $A$, $l$, *SNR*, using both uniform and Gaussian noise. Behaviors similar to those reported in Fig. 22 were always achieved.

### d) *rms error of the amplitude estimates*

Taking into account all the contributions analyzed above we can write:

$$\hat{A}_{eb(d)} \cong A\left(1+\gamma_{d,a\lg}+\gamma_{d,si}\right)+\Delta_{\hat{A}_{eb(d)},n}, \tag{150}$$

and

$$\hat{A}_{eb(i)} \cong A\left(1+\gamma_{i,a\lg}+\gamma_{i,si}\right)+\Delta_{\hat{A}_{eb(i)},n}, \tag{151}$$

where $\Delta_{\hat{A}_{eb(d)},n}$ and $\Delta_{\hat{A}_{eb(i)},n}$ represent the amplitude estimation errors due to wideband noise related to direct and indirect procedures, respectively.

The three different contributions in (150) and (151) can be considered statistically independent. Indeed they are due to distinct phenomena (that is the algorithm, the spectral interference, and noise). Thus, by choosing at random the sine-wave phase, the rms of the estimation errors $\Delta_{\hat{A}_{eb(d)}} = \hat{A}_{eb(d)} - A$ and $\Delta_{\hat{A}_{eb(i)}} = \hat{A}_{eb(i)} - A$ can be expressed as:

$$rms(\Delta_{\hat{A}_{eb(d)}}) \cong \sqrt{A^2\gamma^2_{d,a\lg}+\sigma^2_{\hat{A}_{eb(d)},si}+\sigma^2_{\hat{A}_{eb(d)},n}}, \tag{152}$$

and:

$$rms(\Delta_{\hat{A}_{eb(i)}}) \cong \sqrt{A^2\gamma^2_{i,a\lg}+\sigma^2_{\hat{A}_{eb(i)},si}+\sigma^2_{\hat{A}_{eb(i)},n}}, \tag{153}$$

respectively. In the above expressions the different contributions are evaluated by using the expressions (138) - (142), and (145).

In particular, when $SNR \leq 60$ dB and high values of $l$ are considered, as often occurs in practice, the contribution due to noise prevails over the others. Thus, the analysis performed in the previous subsection shows that the indirect procedure provides more accurate results.

We verified the accuracies of the expressions (152) and (153) through computer simulations. The overall effect of the algorithm error and the spectral interference was firstly investigated. Specifically, the accuracy of (152) and (153) were verified by means of a pure sine-wave signal. Fig. 23 shows the values of $rms(\Delta_{\hat{A}_{eb(d)}})$ and $rms(\Delta_{\hat{A}_{eb(i)}})$ provided by the expressions (152) and (153) and by computer simulations as a function of $\nu$. The sine-wave amplitude $A$ was set to 2 and the number of acquired sine-wave cycles $\nu$ was varied in the range [4, 10] with a step of 1/20. The number of acquired samples was $M$ = 1024. For each value of $\nu$, 1000 runs were considered by choosing the sine-wave phase $\phi$ at random in the range [0, 2π) rad. Results corresponding to coherent sampling are null and are not reported in the figure.

As we can see, the agreement between theoretical and simulation results is very good.

Also, it is of interest to know the behavior of the $rms(\Delta_{\hat{A}_{eb(d)}})$ and $rms(\Delta_{\hat{A}_{eb(i)}})$ for high values of $l$.

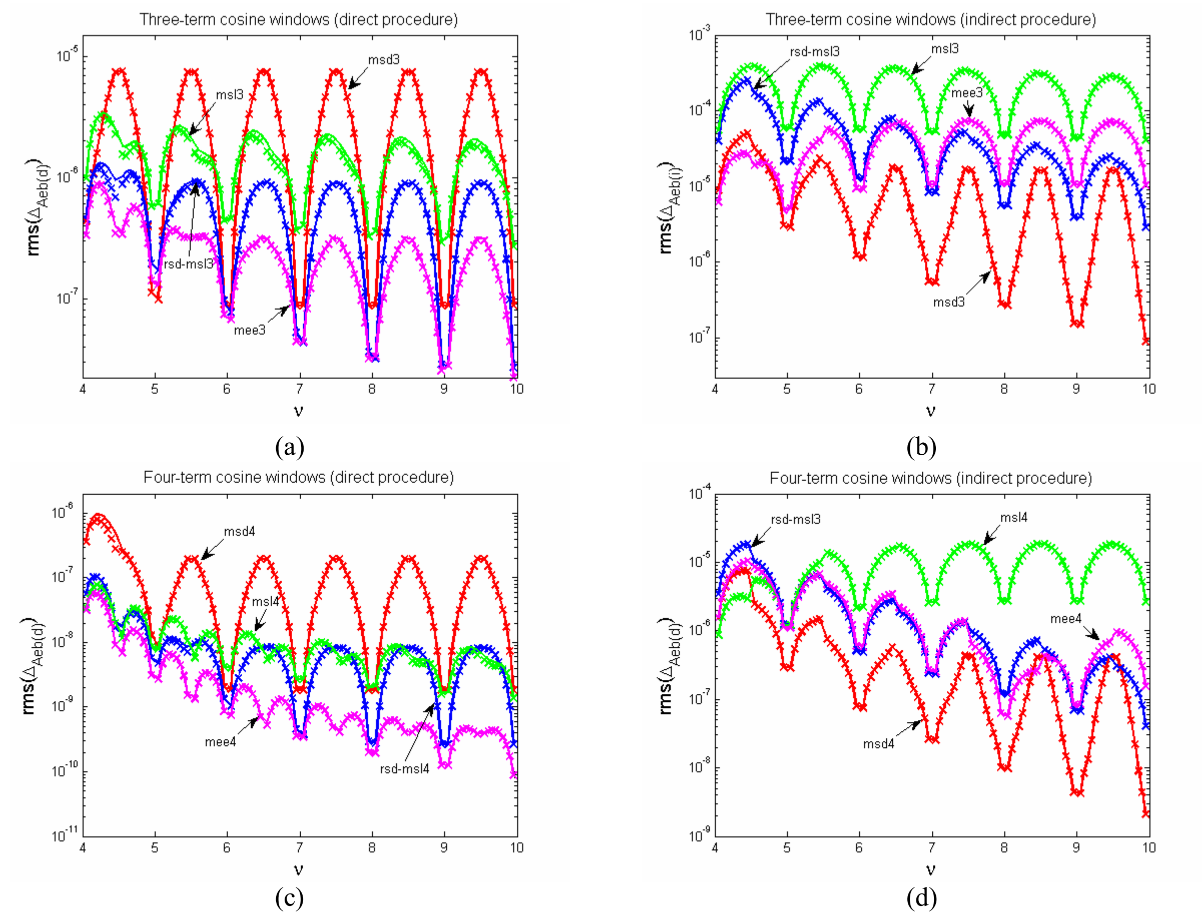


Fig. 23. RMS of the amplitude estimation errors $rms(\Delta_{\hat{A}_{eb(d)}})$ and $rms(\Delta_{\hat{A}_{eb(i)}})$ provided by the theoretical expressions (lines) and computer simulations (crosses) versus $\nu$ for commonly used (a), (b) three-term and (c), (d) four-term cosine windows. Only the algorithm error and the spectral interference are considered and both the direct procedure and the indirect procedures are employed.

Therefore, in Fig. 24, the values of $rms(\Delta_{\hat{A}_{eb(d)}})$ and $rms(\Delta_{\hat{A}_{eb(i)}})$, provided by the expressions (152) and (153) and by computer simulations, are depicted as a function of $l$ for all the considered windows. The same signal and simulation parameters used in the previous figure were employed, except that the integer part $l$ was varied in the range [6, 80] with step of 2 and the fractional part $\delta$ was set to $-0.5$.
Also, Fig. 24 shows a very good agreement between theoretical and simulation results. When the three-term cosine windows are adopted, if the integer part of the acquired sine-wave cycles, $l$, is quite small, the direct procedure based on the *mee3* window exhibits the smallest sensitivity to the algorithm error and the spectral interference from the image component. Conversely, the indirect procedure based on the *rsd-msl3* window provides the best accuracy if a quite large number of sine-wave cycles is acquired. Using the four-term cosine windows, the minimum sensitivity to the algorithm error and the spectral interference is achieved by the direct procedure based on the *mee4* window.
Further simulations were performed by considering the effect of all estimator uncertainty contributions. Also, in this case the agreement between theoretical and simulation results is very good.

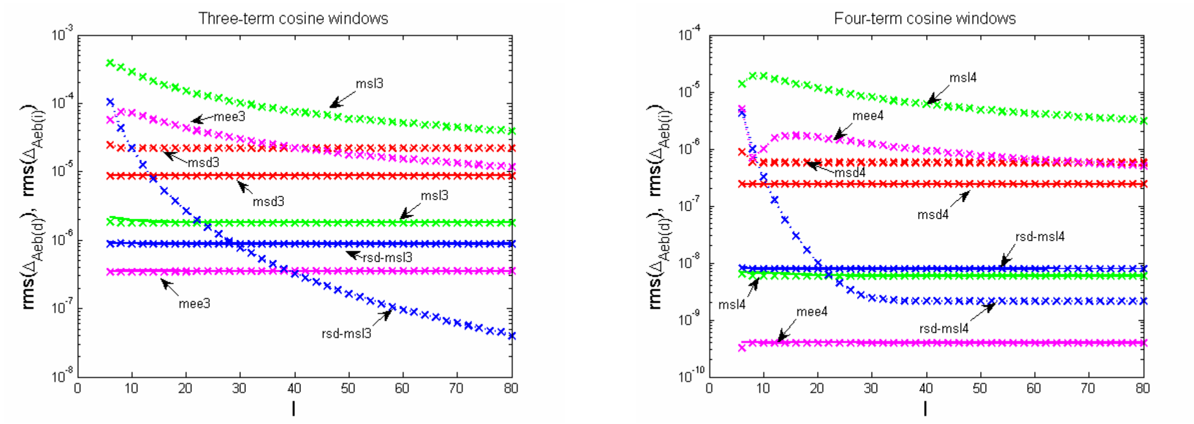


(a) (b)

Fig. 24. The values of $rms(\Delta_{\hat{A}_{eb(d)}})$ and $rms(\Delta_{\hat{A}_{eb(i)}})$ provided by the theoretical expressions (lines) and computer simulations (crosses) versus $l$ for commonly used (a) three-term and (b) four-term cosine windows. Only the algorithm error and the spectral interference are considered and both the direct procedure (continuous line) and the indirect procedures (dotted line) are employed.

Moreover, the overall accuracies of the considered amplitude estimation procedures were compared by means of experimental results. In the experimental runs the sine-waves were supplied by an Agilent 33220A signal generator and acquired by a 12-bit data acquisition board NI-6023E. The Full Scale Range, *FSR*, and the sampling frequency were set to 10 V and 100 kHz, respectively.

In Fig. 25 variances of the estimators $\hat{A}_{eb(d)}$ and $\hat{A}_{eb(i)}$ are depicted as a function of the fractional frequency $\delta$ when the three-term and the four-term cosine windows are adopted. The amplitude of the signals was set to 4 V and the related frequencies were varied between 2.10 and 2.19 kHz with a step of 10 Hz in order to obtain different values of $\delta$. The achieved value for $l$ was 22. For each frequency value 1000 runs of $M$ = 1024 samples each were performed and the variances of the two amplitude estimators $\hat{A}_{eb(d)}$ and $\hat{A}_{eb(i)}$ were calculated. The fractional frequency $\delta$ was estimated by using the mean value of the estimates returned by the EB method based on the *rsd-msd3* window.

The variance of the estimator $\hat{A}_{eb(i)}$ achieved when the *msl3* window is adopted is not reported in Fig. 25(b) since it is too much higher than the variances related to the use of the other windows. Indeed, in the considered setup, the effect of the algorithm error and the spectral interference is significant, as we can derive from Figs. 21 and 24. Besides, also the variance of the estimator $\hat{A}_{eb(i)}$ corresponding to the *mee3* window is quite high because of the same reason. The remaining results show very close behaviors. Indeed, the amplitude estimation error is mainly due to wideband noise. Moreover, as expected, Fig. 25 shows that the indirect procedure provides a lower estimation variance than the direct procedure.

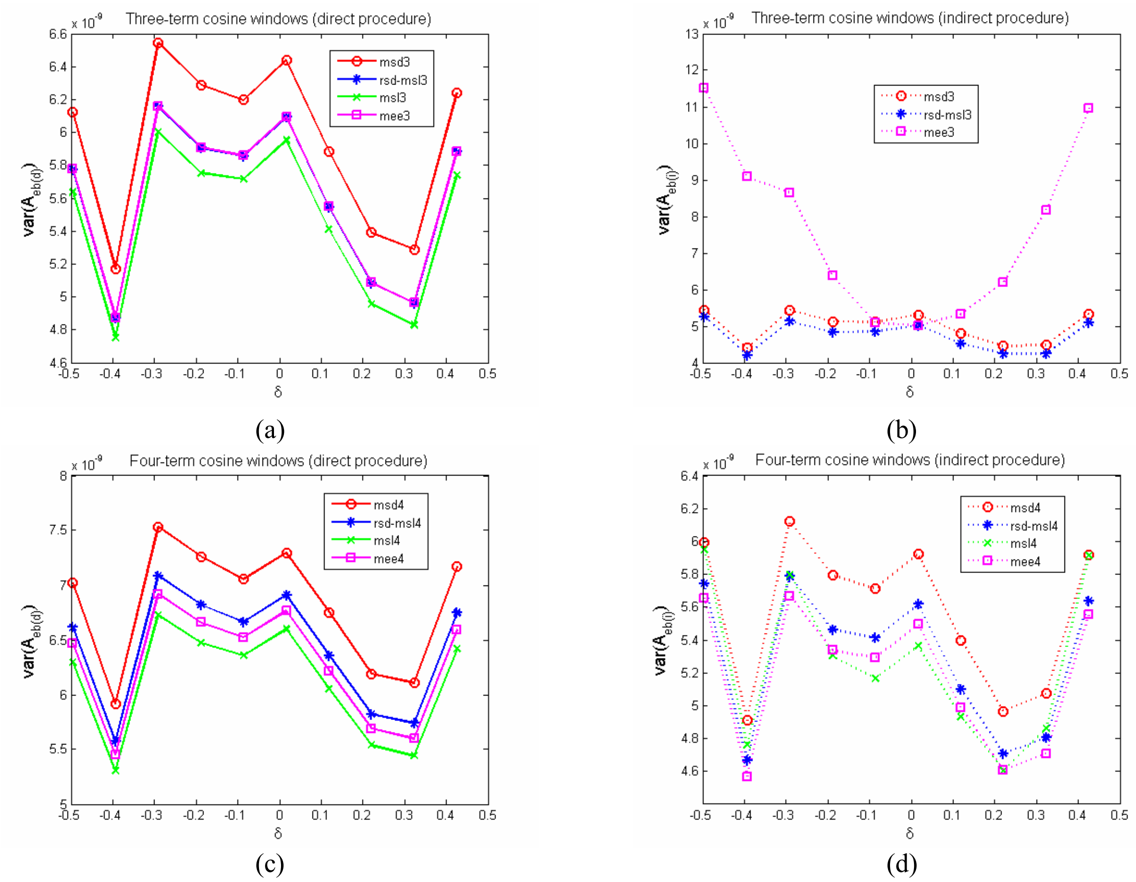


Fig. 25. Variances of the estimators (a) $\hat{A}_{eb(d)}$ and (b) $\hat{A}_{eb(i)}$ versus $\delta$ achieved by means of experimental results when the (a), (b) three-term and (c), (d) four-term cosine windows are adopted.

In [Belega 10c], we compared through both computer simulation and experimental results the accuracy of the amplitude estimates achieved by the IpDFT method with that of the EB method and the multi-harmonic sine-fitting algorithm proposed in [Ramos 06] in the case of a harmonically distorted signal corrupted by a white stationary noise. The simulated signal was affected by the 2nd, 3rd, 4th, and 5th harmonics of a amplitudes $A_2 = 8Q$, $A_3 = Q$, $A_4 = 0.2Q$, and $A_5 = 0.05Q$, in which $Q$ is the ideal code bin width of an 16-bit bipolar ADC, with a Full Sale Range (*FSR*) equal to 5. The amplitude of the fundamental was $A_1 = 2$, the number of the acquired samples $M$ was 4096, the integer part related to the fundamental $l_1$ was 213, and the sampling frequency was 51 kHz. The signal was corrupted only by the ADC quantization noise, which was modelled as an uniformly distributed additive noise. The fractional part $\delta_1$ related to the fundamental was varied in the range of [–0.5, 0.5), with a step of 1/30. For each value of $\delta_1$, the phases of the harmonics were uniformly distributed in the range of [0, $2\pi$) rad and the mean and the standard deviation values of $A_2$, $A_3$, $A_4$, and $A_5$ estimates achieved by the considered methods in 1000 runs were computed. The two-term MSD window was adopted in the IpDFT method. When the EB method was used, the locations of the harmonic components in the signal spectrum were found by means of the IpDFT method based on the two-term MSD window. In the EB method the four-term MEE window was used. In the multi-harmonic sine fitting method the initial frequency was estimated by the IpDFT method based on the rectangular window [Bilau 04]. The algorithm iterations were stopped when the magnitude of the differences between the frequency deviations estimated in two consecutive iterations was less than $10^{-6}$. Fig. 26

shows the mean and the mean plus or minus the standard deviation of the $A_3$, $A_4$, and $A_5$ estimates obtained by the considered methods as a function of $\delta_1$.

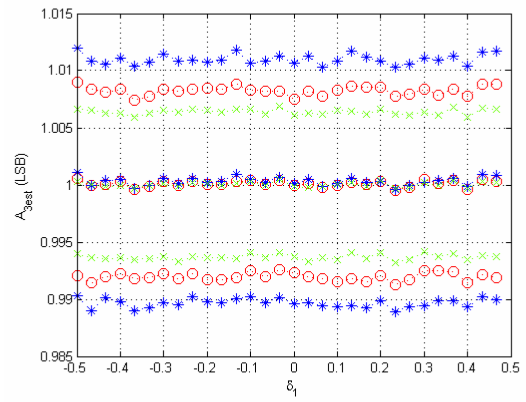


(a)

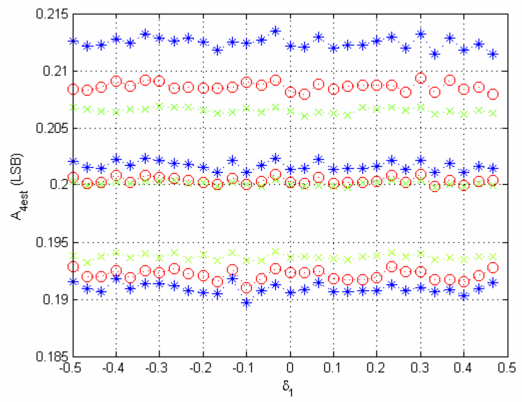


(b)

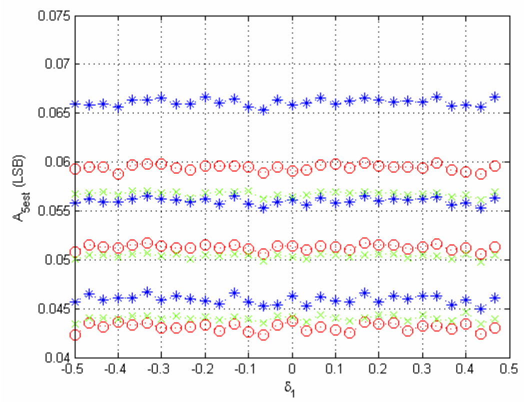


(c)

Fig. 26. Mean and mean plus or minus the standard deviation of the (a) $A_3$ estimates , (b) $A_4$ estimates, and (c) $A_5$ estimates obtained by the IpDFT method ('o'), the energy-based method ('*'), and the multi-harmonic sine-fitting method ('x') as a function of $\delta_1$.

From the results shown in Fig. 26 it follows that the estimation accuracy achieved by the IpDFT method is slightly smaller than that achieved by the multi-harmonic sine-fitting algorithm, and higher than that achieved by the EB method.

In the experimental runs the sine-wave were achieved from an Agilent 33220A signal generator. The signal was characterized by: $A_0$ = 2 V, $A_1$ = 2 V, and $f_1$ = 171 Hz. The ADS1258EVM-PDK system with the ADCPro software was used for signal acquisition. This system contains an 24-bit delta-sigma converter (ADS1258) optimized for fast multi-channel, high-resolution measurements systems, with a maximum channel scan rate of 23.7 kHz. ADS1258 was used in unipolar mode with *FSR* equal to 5 V. The sampling frequency of the ADS1258 was set to 1.92 kHz. The number of acquired samples was 4096. In the IpDFT method the three-term MSD window was adopted and in the EB method the four-term MEE window was adopted. The multi-harmonic sine-fitting algorithm was used as in the simulations, but the first ten harmonics were considered. The mean and the standard deviation values of the first ten harmonic components during 200 runs were computed. The achieved results are given in Table 4.

Table 4. Experimental results obtained using the ADS1258EVM-PDK system.

| | IpDFT method | | EB method | | Multi-harmonic sine-fitting algorithm | |
|---|---|---|---|---|---|---|
| | Mean (LSB) | Std. dev. (LSB) | Mean (LSB) | Std. dev. (LSB) | Mean (LSB) | Std. dev. (LSB) |
| 2nd harmonic | 213.49 | 3.53 | 213.68 | 4.11 | 213.31 | 2.76 |
| 3rd harmonic | 53.24 | 3.11 | 53.71 | 3.57 | 52.97 | 2.36 |
| 4th harmonic | 30.60 | 3.74 | 31.67 | 4.14 | 30.48 | 2.85 |
| 5th harmonic | 38.51 | 3.43 | 39.15 | 3.91 | 38.37 | 2.52 |
| 6th harmonic | 13.00 | 2.99 | 17.58 | 7.06 | 12.68 | 2.43 |
| 7th harmonic | 36.76 | 3.26 | 38.14 | 3.80 | 36.71 | 2.45 |
| 8th harmonic | 10.80 | 2.99 | 15.59 | 4.59 | 9.74 | 2.20 |
| 9th harmonic | 9.63 | 2.88 | 15.02 | 3.56 | 8.37 | 2.80 |
| 10th harmonic | 7.60 | 2.49 | 12.73 | 2.53 | 5.00 | 2.42 |

As in simulations, from the results shown in Table 4, it follows that the results achieved by the IpDFT method are much closer to those achieved by the multi-harmonic sine-fitting method than the results achieved by the EB method. Also, it can be observed that for small harmonics the EB method provide less accurate estimates as compared with the multi-harmonic sine-fitting algorithm and the IpDFT method.

### 2.2.2. TIME-DOMAIN METHODS

The parameters of a sine-wave component can be accurately estimated by using sine-fitting algorithms [Std. 1057], [Std. 1241]. They are based on the minimization of the squared residual error, i.e. the difference between a generic sinusoidal signal and the available output data. The current IEEE Standards 1057 and 1241 concerning dynamic testing of digitizing waveform recorders and ADCs recommend two sine-fitting algorithms. They are named according to the number of the parameters to be estimated, which are the three- and the four-parameter sine-fitting algorithms.

In the three-parameter sine-fitting (3PSF) algorithm the frequency is assumed to be known and the minimization problem is solved by means of a simple linear least squares approach. Conversely, in the four-parameter sine-fitting (4PSF) algorithm all the sine-wave parameters are assumed to be unknown and a nonlinear least squares approach is needed. The performance of both 3PSF and 4PSF algorithms related to robustness, accuracy of the starting values, number of iterations, and convergence speed have been deeply analyzed in the scientific literature [Händel 00], [Händel 08], [Bilau 04], [Fonseca 04], [Chen 07], [Chen 08]. Also, the effects of noise [Händel 00], [Andersson 06], [Moschitta 05], and harmonics [Deyst 95] on the accuracies of the returned results have been investigated. In [Andersson 06] a decision criterion whether to use the 3PSF or the 4PSF algorithm has been derived by using the parsimony principle [Söderström 89]. To this aim, the algorithm accuracy has been expressed in terms of the expected sum-squared residual error and evaluated in the case of a sine-wave corrupted by white Gaussian noise. When the 3PSF algorithm is of concern, the expected sum-squared residual error was determined by assuming that the signal frequency took a fixed value. In particular, it has been shown that the 3PSF algorithm exhibits a higher accuracy when the sine-wave frequency is known with very low uncertainty [Andersson 06]. An extension of the results derived in [Andersson 06] is performed in [Andersson 05] in order to derive a criterion for model order selection.

It is worth noticing that neither the IEEE Standard 1057 nor Standard 1241 provide any recommendation about how determining the sine-wave frequency to be used in the 3PSF algorithm [Std. 1057], [Std. 1241]. It has been shown in [Belega 11a], that the Effective Number Of Bits (*ENOB*) of an ADC can be accurately evaluated when the sine-wave frequency is estimated by means of the IpDFT method based on the MSD windows. Therefore, in [Belega 12d], we compared the performance of the 3PSF algorithm adopting the sine-wave frequency returned by the IpDFT method (called in the following the 3PSF-IpDFT algorithm) with that of the 4PSF algorithm when estimating the noise power of a non-coherently sampled sine-wave corrupted by a white Gaussian noise. For this purpose, we derived the expressions related to the fitting errors under the assumption that the number of analyzed samples is large enough, which ensures also that the IpDFT frequency estimator bias can be neglected. In the following we present that derivation.

Let us consider that the sine-wave (1) with the offset $d$ is corrupted by a white Gaussian noise $r(\cdot)$ with zero mean and variance $\sigma_r^2$. Thus, the achieved signal can be expressed as:

$$y(m) = x(m) + r(m) = A\sin(2\pi f m + \phi) + d + r(m), \quad m = 0,1,2,\ldots,M-1 \tag{154}$$

The parameters of the sine-wave $x(\cdot)$ can be accurately estimated by applying the 3PSF or the 4PSF algorithm to the $M$ analyzed samples. The best fit is achieved by selecting the parameters that minimize the sum-squared residual error:

$$\kappa = \frac{1}{M}\sum_{m=0}^{M-1} \hat{r}^2(m), \tag{155}$$

in which the residual error $\hat{r}(\cdot)$ represents the difference between the analyzed data and the corresponding sine-fit values:

$$\hat{r}(m) = y(m) - \hat{x}(m), \quad m = 0,1,\ldots,M-1 \tag{156}$$

where:

$$\hat{x}(m) = \hat{A}\sin\left(2\pi\hat{\nu}\frac{m}{M} + \hat{\phi}\right) + \hat{d}, \quad m = 0,1,\ldots,M-1 \tag{157}$$

is the fitted sine-wave, while $\hat{\nu}$, $\hat{A}$, $\hat{\phi}$, and $\hat{d}$ are the estimated sine-wave parameters.
Defining the fitting error as:

$$e(m) = \hat{x}(m) - x(m), \quad m = 0,1,\ldots,M-1 \tag{158}$$

from (154), (156), and (158) we have:

$$\hat{r}(m) = r(m) - e(m), \quad m = 0,1,\ldots,M-1 \tag{159}$$

In order to analyze the algorithm accuracy, we consider the expected value of both the sum-squared residual and the sum-squared fitting errors. This latter quantity is defined as:

$$\varepsilon = \frac{1}{M}\sum_{m=0}^{M-1} e^2(m). \tag{160}$$

The expression of the sum-squared fitting error was derived in [Belega 11a], and it is:

$$\varepsilon = \frac{1}{M}\sum_{m=0}^{M-1} e^2(m) \cong \Delta_d^2 + \frac{\Delta_A^2}{2} + \frac{2\pi^2 A^2 \Delta_\nu^2}{3} + \frac{A^2 \Delta_\phi^2}{2} + A^2 \pi \Delta_\delta \Delta_\phi, \tag{161}$$

where:

$$\Delta_A = \hat{A} - A, \quad \Delta_\nu = \hat{\nu} - \nu = \hat{\delta} - \delta, \quad \Delta_\phi = \hat{\phi} - \phi, \quad \Delta_d = \hat{d} - d. \tag{162}$$

are random variables modeling the estimation errors.

It is known that the parameter estimators provided by the 3PSF and 4PSF algorithms are asymptotically efficient [Kay 93]. Thus, if the sine-wave frequency estimator adopted in the 3PSF algorithm is asymptotically unbiased and the number of analyzed samples is large enough, by taking the expectation of (161), we obtain:

$$E[\varepsilon] \cong \sigma_{\hat{d}}^2 + \frac{\sigma_{\hat{A}}^2}{2} + \frac{2\pi^2 A^2 \sigma_{\hat{\nu}}^2}{3} + \frac{A^2 \sigma_{\hat{\phi}}^2}{2} + \pi A^2 E[\Delta_\lambda \Delta_\phi]. \tag{163}$$

where $\sigma_{\hat{A}}^2$, $\sigma_{\hat{\nu}}^2$, $\sigma_{\hat{\phi}}^2$, and $\sigma_{\hat{d}}^2$ represent the variances of the considered estimators.

Since the phase $\phi$ of the sine-wave (154) at the time reference (that is for $m = 0$) is related to the phase $\phi_0$ at the center of the observation interval (that is for $m = M/2$) by:

$$\phi = \phi_0 - \pi\nu, \tag{164}$$

and the estimators of the phase $\phi_0$ and the frequency $\nu$ are uncorrelated [Offelli 92], [Kay 93], we have:

$$E[\Delta_\nu \Delta_\phi] \cong -\pi \, E[\Delta_\nu^2] = -\pi \, \sigma_{\hat{\nu}}^2, \tag{165}$$

and:

$$\sigma_{\hat{\phi}}^2 = \sigma_{\hat{\phi}_0}^2 + \pi^2 \sigma_{\hat{\lambda}}^2. \tag{166}$$

Using (165) and (166), (163) becomes:

$$E[\varepsilon] \cong \sigma_{\hat{d}}^2 + \frac{\sigma_{\hat{A}}^2}{2} + \frac{\pi^2 A^2 \sigma_\nu^2}{6} + \frac{A^2 \sigma_{\hat{\phi}_0}^2}{2}. \tag{167}$$

Since $M$ is large, the estimator variances provided by the sine-fitting algorithms almost attain the related single-tone CRLB [Offelli 92], [Key 93], [Händel 10], that is (for frequency and amplitude they are also given in (63) and (143), respectively):

$$\sigma_{\hat{d}}^2 \cong \frac{\sigma_r^2}{M}, \tag{168}$$

$$\sigma_{\hat{A}}^2 \cong \frac{2\sigma_r^2}{M}, \tag{169}$$

$$\sigma_{\hat{\phi}_0}^2 \cong \frac{2\sigma_r^2}{A^2 M}, \tag{170}$$

$$\sigma_{\hat{\nu}}^2 \cong \frac{6\sigma_r^2}{\pi^2 A^2 M}. \tag{171}$$

By replacing (168)-(170) in (167), the following expression for the expected sum-squared fitting error provided by the 3PSF algorithm is achieved:

$$E[\varepsilon_3] \cong \frac{3\sigma_r^2}{M} + \frac{\pi^2 A^2 \sigma_{\hat{\nu}}^2}{6}. \tag{172}$$

Conversely, by replacing (168)-(171) in (167), the following expression for the expected sum-squared fitting error provided by the 4PSF algorithm is obtained:

$$E[\varepsilon_4] \cong \frac{4\sigma_r^2}{M}. \tag{173}$$

It should be noticed that when the frequency value used in the 3PSF algorithm is fixed and affected by a constant error $\Delta_\nu$, by using similar arguments as above, it can be shown that (172) still holds, but the variable $\sigma_{\hat{\nu}}^2$ should be substituted by $\Delta_\nu^2$.

From (172) and (173), it follows that $E[\varepsilon_3] \geq E[\varepsilon_4]$ as soon as the following constrain is fulfilled:

$$\sigma_{\hat{\nu}}^2 \geq \frac{6\sigma_r^2}{\pi^2 A^2 M}. \tag{174}$$

Observe that the right term in (174) equals the single-tone unbiased CRLB, $\left(\sigma_{\hat{\nu}}^2\right)_{CR}$, for the normalized frequency estimator (see (171)). Thus, if $\sigma_{\hat{\nu}}^2 = \left(\sigma_{\hat{\nu}}^2\right)_{CR}$, both the 4PSF and the 3PSF algorithms provide the same expected sum-squared fitting error. Conversely, if a non-efficient frequency estimator is used, the 4PSF algorithm outperforms the 3PSF algorithm. That conclusion can be explained as follows. The 4PSF algorithm fits the available data by simultaneously considering all the sine-wave parameters and the resulting expected sum-squared fitting error is given by (173). Conversely, the 3PSF algorithm separates the fitting process into a frequency estimation problem followed by a linear parameter estimation process. Obviously, if the frequency is known the frequency estimation step is not required. In particular, if the true value of the frequency is exactly known, the expected sum-squared fitting error associated with the 3PSF algorithm is equal to $3\sigma_r^2 / M$ , which is smaller than the one related to the 4PSF algorithm. However, frequency estimation is always needed in practice. Hence, the fitting accuracy of the 3PSF algorithm is less than or the same as the one associated with the 4PSF algorithm. Specifically, the same accuracy is achieved only when an efficient frequency estimator is adopted.

From (155), (159) - (162), it follows that the expected sum-squared residual errors provided by the 3PSF-IpDFT and the 4PSF algorithms are expressed by:

$$E[\kappa_3] = E[\varepsilon_3] + \sigma_r^2 \cong \left(1 + \frac{3}{M}\right)\sigma_r^2 + \frac{\pi^2 A^2 \sigma_{\hat{\nu}}^2}{6}, \tag{175}$$

and

$$E[\kappa_4] = E[\varepsilon_4] + \sigma_r^2 \cong \left(1 + \frac{4}{M}\right)\sigma_r^2. \tag{176}$$

It is worth to observe that the above expressions agree with the results reported in [Andersson 06] using the parsimony principle [Söderström 89].

In particular, if the frequency estimator $\hat{\nu}$ is consistent and the number of analyzed samples is large enough, from (172) and (173) we have that $E[\varepsilon_3] << \sigma_r^2$ and $E[\varepsilon_4] << \sigma_r^2$, respectively. Thus, (175) and (176) become:

$$E[\kappa_3] \cong E[\kappa_4] \cong \sigma_r^2, \tag{177}$$

which shows that both algorithms provides an asymptotically unbiased estimator of the noise power.

Furthermore, we compared the accuracy of the 3PSF-IpDFT algorithm based on the MSD windows with that of the 4PSF algorithm. From (44) it follows that the minimum and the maximum values of $\sigma_{\hat{\lambda}}$ occur when $\delta = -0.5$ and $\delta = 0$, respectively. For the two-term MSD window these values are:

$$\min\left(\sigma_{\hat{\nu}}^2\right) \cong \frac{1.56 \cdot \sigma_r^2}{A^2 M} \quad \text{and} \quad \max\left(\sigma_{\hat{\nu}}^2\right) \cong \frac{3.11 \cdot \sigma_r^2}{A^2 M}. \tag{178}$$

Thus, from (171) and (178) we have:

$$2.57 < \frac{\sigma_{\hat{\nu}}^2}{(\sigma_{\hat{\nu}}^2)_{CR}} < 5.12, \tag{179}$$

which, from (172), implies that $E[\varepsilon_3] \geq E[\varepsilon_4]$. So, the 4PSF algorithm provides a more accurate sine-wave fitting than the 3PSF-IpDFT algorithm based on the Hann window. Moreover, from (172) and (178) we achieve:

$$5.57 \frac{\sigma_r^2}{M} < E[\varepsilon_3] < 8.12 \frac{\sigma_r^2}{M}, \tag{180}$$

which is between about 40% and 100% larger than the fitting error associated to the 4PSF algorithm. Finally, observe that for values of $M$ used in practice (e.g. $M \geq 256$), $E[\varepsilon_3] << \sigma_r^2$ and the expression (177) holds. Thus, the 3PSF-IpDFT algorithm based on the Hann window can provide noise power estimates as accurate as the 4PSF algorithm.

Also, we verified through both computer simulations and experimental results the accuracies of the expressions derived above. Moreover, we analyzed the behavior of the PDF of the sum-squared residual error $\kappa$.

Fig. 27 shows both the simulated and the theoretical expected sum-squared fitting errors provided by the 3PSF-IpDFT algorithm and the 4PSF algorithm, normalized to $\sigma_r^2 / M$, as a function of $\delta$. The theoretical values were determined by means of (172) and (173), respectively. The parameters of the sine-wave were $A$ = 1, $\phi = \pi/3$ rad, $d$ = 0.02, and $l$ = 37, while the number of analyzed samples was $M$ = 512 and the $SNR$, was 30 dB. The fractional frequency deviation $\delta$ was varied in the range [–0.5, 0.5) with a step of 0.05 and 10,000 runs were performed for each value of $\delta$. The two-term MSD window was adopted in the 3PSF-IpDFT algorithm. In the 4PSF algorithm the parameter initial values were estimated by means of the IpDFT method based on the rectangular window [Bilau 04] and the iterations were stopped when the absolute value of the difference between each parameter estimates achieved in two consecutive iterations was smaller than $10^{-6}$. This threshold was always attained in no more than three iterations and no significant accuracy improvement was obtained by considering smaller thresholds.

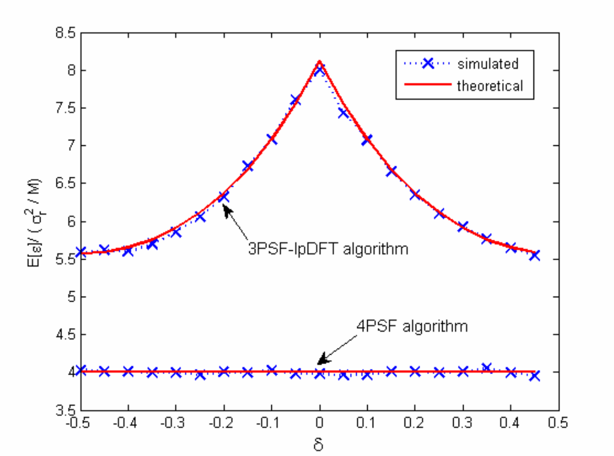


Fig. 27. Simulated and theoretical expected sum-squared fitting errors returned by the 3PSF-IpDFT and the 4PSF algorithms for $M$ = 512, $A$ = 1, and $SNR$ = 30 dB. In the IpDFT method the two-term MSD window was adopted.

The very good agreement between theoretical and simulation results shows by Fig. 27 confirm the accuracies of the expressions (172) and (173). Observe that, the expected sum-squared fitting error provided by the 3PSF-IpDFT algorithm depends on the value of $\delta$ and is always higher than the variance returned by the 4PSF algorithm, as predicted by the theoretical analysis.

Fig. 28 shows the ratio between the simulated expected sum-squared residual errors achieved by the 3PSF-IpDFT and the 4PSF algorithms as a function of $\delta$ for $M = 2^k$, with $k$ = 7 – 12. The same signal parameters used in Fig. 27 were considered.

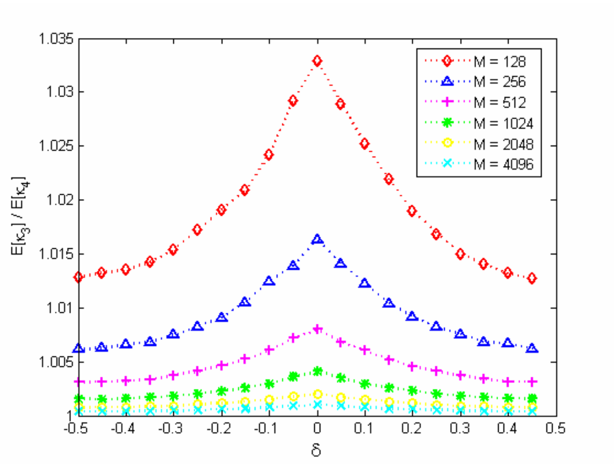


Fig. 28. Ratio between the expected sum-squared residual errors provided by the 3PSF-IpDFT and the 4PSF algorithms versus $\delta$. Simulation results achieved using a data record length $M = 2^k$, with $k = 7$ - 12.

According to the results shown in Fig. 28, the expected sum-squared residual errors returned by the 3PSF-IpDFT and the 4PSF algorithms differ by less than 1.5% soon as $M \geq 256$.

The estimated PDFs of the sum-squared residual errors associated with both sine-fitting algorithms are depicted in Fig. 29 once normalized to the noise power $\sigma_r^2$. They were obtained by considering 100,000 data records of $M$ = 4096 samples each, and dividing the horizontal axis into 100 slots of equal width. The same signal parameters employed in Fig. 27 were used, but with $\delta = 0.2$. A Gaussian PDF with mean $\sigma_r^2$ and variance equal to the corresponding CRLB, that is $2\sigma_r^4 / M$ [Key 93], is also reported in Fig. 29 for a visual comparison.

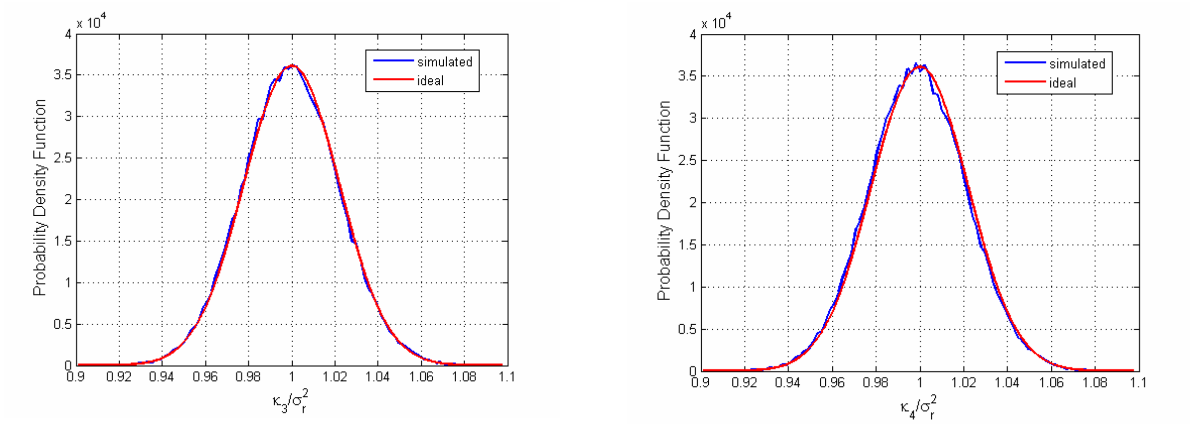


(a) (b)

Fig. 29. Estimated PDF of the sum-squared residual error provided by (a) the 3PSF-IpDFT algorithm and (b) the 4PSF algorithm. The record length is $M = 4096$. A Gaussian PDF with mean $\sigma_r^2$ and variance $2\sigma_r^4 / M$ is also reported.

As we can see, for the considered value of $M$, both sine-fitting algorithms provide an almost normal and efficient estimator of the noise power.

In the experimental runs the signals were provided by an Agilent 33220A signal generator. The data were acquired using a 12-bit data acquisition board NI-6023E. The full scale range and the sampling frequency were set to 10 V and 100 kHz, respectively. Several sine-waves with amplitude 2 V and frequency 3.7, 5.8, 7.7, 10.5, 13.1, 17.3, 20.7 kHz were generated. For each frequency value 5000 records of $M$ = 256, 1024, or 4096 samples were acquired and processed by using the 3PSF-IpDFT and the 4PSF algorithms implemented as for Fig. 27. Fig. 30 shows the ratio between the average sum-squared residual errors achieved from experiments as a function of the input frequency. The mean value of the *ENOB* estimates achieved by applying the 3PSF-IpDFT algorithm for $M$ = 1024 was about 11.1 bits for all the considered frequencies. Thus, the overall noise power is about four times the quantization noise power.

As we can see in Fig. 30, the obtained results strongly agree with the previous theoretical analysis.

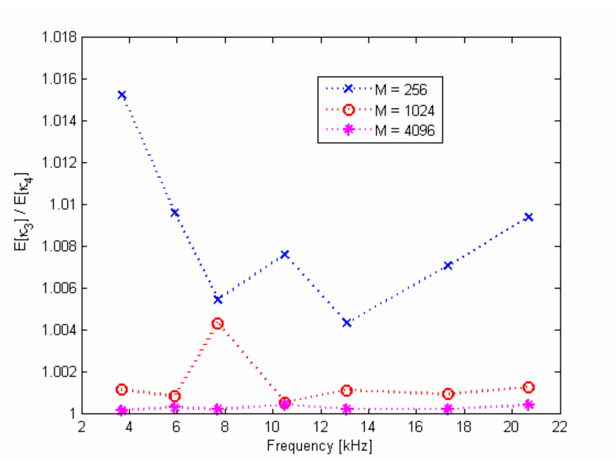


Fig. 30. Ratio between the average of the experimental sum-squared residual errors provided by the 3PSF-IpDFT and the 4PSF algorithms versus the sine-wave frequency. Experiments performed using a data record length $M$ = 256 ('x'), 1024 ('o'), or 4096 ('*').

The experimental PDFs of the sum-squared residual errors returned by either the 3PSF-IpDFT and 4PSF algorithms are depicted in Fig. 31. The signal frequency was 5.2 kHz and 10,000 records of $M$ = 1024 samples each were considered. A Gaussian PDF with mean and variance estimated from the experimental data is also reported for enabling a simple visual verification of the Gaussian behavior.

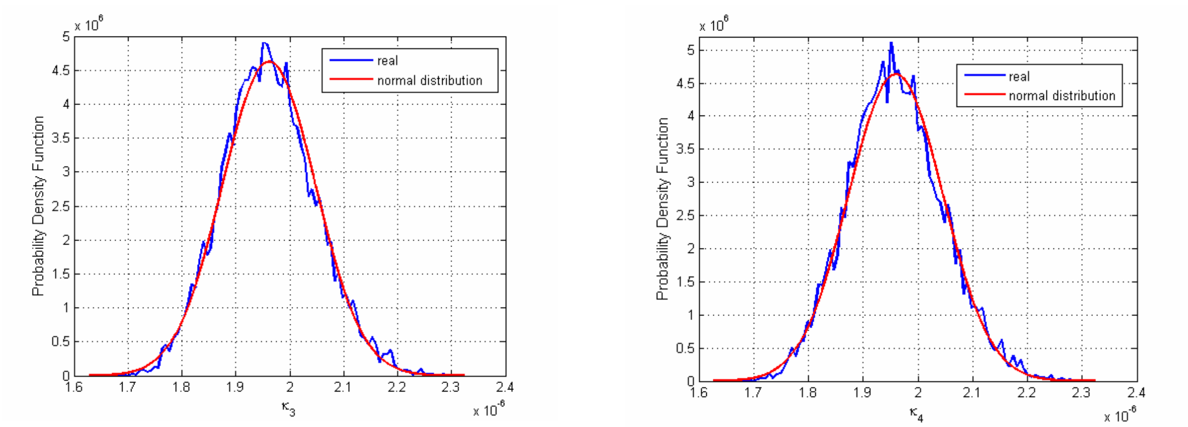


(a) (b)

Fig. 31. Estimated PDF of the sum-squared residual errors provided by (a) the 3PSF-IpDFT algorithm and (b) the 4PSF algorithm. The sine-wave frequency is 5.2 kHz and the record length is $M$ = 1024. A Gaussian PDF with mean and standard deviation determined from the experimental data is also reported.

## 2.3. CONTRIBUTIONS TO ADC TESTING FIELD

In this subection my contributions to the Analog-to-Digital Converter (ADC) testing by means of the frequency-domain and time-domain sine-fitting algorithms are presented.

### 2.3.1. FREQUENCY-DOMAIN AND TIME-DOMAIN SINE-FITTING ALGORITHMS

The overall dynamic performance of an ADC is evaluated by means of different parameters. Two of the parameters mostly used are the SIgnal-to-Noise And Distortion ratio (*SINAD*) and the Effective Number Of Bits (*ENOB*) [Std. 1241], [DYNAD 01]. The first one is defined as the ratio between the rms value of the adopted test sine-wave and the rms value of the overall ADC output noise. Conversely, the *ENOB* represents the number of bits of an ideal ADC with a quantization error rms value equal to the rms value of the overall output noise of the ADC under test. This last parameter is used very often since it provides an easy to understand figure of an ADC dynamic performance [Std. 1241]. The sine-fitting algorithms are a very powerful tool for estimating these parameters. They operate either in the time-domain or in the frequency-domain in order to determine the best sine fit to the output signal of an ADC fed with a pure sine-wave. Then, the parameters of interest are estimated by evaluating the power of the residual signal. To this aim the current Standards for ADC dynamic testing – the IEEE Standard 1241 [Std. 1241] and the European Project DYNAD [DYNAD 01] – suggest the use of time-domain sine-fitting algorithms, which are based on the application of the least squares approach. They are the three-parameter sine-fitting (3PSF) algorithm and the four-parameter sine-fitting (4PSF) algorithm, respectively (see § 2.2.2). Due to the least squares approach the above algorithms are robust with respect to non-coherent sampling, and provide accurate estimates. Besides, they are simple to implement.

In [Belega 11a] and [Belega 11b], we shown that among different frequency-domain sine-fitting algorithms, those based on the Interpolated Discrete Fourier Transform (IpDFT) method or the Energy-Based (EB) method provide accurate *ENOB* and *SINAD* estimates. In the following, they are called FSF-IpDFT algorithm and FSF-EB algorithm, respectively. It is worth noticing that in [Belega 11a], we used for the first time in the scientific literature a frequency-domain sine-fitting algorithm for ADC testing, that was the FSF-IpDFT algorithm. The FSF-IpDFT and the FSF-EB algorithms are very attractive to be used since they exhibit a smaller computational complexity than the 3PSF and 4PSF algorithms, and are very simple to understand and to apply.

### A. Procedure Used to Estimate the *SINAD* and *ENOB* Parameters

In the following, after the definitions of the used parameters, we present the procedure employed to estimate the parameters *SINAD* and *ENOB* of an ADC by means of a sine-fitting algorithm.

We consider an $N$-bit ADC with full-scale range *FSR*, fed with a pure sine-wave. Ideally, to test all the ADC output codes, the sine-wave amplitude should be equal to *FSR*/2, while the sine-wave offset should be zero for bipolar ADCs and *FSR*/2 for unipolar ADCs. The signal obtained at the ADC output can be expressed as follows:

$$y(n) = s(n) + r(n) = A\sin\left(2\pi \frac{f_{in}}{f_s} n + \phi\right) + B + r(n), \quad n = 0,1,2,\ldots,M-1 \tag{1}$$

where $A$, $f_{in}$, $\phi$, and $B$ are, respectively, the amplitude, the frequency, the phase, and the offset of the output sine-wave $s(\cdot)$, $M$ is the number of samples acquired with sampling frequency $f_s$, whereas $r(\cdot)$ is the ADC output noise, which represents the overall error introduced during conversion and includes the effects of random noise, fixed pattern errors, nonlinearities (e.g. harmonic or spurious components), aperture uncertainty, etc. The frequency $f_{in}$ is usually chosen smaller than $f_s/2$ to satisfy the Nyquist theorem. The ratio between $f_{in}$ and $f_s$ can be expressed as:

$$\frac{f_{in}}{f_s} = \frac{\nu}{M} = \frac{J+\delta}{M}, \tag{2}$$

where $J$ and $\delta$ ($-0.5 \leq \delta < 0.5$) are respectively the integer and the fractional parts of the number of recorded sine-wave cycles $\nu$. It is worth noticing that $\nu$ represents also the sine-wave normalized frequency expressed in bins and it is usually evaluated by estimating $J$ and $\delta$ separately. It is well-known that $\delta = 0$ corresponds to the so-called coherent sampling, whereas $\delta \neq 0$ corresponds to non-coherent sampling [Ferrero 92]. The latter mode often occurs in practice due to lack of synchronization between sine-wave and sampling frequencies.

Usually the value of $J$ can be determined exactly by means of (2) when enough accurate estimates for $f_{in}$ and $f_s$ are available, or by using a maximum search routine applied to the DFT samples of the ADC output spectrum. Thus, from (2) it follows that the estimation uncertainties of $\nu$ and $\delta$ coincide.

All the sine-fitting algorithms estimate the *SINAD* and *ENOB* parameters through the following steps [Std. 1241], [Petri 13]:

1. Acquire $M$ consecutive samples of the ADC output signal $y(n)$, $n = 0, 1, 2,\ldots, M-1$.

2. Determine the best sine fitting of the ADC output sequence $y(\cdot)$:

$$\hat{s}(n) = \hat{A}\sin\left(2\pi\hat{\nu}\frac{n}{M} + \hat{\phi}\right) + \hat{B}, \quad n = 0,1,\ldots,M-1 \tag{3}$$

where $\hat{A}$, $\hat{\nu}$, $\hat{\phi}$, and $\hat{B}$ are respectively the amplitude, normalized frequency, phase, and offset of the best fitting sine-wave. In particular, to achieve $\hat{\nu}$, only an estimate of $\delta$, $\hat{\delta}$, is needed since $\hat{\nu} = J + \hat{\delta}$. The above parameter estimates can be determined by means of time-domain or frequency-domain methods [Std. 1241], [DYNAD 01], [Belega 11a], [Belega 11b].

3. Evaluate the residual signal:

$$\hat{r}(n) = y(n) - \hat{s}(n), \quad n = 0,1,\ldots,M-1 \tag{4}$$

4. Evaluate the residual rms value:

$$\hat{r}_{rms}^2 = \frac{1}{M}\sum_{n=0}^{M-1}\hat{r}^2(n). \tag{5}$$

5. Determine the *SINAD* and *ENOB* parameters as:

$$\hat{SINAD} = 10\log_{10}\left(\frac{\hat{A}^2}{2\hat{r}_{rms}^2}\right) \quad (dB) \tag{6}$$

$$\hat{ENOB} = N - \frac{1}{2}\log_2\left(\frac{\hat{r}_{rms}^2}{\sigma_q^2}\right) \quad (bits) \tag{7}$$

where $\sigma_q^2$ is the variance of the quantization error of an ideal quantizer, which is usually assumed uniformly distributed [Std. 1241], that is

$$\sigma_q^2 = \frac{Q^2}{12} = \frac{1}{12}\left(\frac{FSR}{2^N}\right)^2, \tag{8}$$

where $Q$ is the theoretical code bin width of the ADC under test.
It is worth noticing that when the input sequence can be described as a zero-mean, uniform and stationary random process, the quantization noise can be modeled as additive white noise, uniformly distributed over the range ($-Q/2$, $Q/2$), and uncorrelated with the input [Kollár 94], [Widrow 96].
It is well known that a linear relationship exists between the *ENOB* and *SINAD* (in dB) [Std. 1241]:

$$SINAD\,(dB) = 6.02ENOB + 1.76. \tag{9}$$

Due to (9) we limit our analysis to the *ENOB* parameter only without any loss of generality.

## B. Sine-Fitting Algorithms Accuracy Comparison

In [Petri 13], we compared the accuracy of the sine-fitting algorithms based on the IpDFT and EB methods with those achieved by the 3PSF and 4PSF algorithms through both theoretical and simulation results. To this aim, we derived the expressions of the expected sum-squared fitting and residual errors for each above algorithms. The analysis was performed assuming that the overall ADC output noise can be modelled as a zero mean white Gaussian noise. This comparison is presented in the following.
In [Belega 12d], we derived the expression of the expected sum-squared fitting error, which is given by:

$$E[\varepsilon] \cong \sigma_{\hat{B}}^2 + \frac{\sigma_{\hat{A}}^2}{2} + \frac{\pi^2 A^2 \sigma_{\hat{\nu}}^2}{6} + \frac{A^2 \sigma_{\hat{\phi}_c}^2}{2}, \tag{10}$$

where $\sigma_{\hat{A}}^2$, $\sigma_{\hat{\nu}}^2$, $\sigma_{\hat{\phi}_c}^2$, and $\sigma_{\hat{B}}^2$ represent the variances of the estimators provided by the considered sine-fitting algorithms for signal amplitude, fractional frequency, phase at the center of the observation interval (that is for $n = M/2$), and offset.
In the following, the above expression will be evaluated for each of the considered algorithms.

• *Sine-fitting based on the IpDTF or EB methods*

When the IpDFT or the EB methods are employed, the offset was estimated as [Belega 11a], [Belega 11b]:

$$\hat{B} = \frac{Y_w(0)}{M \cdot NPSG} = \frac{\sum_{n=0}^{M-1} y(n)}{M \cdot NPSG}, \tag{11}$$

where $Y_w(\cdot)$ is the Discrete Fourier Transform (DFT) of the windowed ADC output signal $y_w(\cdot)$, where $w(\cdot)$ is the window used with the Normalized Power Signal Gain *NPSG*, given by ((8) in §2.2.1.A).
The variances of the estimators $\hat{A}$, $\hat{\nu}$, $\hat{\phi}_c$, and $\hat{B}$ provided by the IpDFT or the EB methods are given by [Belega 11a]:

$$\sigma_{\hat{B}}^2 \cong ENBW \frac{\sigma_r^2}{M}, \tag{12}$$

$$\sigma_{\hat{A}}^2 \cong \frac{2ENBW}{SL^2(\delta)} \frac{\sigma_r^2}{M}, \tag{13}$$

$$\sigma_{\hat{\phi}_c}^2 \cong \frac{2ENBW}{A^2 SL^2(\delta)} \frac{\sigma_r^2}{M}, \tag{14}$$

where *ENBW* and $SL(\delta)$ are respectively the Equivalent Noise BandWidth and the Scalloping Loss of the used window, and are given in §2.2.1.A by (10) and (15), respectively,.
Using (12) - (14), expression (10) becomes:

$$E[\varepsilon] \cong ENBW \left(1 + \frac{2}{SL^2(\delta)}\right) \frac{\sigma_r^2}{M} + \frac{\pi^2 A^2 \sigma_{\hat{\nu}}^2}{6}. \tag{15}$$

Thus, the expected sum-squared fitting error that occurs when using the IpDFT method can be expressed as:

$$E[\varepsilon_{ip}] \cong ENBW\left(1+\frac{2}{SL^2(\delta)}\right)\frac{\sigma_r^2}{M}+\frac{\pi^2 A^2 \sigma_{\hat{\nu}_{ip}}^2}{6}, \tag{16}$$

where $\sigma_{\hat{\nu}_{ip}}^2$ is given by ((42) in §2.2.1.B).

It is worth noticing that the minimum and the maximum values of $\sigma_{\hat{\nu}_{ip}}^2$ are reached for $\delta$ equal to –0.5 and 0, respectively [Belega 12a]. Conversely, $SL(\delta)$ assumes its maximum value (equal to 1) for $\delta = 0$, but it remains very close to it for $-0.5 \le \delta < 0.5$. Hence, the minimum and the maximum values of the E[$\varepsilon_{ip}$] are reached for $\delta$ equal to –0.5 and 0, respectively.

Similarly, the expected sum-squared fitting error when using the EB method can be expressed as:

$$E[\varepsilon_{eb}] \cong ENBW\left(1+\frac{2}{SL^2(\delta)}\right)\frac{\sigma_r^2}{M}+\frac{\pi^2 A^2 \sigma_{\hat{\nu}_{eb}}^2}{6}, \tag{18}$$

in which the variance $\sigma_{\hat{\nu}_{eb}}^2$ is given by ((126) in §2.2.2):

Since $\sigma_{\hat{\nu}_{eb}}^2$ does not depend on $\delta$, the minimum and the maximum values of E[$\varepsilon_{eb}$] are reached for $\delta$ equal to 0 and –0.5, respectively.

It is worth noticing that the selection of the optimal window to be used in the FSF-IpDFT algorithm can be performed by the criterion proposed in [Belega 11a] and presented in §2.2.1.B. Conversely, the selection of the optimal window to be used in the FSF-EB algorithm can be performed based on the performance parameter defined in [Belega 11b]. That parameter is the maximum number of bits $NOB_{max}$ above which the absolute value of the *ENOB* estimation error, |Δ*ENOB*|, is smaller than a give threshold (e.g. 0.1 bits) [Belega 11b].

- *3PSF and 4PSF algorithms*

The expected sum-squared fitting error for the 3PSF algorithm is given by ((172) in §2.2.2):

$$E[\varepsilon_{3p}] \cong \frac{3\sigma_r^2}{M}+\frac{\pi^2 A^2 \sigma_{\hat{\nu}}^2}{6}. \tag{18}$$

We showed in [Belega 07c], that accurate *ENOB* estimates can be achieved if the normalized frequency error $\Delta_\nu = \hat{\nu} - \nu$ satisfies the following constraint:

$$|\Delta_\nu| < \frac{\sqrt{2}}{\pi 2^{N+2}}. \tag{19}$$

The above constraint can be satisfied when $\nu$ is estimated by the IpDFT method [Belega 8d]. In this case in (18) we have $\sigma_{\hat{\nu}}^2 = \sigma_{\hat{\nu}_{ip}}^2$. Also, the minimum and the maximum values of the E[$\varepsilon_{3p}$] are reached for $\delta$ equal to –0.5 and 0, respectively.

Conversely, the expected sum-squared fitting error for the 4PSF algorithm is given by ((173) in §2.2.2):

$$E[\varepsilon_{4p}] \cong \frac{4\sigma_r^2}{M}. \tag{20}$$

By comparing the expressions (16), (17), (18), and (20), it follows that: E[$\varepsilon_{4p}$] < E[$\varepsilon_{3p}$] < E[$\varepsilon_{ip}$] < E[$\varepsilon_{eb}$]. Thus, the time-domain sine-fitting algorithms provide more accurate sine-wave fitting than the frequency-domain sine-fitting algorithms. In particular, the best accuracy is provided by the 4PSF algorithm, while the worst accuracy is achieved by the FSF-EB algorithm.

However, the above expressions show that the expected sum-squared fitting error is always proportional to $\sigma_r^2 / M$ . Hence, for values of $M$ used in practice, it is negligible with respect to the noise variance $\sigma_r^2$. This implies that for any sine-fitting algorithm, the expectation of the residual mean square value results very close to the noise variance:

$$E[\hat{r}_{rms}^2] \cong \sigma_r^2. \tag{21}$$

To confirm the above expressions, we reported both theoretical and simulation results for the ratio $E[\varepsilon]/\left(\sigma_r^2 / M\right)$ in Fig. 1 as a function of $\delta$ for all the considered sine-fitting algorithms. The input sine-wave was characterized by the following parameters: $A$ = 5, $\phi$ = π/3 rad, and $B$ = 0.02. It was corrupted by additive Gaussian noise with zero mean and variance $\sigma_r^2$ chosen in such a way that the Signal-to-Noise Ratio (*SNR*) is equal to 60 dB. The integer part $J$ was set to 37. The fractional part $\delta$ was varied in the range [–0.5, 0.5) with a step of 1/20. For each value of δ, 10,000 runs of $M$ = 512 samples each were performed. In the 3PSF algorithm and the FSF-IpDFT algorithm, the two-term Maximum Sidelobe Decay (MSD) window or Hann window was used, while the FSF-EB algorithm is based on the three-term Rapid Sidelobe Decay with Minimum Sidelobe Level (RSD-MSL) window [Belega 11b]. The initial values used in the four-parameter algorithm were estimated through the IpDFT method based on the rectangular window [Bilau 04], while the iterations were stopped when the relative distance between the frequency values estimated in two consecutive iterations was smaller than $10^{-6}$.

Fig. 1 shows that the agreement between theoretical and simulation results is very good.

Moreover, we reported in Fig. 2 both theoretical and simulation results of the ratio $E[\hat{r}_{rms}^2]/\sigma_r^2$ as a function of $\delta$. The adopted parameters were exactly the same as in the previous figure.

As we can see, the ratio $E[\hat{r}_{rms}^2]/\sigma_r^2$ is always very close to 1. Indeed, the contribution of the fitting error to the residual signal is negligible, as suggested by the above theoretical analysis.

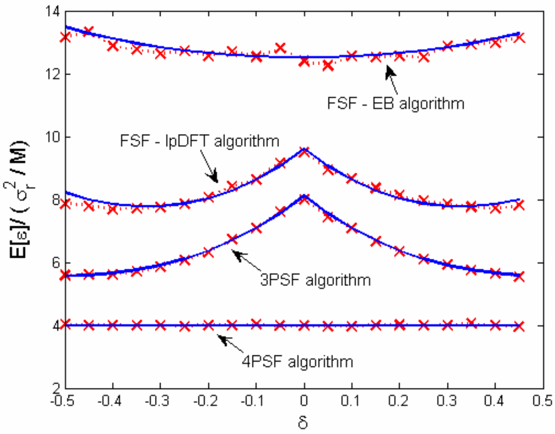


Fig. 1. Ratio $E[\varepsilon]/\left(\sigma_r^2/M\right)$ provided by theoretical (continuous line) and simulation (crosses) results versus $\delta$. The number of acquired samples was $M = 512$.

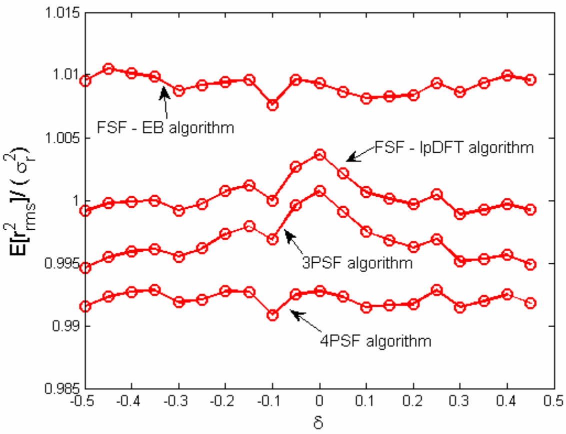


Fig. 2. Ratio $E[\hat{r}_{rms}^2]/\sigma_r^2$ provided by simulation results (circles) versus $\delta$. The number of acquired samples was $M = 512$.

Moreover, we have compared the processing effort related to each sine-fitting algorithm. All the considered sine-fitting algorithms were implemented in MATLAB running on a portable computer with a CPU clock rate of 2 GHz, 2046 MB RAM memory, and equipped with a Microsoft Windows Vista operating system. Choosing $M$ = 512, the average computational time required to determine a single residual mean square value $\hat{r}_{rms}^2$ for a given value of $\delta$ was equal to 0.47, 0.57, 0.74, and 1.28 ms, for the FSF-IpDFT, FSF-EB, 3PSF, and 4PSF algorithms, respectively. Thus, the FSF-IpDFT and the 4PSF algorithms exhibit the smaller and the highest processing burden, respectively. The same conclusion holds regardless the number of acquired samples. Thus, the FSF-IpDFT algorithm is a good choice when dealing with *ENOB* estimation.

## C. Statistical Performance of the ENOB Estimator

In [Belega 13b], we performed a whole statistical description of the *ENOB* estimator provided by a sine-fitting algorithm, which was not available before in the scientific literature. For this purpose the expressions for the bias and variance of the *ENOB* estimator were derived in the case of an ideal ADC and an ADC affected by harmonics, spurious tones, and additive white Gaussian noise. These derivations are given in the following.

From (7), the expectation and the standard deviation of the *ENOB* estimator result:

$$E[\hat{ENOB}] = ENOB - \frac{1}{2}E\left[\log_2\left(\hat{r}_{rms}^2\right)\right] + \frac{1}{2}\log_2\left(\sigma_r^2\right), \tag{22}$$

$$std[\hat{ENOB}] = \frac{1}{2}std\left[\log_2\left(\hat{r}_{rms}^2\right)\right]. \tag{23}$$

In order to determine an accurate expression for $E[\log_2(\hat{r}_{rms}^2)]$ and $std[\log_2(\hat{r}_{rms}^2)]$, we consider a general function $z = f(x)$, in which $x$ is a random variable and $f(\cdot)$ is a derivable function. We have [Petri 02]:

$$E[z] \cong f(\mu_x) + \frac{1}{2}f''(\mu_x)\cdot\sigma_x^2, \tag{24}$$

and

$$std[z] \cong f'(\mu_x)\cdot\sigma_x^2, \tag{25}$$

in which $\mu_x = E[x]$.

Now, considering $z = f(x) = \log_2(x)$ and $x = \hat{r}_{rms}^2$, we obtain:

$$E\left[\log_2(\hat{r}_{rms}^2)\right] \cong \log_2\left(E[\hat{r}_{rms}^2]\right) - \frac{1}{2\ln(2)}\left(\frac{\mathrm{var}[\hat{r}_{rms}^2]}{E^2[\hat{r}_{rms}^2]}\right), \tag{26}$$

and

$$std\left[\log_2(\hat{r}_{rms}^2)\right] \cong \frac{1}{\ln(2)}\frac{std[\hat{r}_{rms}^2]}{E[\hat{r}_{rms}^2]}, \tag{27}$$

where $E[\hat{r}_{rms}^2]$, $std[\hat{r}_{rms}^2]$, $\mathrm{var}[\hat{r}_{rms}^2]$ are respectively the expectation, the standard deviation, and the variance of the random variable $\hat{r}_{rms}^2$.

Using (22) and (26) the expectation of the *ENOB* estimator is expressed as:

$$E[\hat{ENOB}] \cong ENOB - \frac{1}{2}\log_2\left(\frac{E[\hat{r}_{rms}^2]}{\sigma_r^2}\right) + \frac{1}{4\ln(2)}\frac{\mathrm{var}[\hat{r}_{rms}^2]}{E^2[\hat{r}_{rms}^2]}, \tag{28}$$

from which the expression of the bias can be easily derived:

$$bias[\hat{ENOB}] \cong \frac{1}{2}\log_2\left(\frac{\sigma_r^2}{E[\hat{r}_{rms}^2]}\right) + \frac{1}{4\ln(2)}\frac{\mathrm{var}[\hat{r}_{rms}^2]}{E^2[\hat{r}_{rms}^2]}. \tag{29}$$

By replacing (27) in (23) we finally achieve:

$$std[\hat{ENOB}] \cong \frac{1}{2\ln(2)}\frac{std[\hat{r}_{rms}^2]}{E[\hat{r}_{rms}^2]}. \tag{30}$$

It is worth noticing that (29) and (30) hold regardless the characteristics of the overall ADC output noise $r(\cdot)$.
In the following we assume that the ADC output can be expressed as:

$$\begin{aligned} y(n) &= s(n) + r(n) = s(n) + h(n) + w(n) \\ &= A\sin\left(2\pi\frac{f_{in}}{f_s}n + \phi\right) + B + \sum_{k=2}^{K} A_k \sin\left(2\pi\frac{f_k}{f_s}n + \phi_k\right) + w(n), \qquad n = 0,1,2,\ldots,M-1 \end{aligned} \tag{31}$$

where $A_k$, $f_k$, and $\phi_k$ are respectively the amplitude, the frequency, and the phase of the $k$-th ADC output tone (either harmonic or spurious tone), $K$ is the number of tones, and $w(\cdot)$ is a wideband noise, which can be modeled as a white noise with zero mean and variance $\sigma_w^2$. We can reasonably assume that the different ADC output noise components are uncorrelated. Thus, we have:

$$\sigma_r^2 = \sigma_w^2 + \sum_{k=2}^{K}\frac{A_k^2}{2} = \sigma_w^2(1+\rho_t), \tag{32}$$

where:

$$\rho_t = \frac{1}{\sigma_w^2}\sum_{k=2}^{K}\frac{A_k^2}{2}, \tag{33}$$

is the ratio between the power of the tones and the wideband noise power.
For this case, in [Belega 13b], we derived the expressions for the expectation and variance of the residual rms value $\hat{r}_{rms}^2$, which are:

$$E[\hat{r}_{rms}^2] \cong \sum_{k=2}^{K}\frac{A_k^2}{2} + E\left[\frac{1}{M}\sum_{n=0}^{M-1} w^2(n)\right] = \sum_{k=2}^{K}\frac{A_k^2}{2} + \sigma_w^2 \tag{34}$$

$$\mathrm{var}[\hat{r}_{rms}^2] \cong \frac{1}{M}\left[ E[w^4] - \sigma_w^4 + 2\left(\sum_{k=2}^{K} A_k^2\right)\sigma_w^2 \right]. \tag{35}$$

Using (33), (34) and (35) become:

$$E[\hat{r}_{rms}^2] \cong \sigma_w^2 (1+\rho_t), \tag{36}$$

and

$$\mathrm{var}[\hat{r}_{rms}^2] \cong \frac{1}{M}\left[ E[w^4] - \sigma_w^4 (1 - 4\rho_t) \right] \tag{37}$$

By replacing (36) and (37) into (29) and (30), the expressions for the bias and the standard deviation of the *ENOB* estimator become:

$$bias[\hat{ENOB}] \cong \frac{1}{2}\log_2\left(\frac{\sigma_r^2}{E[\hat{r}_{rms}^2]}\right) + \frac{1}{4\ln(2)M}\frac{\frac{E[w^4]}{\sigma_w^4} - (1-4\rho_t)}{(1+\rho_t)^2}, \tag{38}$$

and

$$std[\hat{ENOB}] \cong \frac{1}{2\ln(2)\sqrt{M}}\frac{\sqrt{\frac{E[w^4]}{\sigma_w^4} - (1-4\rho_t)}}{1+\rho_t}. \tag{39}$$

In particular, simulation results showed that, for any considered ADC resolution, the estimator bias (38) is always between about $1/M$ and $4/M$ when white noise only affects the ADC output. Even lower values were achieved when the ADC output noise contains significant harmonics and/or spurious tones. Thus, from (38) and (39) it follows that the *ENOB* estimator is consistent since both its bias and standard deviation tend to zero as $M$ increases.

In addition, we can see that the ratio between the bias and the standard deviation is proportional to $1/\sqrt{M}$ . Hence, for values of $M$ commonly adopted in practice (e.g. $M \geq 256$), the estimator bias is negligible. For this reason, it will be no further analyzed.

In the specific case of ideal ADCs, the harmonics and the spurious tones are null, while $w(\cdot)$ is due to quantization and exhibits a uniform distribution. Thus, we have [Papoulis 89]:

$$E[w^4] = 1.8 \cdot \sigma_w^4, \tag{40}$$

and (39) becomes:

$$std[\hat{ENOB}] \cong \frac{0.65}{\sqrt{M}}. \tag{41}$$

In practice the wideband component $w(\cdot)$ is always due to both quantization and other noise sources, usually normally distributed. If the power of the exceeding noise is significant as compared to the quantization noise, then $w(\cdot)$ itself can be assumed normally distributed [Bertocco 00], and we have [Papoulis 89]:

$$E[w^4] = 3 \cdot \sigma_w^4. \tag{42}$$

Hence, (39) provides:

$$std[\hat{ENOB}] \cong \frac{1.02}{\sqrt{M}} \frac{\sqrt{1+2\rho_t}}{1+\rho_t}. \tag{43}$$

Expression (43) shows that the *ENOB* estimator standard deviation decreases as the contribution of harmonics and spurious tones to the overall ADC output noise increases. In particular, the maximum value of the standard deviation is reached at $\rho_t = 0$ and it is equal to:

$$std[\hat{ENOB}] \cong \frac{1.02}{\sqrt{M}}. \tag{44}$$

By comparing the above expression to (41) it follows that when the noise $w(\cdot)$ of an ADC is white Gaussian and the tones are null the *ENOB* estimator exhibits a higher standard deviation than an ideal ADC since in the first case the power of the overall noise is higher than the power of the quantization noise.

Since the first term in the right hand side of (7) is a constant, the statistical behaviour of any *ENOB* estimator is completely described by the Probability Density Function (PDF) of the random variable $\vartheta = \frac{1}{2}\log_2\left(\sigma_r^2 / \hat{r}_{rms}^2\right)$. It is known that, when $M$ is high enough, the residual rms value $\hat{r}_{rms}^2$ is almost normally distributed, unbiased, and exhibits a variance close to the related Cramér-Rao Lower Bound (CRLB) [Kay 93], [Belega 12d]. Hence, by linearization of (7), we can conclude that the *ENOB* estimator is asymptotically unbiased, efficient, and normally distributed. Thus, we can conclude that it is a statistically optimal estimator. In [Belega 13d], we verified these aspects by means of computer simulations. Fig. 3 shows the estimated PDF of the variable $\vartheta$ for an ideal bipolar 12-bit ADC with *FSR* = 5 when the 3PSF (Fig. 3(a)) or the 4PSF (Fig. 3(b)) algorithm is employed. Also, the PDF of a Gaussian random variable with zero mean and standard deviation (41) are depicted in Fig. 3 for a visual comparison. The phase of the ADC input signal was $\pi/3$ rad, the offset was 0.02, the number of observed cycles was 73.2, and $M = 4096$ samples were acquired. In the 3PSF algorithm the normalized input frequency was estimated by means of the IpDFT method based on the Hann window. In the 4PSF algorithm the initial parameters were estimated by means of the IpDFT method based on the rectangular window [Bilau 04]. The iteration stopping condition required that the magnitude of the difference between two consecutive estimates was smaller than $10^{-6}$ for each parameter. That constraint was always fulfilled with no more than three iterations. The estimated PDFs were achieved using 50,000 realizations and dividing the horizontal axis in 100 slots of equal width. Curves similar to those depicted in Fig. 3 are reported in Fig. 4, but considering an ADC output corrupted by a second harmonic, a third harmonic, a spurious tone with frequency equal to $4.5f_{in}$, and white Gaussian noise. The amplitudes of the tones (set in the ratio 4:1:2), and the noise variance were fixed to achieve 0.75 lost bits respectively, thus resulting in an ADC with $ENOB = N - 1.5 = 10.5$ bits. The harmonics and the spurious tone phases were chosen at random in the range $[0, 2\pi)$ rad. Besides, the PDF of a Gaussian random variable with zero mean and standard deviation (41) is shown in Fig. 4 for a visual comparison.

Both Figs. 3 and 4 show that, for the considered number of acquired samples, the random variable $\vartheta$ is almost normally distributed. Besides, we performed many other simulations using different values for ADC resolution, *ENOB*, and number of acquired samples. The same behaviour depicted in Figs. 3 and 4 was always achieved when values of $M$ used in practice and accurate initial sine-wave parameter estimates were employed. Also, the estimated PDFs resulted closer to a normal distribution as $M$ increases. Thus, we can conclude that, for the values of $M$ commonly used in practice (e.g. $M \geq 256$), the *ENOB* estimator is almost Gaussian, unbiased, and efficient, i.e. it is a statistically optimal estimator.

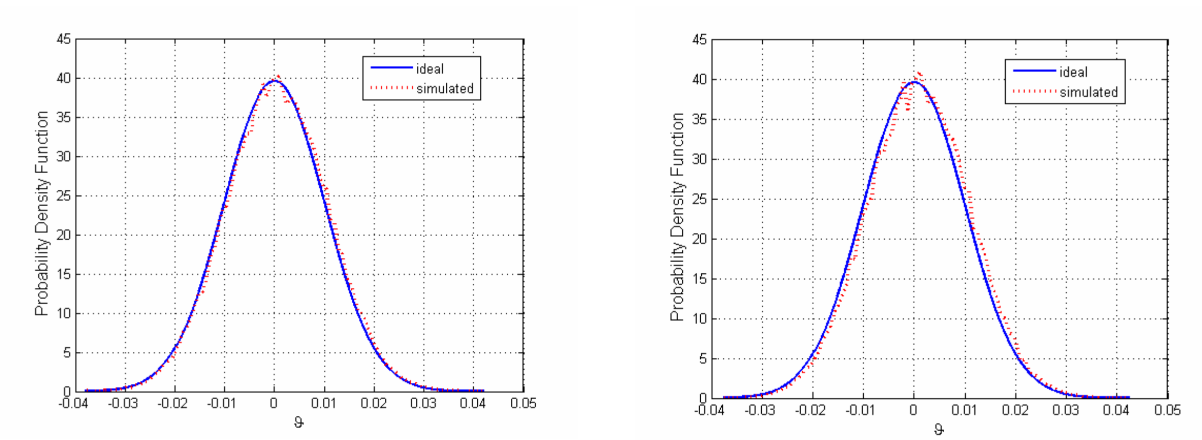


(a) (b)

Fig. 3. Estimated and theoretical PDFs of the random variable $\vartheta$ related to the 3PSF (a) or the 4PSF (b) algorithm. Ideal bipolar 12-bit ADC. Number of acquired samples $M = 4096$.

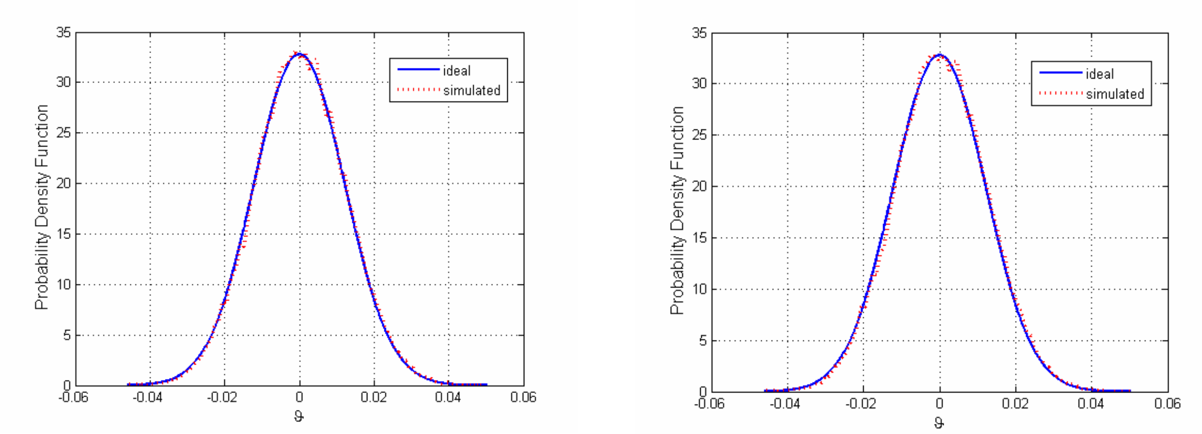


(a) (b)

Fig. 4. Estimated and theoretical PDFs of the random variable $\vartheta$ related to the 3PSF (a) or the 4PSF (b) algorithm. Bipolar 12-bit ADC with $ENOB = 10.5$ bits. Lost bits are equally due to tones and white Gaussian noise. Number of acquired samples $M = 4096$.

Moreover, in [Belega 13b], we verified the accuracy of the expressions derived above through both computer simulations and experimental results.

Fig. 5 shows the simulated and the theoretical values of the *ENOB* estimator bias achieved for an ideal (Fig. 5(a)) and a non-ideal (Fig. 5(b)) bipolar ADC as a function of the ADC resolution $N$. For the non-ideal ADC, 1.5 lost bits equally due to both wideband noise and tones were considered. The same tones as in the previous figure were considered and their amplitudes were set in the same ratio. The sine-wave offset was 0.02 and the number of observed cycles was 123.2. The ADC resolution varied with a step of 2 bits in the range [6, 20] bits for the 3PSF algorithm or in the range [6, 24] bits when the 4PSF algorithm was employed. In the former case, the ADC resolution was bounded to 20 bits due to the limited input frequency estimation accuracy provided by the IpDFT method based on the Hann window. The theoretical bias was determined by applying (38) in which the value of $E[\hat{r}_{rms}^2]$ returned by simulations was used. For each value of the ADC resolution, 10,000 runs of $M$ = 1024 samples each were generated by varying at random the phases of the sine-wave, the harmonics, and the spurious tone.

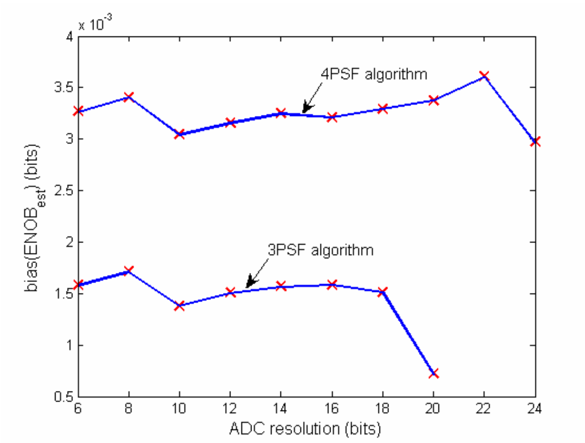


(a)

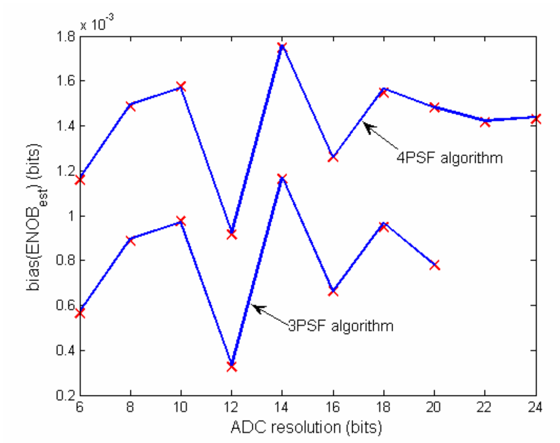


(b)

Fig. 5. *ENOB* estimator bias achieved by simulations (crosses) and by the theoretical expressions (continuous lines) versus ADC resolution: (a) ideal and (b) non-ideal ADCs.

As we can see, the agreement between simulations and theory is very good. Also, the 3PSF algorithm exhibits a lower bias.

Also, Fig. 6 shows the ratio between the standard deviations of the *ENOB* estimator returned by simulations and by the theoretical expressions (41) and (43), respectively for ideal (Fig. 6(a)) and non-ideal (Fig. 6(b)) ADCs. Both the simulations and the signal parameters were chosen as in Fig. 5. As we can see, the theoretical results are very close to the values returned by simulations. We observe also that the *ENOB* estimator standard deviations provided by the 3PSF and the 4PSF algorithms are very close.

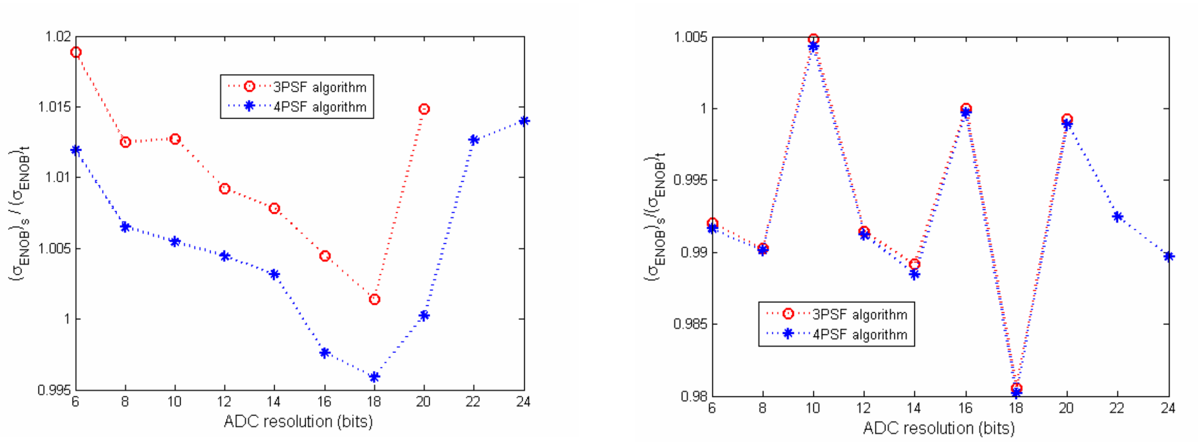


(a) (b)

Fig. 6. Ratio between the *ENOB* estimator standard deviations returned by simulations and by the theoretical expressions versus the ADC resolution for ideal (a) and non-ideal (b) ADCs.

The accuracies of the proposed expressions were also verified by means of experimental results. The sine-waves were supplied by an Agilent 33220A signal generator and acquired using a 12-bit data acquisition board NI-6023E. The *FSR* and the sampling rate were set to 10 V and 100 kHz, respectively. The sine-waves were characterized by an amplitude of 5 V and frequencies equal to 3.1, 7.9, 12.3, 17.5, 22.1, and 26.7 kHz. For each frequency value, 1000 runs of $M$ = 1024 samples were acquired, and the standard deviation of the *ENOB* estimates returned by the 3PSF and the 4PSF algorithms were determined. The algorithm parameters were chosen as above. The ratios between the *ENOB* estimator standard deviations returned by experimental results and expressions (30) are reported in Fig. 7(a) as a function of the input sine-wave frequency. Also, the ratios between the experimental results and the expressions (43) and (44) are reported in Fig. 7(b) for the 3PSF algorithm. The values of $E[\hat{r}_{rms}^2]$ and $\mathrm{var}[\hat{r}_{rms}^2]$ used in (30) were determined experimentally. In (43) the wideband noise power was estimated as the difference between the rms residual value and the power of the first ten highest noise spectral lines, which were estimated by using the IpDFT method based on the Hann window.

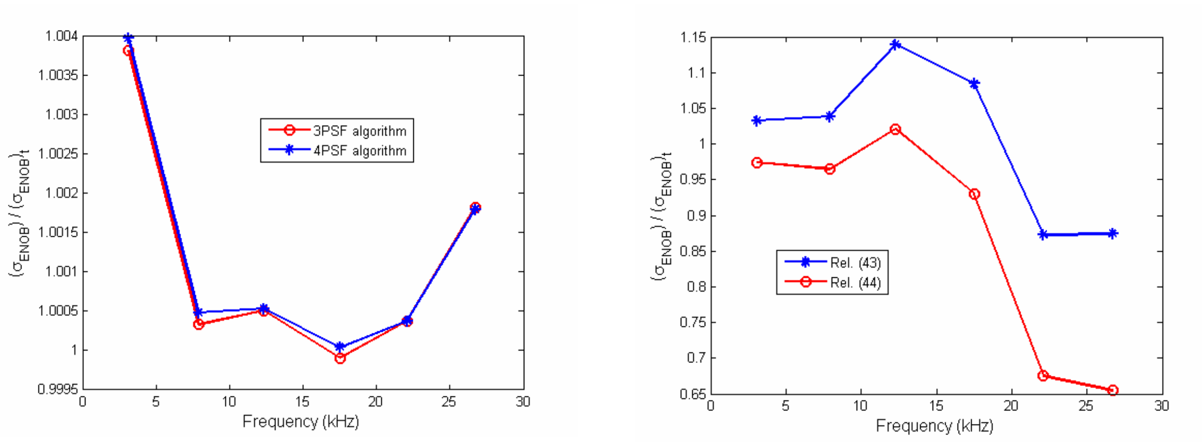


(a) (b)

Fig. 7. Ratio between the *ENOB* estimator standard deviations returned by experimental results and by (a) (30) and (b) (43) and (44) versus the input sine-wave frequency.

Fig. 7(a) clearly confirms that (30) agrees very well with the experimental results. Notice also from Fig. 7(a) that the standard deviations of both the 3PSF and the 4PSF algorithms are almost equal. Fig. 7(b) shows that the experimental *ENOB* estimator standard deviation is close to the value returned by (53) only for input signal frequencies quite smaller than the sampling frequency. Indeed, for frequencies up to 17.5 kHz, the wideband noise dominates the residual signal power. Conversely, at higher frequencies the power of harmonics and spurious tones on the ADC output is significant. Thus, as expected the *ENOB* estimator standard deviation decreases and (44) provides overestimated results. From Fig. 7(b) it follows that the results provided by (43) are quite close to experimental data.

### 2.3.2. APPLICATIONS OF THE SINE-FITTING ALGORITHMS TO REAL DATA

In [Petri 13], we applied the above sine-fitting algorithms to data acquired using a 12-bit data acquisition board NI-6023E. The *FSR* and the sampling frequency were set to 10 V and 100 kHz, respectively. The sine-waves were provided by a signal generator Agilent 33220A. The signal amplitude was set to 5 V, while the frequency was varied in the range [14.70, 14.79] kHz with a step of 10 Hz. The achieved value of $J$ was equal to 151. According to the criterion presented in §2.2.1.B), the Hann window was used for the 3PSF and the FSF-IpDFT algorithms, while the three-term RSD-MSL window was adopted for the FSF-EB algorithm [Belega 11b]. The parameters used in the 4PSF algorithm were the same as in Fig. 1. For each value of $\delta$, 1000 runs of $M$ = 1024 samples each were performed. The mean and the standard deviation of the *ENOB* estimates achieved by all the considered sine-fitting algorithms are reported in Table 1 for different values of the fractional frequency $\delta$. The values of the fractional frequency $\delta$ reported in Table 1 represent the mean value returned by the IpDFT method.

Table 1. *ENOB* mean and standard deviation achieved at different values of $\delta$ by all the considered sine-fitting algorithms.

| δ | FSF-IpDFT algorithm | | FSF-EB algorithm | | 3PSF algorithm | | 4PSF algorithm | |
|---|---|---|---|---|---|---|---|---|
| | mean (bits) | std. dev. (bits) | mean (bits) | std. dev. (bits) | mean (bits) | std. dev. (bits) | mean (bits) | std. dev. (bits) |
| -0.471 | 10.685 | 0.042 | 10.683 | 0.043 | 10.686 | 0.042 | 10.687 | 0.042 |
| -0.368 | 10.687 | 0.045 | 10.685 | 0.045 | 10.689 | 0.045 | 10.689 | 0.045 |
| -0.266 | 10.690 | 0.054 | 10.688 | 0.055 | 10.691 | 0.054 | 10.691 | 0.054 |
| -0.163 | 10.684 | 0.043 | 10.683 | 0.043 | 10.685 | 0.043 | 10.686 | 0.043 |
| -0.061 | 10.686 | 0.040 | 10.684 | 0.040 | 10.687 | 0.040 | 10.687 | 0.040 |
| 0.041 | 10.682 | 0.034 | 10.681 | 0.034 | 10.683 | 0.034 | 10.684 | 0.034 |
| 0.144 | 10.680 | 0.030 | 10.678 | 0.030 | 10.681 | 0.029 | 10.682 | 0.030 |
| 0.246 | 10.681 | 0.028 | 10.679 | 0.029 | 10.682 | 0.028 | 10.683 | 0.028 |
| 0.349 | 10.683 | 0.029 | 10.681 | 0.029 | 10.684 | 0.029 | 10.684 | 0.029 |
| 0.451 | 10.679 | 0.029 | 10.677 | 0.029 | 10.680 | 0.029 | 10.681 | 0.029 |

Coherently with the theoretical results, Table 1 shows that the standard deviations are negligible with respect to the mean values, which are always very close to each other regardless the value of $\delta$. This implies that harmonics did not significantly affect the accuracy of the *ENOB* estimates provided by the 3PSF and the 4PSF algorithms. Moreover, it is worth noticing that the maximum relative difference between the experimental standard deviations and the values returned by (30) when $E[\hat{r}_{rms}^2]$ and $std[\hat{r}_{rms}^2]$ are determined from the acquired data, is less than 0.39% for all the considered algorithms.

The mean and the standard deviation values of the *ENOB* estimates returned by the considered sine-fitting algorithms are reported in Table 2 for different values of the input sine-wave frequency. For each value of $\delta$, 1000 runs of $M = 1024$ samples each were performed.

Table 2. *ENOB* mean and standard deviation achieved at different frequencies by all the considered sine-fitting algorithms.

| $f_{in}$ (kHz) | FSF-IpDFT algorithm | | FSF-EB algorithm | | 3PSF algorithm | | 4PSF algorithm | |
|---|---|---|---|---|---|---|---|---|
| | mean (bits) | std. dev. (bits) | mean (bits) | std. dev. (bits) | mean (bits) | std. dev. (bits) | mean (bits) | std. dev. (bits) |
| 3.1 | 10.837 | 0.031 | 10.836 | 0.031 | 10.837 | 0.031 | 10.838 | 0.031 |
| 7.9 | 10.790 | 0.031 | 10.789 | 0.031 | 10.791 | 0.031 | 10.792 | 0.031 |
| 12.3 | 10.699 | 0.033 | 10.698 | 0.033 | 10.699 | 0.033 | 10.700 | 0.033 |
| 17.5 | 10.544 | 0.030 | 10.543 | 0.030 | 10.544 | 0.030 | 10.545 | 0.030 |
| 22.1 | 10.391 | 0.021 | 10.390 | 0.021 | 10.391 | 0.021 | 10.391 | 0.021 |
| 26.7 | 10.264 | 0.021 | 10.263 | 0.021 | 10.264 | 0.021 | 10.265 | 0.021 |

As expected from the theoretical results, the standard deviation is much smaller than the mean value and, at each considered frequency, all the achieved results are very close to each other. This implies that the effect of harmonics on the *ENOB* estimates provided by the 3PSF and the 4PSF algorithms is negligible. The maximum relative difference between the experimental standard deviation and the value returned by (30) is less than 0.40% for all sine-fitting algorithms.

## 2.4. CONTRIBUTIONS TO SYNCHROPHASOR MEASUREMENT FIELD

My contributions to the Synchrophasor Measurement field are on the phasor estimation by the Discrete Fourier Transform (DFT) algorithm at off-nominal frequency in transient conditions in the absence or presence of the decaying dc offset component in the electrical signal and on the synchrophasor estimation by frequency-domain and time-domain algorithms under steady state, dynamic, and transient conditions. The above conditions comply with the IEEE Standard C37.118.1-2011 about synchrophasor measurements for power systems. In the following my most important contributions in both above research directions are presented.

### 2.4.1. DFT PHASOR ESTIMATOR IN TRANSIENTS CONDITIONS

In power system networks protective relays are required to identify any disturbance occurring in transmission lines. For this purpose the fundamental frequency component is usually extracted by removing all the unwanted components by means of suitable filtering algorithms. Several algorithms have been proposed in the scientific literature to this aim [Phadke 09], [Benmouyal 95], [Gu 00], [Sidhu 03], [Guo 03], [Kang 09], [Yu 06]. Among them, the most popular one is the DFT, which provides an accurate estimate of the phasor of the fundamental component when applied to a steady-state periodic signal coherently sampled. A thorough analysis of the behaviour of the DFT Phasor Estimator (DFT-PE) during transients is very important since it provide useful and prompt information about the effect of a disturbance on the analyzed power system signal. In [Petri 11], we performed such analysis, which was not available before in the scientific literature. In that work a closed form expression of the full-cycle DFT-PE was derived in the case when the observation interval contains both an instantaneous variation in the fundamental component amplitude and/or phase, and a decaying dc offset. The accuracy of all the derived expressions was extensively verified by means of computer simulations. The achieved results are presented in the following.

When an instantaneous disturbance occurs, the analyzed power system signal $x(n)$ can be modeled as [Bertocco 92]:

$$x(n) = \begin{cases} x_{pre}(n), & if \quad n \le S-1 \\ x_{post}(n), & if \quad n \ge S \end{cases} \tag{1}$$

in which $S$ represents the disturbance time, while $x_{pre}(\cdot)$ and $x_{post}(\cdot)$ are respectively the pre- and post-disturbance segments of the signal.

We assume that the pre-disturbance segment $x_{pre}(\cdot)$ contains only the fundamental frequency component, characterized by amplitude $A_1$ and phase $\alpha_1$, and that the observation interval contains exactly one signal period. Thus we have:

$$x_{pre}(n) = \sqrt{2}\, A_1 \cos\left(\frac{2\pi}{N} n + \alpha_1\right), \quad n = 0,1,2,\ldots,S-1 \tag{2}$$

where $N$ represents the number of analyzed samples.

The post-disturbance segment of the signal $x_{post}(\cdot)$ can be expressed as [Benmouyal 95], [Gu 00], [Sidhu 03], [Guo 03]:

$$x_{post}(n) = x_{pre}(n) + x_{chg}(n) + x_{dc}(n), \;\; n = S, S+1, S+2, \ldots \tag{3}$$

where $x_{chg}$ $(\cdot)$ represents an instantaneous change in the fundamental component amplitude and/or phase, while $x_{dc}(\cdot)$ is a decaying dc offset. Since the decaying dc offset exhibits a relatively wideband spectrum, it provides a significant contribution to the DFT-PE uncertainty. Conversely, signal harmonics do not affect the DFT-PE because of the coherent sampling assumption. As a consequence, they are not considered in the following.
We can model the different component in (3) as follows:

$$x_{chg}(n) = \sqrt{2}\, B_1 \cos\left(\frac{2\pi}{N} n + \beta_1\right), \quad n = S, S+1, S+2, \ldots \tag{4}$$

and [Gu 00]:

$$x_{dc}(n) = A_0\, e^{-\frac{n-S}{\tau N}} = A_0\, \Gamma^{-\frac{n-S}{N}}, \quad n = S, S+1, S+2, \ldots \tag{5}$$

in which $B_1$ and $\beta_1$ are the amplitude and the phase of the fundamental component change, while $A_0$ and $\tau$ are respectively the amplitude and the time constant of the decaying dc offset. For the convenience of notation, this latter quantity is expressed as a pure number representing a fraction of the sine-wave period and we define $\Gamma = \exp(1/\tau)$.
It is well-known that the full-cycle DTF-PE of a signal $x(\cdot)$ evaluated over a sliding observation window containing the samples $x(r), \ldots, x(r+N-1)$ is given by [Phadke 09]:

$$\hat{X}(r) = \frac{\sqrt{2}}{N} \sum_{n=0}^{N-1} x(r+n)\, e^{-j\frac{2\pi}{N}n}. \tag{6}$$

The behaviour of the estimator (6) when a disturbance occurs during or before the observation interval was analyzed.

• *Disturbance during the observation interval*
In this case the disturbance time $S$ falls within the observation interval (that is $r \le S \le N + r - 1$). Using (3) and the linearity of the DFT, we obtain:

$$\hat{X}(r) = X_{pre}(r) + X_{chg}(r) + X_{dc}(r) = X(r) + X_t(r) + X_i(r) + X_{dc}(r), \tag{7}$$

where the components of $\hat{X}(\cdot)$, calculated also in [Petri 11], are the followings:

$X(\cdot)$ is the post-disturbance steady-state component of the estimator:

$$X(r) = A_1 e^{j\left(\alpha_1 + \frac{2\pi r}{N}\right)} + B_1 e^{j\left(\beta_1 + \frac{2\pi r}{N}\right)} \stackrel{\Delta}{=} C_1 e^{j\left(\gamma_1 + \frac{2\pi r}{N}\right)} \tag{8}$$

$X_t(\cdot)$ is a transient signal due to the variation of the fundamental component parameters:

$$X_t(r) = -\frac{S-r}{N} B_1 e^{j\left(\beta_1 + \frac{2\pi r}{N}\right)}, \quad r = S - N + 1, \ldots, S-1 \tag{9}$$

$X_i(\cdot)$ is a transient signal rising because of the spectral interference due to the variation of the image component parameters [Bertocco 92]:

$$X_i(r) = \frac{B_1}{N} e^{-j\left(\beta_1 + \frac{2\pi r}{N}\right)} e^{-j\frac{2\pi}{N}(S-r-1)} D_{N-S+r}\left[\frac{2(N-S+r)}{N}\right], \qquad r = S - N + 1, \ldots, S-1 \tag{10}$$

where:

$$D_M(\lambda) = \frac{\sin(\pi\lambda)}{\sin\left(\frac{\pi\lambda}{M}\right)}, \tag{11}$$

is the Dirichlet kernel evaluated on a $M$-samples window, and

$X_{dc}(\cdot)$, is the transform of the decaying dc offset:

$$X_{dc}(r) = \frac{\sqrt{2}A_0}{N} e^{-j\frac{2\pi}{N}(S-r)} \frac{1 - \left(\Gamma^{-\frac{1}{N}} e^{-j\frac{2\pi}{N}}\right)^{N-S+r}}{1 - \Gamma^{-\frac{1}{N}} e^{-j\frac{2\pi}{N}}}, \qquad r = S - N + 1, \ldots, S-1 \tag{12}$$

• *Disturbance before the observation interval*

When the observation interval contains only post-disturbance samples (that is $S \le r$), the linearity of the DFT provides:

$$\hat{X}(r) = X(r) + X_{dc}(r), \tag{13}$$

where $X(\cdot)$ is given by (8) and $X_{dc}(\cdot)$, was also calculated in [Petri 11], and it is given by:

$$X_{dc}(r) = \frac{\sqrt{2}A_0}{N} \Gamma^{-\frac{r-S}{N}} \frac{1 - \Gamma^{-1}}{1 - \Gamma^{-\frac{1}{N}} e^{-j\frac{2\pi}{N}}}, \qquad r \ge S \tag{14}$$

is the transform of the decaying dc offset.

From the above results, we determine the relative estimation error in the phasor amplitude as:

$$e_a(r) = \frac{\left|\hat{X}(r)\right| - \left|X(r)\right|}{\left|X(r)\right|}, \tag{15}$$

where $X(\cdot)$ is given by (8).

Similarly, the estimation error in the phasor angle is determined as:

$$e_\phi(r) = \arg[\hat{X}(r)] - \arg[X(r)]. \tag{16}$$

Due to the terms $X_t(r)$ and $X_i(r)$ and the fact that the module of $X_{dc}(r)$ returned by (12) is higher than the module of (14) we can conclude that, in general, the magnitudes of the errors in the estimated phasor amplitude and angle are greater when the disturbance occurs during the observation interval.
In particular, using expressions (9), (10), and (12) the maximum value $e_{a\_max}(r)$ of the phasor amplitude error can be written as:

$$e_{a\_\max}(r) = \begin{cases} p_1 e_t(r) + p_1 e_i(r) + p_0 e_{dc}(r), & \text{if } r \le S-1 \\ p_0 e_{dc}(r), & \text{if } r \ge S \end{cases} \tag{17}$$

where $p_0 = \sqrt{2}A_0 / C_1$ and $p_1 = B_1/C_1$ represent, respectively, the dc-offset amplitude and the sine-wave amplitude variation as a fraction of the post-disturbance phasor amplitude.
In (17) we have:

$$e_t(r) = \frac{S-r}{N}, \tag{18}$$

which is due to the change in the fundamental component parameters,

$$e_i(r) = \frac{1}{N}\left|D_{N-S+r}\left[\frac{2(N-S+r)}{N}\right]\right|, \tag{19}$$

which is related to the spectral interference from the image component,

$$e_{dc}(r) = \begin{cases} \dfrac{1}{N}\dfrac{\left|1-\left(\Gamma^{-\frac{1}{N}}e^{-j\frac{2\pi}{N}}\right)^{N-S+r}\right|}{\left|1-\Gamma^{-\frac{1}{N}}e^{-j\frac{2\pi}{N}}\right|}, & \text{if } r \le S-1 \\ \dfrac{1}{N}\Gamma^{-\frac{r-S}{N}}\dfrac{1-\Gamma^{-1}}{\left|1-\Gamma^{-\frac{1}{N}}e^{-j\frac{2\pi}{N}}\right|}, & \text{if } r \ge S \end{cases} \tag{20}$$

which is due to the decaying dc offset.

Fig. 1 shows the behavior of the three components $e_t(r)$, $e_i(r)$ (Fig. 1(a)) and $e_{dc}(r)$ (Fig. 1(b)) as a function of $(r - N)$ for $N = 48$ and $S = 70$. In Fig. 1(b) different values of the time constant $\tau$ of the decaying dc offset were considered.

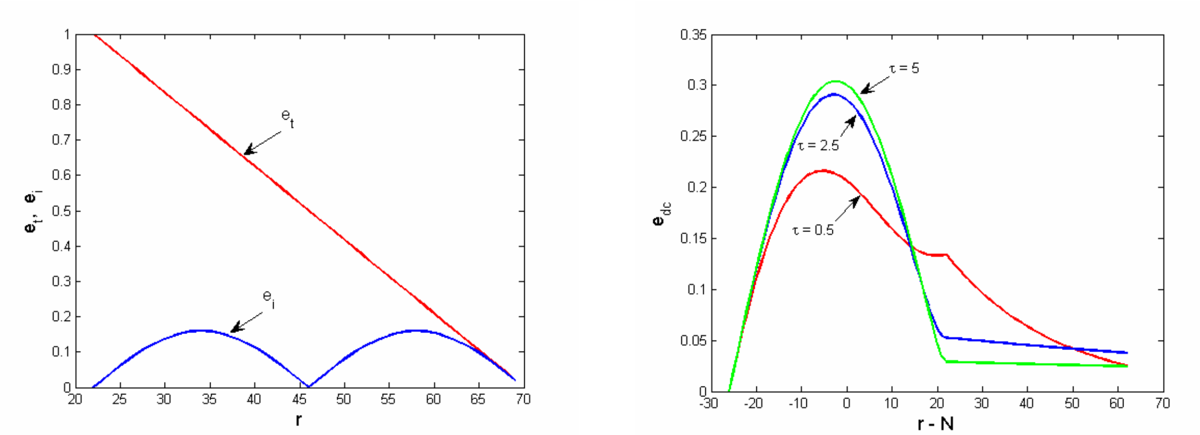


Fig. 1. (a) Components $e_t(r)$, $e_i(r)$ and (b) $e_{dc}(r)$ of the estimation error versus $(r - N)$. The component $e_{dc}(r)$ is shown for different values of the time constant $\tau$ of the decaying dc offset. The number of analyzed samples was $N = 48$.

As we can see, the components $e_t(r)$ and $e_i(r)$ exhibit a linear and sinusoidal behavior, respectively. In particular, at the beginning of the transient $e_t(r)$ is almost equal to one, while it approaches zero at the end of the transient (that is when $r$ is close to $S - 1$).

Conversely, the behavior of $e_i(r)$ is dominated by the sine function at the numerator of (11) and reaches a maximum value close to $1/(2\pi)$ when the disturbance falls on one-fourth or three-fourth of the observation window (that is when $r$ is equal to $S - 3N/4$ or $S - N/4$). Also, $e_i(r)$ is equal to zero when $r = S - N/2$.

Fig. 1(b) shows that the maximum of $e_{dc}(r)$ increases as the time constant $\tau$ increases. Indeed, from (20) we achieve that such a maximum is about $(1+\Gamma^{-1/2})/(2\pi)$ and occurs when the disturbance is close to the middle of the observation window (that is when $r$ is about $S - N/2$). Moreover, for $r \geq S$ the component $e_{dc}(r)$ exhibits an exponential behavior with a decaying rate that decreases for increasing values of the time constant $\tau$.

In Fig. 2 the behavior of the components $e_t(r)$, $e_i(r)$, and $e_{dc}(r)$ is depicted as a function of $r$ for $N = 24$, 48, and 96. The values of the disturbance time $S$, corresponding to the above values of $N$, were 46, 70, and 118, respectively.

From the simulation results it follows that the number of analyzed samples $N$ almost does not affect the behavior of $e_t(r)$, $e_i(r)$, and $e_{dc}(r)$. Indeed different values of $N$ act on these components almost as a time scale factor, that is as an expansion or a compression of the horizontal axis.

Finally, it is worth noticing that the worst-case error $e_{a\_max}(r)$ is proportional to the relative magnitudes of the sine-wave amplitude variation $p_1$ and of the dc-offset $p_0$, as clearly shown by (17). Thus, it is reversely proportional to the amplitude of the steady-state signal $C_1$. As a consequence, the magnitude of $e_{a\_max}$ tends to be smaller when an overvoltage occurs, while it is typically larger in the case of a voltage dip. In any case, the estimation error during transients can be very high.

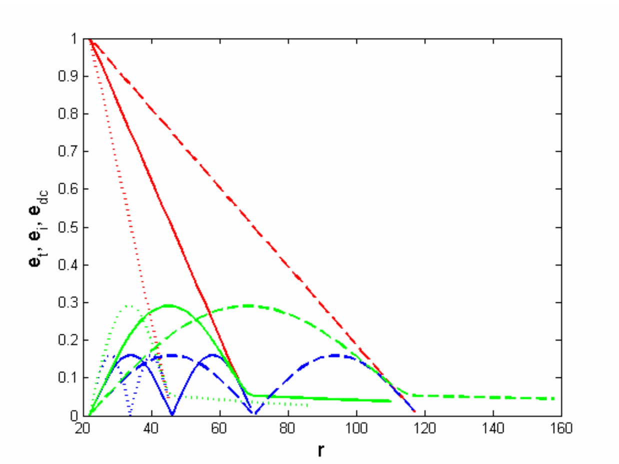


Fig. 2. Components $e_t(r)$, $e_i(r)$, and $e_{dc}(r)$ versus $r$ for $N = 24$ (dotted line), $N = 48$ (continue line), and $N = 96$ (dashed line). The corresponding values of the disturbance time $S$ were equal to 46, 70, and 118, respectively.

The DFT-PE transient behaviour and the accuracy of the expressions derived above were verified by means of computer simulations. For this purpose the amplitudes of the components $x_{pre}(\cdot)$ and $x_{chg}(\cdot)$ were $A_1 = 1/\sqrt{2}$ p.u. and $B_1 = 0.4/\sqrt{2}$ p.u., respectively (thus an overvoltage of 40% was considered). Moreover, the phases of the two sine-waves were $\alpha_1 = \beta_1 = \pi/3$ rad. The time constant of the decaying dc offset $\tau$ was chosen equal to 2.5 sine-wave cycles. The number of analyzed samples was $N = 48$ and the disturbance occurred at the sample $S = 70$. The value of $r$ was varied starting from 1 with a step 1.

The estimated phasor amplitude and phase are shown in Figs. 3(a) and 3(b) as a function of $(r - N)$. Different values of the amplitude $A_0$ of the decaying dc offset are considered. Both simulation results and the values returned by the expressions (7)-(14) are reported for comparison. As we can see, the agreement is very good.

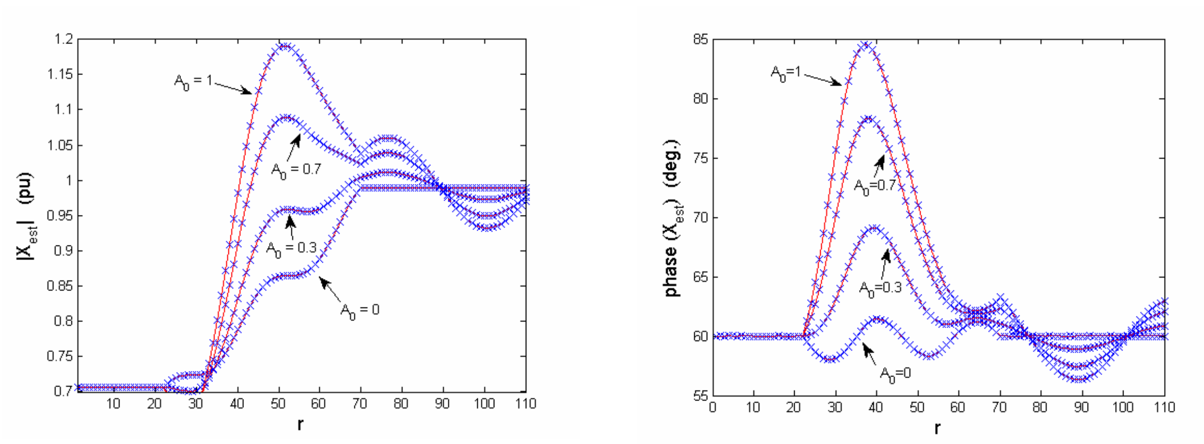


(a) (b)

Fig. 3. (a) Phasor amplitude and (b) phase versus $(r - N)$ for different values of the dc-offset component amplitude $A_0$. The number of analyzed samples was $N = 48$. The theoretical results are represented by continue lines, while the simulation results are marked with crosses.

It is obvious from Fig. 3 that a large error may occur when the values returned by the DFT-PE during a transient are used to estimate the phasor of the steady-state signal. Also, when the observation

interval contains only post-disturbance samples, the DFT-PE error decreases with the amplitude $A_0$ of the decaying dc offset, as expected.
Moreover Fig. 3 shows that the knowledge of the behavior of the phasor amplitude estimator during a transient let us appreciate whether the post-disturbance signal contains or not a significant dc-offset.
The estimated phasor amplitude and phase achieved by considering the same parameters used in Fig. 3 except $N = 96$ are shown in Fig. 4. Notice that only the curves provided by the expressions (7)-(14) are reported since the simulation results fully agree with them.

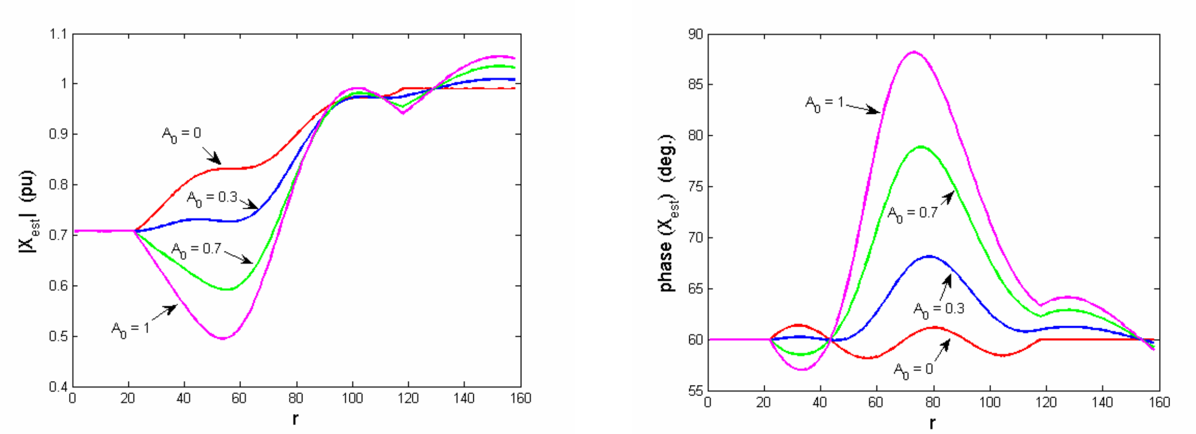


(a) (b)

Fig. 4. (a) Phasor amplitude and (b) phase achieved using the theoretical expressions (7)-(14) versus $(r - N)$ for different values of the dc-offset component amplitude $A_0$. The number of analyzed samples was $N = 96$.

It is clear that the conclusions about the DFT-PE transient behaviour that we can drawn from Fig. 4 are the same as in Fig. 3.
It should be noted that many other simulations were performed considering either an overvoltage or a voltage dip and different values of signal phases and $N$. Behaviors fully coherent with those reported in Figs. 3 and 4 were always achieved.

In [Belega 11c], we analyzed through both computer simulations and experimental results the effect of harmonics and wideband noise on the accuracy of the phasor estimator provided by the DFT-based algorithm proposed in [Yang 00], at off-nominal frequency when a decaying dc offset component is either absent or present in the acquired electrical signal. That analysis, which was not performed before in the scientific literature, is presented in the following.
The electrical signal was modelled as:

$$x(t) = s(t) + d(t) = \sqrt{2}A_1 \cos(2\pi f_{in} t + \alpha_1) + A_0 e^{-\frac{t}{\tau}}, \tag{21}$$

where $s(\cdot)$ is the fundamental frequency component and $d(\cdot)$ is a decaying dc offset. The signal $s(\cdot)$ is characterized by rms value $A_1$, input frequency $f_{in}$, and phase $\alpha_1$. The signal $d(\cdot)$ is described by amplitude $A_0$ and time constant $\tau$. Generally, the input frequency $f_{in}$ differs from the nominal frequency $f_0$ (which is either 50 Hz or 60 Hz) by a relative error $\delta$, that is $f_{in} = (1+\delta)f_0$. By sampling the fault signal at frequency $f_s = Nf_0$, the following discrete-time signal is achieved:

$$x(n) = s(n) + d(n) = \sqrt{2}A_1 \cos\left(2\pi \frac{1+\delta}{N} n + \alpha_1\right) + A_0 \Gamma^{-\frac{n}{N}}, \tag{22}$$

where $\Gamma = \exp(N/(\tau f_s))$.

The DFT of the record $x(r)$, $x(r+1)$,…, $x(r+N-1)$ taken from the signal (22) and evaluated at the nominal frequency is given by:

$$X_r = \sum_{n=0}^{N-1} x(n+r) e^{-j\frac{2\pi}{N}n} = \sum_{n=0}^{N-1} s(n+r) e^{-j\frac{2\pi}{N}n} + \sum_{n=0}^{N-1} d(n+r) e^{-j\frac{2\pi}{N}n} = S_r + D_r, \quad r \geq 0 \tag{23}$$

where $S_r$ and $D_r$ are the DFTs of the components $s(\cdot)$ and $d(\cdot)$, respectively, and 0 is the time instant at which the fault occurs.

After some calculations we obtain:

$$S_r = \frac{\sqrt{2}}{2} A_1 e^{j\alpha_1} e^{j\frac{2\pi r}{N}(1+\delta)} e^{j\pi\frac{N-1}{N}\delta} K_N(-\delta) + \frac{\sqrt{2}}{2} A_1 e^{-j\alpha_1} e^{-j\frac{2\pi r}{N}(1+\delta)} e^{-j\pi\frac{N-1}{N}(2+\delta)} K_N(2+\delta), \tag{24}$$

in which $K_N(\cdot)$ is the Dirichlet kernel, given by (11)

and

$$D_r = A_0 \Gamma^{-\frac{r}{N}} G(\Gamma), \tag{25}$$

where $G(\Gamma) = \dfrac{1-\Gamma^{-1}}{1-\Gamma^{-\frac{1}{N}} e^{-j\frac{2\pi}{N}}}$.

By the DFT-based algorithm proposed in [Yang 00] we can determine the values of $\delta$, $A_1$, $\alpha_1$, and $A_0$, by means of the DFTs $X_r$, $X_{r+1}$, $X_{r+2}$, $X_{r+3}$, and $X_{r+4}$ ($N + 4$ samples from the fault signal are acquired). In particular, when the acquired signal $x(\cdot)$ does not contain the decaying dc offset $d(\cdot)$, only the DFT outputs $X_r$, $X_{r+1}$, and $X_{r+2}$ must be calculated ($N + 2$ samples must be acquired).

We analyzed the sensitivity of the DFT-based algorithm to harmonics and wideband noise by means of computer simulations. In particular, the minimum, the maximum, and the mean values of the estimated phasor amplitude and angle were derived when a decaying dc offset component is either absent or present in the input signal.

In all the simulations discussed in the following the fundamental frequency component of the signal (22) was characterized by rms value $A_1 = 1/\sqrt{2}$ p.u. and phase $\alpha_1 = \pi/3$ rad. The length of the processed records was $N = 32$.

• *Effect of Harmonics*

The effect of the harmonics on the phasor estimator accuracy was analyzed by adding to the signal (22) the following four harmonics components:

$$h(t) = \sum_{h=2}^{5} \frac{1}{h \cdot p} \cos(2\pi h f_{in} t + \phi_h), \tag{26}$$

The parameter $p$ was changed in order to obtain a given value for the Total Harmonic Distortion ratio (*THD*), while the harmonic phases $\phi_h$, $h = 2, 3, 4, 5$, were chosen at random in the range $[0, 2\pi)$ rad.
Fig. 5 shows the results achieved for the estimated phasor amplitude (Fig. 5(a)) and phase (Fig. 5(b)) as a function of $\delta$ for $THD = -40$ dB in the absence and in the presence of the decaying dc offset, respectively. The parameters of the decaying dc offset were $A_0 = 1$ p.u. and $\tau = 0.05$. The relative frequency error $\delta$ was varied in the range $[-0.1, 0.1]$ with a step of 0.01. The time instant $r$ was set to 19. For each value of $\delta$, 1000 runs were performed and the minimum, the maximum, and the mean values of the estimated phasor amplitude and phase were determined.

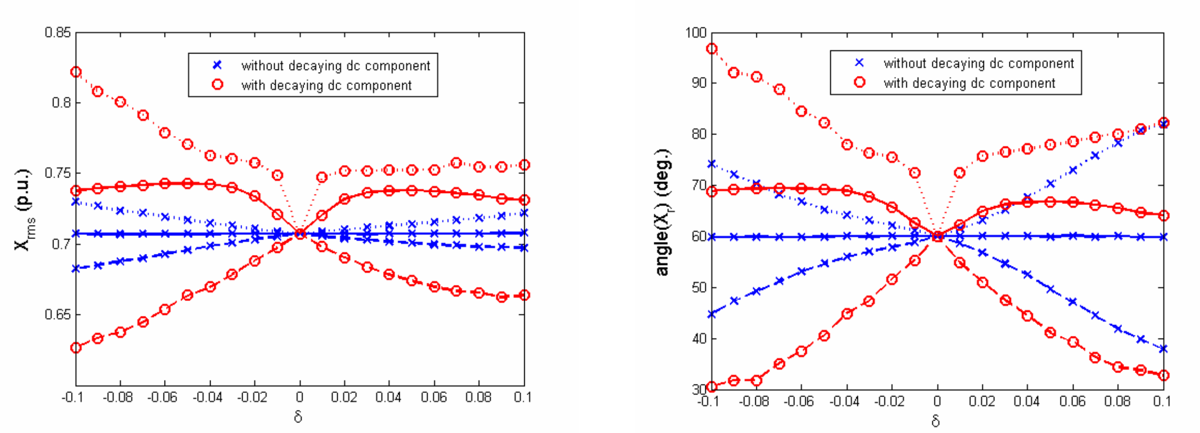


(a) (b)

Fig. 5. Minimum (dashed line), maximum (dotted line), and mean (solid line) values of the estimated phasor (a) amplitude and (b) phase versus $\delta$ for a signal corrupted by harmonics with *THD* = -40 dB and $r = 19$.

Fig. 5 shows that when the signal does not contain the decaying dc offset the estimator bias is negligible, that is, the mean values are almost equal to the true value. Also, the phasor estimation error increases with the magnitude of $\delta$. In particular, the magnitude of the phasor amplitude error is smaller than 1% for $|\delta| \leq 0.03$, while the magnitude of the phasor phase absolute error is smaller than 3.2 deg. for $|\delta| \leq 0.02$. Moreover, the accuracy of the estimated phasor parameters heavily decreases when the decaying dc offset is present and accurate estimates are achieved only for values of $\delta$ very close to zero.
Fig. 6 shows the same parameters as in Fig. 5, but as a function of the first sample of the acquired record $r$, and considering for the frequency error $\delta$ a value near the middle of the range considered in the IEEE Standard C37.118.1-2011 [Std. C37.118.1], that is $\delta = 0.06$. The time instant $r$ was varied with a step of 1 and the results were achieved using the same procedure as in the previous figure.
It can be seen in Fig. 6 that the estimation error is quite small when decaying dc component is absent. Conversely, during transients this error is quite high and the mean value of the estimated phasor parameters exhibits an oscillating behavior over time.

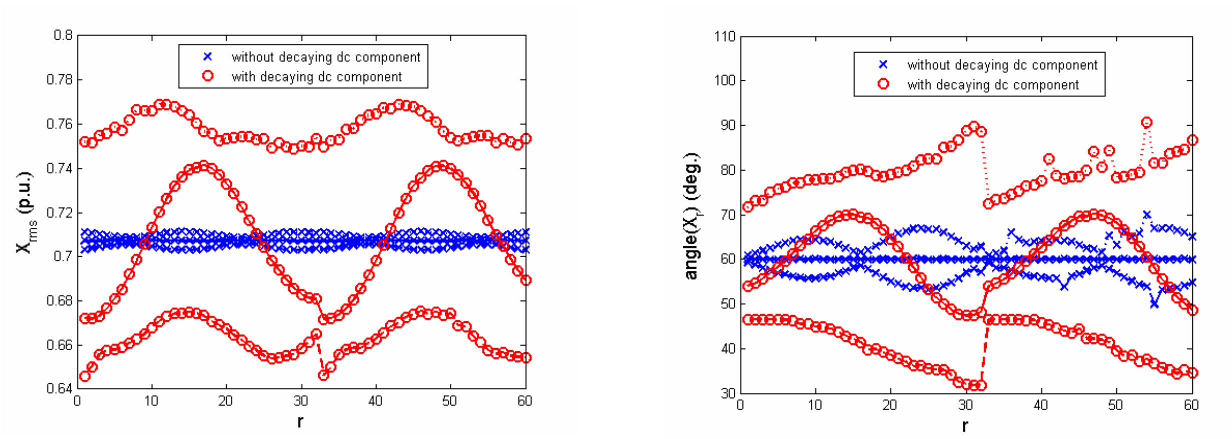


(a) (b)

Fig. 6. Minimum (dashed line), maximum (dotted line), and mean (solid line) values of the estimated phasor (a) amplitude and (b) phase versus $r$ for a signal corrupted by harmonics with $THD$ = -40 dB and $\delta$ = 0.06.

Many other simulations were performed for different values of $r$, $\delta$, and $THD$ values. In all situations behaviors similar to those reported in Figs. 5 and 6 were always achieved. In particular, simulations showed that the accuracy of the estimated phasor parameters decreases as $THD$ and decaying dc offset amplitude $A_0$ increases. Thus, when transients occur, the analyzed algorithm exhibits a high sensitivity to harmonic distortion.

• *Effect of Wideband Noise*

In order to model common real-life situations, we assume that a Gaussian white noise with zero mean and standard deviation $\sigma_n$ is superimposed to the signal (22). Thus, the Signal-to-Noise Ratio ($SNR$) associated to the signal (22) is defined as $SNR = 20\log_{10}(A_1/\sqrt{2}\sigma_n)$ dB. It is known that $SNR$ of power signals usually varies between 50 and 70 dB [Sidhu 99].

The phasor amplitudes and phases estimated when the signal (22) does not contains the decaying dc offset are shown in Fig. 7 as a function of $\delta$, for $SNR$ = 55 dB. The relative error δ was varied in the range [–0.1, 0.1] with a step of 0.01. The time instant $r$ was set to 16. For each value of $\delta$, 1000 runs were performed and the minimum, the maximum, and the mean values of the estimated phasor amplitude and phase were determined.

In the absence of the decaying dc component, similarly to Fig. 5, the phasor estimator bias is negligible. Phasor amplitude error of magnitude smaller than 1% and phasor angle absolute error of magnitude smaller than 3 deg. were achieved for all values of $\delta$. Conversely, the phasor parameters cannot be accurately estimated in transient conditions.

The same parameters analyzed in Fig. 7 are depicted also in Fig. 8, but as a function of $r$, when $SNR$ = 50 dB and $\delta$ = 0.06.

Fig. 8 clearly shows that the estimation error is small in steady state conditions. Conversely, in the presence of decaying dc offset, the estimated phasor parameters mean values exhibit an oscillating behavior over time and the minimum and maximum values are quite different from the corresponding true values. Thus, large estimation errors occur.

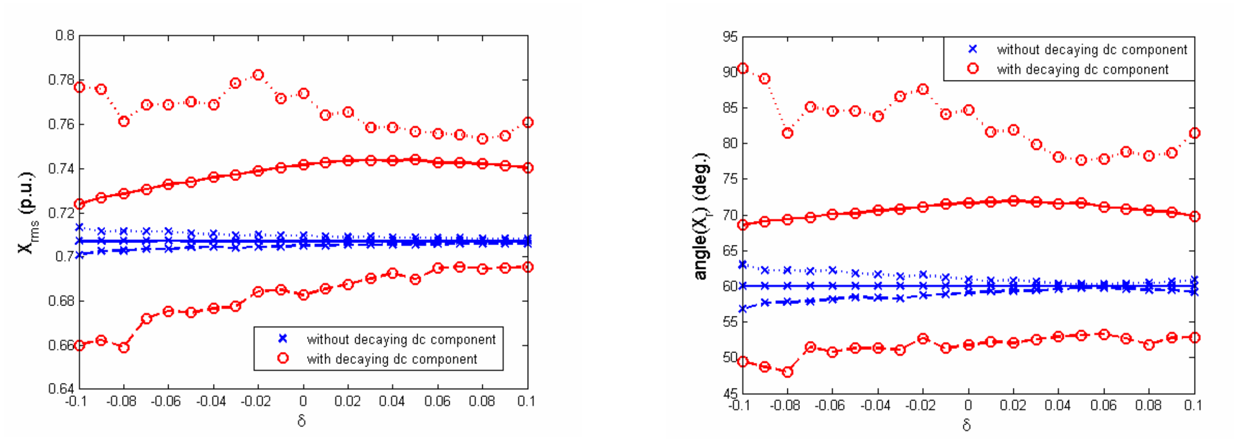


(a) (b)

Fig. 7. Minimum (dashed line), maximum (dotted line), and mean (solid line) values of the estimated phasor (a) amplitude and (b) phase versus $\delta$ for a signal corrupted by wideband noise with $SNR$ = 55 dB and $r$ = 16.

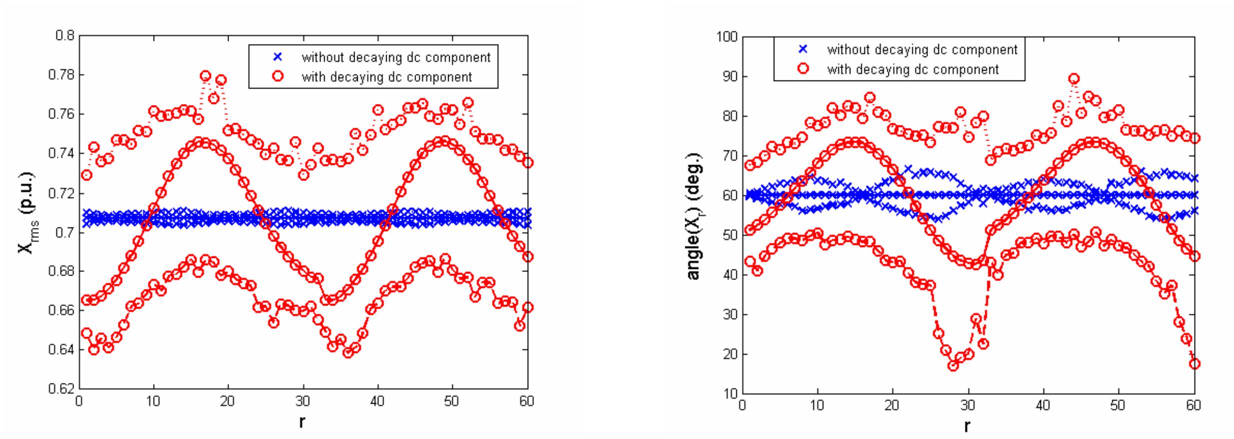


(a) (b)

Fig. 8. Minimum (dashed line), maximum (dotted line), and mean (solid line) values of the estimated phasor (a) amplitude and (b) phase versus $r$ for a signal corrupted by wideband noise with $SNR$ = 50 dB and $\delta$ = 0.06.

Many other simulations were performed for different values of $r$, $\delta$, and $SNR$ values. In all situations behaviors similar to those reported in Figs. 7 and 8 were always achieved. In particular, simulations showed that the accuracy of the estimated phasor parameters decreases as $SNR$ and decaying dc offset amplitude $A_0$ increases.

Thus, we can conclude that, when transients occur, the analyzed algorithm exhibits a quite high sensitivity to both harmonic distortion and wideband noise.

Moreover, we experimentally analyzed the influence of both harmonics and wideband noise on the accuracy of the phasor estimator provided by the above specified algorithm. Since the signal phase changed during subsequent acquisitions only the accuracy of the estimated phasor amplitude was considered.

The input signals were provided by two signals generators, a TG315 and an Agilent 33220A. The TG315 was employed for the generation of both high purity ($THD \cong$ -47 dB) and harmonically distorted ($THD \cong$ -21 dB) sine-waves. The latter signals were asymmetrically sine-waves. Conversely, the Agilent 33220A was employed for the generation of noise and decaying dc offset. The two generated signals were added by using a passive adder, composed of three 50 Ω resistances.

The obtained signals were acquired by using a 12-bit data acquisition board NI-6023E. The full-scale range (*FSR*) and the sampling frequency were set to 10 V and 2 kHz, respectively. The number of samples used in the DFT-based phasor estimator was $N = 40$.

• *Effect of Harmonics*

The minimum, the maximum, and the mean value of the estimated phasor amplitudes when the input signal does not contains the decaying dc offset are shown in Fig. 9 as a function of $r$, in the case of harmonically distorted sine-waves. The relative error $\delta$ was about 0.06 (that is the signal frequency was 53 Hz) and the *THD* was close to −21 dB.

The results achieved by considering high purity sine-waves at the nominal frequency of 50 Hz (that is when the value of the relative frequency error $\delta$ is very close to zero) are also reported in Fig. 9 as a reference. The amplitude of the signals was set to 1 V. For each considered signal, 1000 runs of 200 samples each were acquired.

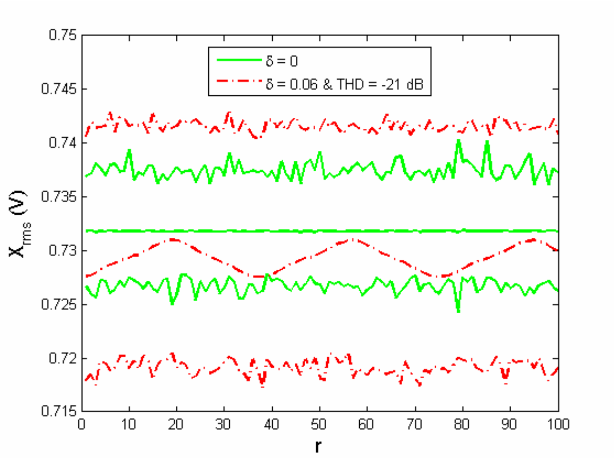


Fig. 9. Minimum, maximum, and mean values of the estimated phasor amplitude versus $r$ for a signal corrupetd by harmonics ($THD \cong -21$ dB). The relative frequency error $\delta$ was set to about 0.00 and 0.06.

Fig. 9 shows that harmonics reduces the accuracy of the estimated phasor amplitude. In the considered set-up the deviations from the mean value achieved at the nominal frequency reach a magnitude of about 2%.

The value of the estimated phasor amplitude when the signal contains a decaying dc offset component is reported in Fig. 10 as a function of $r$. Both high purity and harmonically distorted sine-waves are considered. The relative frequency error $\delta$ is 0.06. The results achieved when acquiring a sine-wave at the nominal frequency and without decaying dc offset are also reported as a reference. The amplitudes of both generated sine-waves and decaying dc offset were set to 2 V. The time constant $\tau$ was about 16.7 ms. The value of $r$ was varied with a step of 1 and, for each considered signal 400 samples were acquired. The data processing started by the first sample in which the decaying dc offset occurs, which was considered as the fault time.

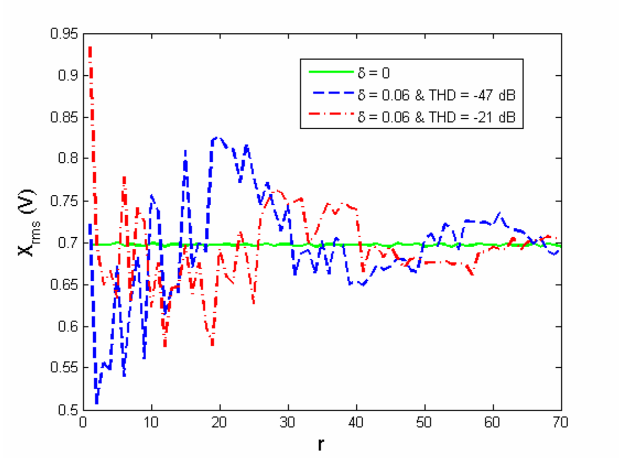


Fig. 10. Estimated phasor amplitude of signals with decaying dc offset versus $r$ for a relative frequency error $\delta=$ 0.06. Both high purity ($THD \cong -47$ dB) and harmonically distorted ($THD \cong -21$ dB) sine-waves are considered. Estimated phasor amplitude for high purity sine-waves at nominal frequency ($\delta = 0$) is depicted as a reference.

Fig. 10 clearly shows that the presence of decaying dc offset strongly reduces the accuracy of the estimated phasor amplitude, especially for records close to the fault time. The maximum magnitude of the difference between the estimated amplitudes and the value achieved for a high purity sine-wave at nominal frequency is reached for $r = 1$ and it is equal to 33.9% in the presence of harmonics distortion and to 27.2% for sine-waves. After a full sine-wave cycle from the fault time this difference reduces to 5.1% when harmonics occur and to 6.8% for sine-waves. So, the effect of decaying dc offset on the estimation accuracy is most important.

• *Effect of Wideband Noise*

Fig. 11 shows the behavior of the minimum, the maximum, and the mean values of the estimated phasor amplitude as a function of $r$ when a steady state signal is corrupted by Gaussian noise with zero mean and amplitude 200 mV. Both high purity and harmonically distorted sine-waves are considered. The relative frequency error $\delta$ is 0.06. Also the results achieved for a sine-wave at the nominal frequency are reported as a reference. The value of $r$ was varied with a step of 1 and, for each signal, 1000 runs of 200 samples each were acquired.

As Fig. 11 shows, the effect of wideband noise on the obtained results is quite small. In the presence of both harmonics and noise, the magnitude of the difference between the estimated amplitudes and the value achieved for a high purity sine-wave at nominal frequency is about 2.6%.

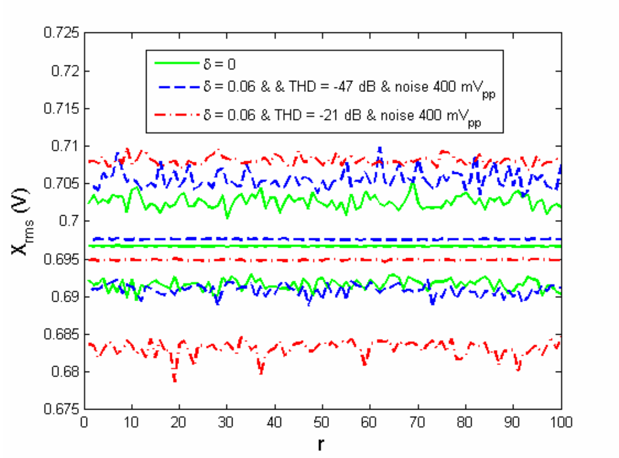


Fig. 11. Minimum, maximum, and mean values of the estimated phasor amplitude of signals without decaying dc offset versus $r$ for a relative frequency error $\delta = 0.06$. Both high purity ($THD \cong -47$ dB) and harmonically distorted ($THD \cong -21$ dB) sine-waves are considered. Estimated phasor amplitude for high purity sine-waves at nominal frequency ($\delta = 0$) is depicted as a reference.

### 2.4.2. SYNCHROPHASOR ESTIMATION BY INTERPOLATED DFT ALGORITHM

The synchronized phasor (or synchrophasor) represents the amplitude and the phase of an electric sine-wave signal at nominal frequency determined at instants defined by the Universal Coordinated Time (UTC). Hence, its knowledge is very useful for monitoring, protection, and control applications in power networks. The IEEE C37.118.1-2011 Standard [Std. C37.118.1] (called simply Standard in the following for the sake of notation) has been specifically developed for assessing the performances of Phasor Measurement Units (PMUs). According to the Standard, these units sample the electric signal and apply suitable algorithms to the acquired data to estimate the signal phasor exactly in the center of the observation interval. The Reporting Rate *RR* of the estimated synchrophasor should be equal to 10, 25, and 50 for 50 Hz power systems and to 10, 12, 15, 20, 30, and 60 for 60 Hz power systems.

Many algorithms for phasor estimation have been proposed in the scientific literature. They consider different observation interval lengths (half-, one-, two-, or more signal cycles) in order to optimize the trade-off between estimation accuracy and response time [Phadke 08], [Premerlani 08], [Serna 07], [Garza 10], [Garza 11], [Castello 11], [Castello 12], [Sidhu 05], [Yu 10], [Macii 12], [Roscoe 12], [Mai 10], [Barchi 13b]. Indeed, longer observation intervals allow to achieve more accurate estimates, but at the cost of a reduced system responsiveness [Castello 11], [Castello 12]. Accurate sine-wave parameter estimates can be obtained by applying the well-known Interpolated Discrete Fourier Transform (IpDFT) algorithm when at least two-signal cycles are observed. In [Belega 13c], we investigated the accuracy of synchrophasor estimators provided by the IpDFT algorithm under both steady state and dynamic conditions when two- or three-cycle length observation intervals are considered. For this purpose, the effect on the estimation accuracy of different window functions, observation interval lengths, and processed DFT samples was analyzed through computer simulations. Among the figures of merit of the adopted window the highest sidelobe peak and the sidelobe decay rate can heavily affect the accuracy of the results returned by the IpDFT algorithms. Hence, the performances obtained when using the Maximum Sidelobe Decay (MSD) or the Minimum Sidelobe Level (MSL) windows [Nutall 81] were analyzed. It is worth noticing that the IpDFT algorithm was not applied before to synchrophasor measurement. The above investigations are presented in the following.

We considered that the electric signal can be modeled by a sine-wave sampled at frequency $f_s$:

$$x(m)=\sqrt{2}A\cos\left(2\pi\frac{f_{in}}{f_s}\left(m+\frac{1}{2}\right)+\phi_0\right), \qquad m=-M/2,\ldots,M/2-1, \tag{27}$$

where $A$, $f_{in}$, and $\phi_0$ are respectively the rms value, the frequency, and the initial signal phase. The frequency $f_s$ is assumed higher than $2f_{in}$ to satisfy the Nyquist theorem. As usual, we assume that the number of acquired samples $M$ is even. Thus, the sampling instants are shifted by ½ sampling period in order to fix the time reference exactly in the center of the observation window.

The relationship between the frequencies $f_{in}$ and $f_s$ can be expressed as:

$$\frac{f_{in}}{f_s}=\frac{\nu}{M}=\frac{l+\delta}{M}, \tag{28}$$

where $l$ and $\delta$ are respectively the integer and the fractional parts of the number of acquired signal cycles $\nu$. The nominal frequency, $f_{nom}$, is assumed to be equal to 50 Hz. In particular, the performance achieved when observing either two or three-signal cycles (i.e. $l$ = 2 or $l$ = 3, respectively) will be analyzed in the following.

In order to estimate the parameters of (27) by means of the IpDFT algorithm, the signal $x(\cdot)$ is firstly multiplied by a suitable window sequence $w(\cdot)$. Windows commonly adopted belong to the cosine class, that is:

$$w(m)=\sum_{h=0}^{H-1}a_h\cos\left(\frac{2\pi h}{M}\left(m+\frac{1}{2}\right)\right), \quad m=-M/2,\ldots,M/2-1 \tag{29}$$

where $H$ is the number of window terms and $a_h$, $h = 0, \ldots, H-1$ are the window coefficients.

The DFT of the windowed signal $x_w(m) = x(m)\cdot w(m)$ is then evaluated. It can be expressed as:

$$X_w(k)=\sum_{m=-\frac{M}{2}}^{\frac{M}{2}-1}x_w(m)e^{-j2\pi\frac{k}{M}\left(m+\frac{1}{2}\right)}=\frac{A}{2}\left[W(k-\lambda_0)e^{j\phi_0}+W(k+\lambda_0)e^{-j\phi_0}\right], \qquad k=0,\ldots,M-1 \tag{30}$$

where $W(\cdot)$ is the Discrete-Time Fourier Transform (DTFT) of the window $w(\cdot)$.

The second term in the last expression of (30) represents the image component of the sine-wave signal.

After some algebra the following expression for the DTFT of the window (29) can be achieved:

$$W(\lambda)=\sum_{m=-\frac{M}{2}}^{\frac{M}{2}-1} w(m) e^{-j2\pi\frac{\lambda}{M}\left(m+\frac{1}{2}\right)}=\sin(\pi\lambda)\sum_{h=0}^{H-1}(-1)^h 0.5a_h\left[\frac{1}{\sin\frac{\pi}{M}(\lambda-h)}+\frac{1}{\sin\frac{\pi}{M}(\lambda+h)}\right], \quad \lambda\in[-M/2, M/2) \tag{31}$$

If $|\lambda| << M$, (31) can be accurately approximated by:

$$W(\lambda)=\frac{M\sin(\pi\lambda)}{\pi}\sum_{h=0}^{H-1}(-1)^h a_h\frac{\lambda}{\lambda^2-h^2}. \tag{32}$$

The IpDFT estimators for the parameters $\delta$, $A$, and $\phi_0$ of the sine-wave (27) are given in §2.2.1.B. When an MSL window is adopted, the function used to achieve the estimator for $\delta$ is approximated in least squares by a polynomial of degree seven.

When $K$-cycles of the sine-wave (27) are observed, windows of order $H \leq K$ need to be used in order to control the effect of the spectral interference due to possible signal harmonics on the phasor estimation accuracy [Offelli 92], [Belega 12a]. In particular, two- and three-term cosine windows (that is $H = 2$ or $H = 3$) provide accurate results when two- or three-signal cycles are observed, respectively. In the following the well-known two- and three-term MSD and MSL windows will be considered [Nuttall 81], which are labelled as *msd2*, *msd3, msl2*, and *msl3* windows (see §2.2.1.A).

We determined the accuracy of the synchrophasor estimator components under both steady state and dynamic conditions specified in the Standard. Sensitivities to off-nominal frequency offsets, harmonics, wideband noise, and out-of-band interferences were analyzed to assess the estimation accuracy in static conditions. Moreover, sinusoidal amplitude and/or phase modulations, linear frequency ramps, and amplitude or phase step variations were considered to examine the estimator dynamic performances. Several simulations were performed by assuming the signal rms value $A$ equal to $1/\sqrt{2}$ p.u. and a sampling frequency $f_s$ of 10 kHz. However, further simulations performed using lower sampling frequencies provided very similar results. Both two (that is $l = 2$) and three (that is $l = 3$) cycle observation interval lengths were considered. As a consequence, the number of acquired samples was $M = 400$ and $M = 600$, respectively. The reference time was always fixed in the center of the observation window.

According to the Standard, the Total Vector Error (*TVE*) is used to quantify the estimation accuracy [Std. C37.118.1]. Indeed, this figure of merit takes into account the contribution of amplitude errors, phase errors, and synchronization uncertainty [Std. C37.118.1], [Castello 12].

*a) Steady-state testing*

Four different sets of simulations were designed to analyze the IpDFT algorithm performance in static conditions.

1) *Off-nominal frequency offset*

At first the sensitivity of the synchrophasor estimator to off-nominal frequency offsets was examined. Fig. 12 shows the maximum *TVE* values achieved when considering 1000 different signal phases $\phi_0$

chosen at random in the range [0, 2π) rad. A maximum off-nominal frequency offset of ±5 Hz (which corresponds to ±10% variation in the normalized number of observed cycles $\lambda_0/l = f_{in}/f_{nom}$) was considered, as recommended in the Standard for *M-class* compliance [Std. C37.118.1].

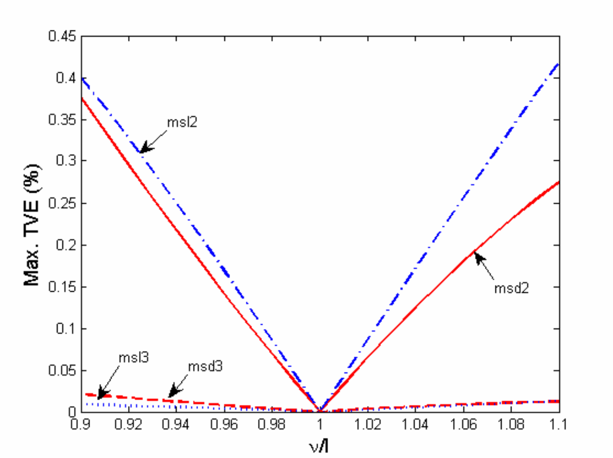


Fig. 12. Maximum *TVE* values provided by the IpDFT estimators versus the normalized number of acquired signal cycles *ν*/*l*. Algorithms are based on: two-signal cycles and the *msd2* or the *msl2* windows; three-signal cycles and the *msd3* or the *msl3* windows.

As we can see, the synchrophasor estimation accuracy decreases when the off-nominal frequency offset increases. When $l$ = 2 the *msd2* window outperforms the m*sl2* window. Indeed, the spectral interference from the image component is greater in the latter case [Belega 12a]. Conversely, when $l$ = 3 the spectral interference from the image component is very small for both the used windows and the achieved accuracy is very high. However, in all the considered cases, the estimated *TVE* values are always well below the 1% threshold recommended in the Standard for both *P-class* and *M-class* performance.

2) *Additive wideband noise*

The effect of additive wideband noise on the synchrophasor estimation accuracy was also investigated. A white Gaussian noise with zero mean and variance chosen in such a way to obtain a *SNR* of 50 dB was considered, thus modeling common real life signals [Sidhu 99]. Fig. 13 shows the achieved maximum *TVE* values as a function of the ratio *ν*/*l*.

By comparing the results depicted in Figs. 12 and 13 it follows that the effect of noise on the synchrophasor estimation accuracy is almost negligible for the two-cycle estimators while it becomes significant for the three-cycle estimators. However, the values of the overall *TVE* still remain very small as compared to the threshold specified in the Standard.

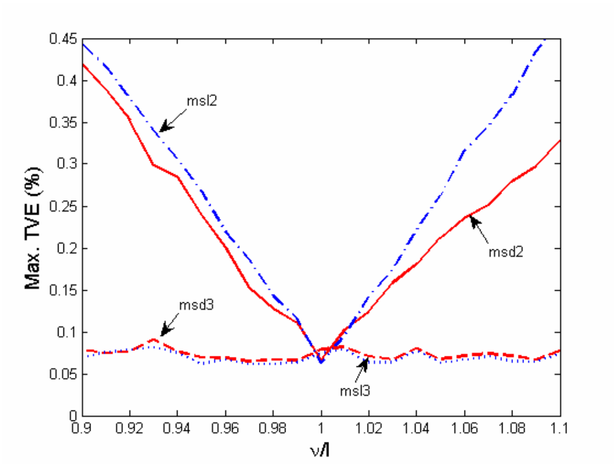


Fig. 13. Maximum *TVE* values provided by the IpDFT estimators versus the normalized number of acquired cycles *ν*/*l* for a signal corrupted by additive white Gaussian noise with zero mean and *SNR* = 50 dB. Algorithms are based on: two-signal cycles and the *msd2* or the *msl2* windows; three-signal cycles and the *msd3* or the *msl3* windows.

3) *Harmonics*

Further simulations were performed to analyze the influence of harmonics. When using the IpDFT algorithm, the worst case spectral interference contribution is due to the second harmonic since it is the closest spectral line to the fundamental component. Thus, the second harmonic amplitude was set to the maximum value specified in the Standard for *P-class* or *M-class* compliance, that is 1% or 10% of the fundamental, respectively. Fig. 14 shows the maximum *TVE* values achieved when 1000 different phase values were chosen at random in the range [0, 2π) rad for both the fundamental and the second harmonic.

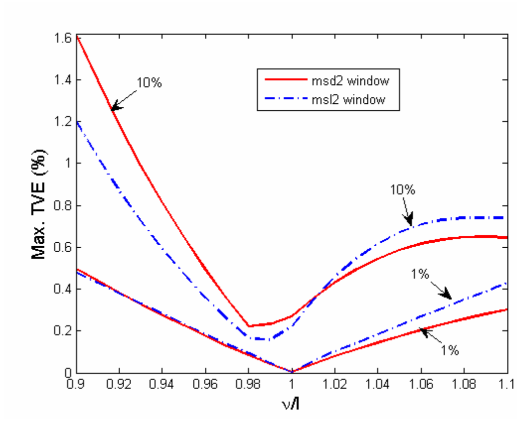


(a)

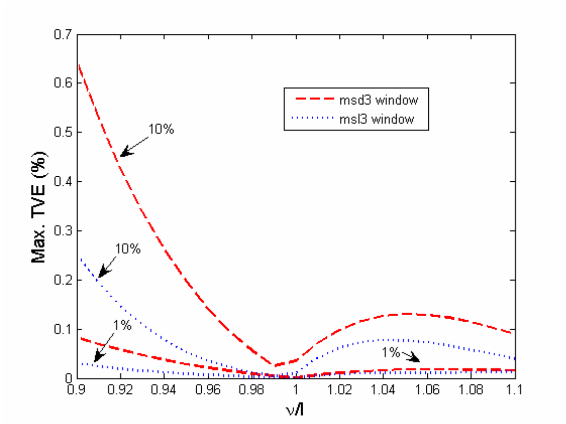


(b)

Fig. 14. Maximum *TVE* values provided by the IpDFT estimators versus the normalized number of acquired cycles *ν*/*l* for a signal affected by a second harmonic of amplitude equal to 1% or 10% of the fundamental. Algorithms are based on: (a) two-signal cycles and the *msd2* or the *msl2* windows; (b) three-signal cycles and the *msd3* or the *msl3* windows.

As expected, the accuracy of the IpDFT synchrophasor estimator decreases as the harmonic amplitude increases. It is worth noticing that, when $l = 2$, harmonic amplitude equal to 10%, and $\nu/l < 1$ (that is the signal frequency is lower than its nominal value), the estimator based on the *msl2* window provides a higher accuracy. Conversely, the estimator based on the *msd2* window is slightly more accurate when $\nu/l > 1$. However, both estimators are only potentially *P-class* compliant because the obtained *TVE* values are above the 1% threshold when the harmonic amplitude is 10%. Opposite, the three-cycle synchrophasor estimates related to the *msl3* window outperform those based on the *msd3* window. Also, the achieved maximum *TVE* values are significantly smaller than those provided by the two-cycle estimators, so potential *M-class* and *P-class* compliance is ensured for both of them.
More accurate synchrophasor estimates can be achieved by removing the contribution of the second harmonic component from the analyzed signal. To this aim, the frequency of the second harmonic component is estimated as twice the fundamental frequency provided by the IpDFT algorithm. Then the harmonic amplitude and phase are estimated by using the same algorithm and the related instantaneous values are evaluated and subtracted from the acquired data. The maximum *TVE* values obtained after the compensation are depicted in Fig. 15 as a function of the ratio $\nu/l$ in the case when the second harmonic amplitude is equal to 10% of the fundamental and two- or three-signal cycles are observed.

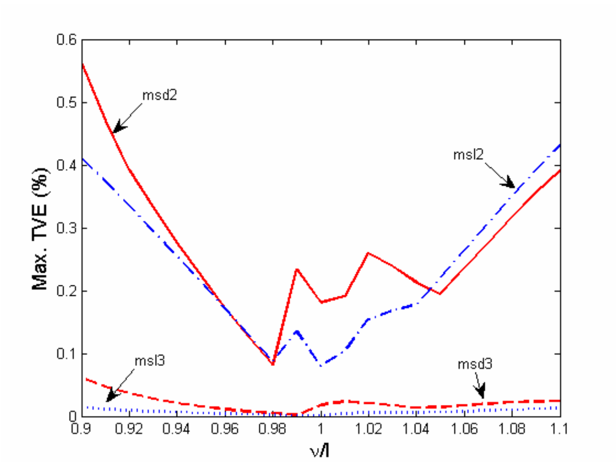


Fig. 15. Maximum *TVE* values provided by the IpDFT estimators versus the normalized number of acquired cycles $\nu/l$ for a signal affected by a second harmonic of amplitude equal to 10% of the fundamental when the second harmonic contribution is removed from the acquired data. Algorithms are based on: two-signal cycles and the *msd2* or the *msl2* windows; three-signal cycles and the *msd3* or the *msl3* windows.

By comparing the results shown in Figs. 14 and 15 it follows that the second harmonic removal increases the synchrophasor estimator accuracy of both two- and three-cycle algorithms. In particular, a *TVE* value lower than the 1% threshold is achieved also by the two-cycle estimators.

4) *Out-of-band interference*

To analyze the influence of out-of-band interferences on the estimated phasor, a single interharmonic was added to the waveform (27). According to the *M-class* requirements specified in the Standard, once the reporting rate *RR* is fixed, the waveform frequency $f_{in}$ should belong to the range $[f_{nom} - RR/20,\ f_{nom} + RR/20]$, the amplitude of the interharmonic should be 10% of the fundamental, and its frequency $f_{ih}$ should be outside the pass-band ($f_{nom}$ – $RR/2$, $f_{non}$ + $RR/2$) [Std. C37.118.1]. Moreover, $f_{ih}$ should be at least down to 10 Hz and not greater than $2f_{in}$ [Std. C37.118.1]. Fig. 16 shows the maximum *TVE* values achieved for interharmonic frequencies $f_{ih}$ falling outside the above defined pass-band when $RR = 25$ and $f_{in} = f_{nom} - RR/20 = 48.75$ Hz.

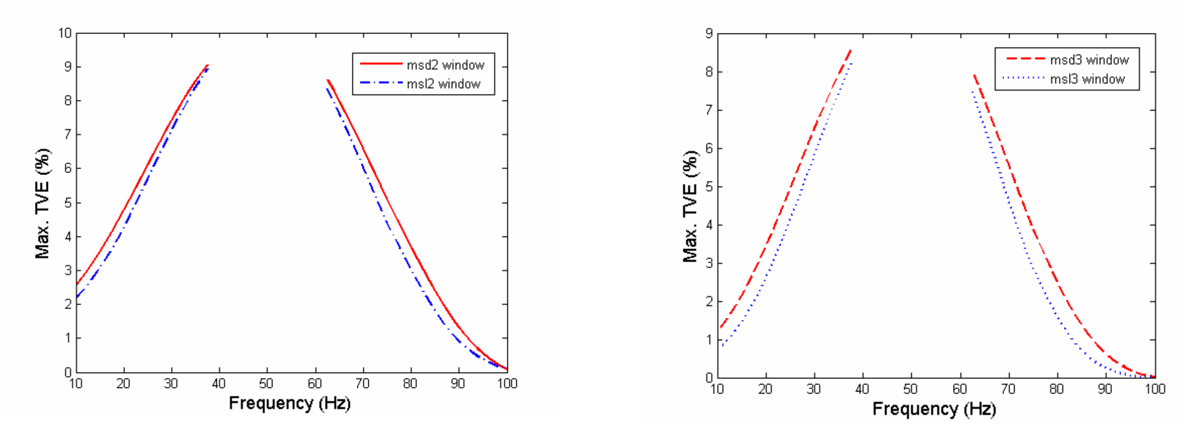


(a) (b)

Fig. 16. Maximum *TVE* values provided by the IpDFT estimators versus the interfering frequency $f_{ih}$ for a signal of frequency $f_{in} = 48.75$ Hz affected by an interharmonic of amplitude equal to 10% of the fundamental. The reporting rate is $RR = 25$ and the analyzed frequency ranges are [10, 37.5] and [62.5, 100] Hz. Algorithms are based on: (a) two-signal cycles and the *msd2* or the *msl2* windows; (b) three-signal cycles and the *msd3* or the *msl3* windows.

It is clear that both IpDFT estimators exhibit a poor out-of-band interharmonic rejection capability, even though slightly better performances are achieved when the MLS windows are adopted. Specifically, maximum *TVE* values smaller than the 1.3% threshold specified in the Standard are achieved only when interfering frequencies are higher than about 85 Hz or, when three-signal cycle are observed, lower than about 15 Hz.

Other simulations were performed by changing the signal frequency $f_{in}$ in the range (48.75, 51.25] Hz. However, results very close to those shown in Fig. 16 were always obtained.

b) *Dynamic testing*

Three different set of simulations were designed to model dynamic testing conditions according to the recommendations of the Standard.

1) *Modulation testing*

Modulation testing allows us to determine the phasor estimator bandwidth [Martin 11]. To this aim the signal (27) was modulated in both amplitude and phase, as described by the following expression [Std. C37.118.1]:

$$x_a(m) = \sqrt{2}A\left[1 + k_a \cos\left(2\pi\frac{f}{f_s}\left(m+\frac{1}{2}\right)\right)\right]\cos\left[2\pi\frac{f_{in}}{f_s}\left(m+\frac{1}{2}\right) + k_p\cos\left(2\pi\frac{f}{f_s}\left(m+\frac{1}{2}\right) - \pi\right)\right], \quad (33)$$
$$m = -M/2, \ldots, M/2-1,$$

where $k_a$ and $k_p$ are respectively the amplitude and phase modulation depth factors and $f$ is the modulation frequency. According to the bandwidth requirements recommended in the Standard, $k_a$ and $k_p$ are chosen equal to 0.1, while the frequency $f$ was set to the maximum specified value, that is 5 Hz. The maximum *TVE* estimates achieved by considering 10,000 consecutive observations intervals continuously shifted sample by sample are depicted in Fig. 17 as a function of $v/l$.

Fig. 17 shows that the accuracy of the synchrophasor estimator decreases when the off-nominal frequency offset increases. Moreover, the MSD windows provide more accurate estimates than the MSL windows. If the signal frequency is close to its nominal value, the two-cycle estimator based on the *msd2* window provides the best results. Conversely, when the off-nominal frequency offset is significant the three-cycle estimator based on the *msd3* window outperform the others. It is worth noticing that any considered estimator is potentially both *P-class* and *M-class* compliant since the achieved *TVE* values are always smaller than the 3% threshold specified in the Standard.

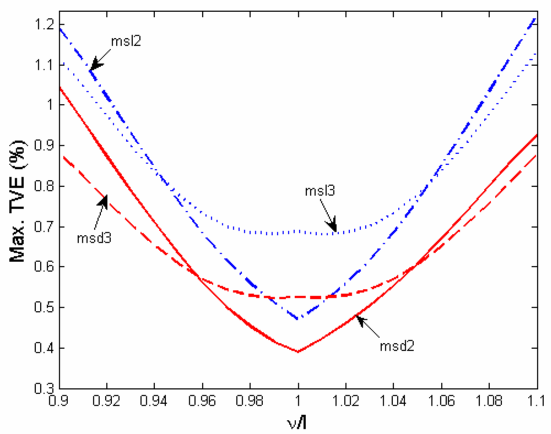


Fig. 17. Maximum *TVE* values provided by the IpDFT estimators versus $v/l$ when the waveform is both amplitude and phase modulated with modulation depth factors $k_a = 0.1$ and $k_p = 0.1$ and modulation frequency $f = 5$ Hz. Algorithms are based on: two-signal cycles and the *msd2* or the *msl2* windows; three-signal cycles and the *msd3* or the *msl3* windows.

The results achieved by performing the same analysis when phase modulation alone affects the signal (that is assuming $k_a = 0$ and $k_p = 0.1$) are reported in Fig. 18.

As we can see, the maximum *TVE* values increases as the off-nominal frequency offset increases when the two-cycle estimators are used. Conversely, the maximum *TVE* values related to the three-cycle estimators are almost independent of the ratio $v/l$ since the interference from the image component is reduced to negligible values by windowing. As above, when the signal frequency is close to its nominal value, the two-cycle estimator based on the *msd2* window provides the best results, while the use of the three-cycle estimator based on the *msd3* window is advantageous when significant off-nominal frequency offsets occur. As in the previous case, the maximum *TVE* values achieved are always smaller than the 3% threshold required for both *P-class* and *M-class* compliance.

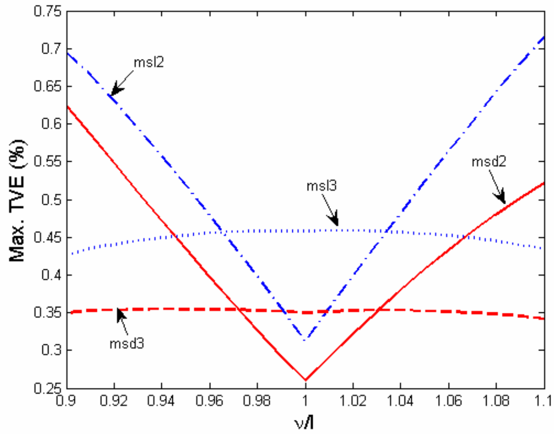


Fig. 18. Maximum of *TVE* values provided by the IpDFT estimators versus $\nu/l$ when the waveform is phase modulated with modulation depth factor $k_p = 0.1$ and modulation frequency $f = 5$ Hz. Algorithms are based on: two-signal cycles and the *msd2* or the *msl2* windows; three-signal cycles and the *msd3* or the *msl3* windows.

2) *Frequency ramp testing*

To analyze the frequency tracking capability of a phasor estimator [Martin 11], the following testing signal is suggested in the Standard :

$$x_r(m) = \sqrt{2}A\cos\left[2\pi\frac{f_{in}}{f_s}\left(m+\frac{1}{2}\right)+\pi\frac{df}{f_s^2}\left(m+\frac{1}{2}\right)^2\right], \qquad m = -M/2,\ldots,M/2-1, \tag{34}$$

where $f_{\text{in}}$ is equal to $f_{nom}$ and d$f$ is the frequency ramp rate, which can assume values in the range ±1 Hz/s [Std. C37.118.1]. Fig. 19 shows the estimated *TVE* values as a function of time when d$f$ = 1 Hz/s, considering an overall observation window duration of 5 s [Std. C37.118.1] and adopting the *msd2* or the *msd3* windows.

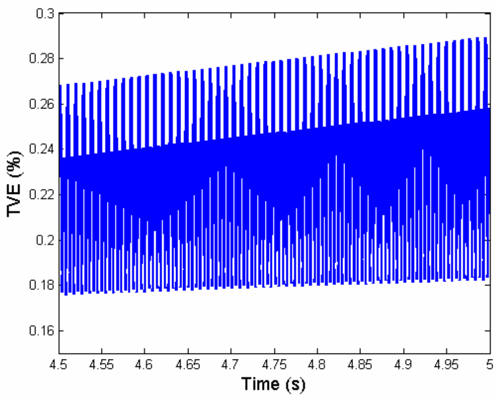


(a)

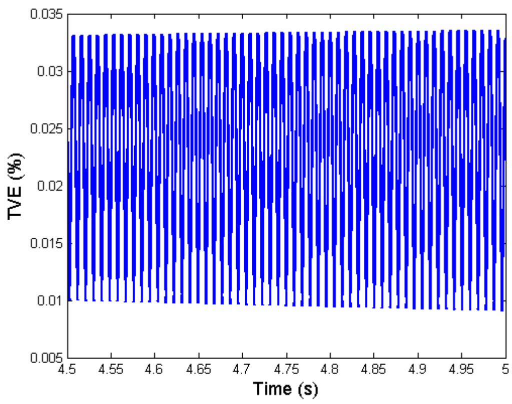


(b)

Fig. 19. *TVE* values provided by the IpDFT estimators versus time when the waveform frequency exhibits a linear variation with a rate 1 Hz/s starting from a nominal frequency of 50 Hz. Algorithm is based on (a) two-signal cycles and the *msd2* window or (b) three-signal cycles and the *msd3* window.

As we can see, the $TVE$ values steadily increase with time and smaller errors are achieved when three-signal cycles are observed. The maximum $TVE$ value reached after 5 s is 0.29% or 0.034% when two- or three-signal cycles are observed, respectively.
Higher maximum $TVE$ values were obtained using the MSL windows. In particular, after an overall observation time of 5 s a $TVE$ value equal to 0.44% or 0.04% is reached when two- or three-signal cycles are observed, respectively. Observe that all the achieved maximum $TVE$ values are smaller than the 1% threshold specified in the Standard.

c) *Transient testing*

1) *Amplitude and phase step testing*

Signals with amplitude or phase steps are employed to determine the response and the delay times of phasor estimators to sudden changes of the electric signal [Std. C37.118.1], [Martin 11]. The response time $t_r$ is defined as the difference between the time at which the $TVE$ overcomes the 1% threshold and the time it return below this threshold, that is [Std. C37.118.1]:

$$t_r = \sup_t \{TVE > 1\%\} - \inf_t \{TVE > 1\%\}, \tag{35}$$

where $t$ is a multiple of the sampling period $T_s = 1/f_s$.
Differently, the delay time $t_d$ is defined as the duration of the time interval between the instant $t_0$ in which a step change is applied to the input, and the time $t_{0.5}$ in which the stepped parameter achieves a value halfway between the initial and the final steady-state values [Std. C37.118.1], i.e.:

$$t_d = t_{0.5} - t_0. \tag{36}$$

It is worth noticing that the time $t_d$ can assume positive or negative values [Std. C37.118.1]. Indeed, since the time reference is chosen in the center of the observation interval, the synchrophasor estimator is affected in advance by possible changes in the electric signal parameters.
In the following, only test results achieved by using the MSD windows are reported for the sake of conciseness.
Fig. 20 shows the estimated amplitude and $TVE$ values as a function of time when an amplitude step of 10% [Std. C37.118.1] occurs 0.13 s after the overall observation window starting instant. The signal frequency was equal to $f_{in}$ = 50 and 55 Hz and the signal phase was $\phi_0 = \pi/3$ rad.
Figs. 20(a) and 20(b) show that the estimated amplitude response does not exhibit overshoot or ripple when the signal is at nominal frequency. Conversely, a small ripple (of magnitude equal to 0.18%.) is present when $f_{in}$ = 55 Hz and two-signal cycles are observed, which is much smaller than the 5% threshold recommended in the Standard.
For signals at nominal frequency, the response time $t_r$ is equal to 18.4 ms or 21.2 ms when considering two- or three-signal cycles, respectively. Conversely, the delay time $t_d$ is close to 1.4 ms for both the observation interval lengths. When $f_{in}$ = 55 Hz, the response time is 19.1 ms or 21.8 ms, while the related delay time is −1.3 ms or −1.0 ms, respectively. It is worth noticing that the response time slightly increases when the waveform frequency increases from 50 Hz to 55 Hz.

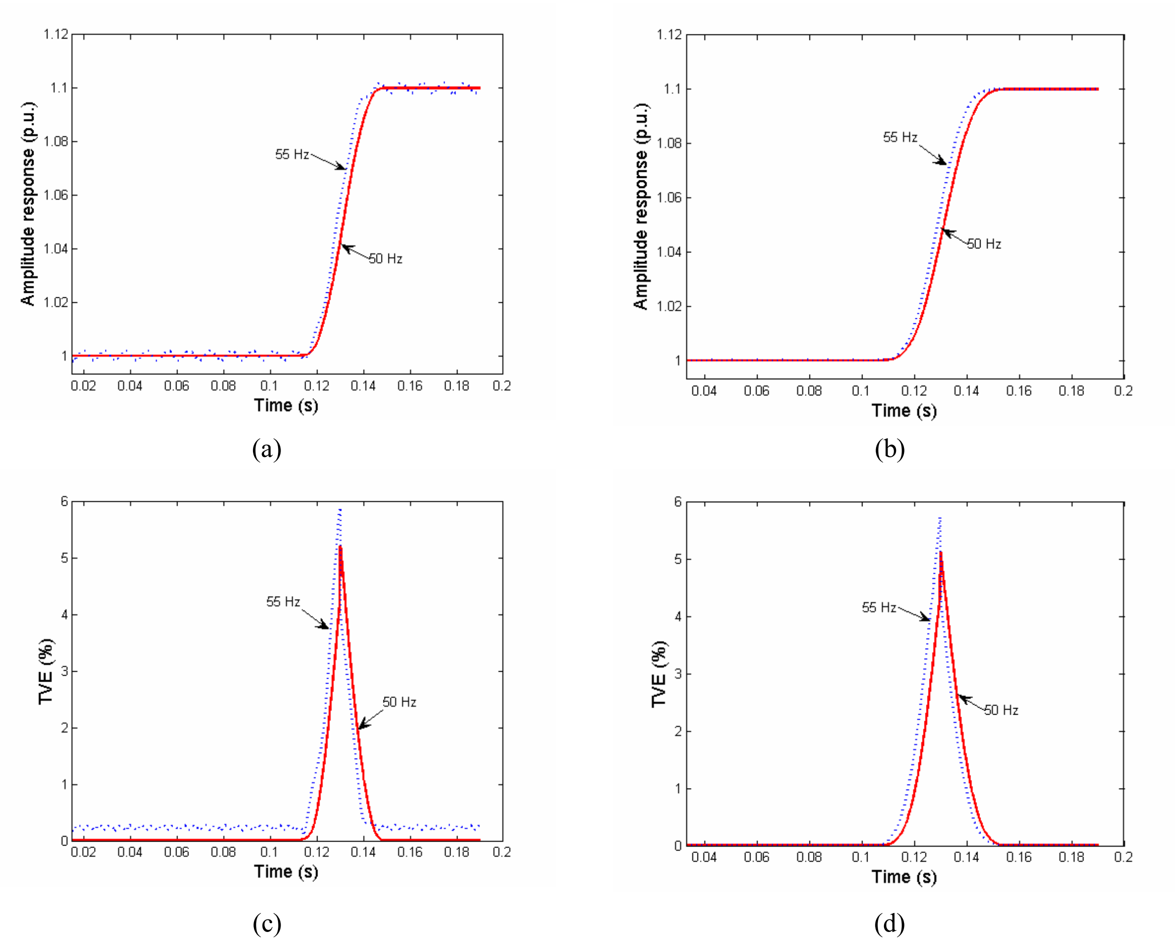


Fig. 20. (a), (b) Estimated amplitude and (c), (d) *TVE* values versus time when the waveform exhibits an amplitude step of 10% and a frequency $f_{in}$ of 50 Hz or 55 Hz. The adopted IpDFT estimator is based on (a), (c) two-signal cycles and the *msd2* window or (b), (d) three-signal cycles and the *msd3* window.

All the above values are compliant with the Standard, in which a maximum value of $1.7/f_{nom}$ (that is 34 ms) for the response time and of $1/(4 \cdot RR)$ (which reaches a minimum value of 5 ms for $RR = 50$) for the delay time is specified for both *P-class* and *M-class* of performance [Std. C37.118.1].

Fig. 21 shows the response time $t_r$ and the delay time $t_d$ as a function of the amplitude step size.

As expected, Fig. 21(a) shows that the response time $t_r$ increases as the amplitude step size or the length of the observation interval increase. In particular, the response time is close to half the observation interval length when the amplitude step size is equal to 20%. Moreover, Fig. 21(a) shows that the $t_r$ values slightly increases when off-nominal frequency offsets occur.

Fig. 21(b) shows that the delay time $t_d$ is almost constant regardless of the observation interval length and the amplitude step size when the signal is at nominal frequency. Conversely, when $f_{in}$ = 55 Hz the delay time becomes negative and increases with the length of the observation interval. In particular, for amplitude steps higher than 10%, the delay times related to both the analyzed observation interval lengths are quite close each other.

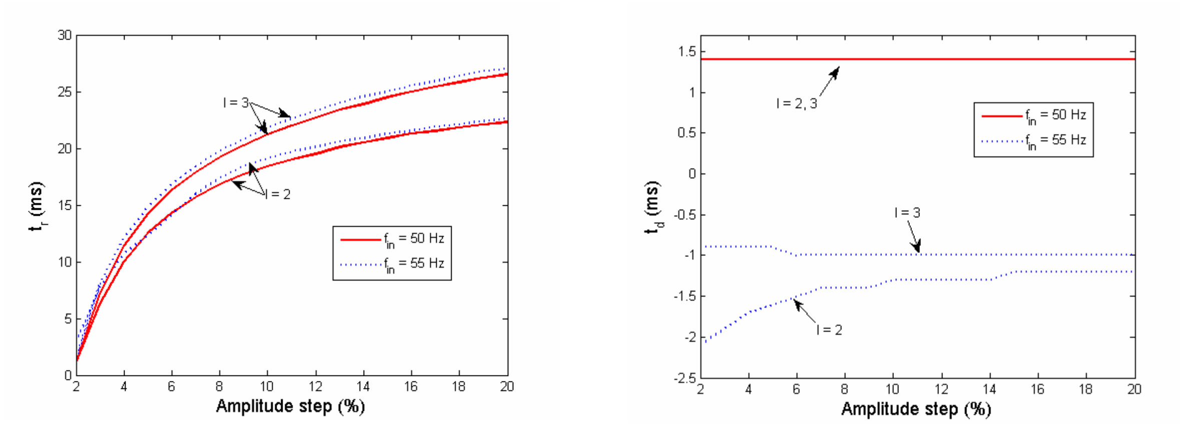


(a) (b)

Fig. 21. (a) Estimated response time $t_r$ and (b) delay time $t_d$ versus the amplitude step size for the IpDFT algorithm based on two- or three-cycles and the *msd2* or the *msd3* window, respectively. The signal frequency $f_{in}$ is equal to 50 Hz or 55 Hz.

Fig. 22 shows the ideal phase, the estimated phase, and the *TVE* values as a function of time when a phase step of π/18 rad [Std. C37.118.1] occurs at 0.13 s after the overall observation window starting instant. The signal frequency was equal to $f_{in}$ = 50 Hz or 55 Hz and the signal phase was $\phi_0 = \pi/3$ rad.

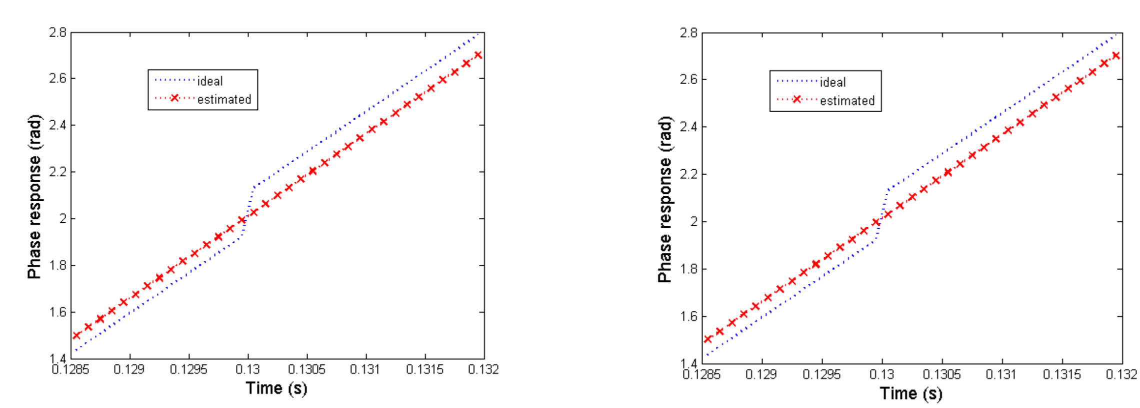


(a) (b)

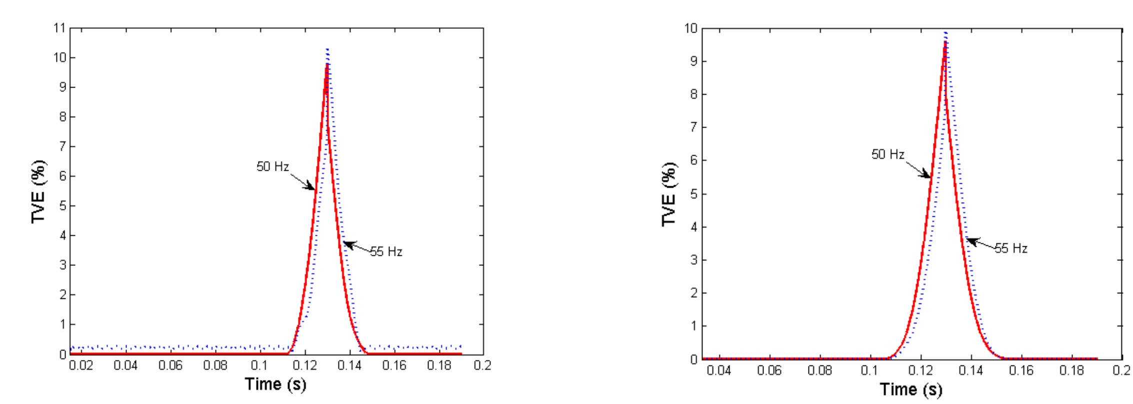


(c) (d)

Fig. 22. (a), (b) Ideal and estimated phase and (c), (d) *TVE* values versus time when the waveform exhibits a phase step of π/18 rad. The adopted IpDFT estimator is based on (a), (c) two-signal cycles and the *msd2* window or on (b), (d) three-signal cycles and the *msd3* window. The signal frequency $f_{in}$ is equal to (a), (b) 55 Hz, or (c), (d) both 50 Hz and 55 Hz.

Figs. 22(a) and 22(b) show that, when the signal frequency is $f_{in}$ = 55 Hz, the estimated phase changes almost linearly if evaluated in the proximity of the phase step.
When the signal is at nominal frequency, the response time $t_r$ is equal to 23.7 ms or 27.4 ms, respectively for the two considered observation lengths. Moreover, the response time becomes equal to 24.5 ms or 26.9 ms, respectively, at $f_{in}$ = 55 Hz. Thus, the response time is almost independent of the off-nominal frequency offset and always smaller than the 34 ms threshold specified in Standard for both *P-class* and *M-class* compliance.
Fig. 23 shows the response time $t_r$ as a function of the phase step size, which varied in the range [0, 20] deg. with a step of 1 deg. As above, both two- and three-signal cycles are considered and the signal frequency $f_{in}$ is equal to 50 Hz or 55 Hz, respectively.

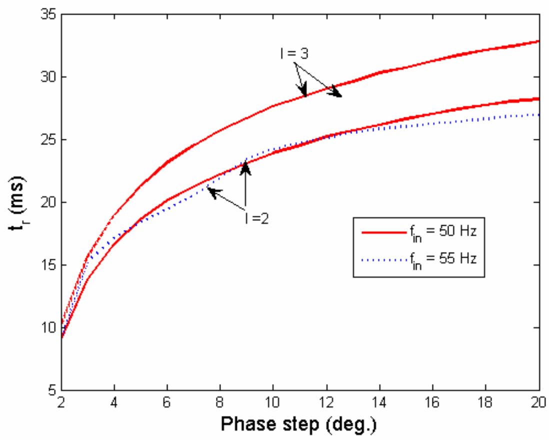


Fig. 23. Estimated response time $t_r$ versus the phase step size for the IpDFT algorithm based on two- or three-signal cycles and the *msd2* or the *msd3* window, respectively. The frequency $f_{in}$ is equal to 50 Hz or 55 Hz.

As expected, the response time $t_r$ increases as the phase step size or the observation interval length increase. Moreover, the response times are almost independent of the off-nominal frequency offset.

Also, in [Belega 13c], we analyzed the effect of the possible alternatives when the two-cycle estimator based on the *msd2* window is employed. When only two DFT samples are used, the following variety of alternatives has been examined: i) the maximum DFT spectrum sample (that is $X_w(l)$ in (30)) and the preceding DFT sample $X_w(l-1)$, ii) the maximum DFT spectrum sample $X_w(l)$ and the subsequent DFT sample $X_w(l+1)$, iii) the two greatest DFT spectrum samples (as in the classical IpDFT algorithm). Among these choices, simulations showed that the classical IpDFT algorithm provides the most accurate synchrophasor estimates.
The three-point IpDFT$_2$ algorithm (see §2.2.1.C) was also considered.
Fig. 24 shows the maximum *TVE* values provided by the classical IpDFT algorithm and the three-point IpDFT algorithm in both steady-state and dynamic conditions. The same simulation parameter values used in the previous Section were considered.

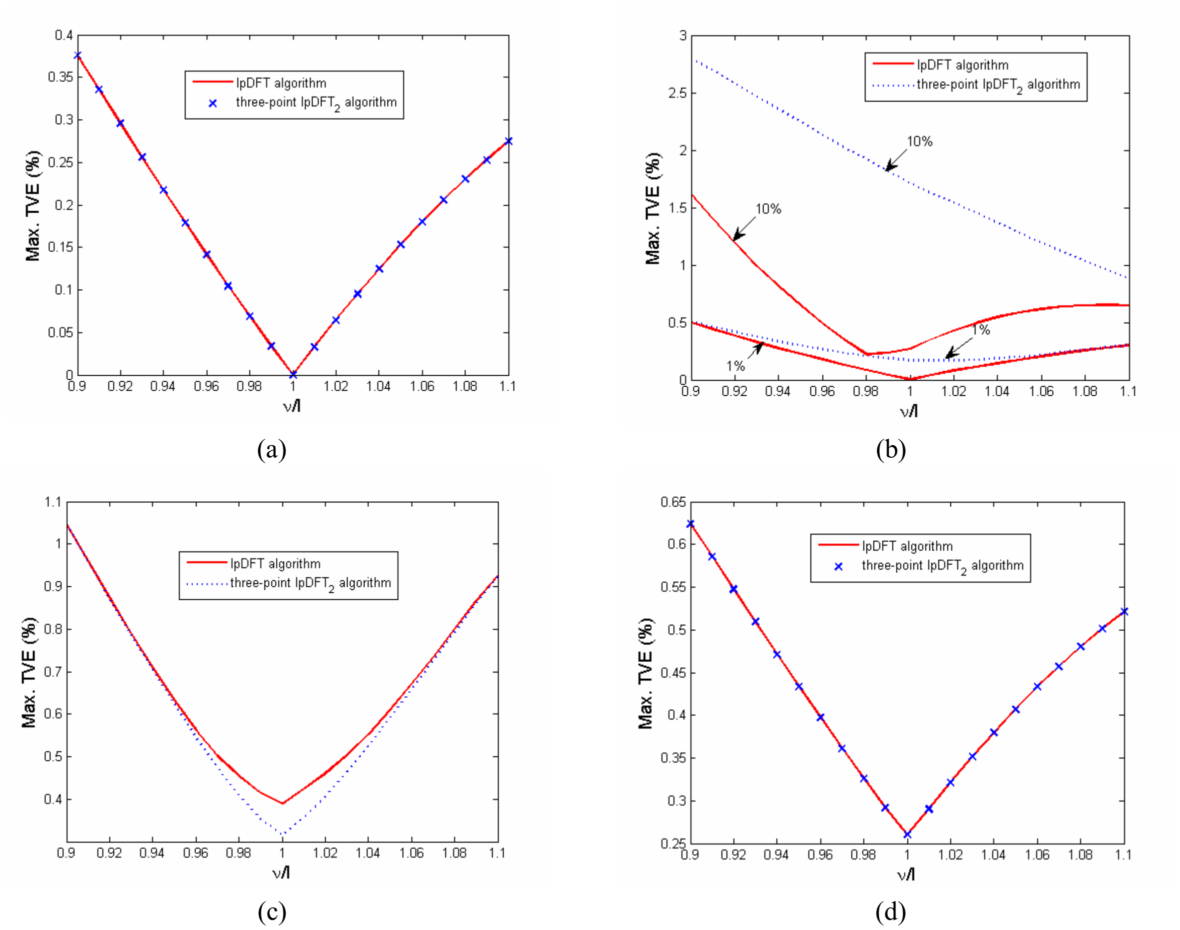


Fig. 24. Maximum *TVE* values provided by the classical and the three-point IpDFT algorithms versus $\nu/l$ when two-signal cycles are observed and the *msd2* window is adopted. Waveform affected by (a) only off-nominal frequency offset, (b) a second harmonic with amplitude equal to 1% or 10% of the fundamental, (c) simultaneous amplitude and phase modulations, (d) phase modulation alone.

As it can be seen, the three-point IpDFT$_2$ algorithm provides slightly more accurate results only when the signal is simultaneously modulated in amplitude and phase and the signal frequency is close to its nominal value. Also, the three-point IpDFT$_2$ algorithm and the classical IpDFT algorithm exhibit almost the same accuracy when only off-nominal frequency offsets or phase modulations occur. Conversely, the IpDFT algorithm provides more accurate results when the signal is affected by a second harmonic disturbance.

Concluding, we can state that the classical IpDFT algorithm is a good choice for synchrophasor estimation when two-signal cycles are observed and the *msd2* window is used.

Also, some experiments were performed in order to confirm the simulation results obtained in steady-state conditions. The electric signals were synthesized by means of suitable signal generators and acquired using a 12-bit data acquisition board NI 6023. The full-scale range and the sampling frequency were set to 10 V and 10 kHz, respectively. The signal frequencies were set to 45, 47, 49, 51, 53, and 55 Hz, while the signal amplitude was equal to 2.5 V. The effect of off-nominal frequency offsets on the estimation accuracy was investigated by acquiring sine-waves provided by an Agilent 33220A signal generator. Conversely, asymmetrical sine-waves provided by a TG315 signal generator were acquired to analyze the phasor estimator sensitivity to harmonics. The two-cycle IpDFT estimator based on the *msd2* window was applied to $M = 400$ waveform samples. For each value of the signal frequency an overall record of 9200 consecutive samples were acquired. The maximum *TVE* value was determined by considering 401 consecutive phasors estimated from $M$-length adjacent records obtained by shifting the observation window sample by sample. The reference values for the sine-wave parameters $\nu$, $A$, and $\phi_0$ were obtained by means of the IpDFT algorithm based on the *msd2* window applied to the overall record. Indeed, this algorithm returns accurate estimates when the number of acquired sine-wave cycles is high enough.

The waveform *THDs* were estimated by means of the multiharmonic sine-fitting algorithm proposed in [Ramos 06] and stopping the algorithm iterations when the absolute value of the difference between two consecutive estimated frequency values was smaller than $1 \cdot 10^{-6}$. The obtained *THD* values were $6 \cdot 10^{-3}$% and 8.6%, respectively. Thus, the Agilent 33220A generator provided almost pure sine-waves suitable for investigating the sensitivity of the proposed estimators to off-nominal frequency offsets. Conversely, the heavily distorted waveforms provided by the TG315 were employed to analyze the effect of harmonics on the phasor estimator accuracy.

The maximum *TVE* values returned by the two-cycle IpDFT estimator based on the *msd2* window are depicted in Fig. 25 as a function of the ratio $\nu/l$ for both analyzed waveforms. The values achieved when removing the second harmonic contribution from the asymmetrical sine-wave are also shown.

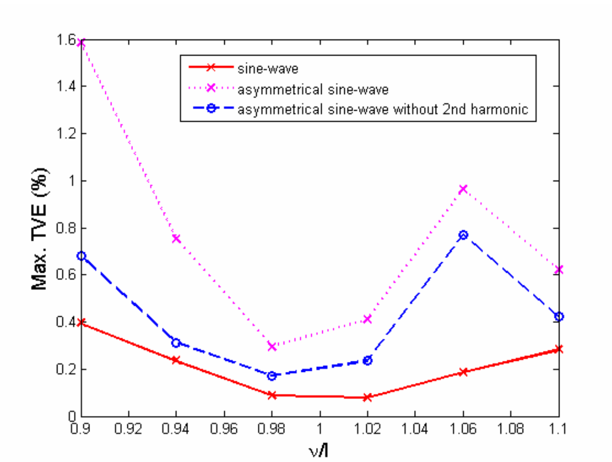


Fig. 25. Maximum *TVE* values returned by the two-cycle IpDFT estimator based on the *msd2* window when applied to sine-waves supplied by the Agilent 33220A or to the asymmetrical sine-waves supplied by the TG315 signal generator. The values achieved when removing the second harmonic contribution from the asymmetrical sine-waves are also shown.

As we can see, the agreement between the experimental and the related simulation results reported in Fig. 12 and Fig. 14(a) is quite good. Moreover, the second harmonic removal allows us to reduce the achieved maximum *TVE* value below the 1% threshold.

## 2.5. DEVELOPMENT. FUTURE WORKS.

In the future I will work also in the same research fields, which are: *Signal Processing*, *Analog-to-Digital Converter (ADC) Testing*, and *Synchrophasor Measurements*.

In the *Signal Processing* field the next our works will be on the reduction of the detrimental effect of spectral interference from both image component and long range leakage on the parameter estimation of a sine-wave. To this aim we will work in two directions. In the first direction the works will be focused on finding of the most suitable weights for the Discrete Fourier Transform (DFT) spectrum samples involved in a multipoint Interpolated DFT (MIpDFT) method in order to achieve a highly effective rejection of the detrimental effect of spectral interference from the image component. The achieved results allow us to propose novel IpDFT method for scientific community. Recently, in [Macii 12], new cosine windows, called Maximum Image interference Rejection (MIR) windows, have been proposed in order to effectively suppress the spectral interference from the image component. As compared with the classical cosine windows, at these windows the coefficients are determined as a function of the integer part of the number of acquired sine-wave cycles. In order to achieve a higher suppression of the spectral interference we will use the MIR windows in the existing MIpDFT methods. The achieved performance will be compared with those achieved by the novel MIpDFT methods specified above by means of both computer simulations and experimental results. Conversely, in the second direction the works will be focused on the developing of new cosine windows exhibiting both maximum image interference rejection and high sidelobe decay rate in order to reduce as much as possible the detrimental effect of the spectral interference from both the image component and the long range leakage. These windows, called MIR-RSD windows, will be used in the IpDFT method. We will try to derive analytical expressions for the parameter estimators provided by the IpDFT method based on the MIR-RSD windows. The accuracies of the parameter estimators will be compared through theoretical, simulation, and experimental results with those achieved by the MIpDFT methods developed in the first research direction.

It is well known that the harmonics affect the fitting accuracy of both three-parameter sine-fitting (3PSF) algorithm and four-parameter sine-fitting (4PSF) algorithm. However, in the scientific literature is not yet given any expression for the fitting error in the presence of harmonics. Hence, we will focus on the derivation of such expression. Moreover, based on the derived expression, we will analyze the contributions of the harmonics to the residual error.

Also, we want to shown through an analytical expression that the non-coherent sampling has a very small influence on the sine-wave parameter estimates returned by a sine-fitting algorithm.

Furthermore, in order to achieve the sine-wave parameters in real-time, we will implement the developed algorithm using systems based on modern Digital Signal Processors (DSPs), such as the TMS320C6416T DSK, which are available in my Department.

It is worth noticing that beginning to 2013, I am member of the Working Group (WG) of the IEEE Standard P1451.001. That Standard, recommended practice, defines signal processing algorithms and data structure in order to share and to infer signal and state information of an instrumentation or control systems. These algorithms are based on their own signal and also on the transducers attached to the system. The recommended practice also defines the commands and replies for requesting information and algorithms for shape analysis such as exponential, sinusoidal, impulsive noise, noise, and tendency. I am involved in the SG1 (Impulse, noise detection mean estimation, tendency, exponential, and sinusoidal patterns) and SG5 (Testing) working subgroups. Thus, the works to this Standard will open new research directions in the *Signal Processing* field.

In [Belega 04] it was shown that in ADC testing in multi-tone mode the required accuracy of the sine-waves of the multi-tone test signal can be smaller than that of the sine-wave used in the single-tone mode testing. Besides, a better dynamic characterization of an ADC is achieved if a multi-tone test signal is used instead of a single-tone test signal. Based on these observations the future works in the *ADC Testing* field will be focused on the ADC testing in multi-tone mode by means of multi-tone frequency-domain and time-domain sine-fitting methods. The statistical performance of the ADC dynamic parameter estimators achieved by the multi-tone sine-fitting methods will be investigated. Furthermore, we will use the IpDFT method for the estimation of Signal-to-NonHarmonic Ratio (*SNHR*), Total Harmonic Distortion ratio (*THD*), and Spurious Free Dynamic Range ratio (*SFDR*) ADC dynamic parameters. The statistical performance of the estimators provided by the IpDFT method for the above parameters will be analyzed in the case of a sine-wave corrupted by an additive stationary white noise. Also, the accuracy of the above estimators will be compared through theoretical, simulation, and experimental results with those of the estimators provided by the Energy-Based (EB) method, which have already been analyzed in the scientific literature.

In the *Synchrophasor Measurement* field we will work in two directions. In the first direction our works will be focused on the Frequency Error (FE) and Rate Of Change Of Frequency (ROCOF) Error (RFE) estimation by means of both frequency-domain and time-domain algorithms. In particular, it should be noted, that accurate RFE estimation is becoming increasingly critical for Phasor Measurement Units (PMUs) implementation due to the need for tracking fast frequency changes in a very short time. As frequency-domain algorithms will be used the DFT-based algorithm and the IpDFT algorithm based on cosine windows. To estimate the above parameters the DFT-based algorithm will be used together with the Least Squares (LS) approach [Phadke 09]. In this case we will analyze how the number of samples acquired in one nominal cycle of the electrical signal affects the estimation accuracy. When the IpDFT algorithm is applied we will analyze how the adopted window and the observation interval length affect the FE and RFE estimations accuracy. Conversely, as time-domain algorithms will be used the Weighted Least Squares (WLS)-based algorithm. The accuracy of the FE and RFE estimates achieved by all above algorithms will be compared. Furthermore, we will work on the development of novel algorithms which ensure both accurate and fast estimates of the synchrophasor, FE, and RFE. Moreover, the algorithms developed during the future works in the *Signal Processing* field (MIpDFT methods and IpDFT method based on the MIR-RSD windows) will be also employed to this task. The performance of the developed *P-class* algorithm will be compared with that of the *P-class* algorithm suggested in the IEEE Standard C37.118.1-2011. The analysis will be performed under steady state, dynamic, and transient conditions, and the test conditions comply with the IEEE Standard C37.118.1-2011. The analysis will be performed through computer simulations.

In the second direction our works will be focused on the parameters estimation of an electrical signal with decaying dc offset under transient conditions by means of frequency-domain algorithms. The achieved estimation accuracy will be verified by means of both computer simulations and experimental results.

For a proper determination of the processing efforts required by the analyzed algorithms they will be implemented using the systems based on DSPs.

In the *Signal Processing*, *ADC Testing*, and *Synchrophasor Measurement* fields I will continue the cooperation with Professor Dario Petri and Professor Dominique Dallet. Also, I will involve in the research works the future PhD students. I intend to have PhD theses in cotutelle agreement between my University and the University of Trento and University of Bordeaux, respectively.

The results achieved during the research works will be submitted for publication in prestigious ISI foreign journals, such as *IEEE Transactions on Instrumentation and Measurements*, *Digital Signal Processing*, *IEEE Transactions on Power Delivery*, and *Measurements*, and to important conferences focused on instrumentation and measurements, power systems, and signal processing. Also, I will include in my courses on *Electrical and Electronic Measurements*, *Measurement Techniques, Sensors, and Transducers*, and *Digital Signal Processors and Acquisition Systems*, some of the achieved results. Further, additional courses focused on the sine-wave parameter estimation and the synchrophasor measurement will be planned at the doctoral school level. These courses are very useful since they allow the doctoral students to achieve important knowledge in the above research fields, as a basis for their works.

In order to achieve funding for our research works we will apply for several national and European grants. If it is possible, I intend to equip a laboratory with modern instruments for power measurements.

From the above presentation it is clear that the main works will be in the *Signal Processing* field. The achieved results will be applied to the other two research fields, especially to the *Synchrophasor Measurement* field. It is very important to use in the modern PMUs, algorithms which provide both accurate and fast synchrophasor, FE, and RFE estimates. Nowadays, this is a great challenge.

# 3. REFERENCES


[Agrež 00] D. Agrež, "Frequency estimation by IDFT and quantization noise," in *Proc. IMEKO 2000, XVI IMEKO World Congress*, vol. IX, pp. 9-14, Vienna, Austria, 2000.

[Agrež 02] D. Agrež, "Weighted multipont interpolated DFT to improve amplitude estimation of multifrequency signal," *IEEE Trans. Instrum. Meas.,* vol. 51, no. 2, pp. 287-292, April 2002.

[Agrež 07] D. Agrež, "Dynamic of frequency estimation in the frequency domain," *IEEE Trans. Instrum. Meas.*, vol. 56, no. 6, pp. 2111-2118, Dec. 2007.

[Andersson 05] T. Andersson and P. Händel, "Robustness of wave-fitting with respect to uncertain parameter values," in *Proc. IEEE Instrum. Meas. Tehnol. Conf.*, pp. 662-665, Ottawa, Canada, May 2005.

[Andersson 06] T. Andersson and P. Händel, "IEEE standard 1057, Cramér-Rao bound and the parsimony principle," *IEEE Trans. Instrum. Meas.*, vol. 55, no. 1, pp. 44-53, Feb. 2006.

[Andria 89] G. Andria, M. Savino, and A. Trotta, "Windows and interpolation algorithm to improve electrical measurement accuracy," *IEEE Trans. Instrum. Meas.*, vol. 38, no. 4, pp. 856-863, Aug. 1989.

[Barchi 13a] G. Barchi, D. Macii, D. Belega, and D. Petri, "Performance of synchrophasor estimators in transients conditions: a comparative analysis," *IEEE Trans. Instrum. Meas.,* accepted for publication.

[Barchi 13b] G. Barchi, D. Macii, and D. Petri, "Synchrophasoe estimator accuracy: a comparative analysis," *IEEE Trans. Instrum. Meas.,* vol. 62, no. 5, pp. 963-973, May 2013.

[Belega 04] D. Belega, "Testing of ADCs by frequency-domain analysis in multi-tone mode," *Proceedings of the Romanian Academy, Series A*, vol. 5, no. 2, pp. 197-212, May-August 2004.

[Belega 05a] D. Belega, "The maximum sidelobe decay windows," *Revue Roumaine des Sciences Techniques Serie Électrotechnique et Énergétique*, no. 3, pp. 349-356, Juillet –Septembre 2005.

[Belega 05b] D. Belega and D. Dallet, "A/D converters testing based on beat frequency method," in *Proc. of the Third IEEE Workshop on Intelligent Data Acquisition and Advanced Computing Systems: Technology and Applications (IDAACS)*, pp. 13-17, Sofia, Bulgaria, Sept. 5-7, 2005.

[Belega 07a] D. Belega and D. Dallet, "Estimation of the multifrequency signal parameters by interpolated DFT method with maximum sidelobe decay," in *Proc. of the IEEE Workshop on Intelligent Data Acquisition and Advanced Computing Systems: Technology and Applications (IDAACS)*, pp. 294-299, Dortmund, Germany, Sept. 6-8, 2007.

[Belega 07b] D. Belega, M. Ciugudean, and D. Stoiciu, "Choice of the cosine-class windows for ADC dynamic testing by spectral analysis," *Measurement*, vol. 40, no. 4, pp. 361-371, 2007.

[Belega 07c] D. Belega and D. Dallet, "Dynamic testing of A/D converters by means of the three-parameter sine-fit algorithm," *Measurement*, vol. 40, no. 1, pp. 1-7, 2007.

[Belega 08a] D. Belega and D. Dallet, "Frequency estimation via weighted multipoint interpolated DFT," *IET Science, Measurement & Technology*, vol. 2, no 1, pp. 1-8, 2008.

[Belega 08b] D. Belega, D. Stoiciu, and D. Dallet, "Uncertainty analysis of the normalized frequency estimation of a sine wave by three-point interpolated DFT method," in *Proc. of the IEEE Workshop on Advanced Methods for Uncertainty Estimation Measurement (AMUEM)*, pp. 84-89, Sardagna, Trento, Italy, July 22-23, 2008.

[Belega 08c] D. Belega and D. Dallet, "A new weighted multipoint interpolated DFT approach for high-accuracy amplitude estimation," in *Proc. of the I2MTC IEEE International Instrumentation and Measurement Technology Conference*, pp. 200-205, Vancouver Island, Canada, May 12-15, 2008.

[Belega 08d] D. Belega and D. Dallet, "Normalized Frequency Estimation for Accurate Dynamic Characterization of A/D Converters by Means of Three-Parameters Sine-Fit Algorithm," *Measurement*, vol. 41, no. 9, pp. 986-993, 2008.

[Belega 09a] D. Belega and D. Dallet, "Multifrequency signal snalysis by snterpolated DFT method with maximum sidelobe decay windows," *Measurement*, vol. 42, no. 3, pp. 420-426, April 2009.

[Belega 09b] D. Belega and S. Zaporojan, "Assessment of influence of systematic errors on the precision with which the normalized frequency of a sinusoidal signal is determined by means of a discrete Fourier transformation with interpolation," *Measurement Techniques*, vol. 52, no. 2, pp. 148-154, Feb. 2009 (translated from *Izmenitel'naya Tekhnika* (Russian Federation), no. 2, pp. 26-30, Feb. 2009)

[Belega 09c] D. Belega, D. Dallet, "Choice of the acquisition parameters for frequency estimation of a sine wave by interpolated DFT method," *Comput. Stand. Interfaces*, vol. 31, no. 5, pp. 962-968, Sept. 2009.

[Belega 09d] D. Belega and D. Dallet, "Amplitude estimation by a multipoint interpolated DFT approach," *IEEE Trans. Instrum. Meas*., vol. 58, no. 5, pp. 1316-1323, May 2009.

[Belega 09e] D. Belega, D. Dallet, and D. Petri, "Uncertainty analysis of the normalized frequency estimation by multipoint interpolated DFT approach," in *Proc. of the IEEE Workshop on Advanced Methods for Uncertainty Estimation Measurement (AMUEM)*, pp. 34-38, Bucharest, Romania, July 6-7, 2009

[Belega 09f] D. Belega and D. Dallet, "Efficiency of the three-point interpolated DFT method on the normalized frequency estimation of a sine-wave," in *Proc. of the IEEE Workshop on Intelligent Data Acquisition and Advanced Computing Systems: Technology and Applications (IDAACS)*, pp. 2-7, Rende (Cosenza), Italy, Sept. 21-23, 2009

[Belega 10a] D. Belega, D. Dallet, and D. Petri, "Accuracy of sine wave frequency estimation by multipoint interpolated DFT approach," *IEEE Trans. Instrum. Meas*., vol. 59, no. 11, pp. 2808-2815, Nov. 2010

[Belega 10b] D. Belega and D. Dallet, "Multipoint interpolated DFT method for frequency estimation," *Transactions on Systems, Signals & Devices*, vol. 15, no. 3, pp. 1-16, 2010, Shaker Verlag GmbH.

[Belega 10c] D. Belega, D. Dallet, and D. Slepicka, "Accurate amplitude estimation of harmonic components of incoherently sampled signals in the frequency domain," *IEEE Trans. Instrum. Meas*., vol. 59, no. 5, pp. 1158-1166, May 2010.

[Belega 11a] D. Belega, D. Dallet, and D. Petri, "A high-performance procedure for effective number of bits estimation in analog-to-digital converters," *IEEE Trans. Instrum. Meas*., vol. 60, no. 5, pp. 1522-1532, May 2011.

[Belega 11b] D. Belega, D. Petri, and D. Dallet, "Sine-fitting by the energy-based method in the dynamic testing of ADCs," in *Proc. of the IEEE Conference on Intelligent Data Acquisition and Advanced Computing Systems: Technology and Applications (IDAACS)*, vol. I, pp. 33-38, Prague, Czech Republic, Sept. 15-17, 2011.

[Belega 11c] D. Belega and D. Petri, "Accuracy of a DFT phasor estimator at off-nominal frequency in either steady state or transient conditions," in *Proc. of the IEEE Conference on Smart Measurements for Future Grids (SMFG)*, pp. 45-50, Bologna, Italy, Nov. 14-16, 2011

[Belega 12a] D. Belega, D. Dallet, and D. Petri, "Statistical description of the sine-wave frequency estimator provided by the interpolated DFT method," *Measurement*, vol. 51, no. 1, pp. 109-117, Jan. 2012.

[Belega 12b] D. Belega, D. Dallet, and D. Petri, "Accuracy of the normalized frequency estimation of a discrete-time sine-wave by the energy-based method," *IEEE Trans. Instrum. Meas*., vol. 61, no. 1, pp. 111-121, Jan, 2012.

[Belega 12c] D. Belega and D. Petri, "Accuracy analysis of the amplitude estimation of a sine-wave by the energy-based method using the direct and indirect procedures," *Measurement*, vol. 45, no. 9, pp. 2264-2274, Nov. 2012

[Belega 12d] D. Belega, D. Petri, and D. Dallet, "Noise power estimation by the three-parameter and four-parameter sine-fit algorithms," *IEEE Trans. Instrum. Meas*., vol. 61, no. 12, pp. 3234-3240, Dec. 2012.

[Belega 13a] D. Belega, "Accuracy analysis of the normalized frequency estimation of a discrete-time sine-wave by the average-based interpolated DFT method," *Measurement*, vol. 49, no. 1, pp. 593-602, Jan. 2013.

[Belega 13b] D. Belega and D. Petri, "Statistical performance of the effective-number-of-bits estimators provided by the sine-fitting algorithms," *IEEE Trans. Instrum. Meas*., vol. 62, no. 3, pp. 633-640, March 2013.

[Belega 13c] D. Belega and D. Petri, "Accuracy analysis of the multicycle synchrophasor estimator provided by the interpolated DFT algorithm," *IEEE Trans. Instrum. Meas*., vol. 62, no. 5, pp. 942-953, May 2013.

[Benetazzo 92] L. Benetazzo, C. Narduzzi, C. Offelli, and D. Petri, "A/D converter performance analysis by a frequency-domain approach," *IEEE Trans. Instrum. Meas*., vol. 4, no. 6, pp. 834-839, 1992.

[Benmouyal 95] G. Benmouyal, "Removal of dc-offset in current waveforms using digital mimic filtering," *IEEE Trans. Power Del*., vol. 10, no. 2, pp. 621-630, April 1995.

[Bertocco 00] M. Bertocco, C. Narduzzi, P. Paglierani, and D. Petri, "A noise model for digitized data,“ *IEEE Trans. Instrum. Meas.*, vol. 49, no. 1, pp. 83-86, Feb. 2000.

[Bertocco 92] M. Bertocco, C. Offelli, and D. Petri, "Dynamic behavior of a digital phase estimator", *IEEE Trans. Instrum. Meas.*, vol. 41, no. 6, pp. 755-761, Dec. 1992.

[Bilau 04] T. Z. Bilau, T. Megyeri, A. Sárhegyi, J. Márkus, and I. Kollár, "Four-parameter fitting of sine wave testing result: Iteration and convergence," *Comput. Stand. Interfaces*, vol. 26, no. 1, pp. 51-56, Jan. 2003.

[Castello 11] P. Castello, C. Muscas, and P. A. Pegoraro, "Performance comparison of algorithms for synchrophasors measurements under dynamic conditions," in *Proc.* of the *IEEE International Workshop* on *Applied Measurements for Power Systems (AMPS)*, pp. 25-30, 2011.

[Castello 12] P. Castello, M. Lixia, C. Muscas, and P. A. Pegoraro, "Impact of the model on the accuracy of synchrophasor measurement,“ *IEEE Trans. Instrum. Meas.*, vol. 61, no. 8, pp. 2179-2188, Aug. 2012.

[Chen 07] K.-F. Chen and Y.-M. Xue, "Improving four-parameter sine wave fitting by normalization," *Comput. Stand. Interfaces*, vol. 29, no. 2, pp. 184-190, Feb. 2007.

[Chen 08] K.-F. Chen and Y.-M. Xue, "Four-parameter sine wave fitting by Gram-Schmidt, orthogonalization," *Measurement*, vol. 41, no. 1, pp. 76-87, Jan. 2008.

[Coşniță 72] C. Coşniță and F. Turtoiu, "Problems of Algebra" (in Romanian), Technique Publishing House, Bucharest, 1972.

[Deyst 95] J. P. Deyst, T. M. Souders, and O. M. Solomon, “Bouds on least-squares four-parameter sine-fit errors due to the harmonic distortion and noise,” *IEEE Trans. Instrum. Meas.*, vol. 44, no. 3, pp. 637-642, June 1995.

[DYNAD 01] *Project DYNAD – SMT4 – CT98 -2214 – Draft Standard – Version 3.4*, July 12, 2001.

[Ferrero 92] A. Ferrero and R. Ottoboni, “High-accuracy Fourier analysis based on synchronous sampling techniques,” *IEEE Trans. Instrum. Meas.*, vol. 41, no. 6, pp. 780-785, Dec. 1992.

[Fonseca 04] M. Fonseca da Silva, P. M. Ramos, and A. Cruz Serra, “A new four parameter sine fitting procedure,” *Measurement*, vol. 35, no. 2, pp. 131-137, Mar. 2004.

[Garza 10] M. Platas-Garza and J. de la O. Serna, “Dynamic phasor and frequency estimates through maximally flat differentiators,” *IEEE Trans. Instrum. Meas.*, vol. 59, no. 7, pp. 1803-1811, Jul. 2010.

[Garza 11] M. A. Platas-Garza and J. A. de la O Serna, “Dynamic harmonic analysis through Taylor–Fourier transform,” *IEEE Trans. Instrum. Meas.,* vol. 60, no. 3, pp. 804-813, Mar. 2011.

[Grandke 83] T. Grandke, Interpolation algorithms for discrete Fourier transforms of weighted signals, *IEEE Trans. Instrum. Meas.*, vol. IM-32, no. 2, pp. 350 – 355, June 1983.

[Gu 00] Jhy-Cherng Gu and Sun-Li Yu, “Removal of dc offset in current and voltage signals using a novel Fourier filter algorithm,” *IEEE Trans. Power Del.*, vol. 15, no. 1, pp. 73-79, Jan. 2000.

[GUM 95] *Guide for the expression of uncertainty in measurement*, International Organization for Standardization, Switzerland, second edition, 1995.

[Guo 03] Y. Guo, M. Kezunovic, and D. Chen, “Symplified algorithms for removal the effect of exponentially decaying dc offset on the Fourier algorithm,” *IEEE Trans. Power Del.*, vol. 18, no. 3, pp. 711-717, July 2003.

[Händel 00] P. Händel, “Properties of the IEEE-STD-1057 four-parameter sine wave fit algorithm,” *IEEE Trans. Instrum. Meas.*, vol. 49, no. 6, pp. 1189-1193, Dec. 2000.

[Händel 08] P. Händel, “Parameter estimation employing a dual-chanel sine-wave model under a Gaussian assumption,” *IEEE Trans. Instrum. Meas.*, vol. 57, no. 8, pp. 1661-1669, Aug. 2008.

[Händel 10] P. Händel, “Amplitude estimation using IEEE-STD-1057 three-parameter sine wave fit: Statistical distribution, bias and variance,” *Measurement*, vol. 43, no. 6, pp. 766-770, July 2010.

[Harris 78] F. J. Harris, “On the use of windows for harmonic analysis with the discrete Fourier transform,” *Proceedings of the IEEE*, vol. 66, no.1, pp 51–83, Jan. 1978.

[Jain 79] V. K. Jain, W. L. Collins, and D. C. Davis, “High-accuracy analog measurements via interpolated FFT,” *IEEE Trans. Instrum. Meas.*, vol. IM-28, no. 2, pp. 113-122, June 1979.

[Kang 09] Sang-Hee Kang, Dong-Gyu Lee, Soon-Ryul Nam, P. A. Crossley, and Yong-Cheol Kang, “Fourier transform-based modified phasor estimation method immune to the effect of the dc offsets,” *IEEE Trans. Power Del.*, vol. 24, no. 3, pp. 1104-1111, July 2009.

[Kay 93] S. M. Kay, *Fundamentals of Statistical Signal Processing: Estimation Theory*, vol. 1, Upper Saddle River, NJ: Prentice-Hall, 1993.

[Kollár 94] I. Kollár, “Bias of mean value and mean square value measurements based on quantized data,” *IEEE Trans. Instrum. Meas.*, vol. 43, no. 5, pp. 733-739, Oct. 1994.

[Macii 12] D. Macii, D. Petri, and A. Zorat, “Accuracy analysis and enhancement of DFT-based synchrophasor estimators in off-nominal conditions,” *IEEE Trans. Instrum. Meas.*, vol. 61, no. 10, pp. 2653-2664, Oct. 2012.

[Mai 10] R. K. Mai, Z. Y. He, L. Fu, B. Kirby, and Z. Q. Bo, “A dynamic synchrophasor estimation algorithm for online application,” *IEEE Trans. Power Del.*, vol. 25, no. 2, pp. 570-578, Apr. 2010.

[Marple 87] S. L. Marple, *Digital spectral analysis*, Prentice-Hall, Englewood Cliffs, 1987.

[Martin 11] K. Martin, “Synchrophasor standards development – IEEE C37.118 & IEC 61850,” in *Proc. of the 44h Hawaii International Conference on System Sciences*, pp. 1-8, Jan. 2011.

[Moschitta 05] A. Moschitta and P. Carbone, “Statistical efficiency of sinewave fitting when using nonlinear quantizers,” in *Proc. of the IEEE Instrum. Meas. Technol. Conf.,* Ottawa, ON, Canada, May 2005, pp. 510-515.

[Novotný 06] M. Novotný, M. Sedláček, Influence of quantization noise on DFT-based DSP algorithms, XVIII IMEKO World Congress, Metrology for a Sustainable Development, September, 17-22, Rio de Janeiro, Brazil, 2006.

[Novotný 07] M. Novotný, D. Slepička, and M. Sedláček, “Uncertainty analysis of the RMS value and phase in frequency domain by noncoherent sampling”, *IEEE Trans. Instrum. Meas.*, vol. 56, no. 3, pp. 983-989, June 2007.

[Nuttall 81] A. H. Nuttall, “Some windows with very good sidelobe behavior,” *IEEE Trans. Acoustics, Speech, and Signal Processing*, vol. ASSP-29, no.1, pp 84–91, Feb. 1981.

[Offelli 90a] C. Offelli and D. Petri, “A frequency-domain procedure for accurate real-time signal parameter measurement”, *IEEE Trans. Instrum. Meas.*, vol. 39, no. 2, pp. 363-368, April 1990.

[Offelli 90b] C. Offelli and D. Petri, Interpolation techniques for real-time multifrequency waveform analysis, *IEEE Trans. Instrum. Meas.*, vol. 39, no. 1, pp 106 – 111, Feb. 1990.

[Offelli 92] C. Offelli and D. Petri, “The influence of windowing on the accuracy of multifrequency signal parameter estimation,” *IEEE Trans. Instrum. Meas.*, vol. 41, no. 2, pp. 256-261, Apr.1992.

[Papoulis 89] A. Papoulis, *Probability, Random Variables, and Stochastic Processes*, New York: McGraw Hill, 1989.

[Premerlani 08] W. Premerlani, B. Kasztenny, and M. Adamiak, "Development and implementation of a synchrophasor estimator capable of measurements under dynamic conditions," *IEEE Trans. Power Del.*, vol. 23, no. 1, pp. 109-123, Jan. 2008.

[Petri 90] D. Petri, *Real-time estimation of the parameters of a multifrequency signal in frequency-domain methods* (in Italian), Ph. D. dissertation, Università degli Studi di Padova, February 1990.

[Petri 02] D. Petri, "Frequency-domain testing of waveform digitizers," *IEEE Trans. Instrum. Meas.*, vol. 51, no. 3, pp. 445-453, June 2002.

[Petri 11] D. Petri and D. Belega, "Transient Behavior of the Full-Cycle DFT Phasor Estimator," in *Proc. of the IEEE Workshop on Applied Measurements for Power Systems (AMPS)*, pp. 31-36, Aachen, Germany, Sept. 28-30, 2011.

[Petri 13] D. Petri, D. Belega, and D. Dallet, *Dynamic testing of analog-to-digital converters by means of the sine-fitting algorithms*, in the book Design, Modeling, and Testing of Data Converters, Springer Verlag, Germany, in press.

[Phadke 08] A. G. Phadke and J. S. Thorp, *Synchronized Phasor Measurements and Their Applications*, Springer Science, 2008.

[Phadke 09] A. G. Phadke and B. Kasztenny, "Synchronized phasor and frequency measurement under transient conditions," *IEEE Trans. Power Del.*, vol. 24, no. 1, pp. 89-95, Jan. 2009.

[Ramos 06] P. M. Ramos, M. F. da Silva, R. C. Martins, and A. M. Cruz Serra, "Simulation and experimental results of multiharmonic least-squares fitting algorithms applied to periodic signals," *IEEE Trans. Instrum. Meas.*, vol. 55, no. 2, pp. 646-651, Apr. 2006.

[Rife 70] D. C. Rife and G. A. Vincent, "Use of the discrete Fourier transform in the measurement of frequencies and levels of tones," *Bell Syst. Tech. J.*, vol. 49, pp. 197-228, 1970.

[Roscoe 12] A.J. Roscoe, I.F. Abdulhadi, and G.M. Burt, "Filters for M class phasor measurement units," in *Proc. IEEE Int. Work. Applied Measurements for Power Systems (AMPS)*, pp. 1-6, Aachen, Germany, Sept. 2012.

[Schoukens 92] J. Schoukens, R. Pintelon, and H. Van Hamme, "The interpolated fast Fourier transform: a comparative study," *IEEE Trans. Instrum. Meas.*, vol. 41, no. 2, pp. 226-232, Apr. 1992.

[Serna 07] J. A. de la O Serna, "Dynamic phasor estimates for power system oscillation," *IEEE Trans. Instrum. Meas.*, vol. 56, no. 5, pp. 1648-1657, Oct. 2007.

[Sidhu 99] T. S. Sidhu, “Accurate measurement of power system frequency using a digital processing technique,” *IEEE Trans. Instrum. Meas.*, vol. 48, no. 1, pp. 75-81, Feb. 1999.

[Sidhu 03] T. S. Sidhu, X. Zhang, F. Albasri, and M. S. Sachdev, “Discrete-Fourier-transform-based technique for removal of decaying dc offset from phasor estimates,” *IEE Proc. Gener. Transm. Distrib.*, vol. 150, no. 6, pp. 745-752, Nov. 2003.

[Sidhu 05] T. S. Sidhu, X. Zhang, and V. Balamourougan, “A new half-cycle phasor estimation algorithm,” *IEEE Trans. Power Del.*, vol. 20, no. 2, pp. 1299-1306, Apr. 2005.

[Söderström 89] T. Söderström and P. Stoica, *System Identification*, Englewood Cliffs, N. J: Prentice-Hall, 1989.

[Solomon 94] O. M. Solomon, “The use of DFT windows in signal-to-noise ratio and harmonics distortion computations”, *IEEE Trans. Instrum. Meas*., vol. 43, no. 2, pp. 194-199, April 1994.

[Std. 1241] *IEEE Std. 1241, Standard for Terminology and Test Methods for Analog-to-Digital Converters*, December, 2000.

[Std. 1570] *IEEE Std. 1057, IEEE Standard for Digitizing Waveform Recorders*, 2007.

[Std. C37.118.1] *IEEE Standard C37.118.1*, *Standard for Synchrophasor Measurements for Power Systems*, Dec. 2011.

[Wagdy 89] M. F. Wagdy and W.-M. Ng, Validity of uniform quantization error model for sinusoidal signals without and with dither, *IEEE Trans. Instrum. Meas*., vol. 38, no. 3, pp. 718-722, June 1989.

[Widrow 96] B. Widrow, I. Kollár, and M. –C. Liu, “Statistical theory of quantization,” *IEEE Trans. Instrum. Meas.*, vol. 45, no. 2, pp. 353-361, Apr. 1996.

[Yang 00] Jun-Zhe Yang and Chinh-Wen Liu, “Complete eliminination of dc offset in curent signals for relaying applications,” in *Proc. of the IEEE Power Engineering Society Winter Meeting*, pp. 1933-1938, 2000.

[Yu 06] Chi-Shan Yu, “A discrete Fourier transfor-based adaptive mimic phasor estimator for distance relaying applications,” *IEEE Trans. Power Del*., vol. 21, no. 4, pp. 1836-1849, Oct. 2006.

[Yu 10] C. S. Yu, Y. S. Huang, and J. A. Jiang, “ A full- and half-cycle DFT-based techniques for fault current filtering,” in *Proc. IEEE Conference on Industrial Technology (ICIT)*, pp. 859-864, Mar. 2010.